UNIVERSITÉ PARIS-SUD

ÉCOLE DOCTORALE 422 :
SCIENCES ET TECHNOLOGIES DE L'INFORMATION DES TÉLÉCOMMUNICATIONS ET DES SYSTÈMES

Laboratoire de Génie Electrique de Paris

THÈSE DE DOCTORAT

PHYSIQUE

par

EL Hadji Sidath DIAO

Fault Tolerant Control for Critical machine-inverter systems used in automotive industry

Date de soutenance : 13/11/2014

Composition du jury :

Directeur de thèse :	Demba DIALLO	Professeur des Universités à l'Université Paris Sud
Encadrant :	Zaatar MAKNI	Docteur-Ingénieur (VALEO EEM)
Président du jury :	Gérard CHAMPENOIS	Professeur des Universités à l'Université de Poitiers
Rapporteurs :	Maria DAVID	Professeur des Universités à l'ENSEEIHT de Toulouse
	Xavier KESTELYN	Professeur des Universités aux Arts et Métiers de Lille
Examinateurs :	Claude Marchand	Professeur des Universités à l'Université Paris Sud
	Jean-François BISSON	Ingénieur-Chef d'équipe (VALEO EEM)

Remerciements

Les travaux de recherche qui font l'objet de ce mémoire se sont déroulés conjointement au Laboratoire de Génie Electrique de Paris (LGEP) au sein de l'équipe COCODI (Conception, Commande et Diagnostic) du département MOCOSEM (Modélisation et Contrôle de Systèmes Électromagnétiques) et dans l'équipe Simulation de VALEO EEM du Groupe d'expertise et de développement de services (GEEDS). Mes plus vifs remerciements vont à toutes les personnes qui ont rendu possible cette collaboration CIFRE et je profite donc un tant soi peu de cette occasion pour les remercier.

Je remercie M. Gérard CHAMPENOIS, Professeur à l'Université de Poitiers, d'avoir accepté de présider le jury de ma thèse. Je remercie également Mme Maria DAVID, Professeur à l'ENSEEIHT et M. Xavier KESTELYN, Professeur à l'Université de Lille, pour l'intérêt qu'ils ont porté à ce travail en acceptant d'en être les rapporteurs, ainsi que pour les remarques pertinentes qu'ils ont apporté.

Je remercie M. Claude MARCHAND, Professeur à l'Université Paris-Sud, Responsable du département MOCOSEM et lui exprime ma gratitude pour son suivi et ses encouragements tout au long de la thèse. Je remercie également M. Frédéric BOUILLAULT, Professeur à l'Université Paris-Sud, Directeur du LGEP.

Aussi, cette thèse n'aurait pas eu lieu sans l'apport et le soutien du chef de l'équipe Simulation de Valeo EEM Jean-François BISSON qui a mis les moyens nécessaires au bon déroulement de cette thèse. Qu'il trouve ici l'expression de ma profonde reconnaissance ainsi que tous mes collègues de l'équipe Simulation avec qui j'ai toujours eu un grand plaisir à échanger (Fatma, Samuel, Delphine, Richard, Hussein, Renan, Jean-Louis).

Je remercie M. Zaatar MAKNI, Docteur Ingénieur à Valeo EEM pour son encadrement durant cette thèse et pour son aide précieuse à certains moments clé de mon travail. Pour les moments qu'il a passé avec moi surtout sur la partie expérimentale, je lui en suis reconnaissant.

Je remercie tout particulièrement mon directeur de thèse M. Demba DIALLO, Professeur à l'Université Paris-Sud pour son soutien durant ces années de thèse. En sus de ses qualités scientifiques dont il m'a fait profiter aux travers de ses remarques pertinentes et constructives, il a fait preuve de patience et m'a offert une certaine autonomie tout en étant disponible aux moments clés.

Je tiens aussi à remercier M. Eric BERTHELOT, Ingénieur d'Etude au département MOCOSEM, pour son aide pour le développement du dispositif expérimental. Je remercie aussi Olivier HUBERT, administrateur du réseau informatique et toute l'équipe administrative dirigée par Françoise JUBIN pour l'aide apportée. Mes remerciements s'adressent également à tous mes collègues et amis pour leurs soutiens et encouragements.

Je remercie enfin, et tendrement, ma famille qui m'accompagne au quotidien, pour m'avoir suivi, encouragé et soutenu durant cette longue aventure.

“Aussitôt qu'on nous montre quelque chose d'ancien dans une innovation, nous sommes apaisés“ F. Nietzsche

“ C’est par la médiation du travail que la conscience vient à soi-même “ F. Hegel

“ Nous ne connaissons a priori des choses que ce que nous y mettons nous-mêmes “ E. Kant

Glossary

Abbreviations

ASIC Application-specific integrated circuit

ADC Analog to Digital Converter

EMC Electromagnetic Compatibility

DSP Digital signal processing

CPU Central Processing Unit

EN European norm

ECU Electronic Control Unit

FPGA Field-programmable gate array

ICE Internal Combustion Engine

IEA International energy agency

IGBT Insulated-gate bipolar transistor

ISO International Organization for Standardization

PMSM Permanent Magnet Synchronous Machine

PI Proportional Integral

SOFRACI Structure onduleur fort rendement à fonction de charge intégrée

PWM Pulse Width Modulation

EMF Electromotive Force

EV Electrical Vehicle

HEV Hybrid Electrical Vehicle

XSG Xilinx System Generator

Mathematical Quantities

d,q	Rotating frame axis
α,β	Stationary frame axis
R	Rotation matrix

Electrical, Mechanical and Magnetic Quantities

C	Capacitor
$e_{s\alpha}$	α,β component of electromotive force
i_{abc}	stator phase currents
$i_{s\alpha\beta}$	α,β component of phase currents
i_d	*direct* axis current

$i_{DC/DC}$	DC Link current
i_h	homopolar current
i_q	quadrature axis current
i_{qref}	quadrature axis current reference
K_t	electromotive force constant
L_d	direct axis inductance
L_q	quadrature axis inductance
p	pole pairs
R_s	stator resistance
T_{em}	electromagnetic torque
T_l	load torque
U_{DC}	DC link voltage
v_{abc}	stator phase voltages
$v_{s\alpha\beta}$	α,β component of phase voltages
v_d	*direct* axis voltage
v_q	quadrature axis voltage
θ	measured electrical position
ϕ_m	magnet flux
ω_e	electrical speed in rad/s
ω	mechanical speed

Figures

Tables

INTRODUCTION

Electric mobility and zero emission vehicles are key factors for sustainable transport. In the wake of the technological advances, automotive suppliers are focusing their efforts on reducing CO_2 emissions and on the "intuitive driving", which combines the connected vehicle, autonomous driving and the man-machine interface, making them accessible to all. Mechanical actuators are being replaced by electric power systems which have faster time response. Despite that the automotive industry is cost sensitive, there are strong incentives to increase system costs in order to improve the level of safety with new risk-based safety standards. Naturally, proper operations of certain functions are of utmost importance and their failure cannot be tolerated since this would drastically compromise safety. Moreover, the dependence on a continuous power supply causes problems with vehicle propulsion and an electric energy source must be carried on-board, which is usually heavy and expensive (storage battery, rotating generator with internal combustion engine, fuel or solar cells). This requires the embedded energy to be smartly used and to cope with faults that highly increase energy consumption (e.g. a sensor fault which induces an over-current).

Electrical drives adopting permanent-magnet synchronous machines (PMSM) are suitable for a wide range of applications in cars. These applications include not only propulsion but also steer and brake-by-wire systems, active suspension, electrical compressors and other electrical subsystems. For PMSM drives used for propulsion, it is evident that increasing the level of reliability that goes with a significant cost cannot be motivated if a fault is not significantly increasing the accident risk or if a post-fault strategy cannot be economically motivated for the specific vehicle model. That's the main difference with aerospace domain where a high safety level is requested and then, needs on Fault Tolerant Control (FTC) are more justified. In addition, with last standards to improve functional safety for automotive electric/electronic system, FTC is well suited to increase the reliability, the availability and the continuous operation of electromechanical systems.

This study focuses on fault responses of PMSM drives as well as methods for increasing the level of fault tolerance for such drives in automotive applications. There is no doubt that a good Fault Detection and Diagnosis (FDD) goes with a well understanding of faults origins and consequences. The term *drive* pertains to both the electric machine as well as its corresponding inverter although faults can arise in other parts including sensors.

Precisely, the objective of this thesis is to detect and isolate the sensors faults at their incipient stage and perform a post-fault reconfiguration if possible. To this purpose, the work goes from theoretical studies toward experimental validations through the model simulation. The outline of the thesis is summarized as follows:

- In **chapter 1**, electrical drives challenges in automotive systems and FTC principle are recalled. Consequences of the faults in the drive operation and the existing solutions proposed to overcome these faults are reviewed.

- **Chapter 2** describes the test bench with the targeted application. The system is designed for traction, battery charging and energy regeneration of an EV with an optimization of the powertrain elements. After the modeling and the simulation of the PMSM and its inverter, the control of the electrical drive is implemented in real time using Matlab/Dspace. Experimental tests on the PMSM torque control are done to illustrate the control low. Then, the diagnosis in traction mode with an emphasis on the most critical sensors (mechanical position, phase currents and the DC-link voltage) can now be performed in the next chapters.

- The position/speed sensor FTC is treated in **chapter 3**. Different ways to estimate the rotor position and the speed are addressed and their advantages/drawbacks listed. Thereafter, a new estimator based on a differential algebraic approach is designed and experimental results are provided to validate this approach. Comparison with respect to existing methods (EKF, Back-EMF Observer) using relevant criteria such as accuracy and implementation capability is also performed to better address the new method. Finally, an observer FTC-based is performed and its validity is tested through experimental position sensor fault injection.

- **Chapter 4** is dedicated to phase current and DC link voltage FDD sensors. In this chapter, only a fault detection and isolation (FDI) is done. Two diagnosis methods have been developed for the currents: a differential algebraic approach and a signal processing one. Because three current sensors are used, the isolation step has a major importance. After a reminder on the commonly used methods and an experimental validation of the solutions mentioned above, a comparative study is done with experimental current sensor fault injection. For the DC link voltage sensor, an observer using the phase currents and the duty cycles is designed to monitor the sensor value. Experimental results are also provided to support the proposed approach.

Chapter I: State of the art of electrical drives fault tolerant control

1.1 Electrical Drives in Automotive Systems

An electrical drive can be defined in terms of ability to efficiently convert energy from an electrical power source to a mechanical load [DeD2011]. It is adaptable to almost any operating conditions and can be designed to operate in all four quadrants of the torque-speed-plane.

Transportation sector is a high mechanical energy consumer. The transformation of primary energy (fossil) produces pollution and according to the International Energy Agency [Iae2013], CO_2 emissions have increased by 1.4% in 2012.

Nowadays, electric power is coming to be seen as a solution to the pollution caused by cars, e.g. reducing the CO_2 emissions [Ber2010]. In new vehicles the number of electrical actuators is growing steadily. They are used for example (Figure 1.1):

- To compress the cooling gas and provide the conditioned air.
- actuate the windscreen wipers,
- to assist the driver for steering; it gives more assistance as the vehicle slows down, and less at higher speeds and the system has an advantage in fuel efficiency compared to a hydraulic system because there is no belt-driven hydraulic pump constantly running.

Figure 1.1 Electrical Drives in Vehicle [*courtesy of Valeo*]

However the challenge is to develop electrical powertrain for vehicle propulsion. After the first attempts at the beginning of the 20th century, the main challenge was the introduction of cost effective electrical power in the propulsion. In fact, the key points are to:

- Embed enough energy in the vehicle to guarantee enough autonomy,
- Guarantee at least the same level of security and performances as a vehicle propelled with Internal Combustion Engine (ICE).

The most mature technologies for energy storage devices in electrical propulsion are electrochemical batteries and fuel cells. Figure 1.2 shows the different solutions sorted depending on their level of maturity and on their high energy or high power capability.

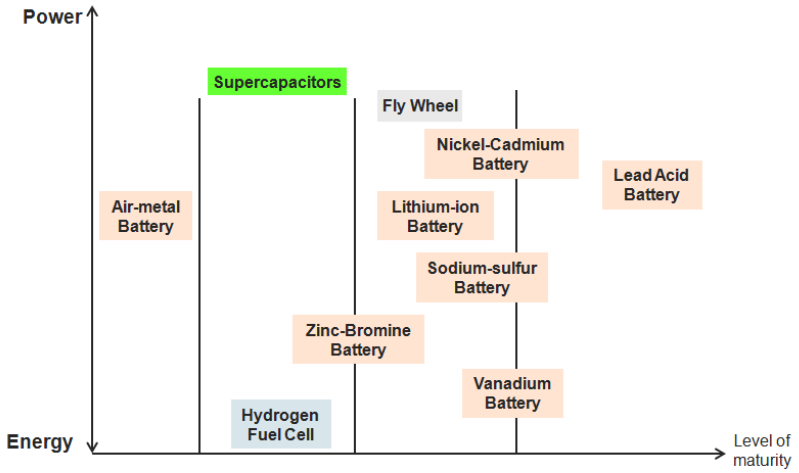

Figure 1.2 Storage devices for electrical propulsion

Many cars using electrical propulsion are already commercially available (Honda Fit EV, Nissan Leaf, Renault Kangoo, Zoe and Fluence, Toyota Prius, Peugeot iOn, Citroen C-Zero and Mitsubishi i-Miev). However, the first step in the use of storage device was its combination with ICE: hybrid vehicle or hybrid electrical vehicle.

Hybrid vehicles are often classified into four categories: Micro hybrid, Mild hybrid, Full hybrid and plug-in hybrid (Figure 1.3). Micro hybrids are essentially conventional vehicles with an starter- alternator allowing the engine to be turned off whenever the car is coasting, braking, or stopped, yet restart quickly and cleanly [Bru2009]. In the Mild hybrids, the starter-alternator is replaced by a more powerful electrical motor improving the regenerative braking [Mor2012]. A full hybrid EV can be propelled by the ICE, the electrical motor or both [Sta2006]. A plug-in hybrid electric vehicle (PHEV) is a full hybrid able to run in electric-only mode, with larger batteries and the ability to recharge from the electric power grid. Their main benefit is that they can be gasoline-independent for daily commuting, but also have the

extended range of a hybrid for long trips. Recently, it has been observed many improvements for conventional vehicles in terms of consumption (injection) or pollution (catalytic converters). Although these changes have been applied to hybrid vehicles, their electrical part grows. Obviously, there is a logical trend toward complete electrification of the entire vehicle. In this evolution, the structure of the powertrain will be simplified by the use of only electric motors, which will allow a more significant reduction of the pollution [Raj2013].

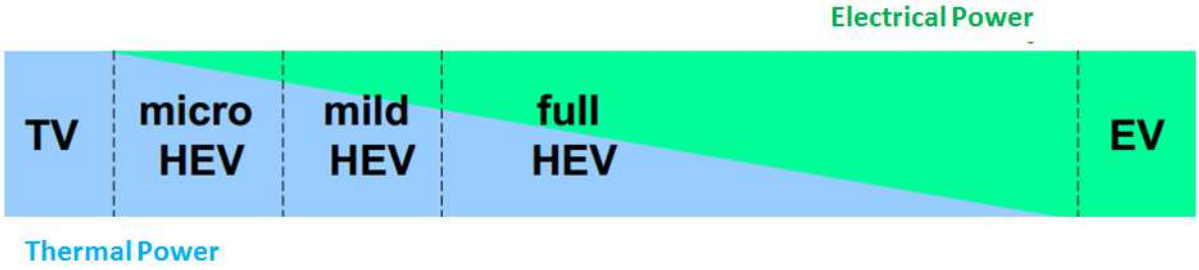

Figure 1.3 Power ratio classification [Chan2007]

In fact, full electrical propulsion has several advantages over its ICE counterpart:

- Environmentally friendly with no CO_2 and Nox emissions,
- The possibility to store braking energy or feed it back to the power line,
- More flexibility and a higher intrinsic efficiency.
- No need of maintenance

However, there are still some drawbacks and issues:

- Energy efficiency must be improved to increase the embedded energy and power densities,
- Because the average failure rate of the electrical powertrain is higher than mechanical components (due to severe operation condition), the design and control of the whole drive (electrical machines, power converters, sensors, electronics) must be conservative and efficient enough to ensure the security and the safety.

For propulsion purposes, the electrical machines must operate in a wide speed range with specific characteristics defined by the car maker as displayed for e.g. in Figure 1.4 for the Fluence Z.E of Renault.

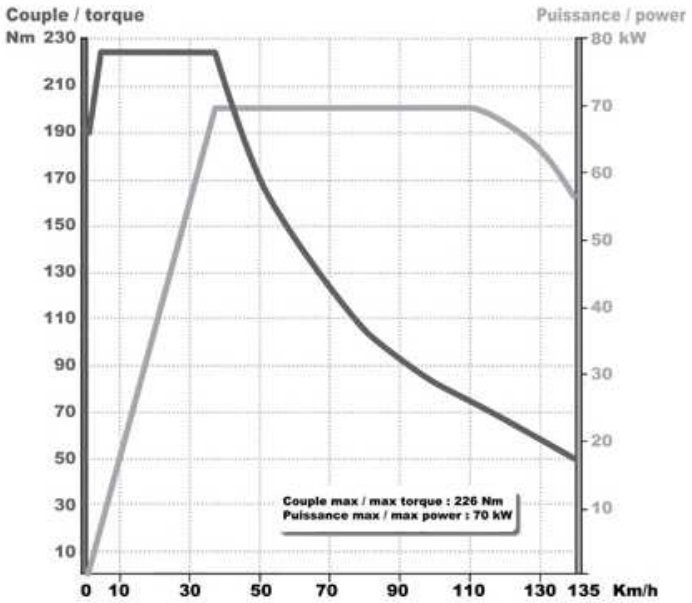

Figure 1.4 Torque and power curves for Fluence Z.E.

Moreover, the electrical machine must be also designed under various constraints such as:

- Limited volume and high efficiency,
- Low cost,
- Free maintenance,
- Robustness.
- Noise

Therefore, there is a big competition between the different technologies. The following table gives some comparative elements.

Table 1.1: Electrical Machines used in automotive industry

	Power Density	Cost	Control	Maintenance	Robustness
DC Machine	--	--	+++	--	--
Induction Machine	**+**	**++**	+	**++**	**+++**
Switched Reluctance Machine	**+**	**+++**	++	**++**	**+++**
Permanent Magnet Synchronous Machine	**+++**	-	**++**	+	**+**
Wound Rotor Synchronous Machine	**++**	-	**+**	-	-

As it can be seen, there is no optimal solution and all the electrical machine are potential candidates and have been used in electrical vehicle propulsion (Induction Machines for GM

and the Renault Kangoo, Synchronous Machine for the Toyota Prius, DC Machine in the hybrid Citroen Berlingo, Switched Reluctance Machine for Holden ECOmmodore). The question is still opened for research activities [Hag2014]. Despite the difficulties related to the cost of rare earth used in magnets, Permanent Magnet Synchronous Machine (PMSM) is a valuable candidate for electrical drives in many applications.

For systems with low security and safety requirements, such as flaps and nose wheel steering, electrical drives can fulfill them. However, if the electrical drive is used in the vehicle propulsion, safety becomes mandatory with the highest standards as mentioned in ISO26262 [Iso2009]. Risk analysis performed for electrical vehicles lead to conservative design rules and to the necessity of monitoring the electrical drive to detect and diagnose faults at their earliest stage to avoid any failure.

1.2 Fault Management

The Functional Safety is to know, assess, predict, detect and control failures of technological systems and human failures to avoid the consequences on the health and safety of people, loss of productivity, damage to the environment and the preservation of the planet resources. Historically, the first studies appeared primarily in rail transport for the development of statistical compilations of mechanical parts. Quantitative studies were based on the identification of elements supposed to be critical, for which improvements of the technical design were needed. The development of aviation led to the evaluation of the operational flight safety of aircraft propelled by several motors. From that moment, objectives in terms of probability of accidents occurrence per hour of operation were introduced [Zwi2009].

In the 1950s, the advent of electronics in complex equipments made aware of the importance of their reliability. The 1970 decade saw the dissemination of operational evaluation methods of reliability in industrial sectors presenting risks to people and the environment. Currently, there is almost no industrial activity where the functional safety is not taken into account throughout the life cycle of the product (design, manufacturing, operation and maintenance).

In addition, the implementation of embedded systems in industrial systems has imposed very stringent security constraints in transportation (automotive, aeronautic, rail industry).

1.2.1 Fault detection and diagnosis principle

Let us first underline the difference between a failure and a fault. A failure is the inability of an element or a system to perform a function as required while a fault is an abnormal condition that can cause an element or a system to fail [Iser2006]. For example, a steering column locked is a failure and an open resistor a fault.

In industrial systems, the monitoring system, which includes hardware (data collection) and software processes the data (monitors fault conditions and generates alarms) and gives a graphical representation updated periodically. Its role is to assist the human operator for emergency management to increase the reliability, availability and functional safety. Supervision takes place in a hierarchical structure (with at least two levels), and covers the occurrence of normal and abnormal operation: the faults are modeled based on events or binary states [Bat2011]. The main activities involved in the supervision of a continuous system are grouped in the fault tolerant control which is divided into three stages: detection, isolation and reconfiguration. The detection consists in identifying online changes on variable behavior. The isolation is then to discriminate which faulty variable has generated the symptom detected from the alarms enabled in the multi-sources case. Then the reconfiguration is to provide corrective control action to bring the system to normal operation (or in a limp mode that is to say, tolerated by the system).

The concept of integrating automated fault detection and diagnosis came at the beginning of the 1980's, as a functionality of supervision systems. The specification for a monitoring system is to determine the relevant equipments to supervise, while minimizing false alarms, non-detections and delays in the detection. Obviously, constraints in terms of computer memory and costs must be taken into account. Therefore, there is always a compromise between the number of faults to monitor and diagnosis performance. Generally, relevant equipments can be determined off-line by the FMEA (Failure Mode and Effects Analysis) [SAE1967]. Then after the fault detection, different actions can be taken to ensure the continuity of the process even if in some cases only a safe stop is possible. However, a little attention has been paid to the analysis and design with the overall system structure and interaction between **F**ault **D**etection and **D**iagnosis (FDD) and **R**econfigurable **C**ontrol (RC).

How to analyze systematically the interaction between FDD and RC? How to design the FDD and RC in an integrated manner for on-line and real-time applications?

These challenging issues still remain opened for further research and the solutions vary, depending on the severity and the fault type (gradual, abrupt and intermittent).

Historically, a significant amount of research on FDD systems was motivated by aircraft flight control system designs and nuclear power plants. The goal, therein, was to provide a

safe mode in the event of severe faults. More recently, the fault-detection and diagnosis problem has begun to draw more and more attention in a wider range of industrial and academic communities such as automotive industry, due to increased safety and reliability demands beyond what a conventional control system can offer [Cap2007]. For high-critical safety systems (nuclear plants, aerospace industry), the designers multiply the hardware system so that, for a failure in one system, another system will immediately replace it. This type of maintenance (material redundancy) is clearly too expensive and adds complexity to the design. One can also use an analytical redundancy called software redundancy which models the healthy operation of a certain part of the system. With recent progress in high performance processors, software redundancy has become a promising alternative. This last solution is much more attractive because of its flexibility and its capability of evolution.

The diagnosis methods are mainly classified into two categories: model-based (quantitative) and data-driven-based (qualitative) methods (Figure 1.5).

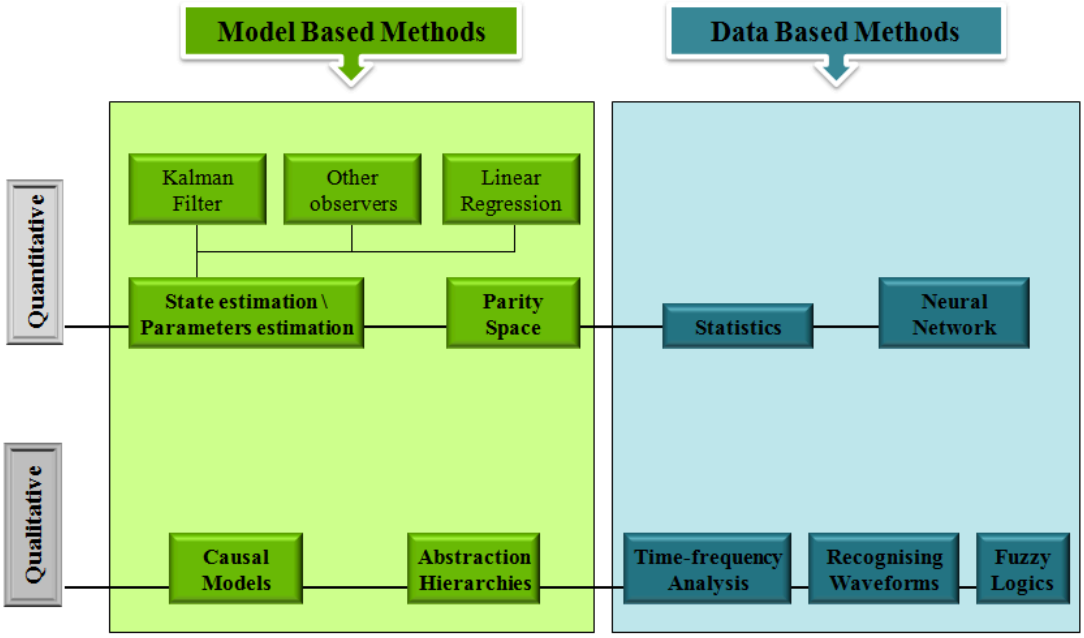

Figure 1.5 Diagnosis methods

For a model-based method (observers, state estimators), the detection scheme relies on a prior knowledge of the system. Signals generated by the models (estimated data) enable detection as well as the identification of the fault [Chen1999]. The objective is for the observers to generate residuals by making the difference, eventually filtered, between the actual and the estimated features (variables or parameters). Then, faults are detected by analyzing these residuals.

Data-driven-based methods, which can be considered as signal processing methods are based on the knowledge of signatures ([Yin2014, Ven2003]). The most common methods are

spectral analysis, spectrogram and temporal analysis. They allow fault detection by analyzing relevant criteria such as variable probability density. Artificial Neural networks are also of high interest and they act as a reference tool for processing problems of classification. The neural network is responsible for the knowledge and the classification of faults using a training database.

1.2.2 Fault Tolerant Control principle

Depending on how the redundancy is being used, existing efforts in FTC design can be classified into two main approaches: passive and active (Figure 1.6). In a passive approach, the conceivable system component's faults and/or failures are assumed to be known a priori, and the control system takes into account all these faults and/or failure modes at the design stage [Yan2000]. Once the control system is designed (if it exists), it will remain frozen during the entire system operation. Even in the event of component faults and/or failures, the control system should still be able to maintain the initial performances. In other words, in a passive FTCS, one has to ensure that the control system works under all possible system operating scenarios that have been considered at the design stage, including potential component faults and/or failures. However, the system performance could be unacceptable in the presence of un-anticipated failures. Because a passive FTCS has to maintain the system stability with various component failures, from the performance viewpoint, the designed controller has to be conservative. From typical relationships between the optimality and the robustness, it is very difficult for a passive FTCS to be optimal.

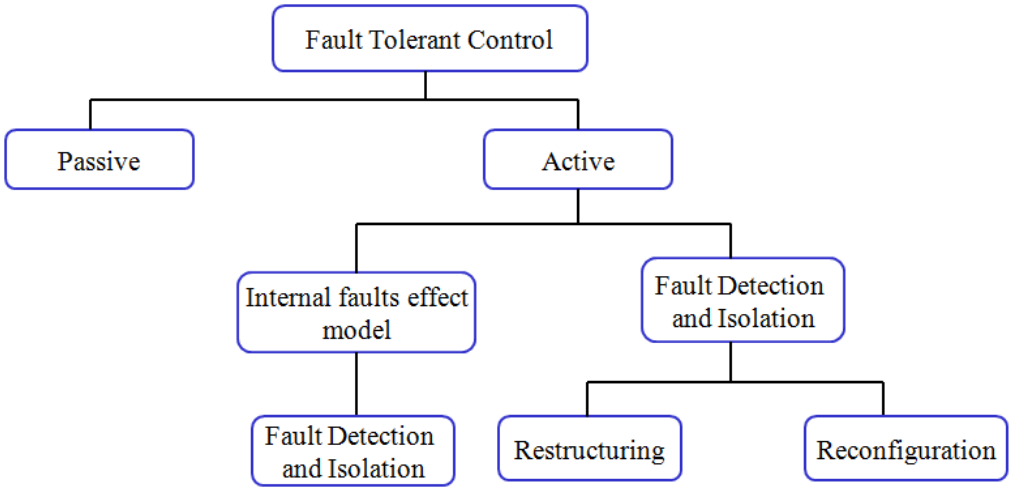

Figure 1.6 General view of Fault Tolerant Control

In contrast, an active FTCS reacts to the system component faults and/or failures actively by properly reconfiguring its control actions so that the stability/performance of the entire system can still be acceptable.
To achieve a successful control system reconfiguration, this approach relies heavily on a real-time fault detection/diagnosis scheme for the most up-to-date information about the status of the system and the operating conditions [Pat1997]. The critical issue facing any active FTCS is the shortness of the reaction time available to perform fault detection and diagnosis and control system reconfiguration. The speed, the accuracy, and the robustness of these schemes are the factors to the success of any active FTCS. If designed properly, an active FTCS will be able to deal with unforeseen faults and will have the potential to achieve optimal performance for different operating scenarios.

Given the fact that only a limited amount of time and information may be available, it is potentially likely that nature and the exact location of the faults may not be accurately pinpointed out for an active FTCS. In case of a rapidly developing fault, it would be highly desirable if one could have a FTCS that possesses the guaranteed stability property as in a passive FTCS, but also with the performance optimization attribute as in an active FTCS. This is the main motivation behind the recent development on hybrid fault-tolerant control systems by combining both active and passive approaches [Fek2006].
In any cases, there are currently numerous detection methods in the literature but they have generally been validated on simple experimental test bench or simulation tests. Moreover, these methods are based for a large part on advanced control theory which is unfamiliar in the industry, excepted Proportional-Integral-Derivative (PID) control technologies that are completely adopted since their introduction. Currently, monitoring systems and tools for decision support are managed primarily by the expertise of the human operator, which still remains at the center of the supervision system. But beside the safety and security related constraints, cost of materials and energy has become a serious issue. Therefore the two-step classical approaches that consists in designing the process and then build the controller (including diagnosis and reconfiguration) has to be thought differently.
In automotive systems, there is an increasing trend towards online real-time diagnostic algorithms embedded in the Electronic Control Units (ECU). With the advance in remote support, the maintenance technician can use new tools with optimized and adaptive state-dependent test procedures. At this stage, if the root cause is still not identified, the history of sensor data and symptoms are processed for further refined diagnosis.

The automotive industry has adopted quantitative simulation as a vital tool for a variety of functions including algorithm design for ECU, rapid prototyping, Hardware in the loop (HIL) simulation system development and production code generation [Luo2007]. However, there is a lack of investigation on the implementation of mathematical and graph-based diagnosis model. The best choice for fault diagnosis is an integrated diagnostic process that combines data driven techniques, graph based dependency, models and mathematical/physical models, thereby taking advantages of each method.

1.3 Application to an electrical system

The general principles of Fault management recalled in the last section are now applied to an electrical drive. For functional safety aspects, ISO26262 is the new international standard for automotive industry. For control algorithms like Simulink models, Model-Based Design (MBD) is necessary to perform specific analyses and consistency checks. Table 2 gives the requirements and methods needed to fulfill the safety standard when using MBD.

Table 1.2: ISO26262 Safety requirements related to Model Based Design [Iso2011]

Requirement	Method	ASIL[a, b]			
		A	B	C	D
Methods for software unit testing	Fault injection test	+	+	+	++
	Back-to-back comparison test between model and code, if applicable	+	+	++	++
Structural coverage metrics at the software unit level {In case of MBD, structural coverage can be performed at the model level}	Statement coverage	++	++	+	+
	Branch coverage	+	++	++	++
	MC/DC (Modified Condition/Decision Coverage)	+	+	+	++
Methods for software integration testing	Fault injection test	+	+	++	++
	Back-to-back comparison test between model and code, if applicable	+	+	++	++

[a] ASIL stands for Automotive Safety Integrity Level (ASIL)-oriented and safety-oriented analyses

[b] For each method, the degree of recommendation to use the corresponding method depends on the ASIL and is categorized as follows:

- "++" indicates that the method is highly recommended for the identified ASIL;
- "+" indicates that the method is recommended for the identified ASIL;

The fault injection test includes injection of arbitrary fault (inserting bias, introducing code mutations…) while the back-to-back tests are used to ensure the matching between the behavior of the model with respect to the test objectives and the automatically-generated codes.

An example of implementation of a FTC for an electrical drive is given in Figure 1.7. The data used for the diagnosis is a combination of the inverter outputs and the sensors. Healthy characteristics of the variables to diagnose are sometimes added. The choice of using healthy characteristics and their availability depends on the fault type.

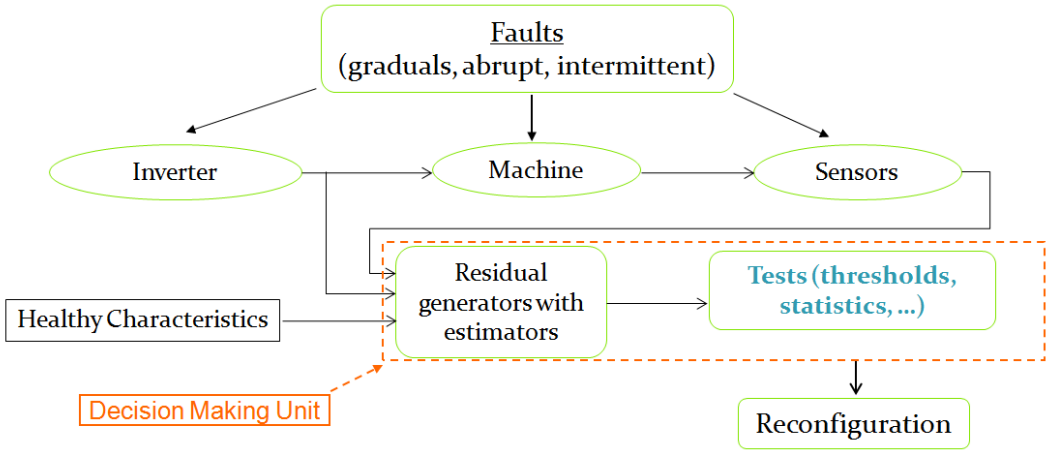

Figure 1.7 Fault Tolerant Control System

1.3.1 Fault types in electrical drive

For a variable speed drive, the main faults that may arise are summarized in Figure 1.8 where the actuator stands for the inverter and the energy supply.

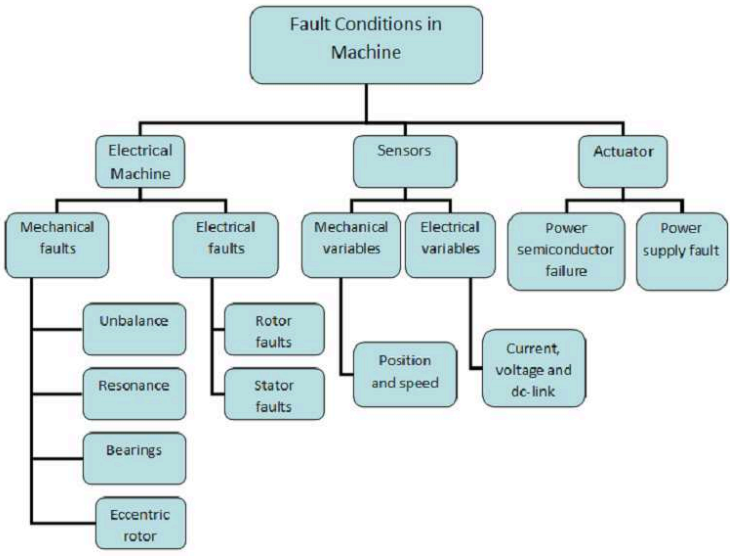

Figure 1.8 Origins of failures in an electrical drive [Del2008]

1) *Actuator fault*

Most of the failures in the energy conversion chain are due to the control circuit and the power converter. In chapter 9 of [Tri2013], one can find the failure rate for the power converter and the components (Tables 3, 4).

Table 1.3: Failure rate of components in the energy conversion chain

Converter failure	38 %
Control circuit failure	53 %
Failure of external and auxiliary components	9 %

Table 1.4: Failure rate of converter components

Continuous bus capacitor	60 %
Power transistors	31 %
Diodes	3 %
Inductive elements	6 %

Most commonly, the power inverter failure is caused by the loss of conduction of one leg apart from natural aging of the components. The main failures are an open gate or base drive, short-circuit in power semi-conductor and power converter switches. The origins of the inverter faults are multiple and are generally caused by hard operating conditions.

If the automated process is running under harsh conditions or simply because of mechanical wearing and aging effects, faults may lead to the interruption of energy transfer.

A power electronic device short-circuit failure produces a similar condition to a winding terminal short circuit. In this case, the faulted device can experience large thermal stresses, which may lead to disintegration of the packaging and propagation of the fault into surrounding power devices. For the reconfiguration, even if oversizing the power components is a good solution, the cost of adding some hardware redundancy to the power actuators must be evaluated. In some cases, expensive solutions for overvoltage protection can be required and this must be compared with a solution using complete hardware redundancy.

There are also external failures such as a power supply or a control interface that can damage the system. Diagnosing the components, and therefore the converter will depend on the availability of measurements, and the ability to interpret them in order to analyze their behavior. The main difficulty lies in the limited number of sensors used, due to cost constraints and packaging problems. Thus, current sensors are mainly find and, more rarely voltage and temperature sensors, which information is useful in controlling the actuator chain.

2) *Sensor faults*

The most usual faults in sensor are DC bias in sensor measurement, high or low saturation of the measurement, gain error or a complete sensor outage. In an electrical drive, a position/speed sensor, two/three phase current sensors and DC link voltage sensor are generally used.

When the position sensor is lost, the standard control which takes place in the rotating frame fails [Akr2010]. The torque production is affected by the misalignment between measured and actual rotor positions. As for the measurement errors, they are due to the quantization or to an accumulation of a periodical error. Phase current sensor fault induce torque ripples and a loss of the drive control for severe cases. The severity of the distortion from normal waveform depends mainly on the fault origin. The measurements coming from the DC energy source (DC voltage and incidentally the DC current) are needed to control the inverter PWM. Their failure causes a variation of the requested voltage for the machine to follow torque/speed reference.

3) *Electrical machine faults*

The most usual machine faults are listed as follows:

- Air-gap eccentricity;
- Bearing damages;
- Broken rotor bars and end-ring faults;
- Stator faults;

There are two types of air-gap eccentricity: static eccentricity and dynamic eccentricity. For a dynamic eccentricity fault, the rotor center is different from the center of the rotation. We have a static eccentricity fault when the rotor moves about its own centerline which doesn't coincide with that of the stator bore. Harsh air-gap eccentricity may lead to unbalanced magnetic pull with eventually a stator to rotor friction. The motor magnetic field is then asymmetric. Bearing faults are characterized by a rotor asymmetry [Zho2007], which is usually covered under the category of eccentricity-related faults quoted above.

Often caused by the high thermal stresses during starting, broken rotor bars and end-ring faults can lead to shaft vibration, and thus induce bearing failures and air-gap eccentricity. Its diagnosis is essential for the rotor protection [Zha2009].

Stator short-circuit faults are very troublesome for permanent-magnet (PM) machines because of a high magnetic field intensity. Consequently, demagnetization could occur and damages the machine.

1.3.2 Fault diagnosis and fault tolerant control for electrical drive

1) Fault Diagnosis

The most used solutions for the detection and the isolation of failures in electrical drives are the data-based and the observer-based methods. A non-exhaustive list of the main faults in an energy conversion chain is given in Table 5.

Table 1.5: Faults and Detection Method in the energy conversion chain

Faults	*Location*	*Detection Method*
Unbalanced voltage or oscillations	Power Supply	*Artificial Intelligence*
Power semiconductor	Inverter	*Data analysis, Artificial Intelligence*
Switches (open or closed)	Inverter	*Artificial Intelligence, Time-Frequency analysis*
Drivers	Inverter (electronic interface)	*Artificial Intelligence or data analysis*
Mechanical sensor DC bias, outage or gain	Sensor and/or electronic interface	*Observers*
Phase currents sensor DC bias, outage or gain	Sensor and/or electronic interface	*Observers, Test voltage at stop*
DC-link voltage sensor, DC bias, outage or gain	Sensor and/or electronic interface	*Power balance equation, Observers*
Eccentricity (dynamic and/or static)	Electrical Machine	*Signal processing*
Broken bar rotors	Electrical Machine	*Signal processing Observers*
Stator interturn short circuit	Electrical Machine	*Artificial Intelligence, Signal processing (Motor current signature analysis, Time-frequency analysis) Observers*
End-ring faults	Electrical Machine	*Signal processing (Statistical Process Control, Time-frequency analysis)*

For converter faults, [Zhou2010] shows a post-fault control strategy for a hexagram inverter. The hexagram inverter motor drive system can realize real two-phase motor operation without modifying the power circuit topology, which is a distinct advantage over conventional three-phase inverter motor drives or other multilevel motor drive systems. When an outer leg fails, since the three output currents in the hexagram motor drive system are independent, it is possible to precisely control the remaining two-phase currents.
For sensor faults, observer-based approach has shown his effectiveness [Akr2011] even if it requires robust observers. Observers are used with a reference model to generate residuals, which may lead to fault detection. However, the observer-based approach to the detection problem has a number of drawbacks. First, it requires the observability of the signal to diagnose (not always guaranteed) and an observer for the entire states variable because the correction part needs full states estimation. Second, while it is clear that in the absence of disturbances and faults, such a residual is typically zero, it is a fact that its dynamics is controlled in part by the fault and can lead to undetected faulty events.

Several observers have been designed to track the rotor position, the speed, phase currents and the dc-link voltage. However, the operation of the observers in the whole speed range is still an open problem. Also, functional safety rules require uncorrelated sources for data reconstruction, which limits the reconfiguration options.

Signal processing method performs time, frequency or time-frequency analysis to extract relevant features [Xue2013, Yin 2014]. Examples based on the behavior of the current-vector trajectory and the instantaneous frequency tracking in faulty mode can be found in [Dia2004, Delp2008].Neural network architecture with a selection of training parameters and training data can also be used. The input space is defined as a feature space with the features extracted from torque, voltage and current signals in the electric drive system. For a given input feature vector, the neural network system generates the output vector and the diagnostic decision can be derived from this output vector using rules based on unknown faulty condition, normal operating condition, and known faulty condition.

2) *Fault Tolerant Control or Design*

For certain faults, the two-step classical approach, that consists in designing the process and then build the controller (including diagnosis and reconfiguration) has to be thought differently. So, in some cases, the question is how to design the component (electrical machine or inverter) so as to facilitate the diagnosis and improve the reconfiguration and

availability capability. In aerospace applications, machines that have been designed with fault tolerance in mind are found in [Atk2005, Ram2011 and Ben2011]. The case of automotive (electric cars) industry is also mentioned by [Bia2003, Wel2004].
For the design of the actuators, increase the number of stator phases to achieve high reliability for the power stage has shown his effectiveness and in addition, a functional post-fault structure may lead to generate the references for the switching patterns [Bau2012].

Modern technological systems rely heavily on sophisticated control systems to meet safety requirements. This is particularly the case of safety critical applications such as automobile industry where a minor and often fault could potentially lead to unwanted events. To prevent fault induced losses and to minimize the potential risks, new control techniques and design approaches need to be developed to cope with system component malfunctions while maintaining a good limp mode.

In automotive industry, it is highly appreciated that the faulty drive could remain operating, of course apart the cases of unrecoverable damages to the motor or to the power supply. The most common way is to do complete hardware redundancy but it has an additional cost that cannot be ignored and the objective of FTCS is to reduce this cost while having a safe system. Generally, for sensors, a fault tolerant design is not needed but for a specific method (High-Frequency signal injection for position estimation), the design has its importance. In this case, the rotor position is estimated by exploiting the magnetic saliency. The degree of saliency, and therefore the resulting inductance variation, is highly dependent upon machine design, and comparisons between different PM machines have shown that, under specific operating conditions, certain rotor topologies and saliency profiles are more suitable to sensorless control than others. So, the rotor topology influences the selection of an appropriate injection-based sensorless control strategy, particularly for use under high-load conditions and rotor geometry has significant influence on the accuracy of the estimation method. Therefore, consideration may be given to the saliency profile at the design stage of the PM machine. In [Wro2011], a high-frequency injection sensorless position estimation algorithm has been directly incorporated into the Finite Element design procedure for an IPM machine, resulting in a machine that exhibits the required electrical characteristics while being tailored for sensorless control.
For the power converter failures, many strategies have been proposed to reconfigure the control of the machine. The best way here is to perform hardware redundancy due to the difficulty to have an effective component model. Moreover, these strategies need mostly, for

the reconfiguration, to have access to the neutral point of the machine (an access to the neutral point should have been planned or the phases of the machine decoupled) to continue to operate safely in a degraded mode. As an example, for a good fault tolerant control of a permanent magnet machine drive, the machine should be driven from separate single phase bridges, and must be capable of withstanding a short-circuit terminal fault.

For sensor fault, FTC doesn't need, in general to reconfigure the control but only ensuring a quick switch from the faulty sensor to a software sensor, which is a state reconstruction. However, the switch strategy must be performed so as to ensure a smooth transition and avoid a harsh transient.

According to this state of the art, for fault detection and diagnosis these following issues still need to be addressed:

- Initialization and low speed operation of rotor position observer,
- Fault Detection and identification of DC-link voltage and phase current sensors,
- Information on the detection time of FDD methods and their consistency with functional safety rate of coverage,
- Estimation of DC-link voltage.

And for fault tolerant issues:

- Power device reconfiguration,
- Controller reconfiguration

As a conclusion, it's actually important to take Fault Tolerant Design considerations in advance because they determine the capability to do the reconfiguration. Furthermore, FTC methods must be assessed regarding the new international standard for automotive system. The scope of our study will be limited to the detection and the isolation of the sensors faults (position, phase currents and DC link voltage) and to perform a post-fault reconfiguration. In the next chapter, the experimental platform will be described.

References

[Akr2011] **Design of a Fault-Tolerant Controller Based on Observers for a PMSM Drive;** A. Akrad, M. Hilairet and D. Diallo, *IEEE Transactions On Industrial Electronics*, Vol. 58, N° 4, pp. 1416 - 1427, April 2011

[Bau2012] **Torque Control Strategy of Polyphase Permanent-Magnet Synchronous Machines With Minimal Controller Reconfiguration Under Open-Circuit Fault of One Phase;** F. Baudart , B. Dehez, E. Matagne, D. Telteu-Nedelcu, *IEEE Transactions on Industrial Electronics,* Vol. 59, n° 6 , pp. 2632 – 2644, June 2012

[Bat2011] **Diagnosability and diagnosis of technological systems: tool-chain development for diagnosis system design of technological systems.** M. Batteux, PhD, *Université Paris-Sud,* Dec 2011.

[Ben2011] **Safety-critical design of electromechanical actuation systems in commercial aircraft;** Bennett, J.W.; Mecrow, B.C.; Atkinson, D.J.; Atkinson, G.J.; *Electric Power Applications, IET,* vol.5, n°1, pp. 37-47, January 2011

[Ber2010] **Automotive Electricity: Electric Drive;** J. Beretta, *Wiley*, 2010

[Bia2003] **Innovative Remedial Strategies for Inverter Faults in IPM Synchronous Motor Drives;** Bianchi, N.; Bolognani, S.; Zigliotto, M.; Zordan, M.; *Energy Conversion, IEEE Transactions on*, vol.18, no.2, pp. 06- 314, June 2003

[Bru2009] **Modelling and control of a 7-phase starter-alternator for an automotive micro-hybrid application** A. Bruyère, PhD, Arts et Métiers ParisTech, 2009.

[Cap2007] **Real-Time Implementation of IFDIA Scheme in Automotive Systems;** D. Capriglione, C. Liguori, A. Pietrosanto, *IEEE Transactions on Instrumentation and Measurement*, vol. 56, n° 3, pp.824-830, June 2007

[Chan2007] **The state of the art of electric, hybrid, and fuel cell vehicles**, C.C. Chan, *Proceedings of the IEEE*, Vol. 95, No.4, pp. 704 – 718, April 2007

[Chen1999] **Robust Model-based Fault Diagnosis for Dynamic Systems,** J. Chen, R.J. Patton, *Kluwer Academic Publishers, Boston ,* 1999

[Dia2004] **A robust hybrid current control for permanent-magnet synchronous motor drive**, M. Kadjoudj, M.E.H. Benbouzid, C. Ghennai, D. Diallo, *IEEE Transactions on Energy Conversion,* vol.19, no.1, pp.109-115, March 2004

[DeD2011] **Advanced Electrical Drives: analysis, modeling, control**, R. De Donker, W.J. Pulle, A. Veltman, *Springer, Power Systems,* 2011

[Delp2008] **Application of classification methods in fault detection and diagnosis of inverter fed induction machine drive: a trend towards reliability**, C. Delpha, D. Diallo, M.E.H. Benbouzid and C. Marchand, *European Journal of Applied Physics*, Vol. 43, no. 2, August 2008

[Fek2006] **Robust Fault Tolerant Control Strategy for a Class of Nonlinear Uncertain Systems;** A. Fekih, F.N. Chowdhury, *American Control Conference*, pp.5474-5480, 14-16 June 2006

[Hag2014] **Optimal design methodologies of electromechanical systems**, M. Hage-Hassan, PhD, Université Paris Sud, 2013.

[Jiang2005] **Fault Tolerant Control Systems – An introductory Overview;** J. Jiang; *Acta Automatica SINICA*, vol.31, no.1, pp. 161–174, January 2005

[Luo2007] **An Integrated Diagnostic Development Process for Automotive Engine Control Systems;** J. Luo, K. R. Pattipati, L.Qiao, S. Chigusa, *IEEE Transactions on Systems, Man, and Cybernetics, Part C: Applications and Reviews*, vol.37, Issue 6, pp. 1163- 1173, Nov 2007

[Mor2012] **Mild-hybrid traction system based on a bidirectional half-bridge interleaved converter and a three-level active NPC inverter-fed PMSM,** M. Morandin, S. Bolognani, R. Petrella, A. Pevere, S. Calligaro, *IEEE Applied Power Electronics Conference and Exposition (APEC),* pp.1644,1651, Feb. 2012

[Pat1997] **Fault-tolerant control: The 1997 situation** R. J. Patton, *In Proceedings of the 3rd IFAC symposium on fault detection, supervision and safety for technical processes*, pp. 1033–1055, August 1997

[Raj2013] **Present Status and Future Trends in Electric Vehicle Propulsion Technologies**; K. Rajashekara, *IEEE Journal of Emerging and Selected Topics in Power Electronics*, vol.1, no.1, pp.3,10, March 2013

[Tri2013] **Electrical Machines Diagnosis;** J.C. Trigeassou, *ISBN: 978-1-84821-263-3, Wiley,* 2013

[Ven2003] **A review of Process fault detection and diagnosis Part III: Process history based methods,** V. Venkatasubramanian, R. Rengaswamy, S.N. Kavuri and al., *Computers and Chemical Engineers,* 27 (3), pp. 327‑346, 2003

[Wro2011]**Rotor Design for Sensorless Position Estimation in Permanent-Magnet Machines;** R. Wrobel, A. S. Budden, D. Salt, D. Holliday, P.H. Mellor, A. Dinu, P. Sangha, M. Holme, *IEEE Transactions on Industrial Electronics*, vol.58, Issue 9, pp. 3815- 3824, Sept 2011

[Xue2013] **From Model, Signal to Knowledge: a data-driven perspective to fault detection and diagnosis**; D. Xuewu, G. Zhiwei, *IEEE Transaction on Industrial Informatics*, vol. 9, n°4, pp. 2226-2238, 2013

[Yan2000] **Reliable LQG control with sensor failures;** G.H. Yang, J. L. Wang, and Y. C. Soh, *IEE Proceedings on Control Theory and Applications,* 147(4), 433– 439, 2000

[Yin2014] **A review on basic data-driven approaches for industrial process monitoring**; S. Yin, S.X. Ding, X. Xie, H. Luo, *IEEE Transaction on Industrial Electronics*, vol. 61, n°11, pp. 6418-6428, 2014

[Zho2007] **Bearing Condition Monitoring Methods for Electric Machines: A General Review,** W. Zhou; T.G. Habetler, R.G. Harley, *International Symposium on Diagnostics for Electric Machines, Power Electronics and Drives SDEMPED,* pp.3,6, 6-8 Sept. 2007

[Zhou2010] **Postfault Control Strategy for the Hexagram Inverter Motor drive;** L. Zhou and K. Smedley, *IEEE Transactions on Industrial electronics,* Vol. 57, n° 8, pp. 2719-2729, Aug. 2010

[Zwi2009] **Sûreté de fonctionnement des systèmes industriels complexes – Principaux concepts ;** G. Zwingesltein, *Techniques de l'ingénieur*, s8250, Juin 2009

Standards and Reports

[IAE2013] **World Energy Outlook Special report,** International Energy Agency, November 2013

[Iso2009] **ISO/DIS 26262, ISO standard (Draft International Standard),** June, 2009,

[Iso2011] **ISO 26262 "Road vehicles - Functional safety - Part 6: Product development: software level**," International Standard, 2011.

[SAE1967] **Design Analysis Procedure For Failure Modes, Effects and Criticality Analysis (FMECA),** *Society for Automotive Engineers,* 1967

[Sta2006] **Evaluation of 2004 Toyota Prius hybrid electric drive system;** R. Staunton, C. Ayers, L. Marlino, J. Chiasson and T. Burress, *Oak Ridge National Laboratory Technical Report,* 2006

Chapter II: SOFRACI Platform modelling and description

2.1 SOFRACI Structure: A System Designed for Fault Tolerance

2.1.1 Combined architecture for traction and battery charging

The objective of the SOFRACI (high efficiency Inverter with integrated charge function) project was to develop an innovative architecture for achieving the functions of traction, regeneration and charging [Sil2009]. To do so, a unique powertrain is used for the charging and the traction of the vehicle, allowing to:

- Reduce the global number of components
- Integrate charging function without additional electronic component
- Provide a limp mode to the user in case of critical faults

Because the traction and charging modes cannot be simultaneous, the inductances of the machine and the power converter can be used to perform the battery charging. The level of current is enforced by the traction design, which requires high power to drive the vehicle; then it is also possible to sustain high power in charging mode. The power converter used for traction has already been used for battery charging [Shi1994]. However, high current relays were required to pass through one mode to the other. In addition, these electromechanical components increase the design complexity.

Figure 2.1 shows the proposed topology. In charging mode, the three-phase grid is connected to the midpoints a'', b'' and c'' of each machine's coils and no relay is necessary. It could be possible to connect the grid to the extremities a, b, c or a', b', c' but the charging three-phase currents would generate an undesirable rotating magnetic field [Bru2010]. By connecting the grid to the midpoints of each phase, the current will be split in two equal and opposite components and therefore nullify the Magneto-Motive Force at the stator level. This cancellation ensures a magnetic decoupling between the rotor and the stator. Another consequence is that the same amount of current flows in each leg of the same bridge and is in phase with the 50Hz or 60Hz input voltage [Lac2013]. The ac current is therefore rectified to source the DC link (Figure 2.1b). Then each power switch can be sized with the half maximum current.

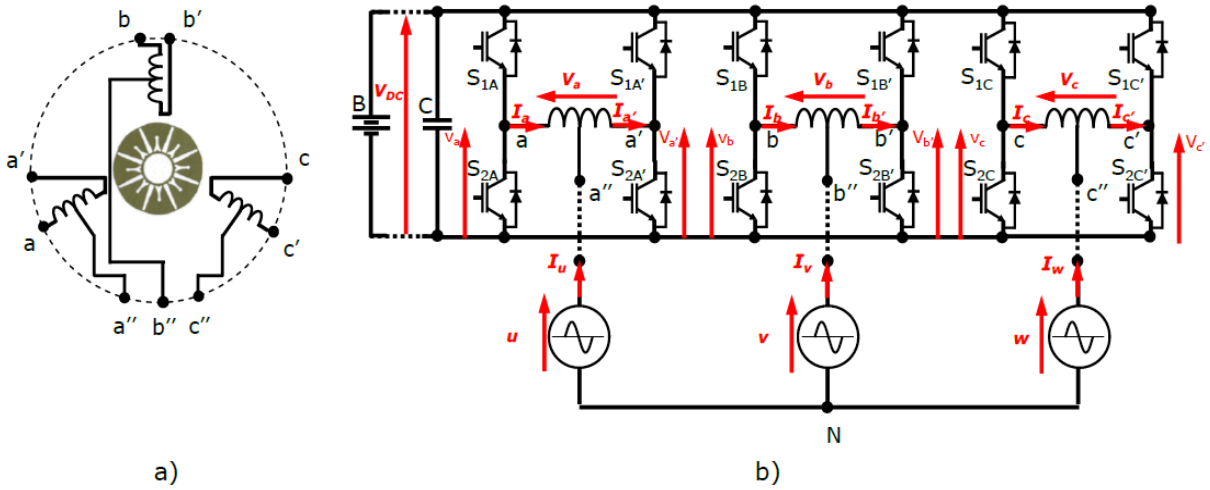

Figure 2.1 SOFRACI Structure [Lac2013]

In traction mode, the midpoints are isolated and all the DC voltage can be applied to the machine terminals and the phase current can be minimized therefore reducing the switch losses.

However, one disadvantage of the SOFRACI structure is the existence of a zero-sequence current. Indeed, given that the machine is not wye-connected, the 3rd harmonic current is non-zero and the zero-sequence current must be under control. Additional Joule losses and torque ripple can be the consequences of this undesirable current. The minimization of this zero-sequence current can be done in the control loop using the homopolar inductance or by choosing the most suitable PWM [San2013]. This can be considered as a compromise between third harmonic reduction and torque performance.

Despite this inconvenience, this innovative architecture is still attractive and has numerous advantages for a combined structure for traction and battery charging. Nevertheless, the sharing of the machine and the power electronics for both modes increases their utilization and then will have an impact on their life cycles and increase the failure rates.

Therefore this structure will be used as a test bench to evaluate fault tolerant algorithms developed in the scope of this PhD thesis. This work is done in the continuity of SOFRACI (high efficiency Inverter with integrated charge function) project, which has mainly focused on the design of controllers in both charging [Lac2013] and traction modes [San2013].

However the Fault Detection and Diagnosis methods and Fault Tolerant Control algorithms developed are intended to be applicable to any inverter-fed AC current machines.

2.1.2 Diagnosis capabilities

For critical applications, the requested reliability level can be reached with two electrical machines in parallel (the second one is used in the limp mode) or by using poly-phase machines [Gre2003]. Three-phase machine with decoupled phases is a poly-phase machine because it has a high number of degrees of freedom compared to the conventional three-phase machines. In addition to the possibility of avoiding the propagation of faults between phases, the ability to control the three currents independently by 3 H-bridges is the starting point of all the reconfiguration solutions. Indeed, a short circuit at the semi-conductor level shall not be spread to the machine windings [Bau2012]. Another type of poly-phase machine is the dual three-phase Permanent Magnet Synchronous Machine (PMSM), which is designed with two sets of three phase stators windings spatially shifted. It allows the extension of the power speed range [Had2006]. Their main advantages are power segmentation, reliability, and minimized torque pulsations.

For diagnosis concerns, the SOFRACI topology provides many advantages. Indeed, the machine phases being physically, magnetically and electrically isolated; it is designed to ensure a continuity of operation after severe faults (for e.g. loss of one inverter leg) [Kol2013].

For three-phase inverters, when an inverter leg fails, reconfiguration schemes use the remaining phases by connecting the DC bus mid-point to the machine neutral. However in this case, having access to the neutral point of the machine is primordial for the reconfiguration even if this practice is very uncommon. Also, the use of an inverter with 4 legs can be considered as a fault tolerant control both in the constant torque region and beyond the base speed, provided to use bidirectional switches to bypass the faulty semiconductor after a failure [Bol2001].

For sensors' faults (position, phase currents and DC link voltage), the same FTC abilities are maintained compared to the conventional three-phase structure. Indeed, the ability to diagnose a faulty sensor is independent of the topology of the machine. It is more related to the design of the system and the remaining available information (availability of other sensors) at fault occurrence.

2.2 Bench Description

2.2.1 PMSM and Sensors

The energy conversion chain is composed of: an electrical machine (PMSM), a power supply, a power converter and sensors for the measurements required by the control loop. Synchronous motors with rare earth permanent magnets have higher power density than comparable DC motors because there is no limiting effect due to the mechanical commutator [Ref2006]. The SOFRACI electrical machine is a poly-phase Permanent Magnet Synchronous Machine (PMSM) designed by Leroy SOMER. The machine is a radial flux type and has been chosen for its robustness and reliability properties. It can develop high torque density and has the ability to reach high speeds [San2013]. This makes it practical to magnetise the pole pieces separately rather than magnetising the complete assembly and requires also much less space.

The windings are distributed around the stator teeth with concentrated coils (Figure 2.2). This allows to limit short-circuit phases and to reduce conductors Joule losses [Kha2011]. The PMSM has 12 stator slots and 4 pairs of poles on the rotor with a rated nominal power of 15kW and a maximal speed of 13000 rpm. The eight magnets with a length of 40 mm are in Neodymium Iron Boron (NdFeB).

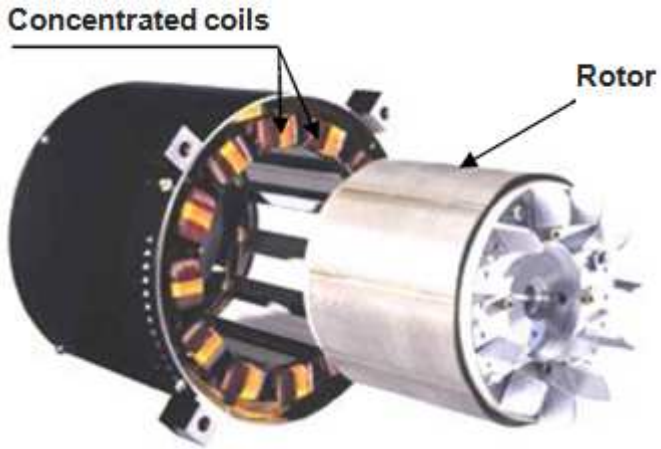

Figure 2.2 PMSM Stator and Rotor [Ses2011]

Implementation of the regulators requires measurements of the rotor position, the phase currents and the DC link voltage. An incremental encoder BEI KHO5S14 with block commutation (bandwidth of 300 kHz, resolution up to 5000 points) gives the mechanical position of the rotor. It provides three signals: A and B shifted by 90° and each step of A (and

then also B) indicates that the encoder has performed one step; the third signal is a top zero which is used to readjust the electronic counter in synchronism with the zero position of the encoder. The zero position indexing is obtained by rotation of the sensor, following an angle of ±10°. The block commutation signals are transmitted as TTL square-wave signals. Then an incremental encoder interface DS3001board provides the position in radians.

The current measurements are performed by 3 Hall Effect LEM transducers (LEM LA 55-P). They can measure DC and AC currents up to 50 A (bandwidth of 200 kHz, accuracy of ±0.65%). The DC bus voltage is measured by a Varistor V661BA60.

2.2.2 Inverter and Power supply

The ARCEL power converter consists of six IGBT legs (Figure 2.3). The decoupling of the DC bus is performed by a series of polypropylene capacitors with a total value of 2.3 mF.

The IGBTs from Fuji Electric Device Technology (1200 V, 450 A) are placed on an air-cooled radiator using a centrifugal turbine (Figure 2.4). The minimal dead-time between the opening and closing of the switches is 1.5 µs.

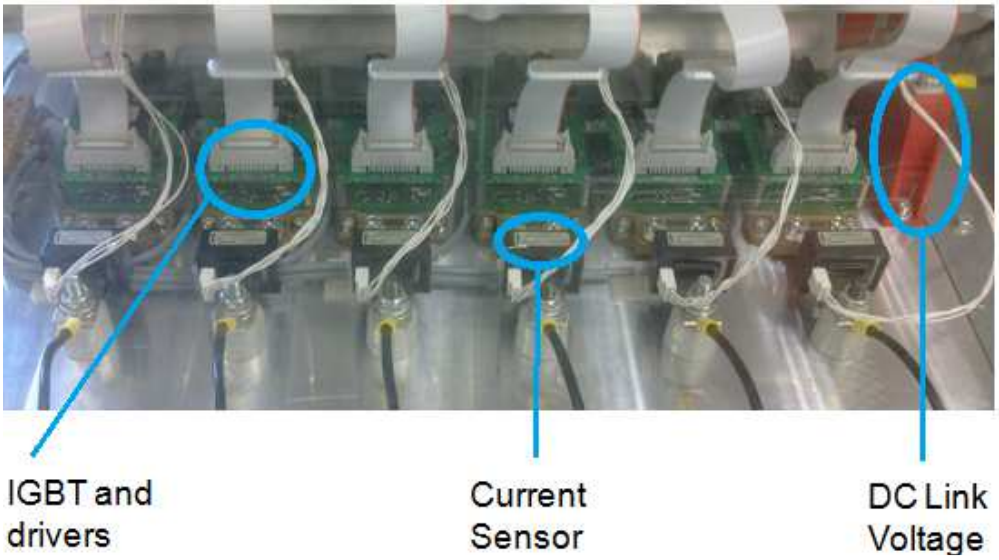

Figure 2.3 Power Converter

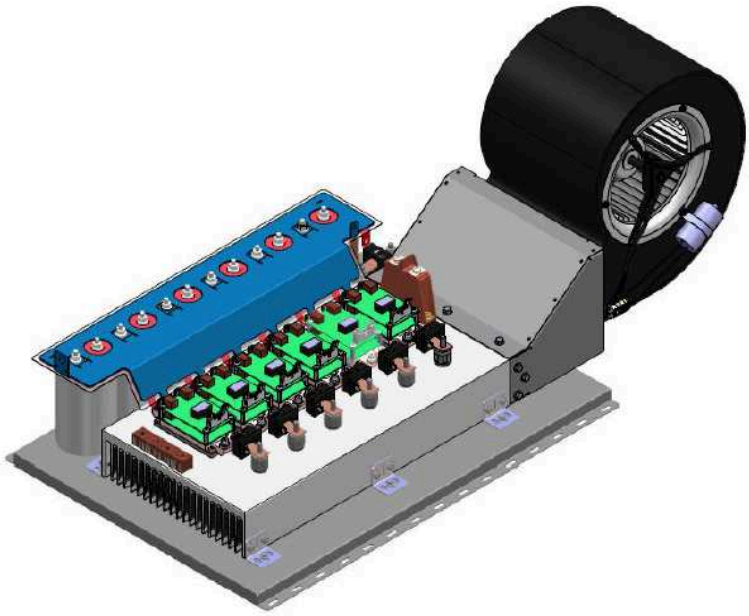

Figure 2.4 Power converters with air-cooling system

For the converter control, the 2SD316EI dual-channel driver based on CONCEPT's proprietary SCALE chipset is used. It allows managing the half bridge mode or a free control of the two switches of the leg. Each channel of the SCALE driver is equipped with a monitoring circuit for over-current and short-circuits issues. When the four windings are coupled in parallel for each phase, the maximum DC voltage is limited to 450V while the maximal RMS current per phase is 30A.

2.2.3 Real-Time implementation of the controller

The control of electrical drives is executed by microelectronic components, which are manufactured from semiconductor materials. The important progress in semiconductor technology combined with high speed signal processing at reasonable cost has been the essential force behind the development of high performance electrical drives controller [Men2011]. Over the last decades, the micro-processors have also become both increasingly powerful and affordable.

Embedded systems require flexible and high-performance architectures to support the increasing amount of programmability. Digital implementation has allowed limiting the high sensibility of systems with respect to thermal and electromagnetic constraints in contrast to analogical implementation [Gat2010]. To this purpose, hardware and/or software design are used to implement the controller that fits to a given algorithm. The DSP (Digital Signal Processor) and the micro-controller are well suited for most of the software designers because

they are easier to reconfigure and are cost effective. Hardware implementation is defined by the use of Field-Programmable Gate Array (FPGA) or Application-Specific Integrated Circuit (ASIC). They are very useful for their ability to process signals beyond high frequencies (beyond GHz) and below low frequencies (a few Hz), with a short execution time.

Recent advances in the synthesis have prompted mixed implementation referred to as hardware/software co-design [Bah2013]. It consists to allocating to each target a functionality of the algorithm. The Hardware/Software is partitioned with respect to the control requirements (bandwidth and stability margin) and the architectural constraints (e.g., available area, memory, and hardware multipliers). For e.g., in electrical machine control, the tasks requesting a critical computational time (generation of PWM signals) are run on hardware targets while the regulation of the currents and the speed are executed by the processor.

A mixed implementation will be used for the experimental tests on SOFRACI bench, with a DS1006 Processor board and a DS5203 FPGA board. The illustration of the mixed implementation applied to the electrical drive is shown in Figure 2.5.

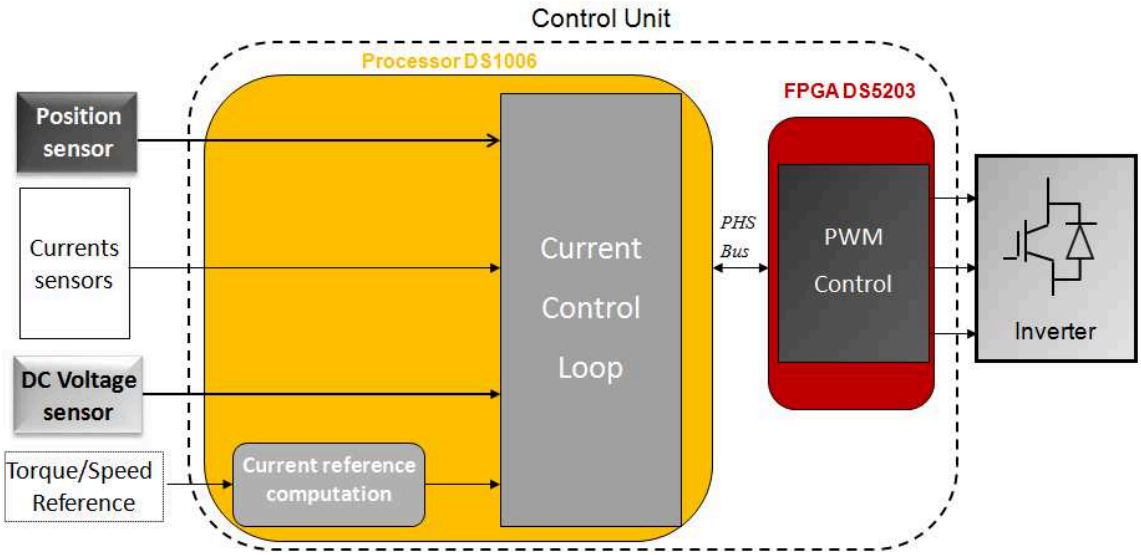

Figure 2.5 Drive layout for the real time implementation

The processor board provides the computing power for the real-time system and also operates as an interface to the I/O boards and the host PC. It is combined with a DS2004 board allowing the acquisition and conversion of input data (sensors and speed reference). The FPGA DS5203 board is a freely programmable FPGA equipped with a Xilinx System generator for Simulink and offers 6 Analog-to-Digital Converters (ADC), 6 DACs and 16 digital I/O channels. The DS1006 is directly connectable to all dSPACE I/O boards via PHS bus and the DS5203 FPGA is connected to the processor board also via PHS bus.

2.3 PMSM Modelling

For PMSM modelling, some assumptions are usually adopted. The stator of the PMSM is assumed to be a hollow iron cylinder with circular cross section. The permeability of the laminated stator and rotor iron is assumed to be infinite; the saturation, iron losses, end-windings and slot-effects are ignored [Leo2001]. The electrical model of the poly-phased machine with 3 independent phases is given in Annex 2. In the following, a simplified model will be used.

2.3.1 Electrical Equations

The stator windings can again be considered as being fed by current sources following the commands from a set of reference values. In steady state condition, the phase currents are approximately sinusoidal and due to the induced back voltage, the lag is increasing at higher speed. The stator voltages in the (*a,b,c*) three-phase frame are expressed as follows [Chi2005]:

$$\begin{bmatrix} v_a \\ v_b \\ v_c \end{bmatrix} = R_s \begin{bmatrix} i_a \\ i_b \\ i_c \end{bmatrix} + [L_{ss}] \frac{d}{dt} \begin{bmatrix} i_a \\ i_b \\ i_c \end{bmatrix} + \frac{d}{dt} \begin{bmatrix} \cos(\theta) \\ \phi_m \cos(\theta - \frac{2\pi}{3}) \\ \cos(\theta + \frac{2\pi}{3}) \end{bmatrix} \quad (2.1)$$

Where $[v_a, v_b, v_c]^T$ stands for the stator voltages, $[i_a, i_b, i_c]^T$ the stator phase currents, R_s the stator winding resistance, ϕ_m the flux produced by the magnets and [L_{ss}] the stator inductance matrix and is function of the electrical position θ for salient machines. For non salient machines, [L_{ss}] can be expressed as follows:

$L_{ss} = \begin{bmatrix} L_0 & M_0 & M_0 \\ M_0 & L_0 & M_0 \\ M_0 & M_0 & L_0 \end{bmatrix}$ where L_0 and M_0 are respectively the proper inductance and the mutual inductance.

For an easier control, the electrical quantities are expressed in a rotating frame using a mathematical transformation called Park's transformation. This last is a combination of the well-known Concordia transformation and a rotation. The Concordia transformation is a projection of three phase quantities onto two fixed axes (α,β). Then, it is followed by a rotation which transforms the AC components of the (α,β) frame to DC components (in steady

state) in a direct and a quadrature axis (Figure 2.6) called (*d,q*) frame. The main advantages of these transformations are: the system order reduction, control of DC quantities (in steady state) instead of sinusoidal quantities, and an easy way to compensate the coupling effects between the two axes.

The application of the Concordia transformation to the equation (2.1) gives:

$$\begin{bmatrix} v_{s\alpha} \\ v_{s\beta} \end{bmatrix} = R_s \begin{bmatrix} i_{s\alpha} \\ i_{s\beta} \end{bmatrix} + \frac{d}{dt} \begin{bmatrix} \phi_\alpha \\ \phi_\beta \end{bmatrix} \tag{2.2a}$$

$$v_h = R_s i_h + L_h \frac{d}{dt} i_h + \omega e_h \ , \ i_h = \frac{1}{\sqrt{3}}(i_a + i_b + i_c) \tag{2.2b}$$

$v_{s\alpha}$, $v_{s\beta}$, $i_{s\alpha}$, and $i_{s\beta}$ are the phase voltages and currents in the (α,β) reference frame. L_h is the zero-sequence inductance and e_h the zero sequence emf composed of a third harmonic component. ω is the angular velocity measured in electrical radians per second. The rotation matrix $P(\theta)$ is expressed as follows:

$$P(\theta) = \begin{bmatrix} 1 & 0 & 0 \\ 0 & \cos(\theta) & \sin(\theta) \\ 0 & -\sin(\theta) & \cos(\theta) \end{bmatrix}$$

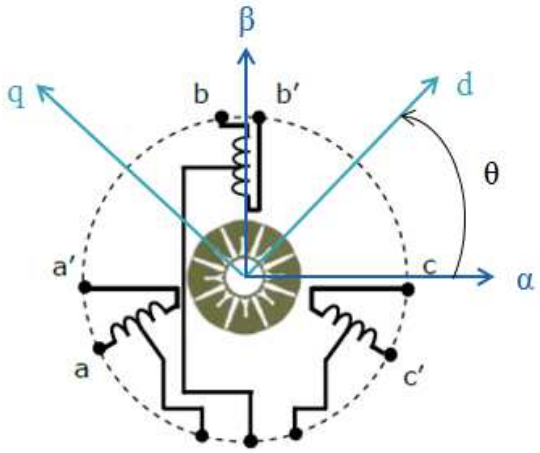

Figure 2.6 (α,β) and (*d,q*) reference frames

Applying the rotation to the equation (2.2), the vectors can be expressed in the rotating frame:

$$\begin{bmatrix} v_d \\ v_q \end{bmatrix} = R_s \begin{bmatrix} i_d \\ i_q \end{bmatrix} + \frac{d}{dt} \begin{bmatrix} \phi_d \\ \phi_q \end{bmatrix} + \omega \begin{bmatrix} \phi_q \\ \phi_d \end{bmatrix} \tag{2.3}$$

Where v_d and v_q are the voltages and i_d and i_q the currents in the (*d,q*) frame.

In a synchronous machine with sinusoidal repartition, ϕ_d and ϕ_q are linear functions of i_d and i_q.

$\begin{bmatrix}\phi_d\\ \phi_q\end{bmatrix}=\begin{bmatrix}L_d & 0\\ 0 & L_q\end{bmatrix}\begin{bmatrix}i_d\\ i_q\end{bmatrix}+\begin{bmatrix}\phi\\ 0\end{bmatrix}$ with $\phi=\sqrt{\frac{3}{2}}\phi_m$ and L_d, L_q are respectively direct and quadrature stator inductances.

The equation (2.1) can now be written in the standard (d,q) synchronous rotating reference frame as follows:

$$\begin{bmatrix}v_d\\ v_q\end{bmatrix}=\begin{bmatrix}R_s & \omega L_q\\ -\omega L_d & R_s\end{bmatrix}\begin{bmatrix}i_d\\ i_q\end{bmatrix}+\begin{bmatrix}L_d & 0\\ 0 & L_q\end{bmatrix}\frac{d}{dt}\begin{bmatrix}i_d\\ i_q\end{bmatrix}+\begin{bmatrix}0\\ \phi\omega\end{bmatrix} \tag{2.4a}$$

$$v_h=R_s i_h+L_h\frac{d}{dt}i_h+\omega e_h \tag{2.4b}$$

For control purpose, we will only consider the d,q components. The zero sequence component represented by (2.4b) will be seen as a disturbance for the control. Extensive studies on the influence of the zero-sequence component in this electrical drive have been performed in [San2013].

2.3.2 Mechanical Equation

The following equations describe the dynamic behaviour of a mechanical drive with constant inertia:

$$J\frac{d\Omega}{dt}=T_{em}-T_l-f\Omega \tag{2.5}$$

Where J is the moment of inertia, f the viscous friction coefficient. T_{em} stands for the electromagnetic torque and T_l the load torque. The electromagnetic torque is produced by interaction between the magnetic field created by the rotor magnets and the magnetic field created by the stator coils. T_{em} is a nonlinear function of stator currents and system parameters and Ω the mechanical speed.

2.3.3 Nonlinear state space modelling

Nonlinear state space modelling tends to have a mathematical model that sufficiently represents the system by a set of trajectories (inputs, outputs and state variables) in some affine space [Wil1979]. It allows, then to skirt the representation of the system using differential equations or transfer functions. In addition, for this study, most of the developed

diagnosis methods are based on observers that are synthesized from a state space representation.

Despite the fact that non linear controllers can also be designed [Ort93], in this work linear controllers will be used for sake of simplicity as the main efforts are dedicated to the Fault Tolerant Control including the fault detection and diagnosis.

The nonlinear system represented by state variables is expressed as follows:

$$\begin{cases} \dot{x} = f(x,u), \\ y = h(x), \end{cases} \tag{2.6}$$

The externally applied controls (inputs) are represented by *u*, the data to process by *x* and the output by *y*. *f* and *h* are differentiable functions which represent respectively the evolution of the state variables and the measurability of the system variables [Her1977].

From (2.4) and (2.5), the salient PMSM state space representation (including the mechanical equation) in the (*d,q*) reference frame is as follows:

$$\frac{d}{dt}\begin{bmatrix} i_d \\ i_q \\ \omega \\ \theta \end{bmatrix} = \begin{bmatrix} -\frac{R_s}{L_d} & \frac{L_q}{L_d}\omega & 0 & 0 \\ -\frac{L_d}{L_q}\omega & -\frac{R_s}{L_q} & -\frac{\phi}{L_q} & 0 \\ 0 & \frac{p^2((L_d - L_q)i_{sd} + \phi)}{J} & -\frac{pf}{J} & 0 \\ 0 & 0 & 1 & 0 \end{bmatrix} \begin{bmatrix} i_d \\ i_q \\ \omega \\ \theta \end{bmatrix} + \begin{bmatrix} \frac{\cos(\theta)}{L_d} & \frac{\sin(\theta)}{L_d} & 0 \\ \frac{-\sin(\theta)}{L_q} & \frac{\cos(\theta)}{L_q} & 0 \\ 0 & 0 & -\frac{p}{J} \\ 0 & 0 & 0 \end{bmatrix} \begin{bmatrix} v_{s\alpha} & v_{s\beta} & T_l \end{bmatrix} \tag{2.7a}$$

$$y = \begin{bmatrix} \cos(\theta) & -\sin(\theta) & 0 & 0 \\ \sin(\theta) & \cos(\theta) & 0 & 0 \end{bmatrix} \begin{bmatrix} i_d \\ i_q \\ \omega \\ \theta \end{bmatrix} = \begin{bmatrix} i_{s\alpha} \\ i_{s\beta} \end{bmatrix} \tag{2.7b}$$

With the state variables $x = [x_1, x_2, x_3, x_4]^T = [i_d, i_q, \omega, \theta]^T$, the inputs $u = [u_1, u_2]^T = [v_{s\alpha}, v_{s\beta}]^T$ and the outputs $y = [y_1, y_2]^T = [i_{s\alpha}, i_{s\beta}]^T$.

The connection between electrical and mechanical variables is ω = pΩ, where p is the number of pole pairs.

For a non salient PMSM ($L_d = L_q = L$), the model becomes:

$$\frac{d}{dt}\begin{bmatrix} i_d \\ i_q \\ \omega \\ \theta \end{bmatrix} = \begin{bmatrix} -\frac{R_s}{L} & \omega & 0 & 0 \\ -\omega & -\frac{R_s}{L} & -\frac{\phi}{L} & 0 \\ 0 & \frac{p^2\phi}{J} & -\frac{pf}{J} & 0 \\ 0 & 0 & 1 & 0 \end{bmatrix} \begin{bmatrix} i_d \\ i_q \\ \omega \\ \theta \end{bmatrix} + \begin{bmatrix} \frac{\cos(\theta)}{L} & \frac{\sin(\theta)}{L} & 0 \\ \frac{-\sin(\theta)}{L} & \frac{\cos(\theta)}{L} & 0 \\ 0 & 0 & -\frac{p}{J} \\ 0 & 0 & 0 \end{bmatrix} \begin{bmatrix} v_{s\alpha} & v_{s\beta} & T_l \end{bmatrix} \tag{2.8}$$

In the following, these state space representations of the PMSM will be used to design the controllers and the observers used in the FTC.

The control objectives are:

- the reference trajectories tracking of the currents i_d and i_q;
- the regulation of i_d and i_q to reject the disturbances due to the electrical parameters uncertainties;
- the stability, defined as the ability of a closed loop system to return to its equilibrium point after a disturbance in a finite time.

For the observers, they will be designed as redundant artificial sensors with the following objectives:

- the estimation errors should be as small as possible for all the operating points;
- the convergence should be at least asymptotical;
- distinct inputs will be needed to increase the robustness of the whole FTC.

2.4 Electrical Drive Control in traction mode

Generally, for AC current machines, the Field Oriented Control (FOC) is employed usually based on two nested loops: a position or/and speed controller and a current controller [Col2012].

Linear regulators (for example a Proportional Integral (PI)) are easier to implement and reach the required performances for many practical applications [Bou2006]. However, real systems are usually complex with coupled phenomena and non-linearities. Therefore linear models used to tune the linear regulators cannot cope with the entire model's complexity. Compensation techniques are then used to reject disturbances induced by nonlinear effects. However these techniques are not effective when only a rough description of nonlinear uncertainties is available (for e.g. the presence of friction).
Then other methods have been implemented in electrical drives, seeking to overcome the limitations of the conventional controllers. Among them; optimal controls, bang-bang control (based on linear model) and adaptive control, predictive control, flatness-based control,

passivity-based control or sliding mode control (based on nonlinear model) are the most popular.

Optimal control (linear quadratic, linear quadratic Gaussian…) allows improving the response of the system when quick transients are needed [Moh2008, Car2008]. Besides, its major drawback is that the entire state must be measured exactly when generating the control.

Predictive control has already been used in electrical drive [Rod2012, Lin2005] using an explicit model and an identifiable model to define the optimal value of the controlled variable. In addition, the execution time needed by the model predictive controller matches up with high sampling rate in drive control [Hyu2003].

In the sliding mode control approach [Utk1993], a discontinuous control signal constrains the trajectories of the system on the so-called sliding surfaces. It is well–known for its robustness properties with respect to electrical parameters uncertainties [Tal2009]. However, its application in industrial process is limited by the chattering phenomena. However sliding mode of higher order mitigates this drawback and exhibits better performances [Jez2013, Bel2008].

Flatness-based control [Fli1992] has been successfully applied for the control of electrical machine [Dan2006, Che1996]. It defines a control law using the flat outputs to lead the system toward the reference trajectory. It allows representing the control inputs as unique function of the flat outputs and is very useful for nonlinear systems.

The passivity-based control [Ort98] achieves an output feedback stabilization of the torque or the speed by assigning a storage function with a minimum at the desired equilibrium [Akr2007]. The storage function is generally the difference between the stored and the supplied energy.

All these methods provide satisfactory solutions but require a higher understanding of control theory. Moreover their implementation can be tedious and they have a high computational cost.

Finally in the following linear regulators with compensation terms will be used as they give satisfactory results which are sufficient to develop the Fault Tolerant Control.

2.4.1 PI Controller Synthesis

The control structure is the well-known FOC. Within the Current Controller in Figure 2.7, two PI controllers are designed and tuned to ensure a good tracking of the current references i_{d_ref}

and i_{q_ref} in the aforementioned Park frame. The speed controller (also a PI) output is the torque current reference and the d axis current reference i_{d_ref} is computed from the speed, the flux reference and the machine parameters. Once the reference voltages v_{abc} are computed by the Current Controller, the PWM block generates the command signals to drive the inverter.

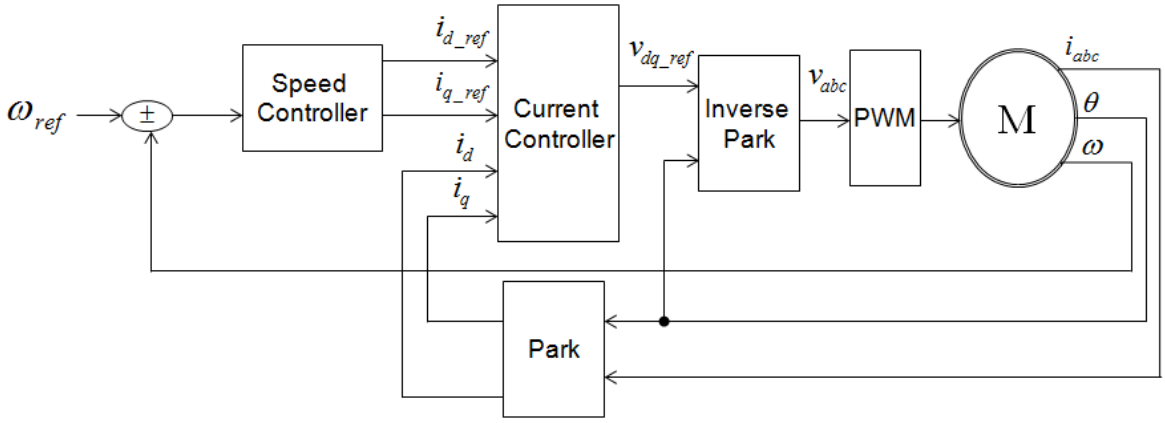

Figure 2.7: PMSM Speed Controller

A transfer function representation is used to tune the PI controllers. From (1.4) and using the Laplace transform (with null initial conditions) gives:

$$\begin{bmatrix} v_d(s) \\ v_q(s) \end{bmatrix} = \begin{bmatrix} sL_d + R_s & \omega L_q \\ -\omega L_d & sL_q + R_s \end{bmatrix} \begin{bmatrix} i_d(s) \\ i_q(s) \end{bmatrix} + \begin{bmatrix} 0 \\ \phi\omega \end{bmatrix} \tag{2.9}$$

Because of the coupling terms $\omega L_q\, i_q(s)$ and $\omega L_d i_d(s)$ the equation (2.9) is split in the following way:

$$\begin{bmatrix} v_d(s) \\ v_q(s) \end{bmatrix} = \underbrace{\begin{bmatrix} sL_d + R_s & 0 \\ 0 & sL_q + R_s \end{bmatrix}}_{H(s)} \begin{bmatrix} i_d(s) \\ i_q(s) \end{bmatrix} + \underbrace{\begin{bmatrix} \omega L_q i_q(s) \\ \phi\omega - \omega L_d i_d(s) \end{bmatrix}}_{E(s)} \tag{2.10}$$

E(s) includes all the nonlinear terms and the PI is designed using the transfer function *H(s)*. As a consequence, if the coupling terms are compensated the flux current component i_d and the torque current component i_q can be controlled independently.

The PI corrector is written as follows: $C(s) = k_p(1 + \frac{k_i}{s})$. Where k_p is the proportional gain, k_i the integral gain. The proportional action improves the system rapidity and then allows adjusting the quality of the transient response. The integral action ensures a null static error in steady state. It is well known that the performance of Field Oriented Control critically depends on the tuning of PI gains, a task complicated by the natural variations of the electrical

parameters. The stator resistance, stator inductances and flux's constant vary with the speed, the saturation level and the temperature and there is no reliable and robust analytical models which can be used for online updating. For an efficient control, the gains of the PI must be tuned with respect to the specifications. These last can be declined in time or/and frequency domains meaning phase and gain margins criteria or, when having a closed loop system identified to a 2nd order system, the specifications can reside in the response time, overshoots, etc.

2.4.1.1 Synthesis by identification to a 2nd order system

Under the assumption that the inverter behaves like a gain with no delay and the feedback has a unit gain, from (1.10), the transfer function in d-axis (the same for the q-axis by substituting the d lower script by q) can be written as follows:

$G_d(s) = \frac{i_d(s)}{v_d(s)} = \frac{1}{sL_d + R_s}$, and so, the closed-loop system $\frac{i_d(s)}{i_{dref}(s)}$ for d-axis is defined by:

$$F_{d,bf}(s) = \frac{C(s)*G_d(s)}{1+C(s)*G_d(s)} = \frac{\frac{sk_p + k_p k_i}{s(sL_d + R_s)}}{1+\frac{sk_p + k_p k_i}{s(sL_d + R_s)}}$$

$$F_{d,bf}(s) = \frac{sk_p + k_p k_i}{s(sL_d + R_s) + sk_p + k_p k_i} = (1+\frac{s}{k_i})\frac{1}{1+s(\frac{R_s}{k_p k_i}+\frac{1}{k_i})+\frac{L_d}{k_p k_i}s^2} \quad (2.11)$$

Now the closed loop transfer function is identified to a 2nd order system with:

$$\omega_0^{\,2} = \frac{k_p k_i}{L_d},\ \frac{2m}{\omega_0} = \frac{1}{k_i}(\frac{R_s}{k_p}+1) \quad (2.12)$$

Where ω_0 is the natural frequency (in rad/s) and *m* the damping coefficient. The time constant is defined as $\tau_d = \frac{L_d}{R_s}$.The time t_r needed for a unit step response to reach its steady state and to stay within 5% of the final value is defined by: $t_r = \frac{3\tau_d}{m}$. For $m = 0.707$, the

abacus of a second order system (Annex 3) gives $\omega_0 t_r = 3$ and then $\omega_0 = \frac{m}{\tau_d}$. A dominant-pole compensation gives $\tau_d = \frac{1}{k_i}$ and from (2.12), $k_p = \frac{R_s}{(k_i \frac{2m}{\omega_0} - 1)}$ (2.13)

The same method is applied for the q-axis PI controller design.

2.4.1.2 Speed controller

The reference of the FOC is provided by the mechanical part. A controller is then needed to correctly transform the mechanical reference into an electrical reference (Figure 2.8).

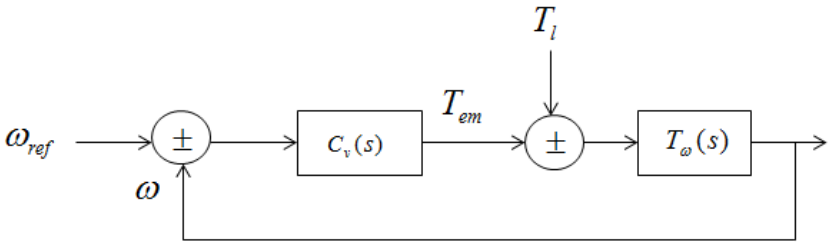

Figure 2.8 Speed regulation

The speed controller is written as follows: $C_v(s) = k_{pv}(1 + \frac{1}{T_{iv}s})$

From the mechanical equation (1.5), it yields: $Js\Omega(s) = T_{em}(s) - T_l(s) - f\Omega(s)$

Given ($L_d = L_{q=} L$), $T_{em} = K_t i_q$ where $K_t = p\phi$

⇨ $Js\Omega(s) = K_t i_q(s) - T_l(s) - f\Omega(s)$

⇨ $(Js + f)\Omega(s) = K_t i_q(s) - T_l(s)$

The transfer function of the system and its controller is given by:

$$H_{w,bo}(s) = \frac{K_{pv}}{T_{iv} f} \frac{1 + T_{iv} s}{s + \frac{J}{f} s^2} \quad (2.14)$$

Similarly to the current control loop with an identification of the closed loop system to a 2nd order system and $\tau_m = \frac{J}{f}$, it yields:

$$\Rightarrow \begin{cases} \omega_0 = \sqrt{\dfrac{K_{pv}}{JT_{iv}}} \\ m = \dfrac{1}{2}\sqrt{\dfrac{T_{iv}}{JK_{pv}}}\left(K_{pv} + f\right) \end{cases} \quad (2.15)$$

The abacus of a second order system give a response time $t_{r_{(5\%)}}\omega_0 = 3$ for a damping m = 0,7. The open loop response time of the system is around $3\tau_m$. To setup the controller, we choose a ratio of **20** between the response times in open loop and closed loop. Then it comes:

$$\Rightarrow \quad t_{r_{(5\%)}} = \frac{3\tau_m}{20}$$

The gains of the controller are finally:

$$\Rightarrow \begin{cases} K_{pv} = 2mf * 20 - f \\ T_{iv} = \dfrac{JK_{pv}}{(f * 20)^2} \end{cases} \quad (2.16)$$

2.4.2 3H bridge Inverter Control

The Pulse Width Modulation (PWM) converters technique processes by interrupting the power flow with harsh switching. Consequently, switching losses and additional noise can arise, especially at high frequencies [Hua1995]. In our electrical drive, the model uses a scalar calculation of the duty cycles to be applied to the three H-bridges inverter. A low duty cycle corresponds to a small voltage level, while a high duty cycle corresponds to a high voltage level. The inputs of the model are the three phase reference voltages and the DC link voltage. An intersective modulation is performed to determine the 6 duty cycles using the three-phase reference voltages without any transformation. The vector sequencing is chosen so as to minimize the number of switches by switching only one leg to move from one vector to another.

For each phase, the duty cycle α is given by the ratio between the reference voltage and the DC link voltage. Then, the PWM signal, which defines the command voltage of the IGBTs, is obtained by the intersection of a PWM carrier (High frequency triangular carrier wave) and the duty cycle (Figure 2.9). With a clock of the FPGA board at 100 MHz, the

triangular signal is generated from a counter from 0 to 5000. The resulting switching frequency is equal to 20 kHz.

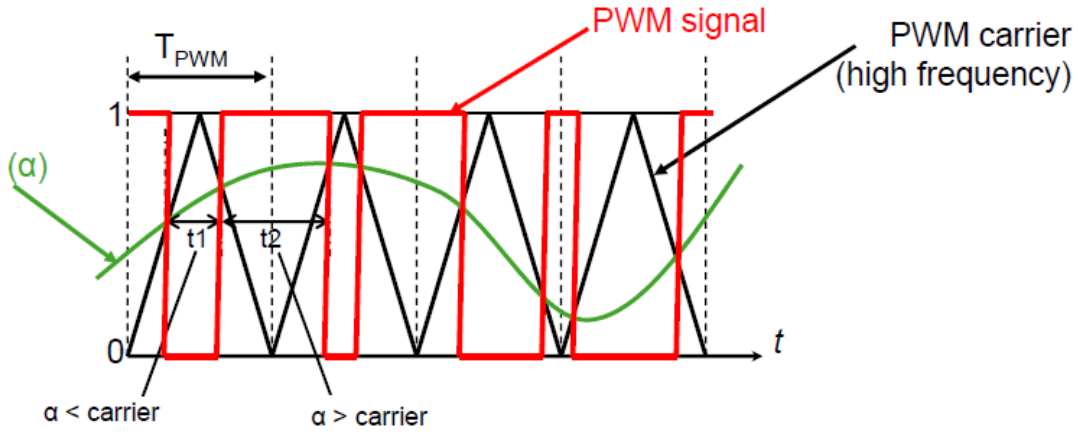

Figure 2.9 PWM Principle

The synchronization at the switching frequency of the inputs and outputs is performed by a latch enabled at the top of triangular carrier. In this way, the duty cycle stay unchanged during one switching period while tasks in the FPGA are clocked at 100 ns. This judicious sampling of the acquisitions has the advantage of reducing the noise induced by the switching on current measurements. Then, an interrupt can be sent from the FPGA to the processor to synchronize the current measurements and the DC voltage measurement.

2.4.3 Simulation and experimental results

In this section, the simulation and experimental results obtained with the controllers designed in the previous sections are presented. The tuning of the PI current controllers used for the simulations is that given by the synthesis with identification to a 2nd order system (1.13). The sampling period T_e of the electrical quantities and the speed control loop is 100μs.

2.4.3.1 Simulation Results

The performances of the controllers are first evaluated through simulations performed with Matlab/Simulink. To validate the controller, a model of the PMSM based on the electrical and mechanical equations is used with a speed profile as a mechanical reference for the real time simulation. A 3H bridge inverter is also modelled with its associated PWM control.

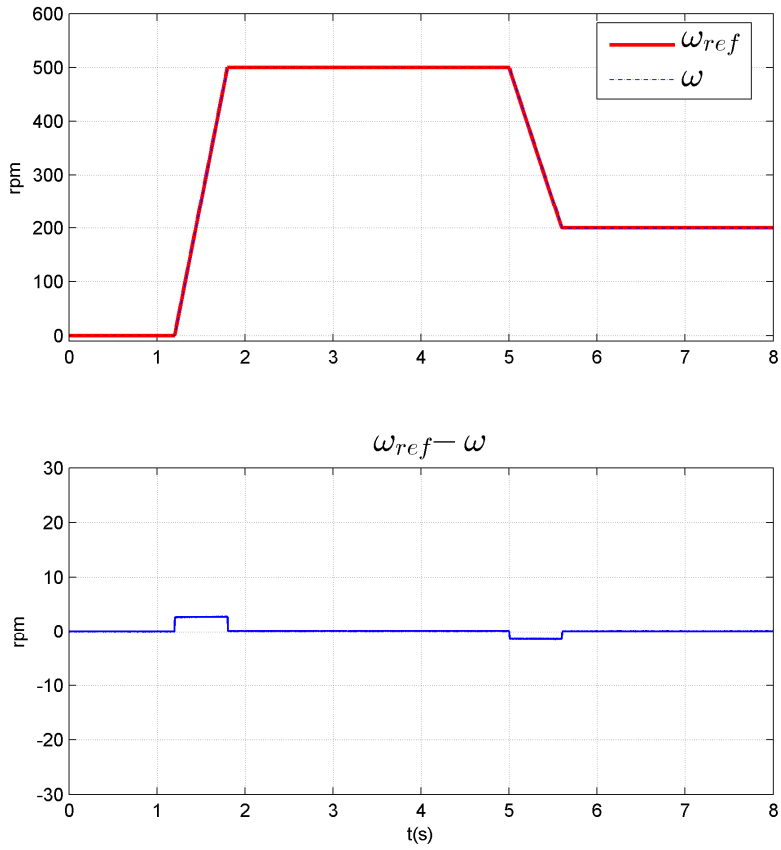

Figure 2.10 Simulation results of the speed controller

The transient error of the speed tracking is lower than 1%. The current PIs are settled with a unit damping (m=1) and are tested by applying a step impulse in the Q axis current at zero speed (locked rotor).

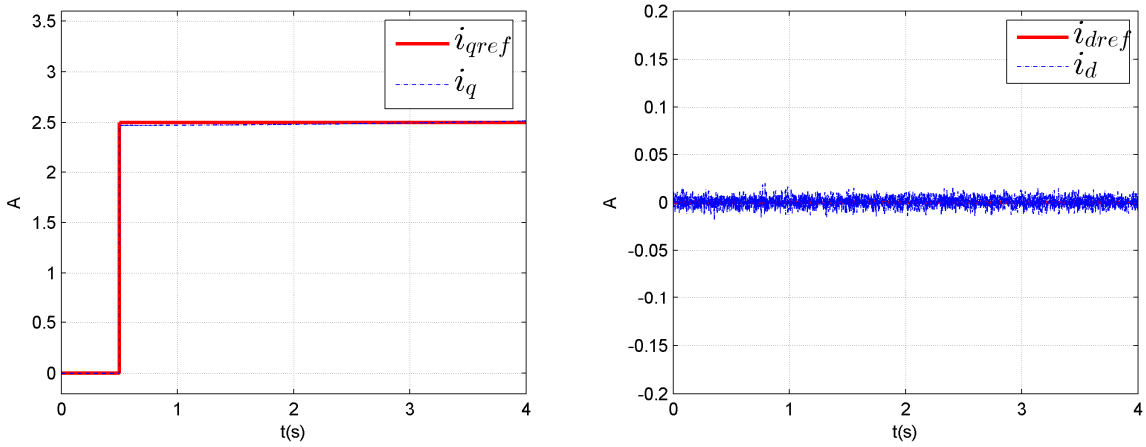

Figure 2.11 Simulation results of current controller

Figure 2.11 represents the tracking of the d,q currents with a step response and a good operation of the PI is noticed. For an optimal torque control strategy, the d-axis reference

current i_{dref} is set to zero. The response time expected with respect to the settling was $t_r = 3\tau_d = 0.0536s$ and is also retrieved in simulation (Figure 2.11).

2.4.3.2 Experimental Results

The machine is fed through a Voltage Source Inverter (3H bridge with a switching frequency of 20 kHz) with a DC supply of 300 V and the algorithms are run on a dSpace board. An induction machine which parameters are given in the annex is used as a load. The dead time effects of the voltage inverter are not compensated. The contribution of the zero sequence current is not taken into account in the control to finger out its impact.

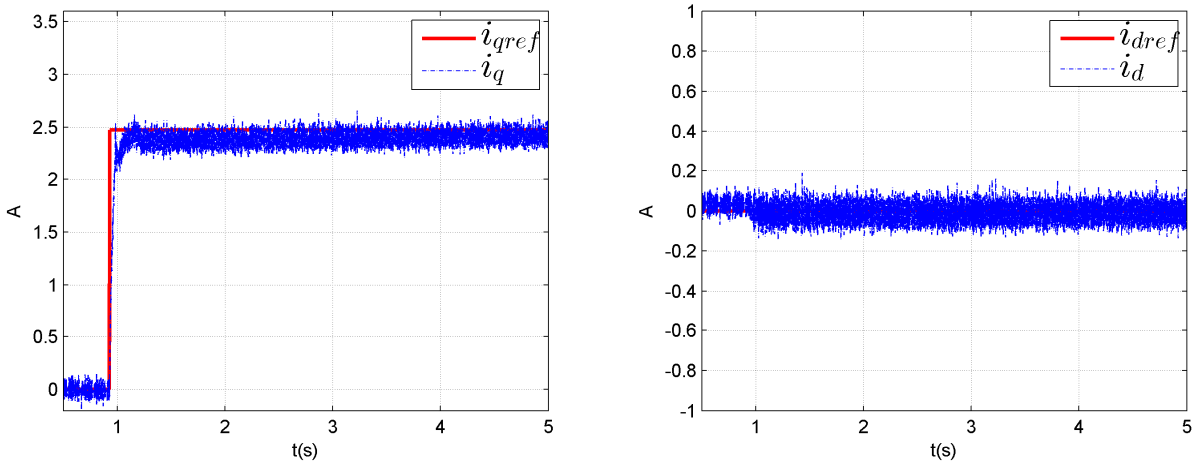

Figure 2.12a Experimental results of current controllers

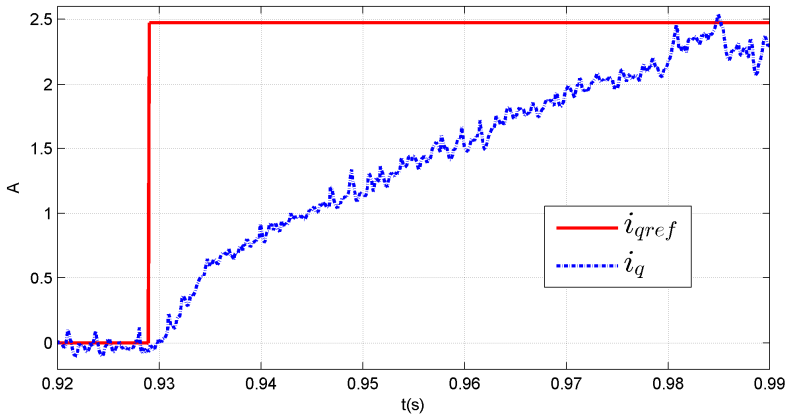

Figure 2.12b zoom in the step response

Similarly to the simulation, the current loops are tested by applying a step impulse in the *q* axis current at zero speed. Figure 2.12a shows the step response of the current PI controller for a unit damping (*m*=1). The measured 5% response time is almost (0.0567 s in Figure

2.12b) while the expected one is 0.0536 s. This difference of 6% can be attributed to the modelling imperfections (inverter, parameter mismatch, etc.). Also, compared to the simulation results, ripples in the *d,q* currents are noticed. These ripples can be declined in high frequency ripples (inverter switching) and low frequency ripples. These last can be explained for a large part by the zero sequence current which was not controlled in these experimental tests.

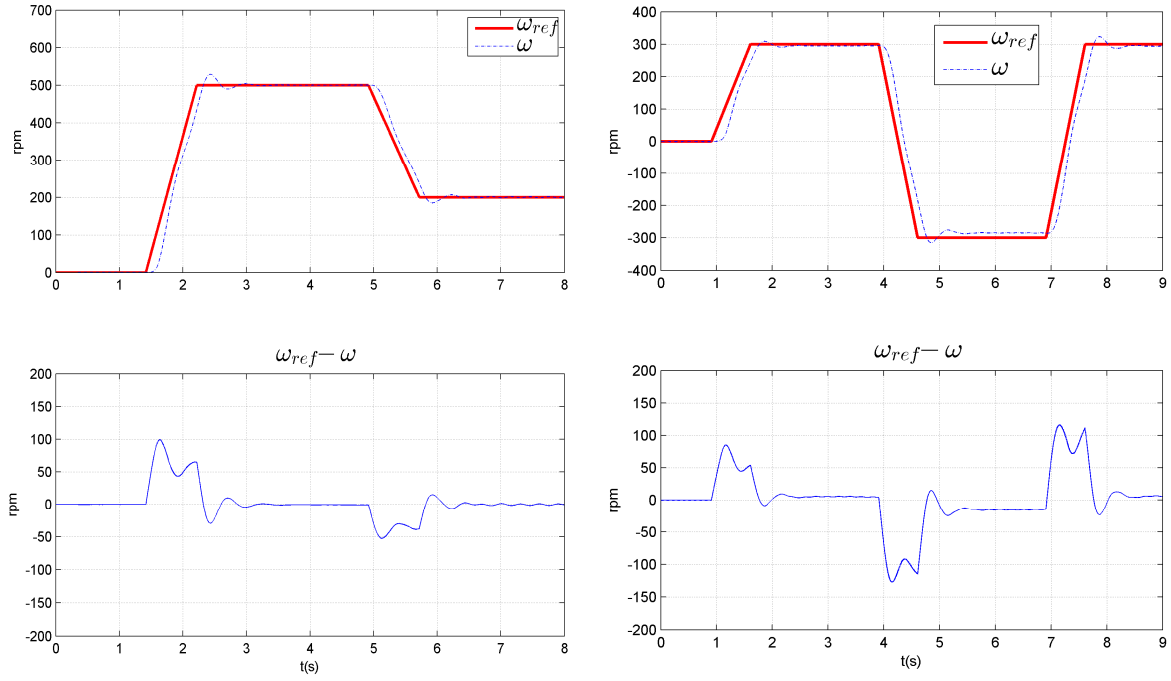

a) b)

Figure 2.13 Speed regulation

When the machine is running, the q-axis current reference will be defined from the tracking error between the reference speed and the actual speed. So, the speed regulation is also tried out in Figure 2.13a. The steady state error is null while the overshoot in transient is inferior to 5%. The controller is also tested under speed reversal response (Figure 2.13b). The result shows a good speed tracking with an acceptable transient error (16%) and a quasi-null steady state error.

2.5 Conclusion

In this second chapter, we have firstly presented the SOFRACI project benchmark. It's an innovative combined structure for battery charging and EV traction [Des2010]. One of its main features is the use of the machine windings for inductive filtering when the vehicle operates in charging mode. This is obtained with a three-phase machine with three distinct stator coils having an accessible midpoint. The power converter is composed of three independent H bridge each one feeding one phase.

Secondly, we have presented the control of the electrical drive for the traction mode. The principles of the PMSM field oriented control have been recalled. Then the synthesis of the speed and current PI controllers has been presented.

Finally, to validate the controllers, both simulation and experimental results are presented. They confirm that in healthy state, the EV power train is under control and we have obtained satisfactory results in terms of performances despite the use of linear regulators.

The main contributions are:

- Description of the architecture in charger and traction mode
- Design and implementation of the electrical drive control

In the next chapter, the fault tolerant control to the mechanical position sensor fault will be addressed.

References

[Akr2007] **Interconnection and Damping Assignment Approach for Reliable PM Synchronous Motor Control,** Akrad A., Hilairet M., Ortega R., Diallo D., *Colloquium on Reliability in Electromagnetic Systems IET*, France, 2007

[Bah2013] **Hardware/Software Codesign Guidelines for System on Chip FPGA-Based Sensorless AC Drive Applications**, Bahri, I.; Idkhajine, L.; Monmasson, E.; El Amine Benkhelifa, M., *IEEE Transactions on Industrial Informatics,* vol.9, no.4, pp.2165,2176, Nov. 2013

[Bau2012] **Torque Control Strategy of Polyphase Permanent-Magnet Synchronous Machines with Minimal Controller Reconfiguration Under Open-Circuit Fault of One Phase**, Baudart, F. ; Dehez, B. ; Matagne, E. ; Telteu-Nedelcu, D. ;Alexandre, P. ; Labrique, F., *IEEE Transactions on Industrial Electronics*, vol.59, no.6, pp.2632,2644, June 2012

[Bel2008] **Sliding Mode Power Control of Variable-Speed Wind Energy Conversion Systems**, Beltran, B. ; Ahmed-Ali, T. ; Benbouzid, M.E.H., *IEEE Transactions on Energy Conversion,* vol.23, no.2, pp.551-558, 2008

[Bru2010] **A multiphase traction /fast –battery-charger drive for electric or plug-in hybrid vehicles** A. Bruyère, L. De-Sousa, B. Bouchez, P.Sandulescu, X. Kestelyn, E. Semail, *IEEE Vehicle Power Propulsion Conference*, Lille, Sept. 2010.

[Bol2001] **Experimental fault-tolerant control of a PMSM drive**, S. Bolognani, M. Zordan, M. Zigliotto, *IEEE Transactions on Industrial Electronics,* vol.47, no.5, pp.1134-1141, 2001

[Bou2006] **Systèmes linéaires : de la modélisation à la commande**, H. Bourles, *Hermes Lavoisier*, 2006.

[Car2008] **Optimal LQI Synthesis for Speed Control of Synchronous Actuator under Load Inertia Variations**, S. Carriere , S. Caux, M. Fadel, *Proceedings of the 17th World Congress of The International Federation of Automatic Control*, pp. 5831- 5836, Seoul-Korea, 2008.

[Che1996] **Differential flatness and control of induction motors** A. Chelouah, E. Delaleau, P. Martin and Rouchon, *Proceedings of CESA Conference*, pp.80-85 , Lille, France 1996

[Chi2005] **Modeling and High-Performance Control of Electrical Machines**, J. Chiasson, *Wiley-Interscience,* 2005.

[Col2012] **A modified synchronous current regulator for field oriented control of permanent magnet synchronous motors,** S.W. Colton, *IEEE Vehicle Power and Propulsion Conference (VPPC),* pp 7 – 12, 2012

[Fli992] **Sur les systèmes non linéaires différentiellement plats**, M. Flies, J. Lévine, Ph. Martin, P. Rouchon, *Comptes rendus de l'Académie des sciences*, Série 1, Mathématique, I-315, pp. 619-624, 1992

[Gat2010] **Comparison Between Analog and Digital Neural Network Implementations for Range-Finding Applications**, Gatet, L.; Tap-Beteille, H.; Bony, F., " *IEEE Transactions on Neural Networks*, vol.20, no.3, pp.460-470, March 2009

[Gre2003] **Fault tolerant, variable frequency, unity power factor converters for safety critical PM drives**
S. Green, D.J. Atkinson, B.C. Mecrow, A.G. Jack, B. Green, *IEE Proceedings Electric Power Applications,*
vol. 150 , no. 6, pp. 663 - 672, 2003

[Had2006] **Space-Vector PWM Techniques for Dual Three-Phase AC Machine: Analysis, Performance Evaluation and DSP Implementation**, D. Hadiouche, L. Baghli and A. Rezzoug, *IEEE Transactions on Industry Applications*, vol.42, no.6, pp.1112-1122, Aug2006

[Her1977] **Nonlinear Controllability and Observability**, R. Hermann, A.J. Krener, *IEEE Transactions on Automatic Control*, no.5, pp. 728-740, Oct 1977

[Hua1995] **Soft-switching techniques in PWM converters**, G. Hua, F.C. Lee, *IEEE Transactions on Industrial Electronics*, vol.42, no.6, pp.595-603, Dec 1995

[Hyu2003] **A discrete-time predictive current control for PMSM**, Hyung-Tae M. ; Hyun-Soo K. ; Myung-Joong Y. , IEEE Transactions on Power Electronics, vol. 18, pp. 464 - 472 , no.1, part 2, 2003

[Jez2013] **PMSM sliding mode FPGA-based control for torque ripple reduction**, Jezernik, K. ; Korelic, J. ; Horvat, R., IEEE Transactions on Power Electronics Vol. 28, pp 3549 – 3556, 2013

[Kha2011] **Design and Study of a Permanent Magnet Synchronous Motor for an Electric Compressor**, M. Khanchoul, G. Krebs, C. Marchand, F. Alves, A. Battelier, M. Roze, *Piers Proceeding,* Vol. 1 of 2, pp. 171-175, Marrakech, March 2011

[Kol2013] **Analyse d'une architecture de puissance dédiée aux modes traction-recharge dans un véhicule électrique. Optimisation de la commande et fonctionnement en mode dégradé**, A. Kolli, PhD, Université Paris- Sud, Dec 2013.

[Lac2013] **Modélisation et commande d'une chaîne de conversion pour véhicule électrique intégrant la fonction de charge des batteries**, S. Lacroix, PhD, Université Paris- Sud, Mai 2013.

[Leo2001] **Control of Electrical Drives;** W. Leonhard, *Springer*, 3rd edition, 2001

[Lin2005] **Model Predictive Control for Electrical Drives**, A. Linder, R. Kennel, *IEEE 36th Power Electronics Specialists Conference,* pp 1793-1799, Recife, 2005

[Men2011] **Real time control of electrical machine and drives: a review**, PM Menghal, AJ Laxmi, *International Journal of Advances in Engineering & Technology,* Sept 2011.

[Moh2008] **A Current Control Scheme With an Adaptive Internal Model for Torque Ripple Minimization and Robust Current Regulation in PMSM Drive Systems,** Mohamed, Y.A.-R.I. ; El-Saadany, E.F. *IEEE Transactions on Energy Conversion*, vol. 23 , no. 1, pp 92 – 100, 2008

[Ort1993] **Nonlinear control of Induction motors: Torque Tracking with Unknown Load Disturbance** , R. Ortega, C. Canudas, S. Seleme, *IEEE Transactions on Automatic Control*, vol. 38 , pp 1675 – 1680, 1993

[Ort1998] **Passivity based control of Euler-Lagrange systems**, R. Ortega, A. Loria, P.J. Nicklasson, H. Sira-Ramirez, *Springer-Verlag*, Berlin, 1998

[Rod2012] **Predictive Control of Power Electronics and Electrical drives**, J. Rodriguez, P. Cortes, *Wiley-IEEE Press*, ISBN: 978-1-119-96398-1, 2012

[Ref2006] **Scalability of surface PM machines with concentrated windings designed to achieve wide speed ranges of constant power operation**, EL-Refaie A. M., Jahns T.M., *IEEE Transactions on Energy Conversion*, vol. 21, no. 1, pp. 362 – 3690, 2006

[San2013] **Modélisation et commande d'un système à trois phases indépendantes à double fonctionnalité : Traction Électrique et Chargeur Forte Puissance pour application automobile**, P. Sandulescu, PhD, École Nationale Supérieure des Arts et Métiers, Sept 2013.

[Ses2011] **Optimisation de gammes : application à la conception des machines synchrones à concentration de flux**, B. Sesanga, PhD, Institut Polytechnique de Grenoble, 2011.

[Utk1993] **Sliding mode control design principles and applications to electric drives**, Utkin, V., *IEEE Transactions on Industrial Electronics*, vol. 40, no. 1, pp. 23 – 26, 1993

[Wil1979] **System theoretic models for the analysis of physical systems**, J. C. Willems, *Ricerche Di Automatica,* 10:71-106, 1979

Patents and Reports

[Cha1996] **Système d'alimentation électrique mixte onduleur et convertisseur alternatif-continu**, B. Chauchat, M. Brunello, J-P Ferrieux, Pb. Delbosc, D. Richer, Brevet Européen n° WO 97/08009 déposé le 30 août 1996.

[Shi1994] **Electric System for Electric Vehicle**, Kinoshita Shigenori, Japanese patent JP6276615, Fuji Electric Co LTD, Sept. 30, 1994

[Sil2009] **Projet SOFRACI (Structure Onduleur Fort Rendement A fonction de Charge Intégrée)**, B. Silvestre, Document interne Valeo, mars 2009.

[Des 2010] **Procédé et dispositif électrique combiné d'alimentation et de charge à moyens de compensation**, L. De Sousa, B. Bouchez, Brevet International WO 2010/057893 A1, Mai 2010.

Chapter III: Position/Speed Sensor Fault Tolerant Control

3.1 Impact of a position sensor fault on the PMSM control

High-performance PMSM control systems are generally equipped with position/speed sensor. Actually, the commonly used Field Oriented Control requires the position to be accurately determined to make effective torque production. In this control, the rotor position is needed to transform the stator currents two decoupled components. One to control the torque and the other to control the phases magnetization. The control fails when an error occurs on the rotor position measure. Another challenge is related to the role of the rotor position in PMSM parameters identification (magnet flux, resistance and inductances). This identification is needed because the parameters vary due to the motor heating, and then the maximum torque and power available according to the speed can decrease with a minor position error [Hen2011]. Naturally, identification is done because using temperature sensors on the rotor surface and the stator windings is too expensive for a large-scale production in automotive industry.

Rotary Position Sensor types are composed of resolvers, incremental encoders and absolute encoders. First, we recall that the accuracy of a position sensor is defined by its precision, resolution and repeatability. For both resolvers and encoders, precision depends on the manufacturing process variability for a given design [Bar2013].
The main advantage of the resolver is its robustness [Lep2003]. However, its implementation is quite difficult and the processing of the output data to get the position is intricate. In addition, a resolver-to-digital converter is needed as electronic interface to digitize resolver signals for the controller and deviation could arise after a rotor motion induced by a voltage fluctuation. Incremental encoder generates TTL square-wave signals from which the position is computed. It needs a calibration sequence for the alignment at each start owing the incremental nature of the information. Its main drawback is its sensitivity to line noise (for e.g. inverter switching) which can be interpreted as an increment signal and give rise to bias. In addition, the errors are cumulative and any missed count increases the bias. Also, after a power loss, the last position is also lost. An absolute encoder is a rotary optical encoder and relies on optoelectronic components to detect rotary motion. It can be seen as a digital version of a resolver. In contrast to the incremental encoder, there is no need of alignment and it is less sensitive to line noise.

There is a logical trend to use encoder for its easy implementation and its accuracy (provided to have enough lines per revolution in the codewheel pattern). However, if the environment requires a high immunity to noise, then the best choice is resolver feedback.

Generally, the tolerable position sensor error is linked to the motor poles. For e.g. with a low cost Hall-effect sensor, a resolution of 5.0 electrical degrees is accepted for a 4 pole-machine, 7.5 electrical degrees for a 6 pole-machine [Liu2003]. These tolerances can also be specified in terms of torque ripple. In Electrical Power Steering, manufacturers have specified the torque ripple requirements between 4% and 5% of the average torque output. The contribution of the PMSM is within 1% while those due to the electronics is around 1.5%. It remains then a margin of 1.5% to 2.5% for the position sensor error contribution to meet the overall torque ripple requirements. This case reflects the difficulty for defining a general threshold tolerance for a position sensor error. Each application, according to its specifications and its safety level, requires a rate of error corresponding to the global desired torque ripple and to the current consumption.
A solution for diagnosing the position/speed sensor is the estimation. As a software solution, it is an efficient back-up solution to reduce the risk level due to mechanical sensor fault (complete outage, drift...). In fact, several recent works [Akr2011, Ben2007] deal with robust control of electrical drives. They are aimed at proposing new control strategies without position/speed sensor. Obviously, they cannot claim to the same range of accuracy than a resolver sensor. Nonetheless, the sensorless method shall not bring too much position error and exceeds the permitted application's torque ripple and maximal current.

The rest of the chapter is organized as follows. Section 2 is devoted to a study of the position/speed estimator's types. Then section 3 establishes the algebraic position and speed estimator with experimental results. Section 4 presents the fault tolerant control of the position sensor based on a combination of estimators while a conclusion is performed in section 5.

3.2 Position /speed Estimators and their various uses

Foremost, a position/speed estimator can be used for two purposes: monitor the sensor or replace a sensor (sensorless). In the first case, we perform a FTC if the reconfiguration

involves the estimator, otherwise the estimation helps only to diagnose a sensor fault and perform a safe stop. Monitoring the position sensor is well suited for high critical applications in which safety rules require a mechanical sensor for the operation but authorize a software solution for the diagnosis instead of setting a hardware redundancy. For some less-safety critical applications, no mechanical sensor is mounted on the PMSM and the position is obtained with the help of sensorless methods.

Sensorless control of PMSM has been under investigation for decades both in industry and academic research fields [Hol1996, Bat2005] and is still an open issue. In [Vac2013], the rotor position observability of a salient PMSM is demonstrated, including the zero speed region. However, for a non-salient PMSM, the problem is still relevant.

Thereby, the back-EMF based methods are efficient in medium to high-speed range. A general point of view is that the back-EMF-based sensorless algorithm suffers from the small amplitude of back-EMF signals at low speed [Wan2011]. Nonetheless, good results have been obtained in [Sar2012]. The Extended Kalman Filter (EKF) is another candidate. It has strong robustness properties but its design is quite difficult [Bou2005]. In addition, the algorithm initialization is nondeterministic due to unknown initial values of the covariance. Also, the EKF ensures only a local convergence, which can be troublesome for the starting. More precisely, if the EKF doesn't start very close to the initial value, the estimation will not converge. In last, High Frequency signal Injection (HFI) uses signal processing to give accurate position information at very low and zero speed but it is only applicable to machines with magnetic saliency. It has a limited speed range and its implementation is tedious and requires high computation accuracy ([Zhu2011, Bol2011]).

Our concern being the positioning of the new estimator based on an algebraic approach with respect to the current methods, especially its advantages and drawbacks, the full details of the observers mentioned thereafter in this chapter won't be provided. For the EKF and the back-EMF methods, we limit ourselves to a brief recall of the observer's principle and an implementation of the existing algorithms widely used in the literature (with experimental validation for comparison features). The HFI method is presented here as an alternative to the observer-based approach but with no test results. As it is becomes popular in PMSM drives, its principle is recalled and a brief presentation of the basics are given. Relevant references are given to the reader.

3.2.1 Extended Kalman Filter

The method uses the theory of Kalman filter for nonlinear state estimation so called Extended Kalman Filter (EKF). Notice that EKF is not a purely nonlinear observer because the observation gain is computed on a linearized subspace. Estimation of the speed and the position is done using the reference voltages and phase current measurements, which are uncorrelated from the mechanical sensor. Notice that using uncorrelated sources is a key point of fault detection and reconfiguration.

Using equations (2.7) with $x = [i_d, i_q, \omega, \theta]$, $u = [v_{s\alpha}, v_{s\beta}]$ $y = [i_{s\alpha}, i_{s\beta}]$ yields to:

$$\begin{cases} \dfrac{d}{dt}x(t) = Ax(t) + Bu(t) \\ y(t) = Cx(t) \end{cases} \tag{3.1}$$

Where

$$A = \begin{bmatrix} -\dfrac{R_s}{L_d} & \dfrac{L_q}{L_d}\omega & 0 & 0 \\ -\dfrac{L_d}{L_q}\omega & -\dfrac{R_s}{L_q} & -\dfrac{\phi}{L_q} & 0 \\ 0 & 0 & 0 & 0 \\ 0 & 0 & 1 & 0 \end{bmatrix}, \; B = \begin{bmatrix} \dfrac{\cos(\theta)}{L_d} & \dfrac{\sin(\theta)}{L_q} \\ -\dfrac{\sin(\theta)}{L_q} & \dfrac{\cos(\theta)}{L_d} \\ 0 & 0 \\ 0 & 0 \end{bmatrix}, \; C = \begin{bmatrix} \cos(\theta) & -\sin(\theta) & 0 & 0 \\ \sin(\theta) & \cos(\theta) & 0 & 0 \end{bmatrix}$$

The main assumption is that the mechanical part is neglected in (3.1) that is the variation of the speed (third state of the system) is assumed to be very low ($\dfrac{d}{dt}\omega = 0$).

For the digital implementation of an estimator, a discrete-time state-space model is required. Assume that the input vector u is nearly constant during a sampling period T_s, a first-order series expansion of the matrix exponential is used to discretize the model: $e^{AT_s} \approx A_d = I + AT_s$, $A^{-1}(e^{AT_s} - I)B \approx B_d T_s$.

The previous continuous model leads to the following discrete-time state-space model:

$$\begin{aligned} x(k+1) &= A_d x(k) + B_d u(k) \\ y(k) &= Cx(k) \end{aligned} \tag{3.2}$$

Where $A_d = \begin{bmatrix} 1-\frac{R_s}{L_d}T_s & \frac{L_q\omega}{L_d}T_s & 0 & 0 \\ -\frac{L_d\omega}{L_q}T_s & 1-\frac{R_s}{L_q}T_s & -\frac{\phi}{L_q}T_s & 0 \\ 0 & 0 & 1 & 0 \\ 0 & 0 & T_s & 1 \end{bmatrix}, B_d = \begin{bmatrix} \frac{\cos(\theta)}{L_d}T_s & \frac{\sin(\theta)}{L_q}T_s \\ -\frac{\sin(\theta)}{L_q}T_s & \frac{\cos(\theta)}{L_d}T_s \\ 0 & 0 \\ 0 & 0 \end{bmatrix}$

A_d is the evaluation matrix and B_d the control matrix. The application of the EKF to the synchronous machine model is described as follows with the prediction and correction steps.

Prediction:

$$\begin{aligned} \hat{x}(k/k-1) &= A_d(k-1)\hat{x}(k-1/k-1) + B_d(k-1)u(k-1) \\ \Sigma(k/k-1) &= A(k-1)\Sigma(k-1/k-1)A(k-1)^T + Q(k-1) \end{aligned} \tag{3.3}$$

Correction

$$\begin{aligned} K(k) &= \Sigma(k-1){C_d}^T(k)\left(C_d(k)\Sigma(k-1){C_d}^T(k) + R(k)\right)^{-1} \\ \Sigma(k/k) &= \Sigma(k/k-1) - K(k)\,C(k)\Sigma(k/k-1) \\ \hat{x}(k/k) &= \hat{x}(k/k-1) + K(k)\left[y(k) - C_d(k)\hat{x}(k/k-1)\right] \end{aligned} \tag{3.4}$$

The estimation is done in a way that minimizes the mean of the quadratic error Σ between the measured phase currents and the estimated ones by taking into account the measurement noise and modelling errors. The covariance matrices Q and R characterize the noises that take into account the model approximations and the measurement errors. Some authors use a physical approach to obtain a more realistic tuning that allows one to roughly evaluate the state and parameter uncertainties [Lar2008]. However, a fine evaluation of the matrices is very difficult, and generally, a simplified analysis is used. Without additional information, the noises are considered as uncorrelated, time independent and free-tuning parameters. Σ represents the variance of the observation error and K is the observer gain.

3.2.2 Back-EMF based Observer

For purpose of observer synthesis, the salient PMSM is modeled with a state representation in the standard (α,β) reference frame as follows:

$$\frac{d}{dt}\begin{bmatrix} i_{s\alpha} \\ i_{s\beta} \end{bmatrix} = \frac{1}{L_d}\begin{bmatrix} -R_s & -\omega(L_d - L_q) \\ \omega(L_d - L_q) & -R_s \end{bmatrix}\begin{bmatrix} i_{s\alpha} \\ i_{s\beta} \end{bmatrix} + \frac{1}{L_d}\begin{bmatrix} -1 & 0 \\ 0 & -1 \end{bmatrix}\begin{bmatrix} e_{s\alpha} \\ e_{s\beta} \end{bmatrix} + \frac{1}{L_d}\begin{bmatrix} v_{s\alpha} \\ v_{s\beta} \end{bmatrix} \quad (3.5a)$$

$$\begin{bmatrix} e_{s\alpha} \\ e_{s\beta} \end{bmatrix} = ((L_d - L_q) * (\omega i_{sd} - \frac{d}{dt} i_{sq}) + \phi\omega)\begin{bmatrix} -\sin\theta \\ \cos\theta \end{bmatrix} \quad (3.5b)$$

The equation (2b) gives the relation between the EMF and the position and its details can be founded in [Chen2003]. The following diagram (Figure 3.1) shows the relative positions of flux and back-EMF vectors in the α-β frame where E is the Back-EMF vector.

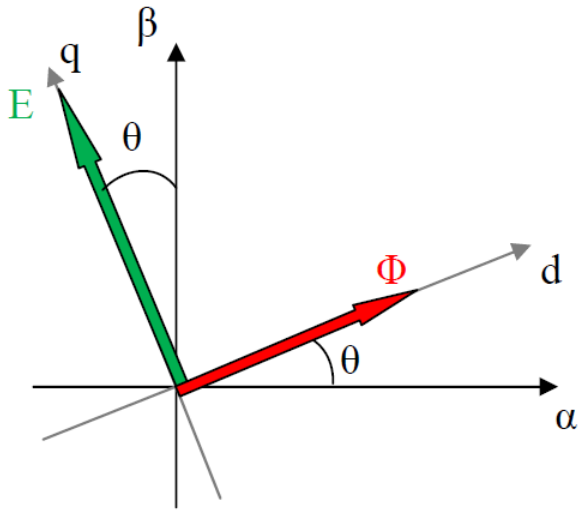

Figure 3.1 Flux and back-EMF vectors

In order to estimate the position, the currents are first estimated. Then, back-emf components are deduced from current estimation. Finally, the relation between (α,β) components of the back-emf gives the position. A Luenberger observer is used to estimate the currents is the (α,β) frame from the measured currents ($i_{s\alpha}$, $i_{s\beta}$) and the reference voltages ($v_{s\alpha}$, $v_{s\beta}$). For this observer, the gain is chosen so as to bring asymptotically the trajectories of the state estimation errors to zero.

Now, this theory is applied and considering a non-salient PMSM (L_d = L_q= L) using (2.3a) gives:

$$\frac{d}{dt}\begin{bmatrix} \hat{i}_{s\alpha} \\ \hat{i}_{s\beta} \end{bmatrix} = \frac{1}{L}\begin{bmatrix} -R_s & 0 \\ 0 & -R_s \end{bmatrix}\begin{bmatrix} \hat{i}_{s\alpha} \\ \hat{i}_{s\beta} \end{bmatrix} + \frac{1}{L}\begin{bmatrix} v_{s\alpha} - \hat{e}_{s\alpha} - K_1\tilde{i}_{s\alpha} \\ v_{s\beta} - \hat{e}_{s\beta} - K_2\tilde{i}_{s\beta} \end{bmatrix} \quad (3.6)$$

Where $\tilde{i}_{s\alpha} = \hat{i}_{s\alpha} - i_{s\alpha}$, $\tilde{i}_{s\beta} = \hat{i}_{s\beta} - i_{s\beta}$ and K_1, K_2 are the observer gain.

The convergence of the current observer described by (3.6) is then studied. More precisely, the stability of the observer is investigated.

Combining (3.5a) and (3.6) gives:

$$\frac{d}{dt}\begin{bmatrix}\tilde{i}_{s\alpha}\\ \tilde{i}_{s\beta}\end{bmatrix}=\frac{1}{L}\begin{bmatrix}-R_s & 0\\ 0 & -R_s\end{bmatrix}\begin{bmatrix}\tilde{i}_{s\alpha}\\ \tilde{i}_{s\beta}\end{bmatrix}+\frac{1}{L}\begin{bmatrix}-K_1\tilde{i}_{s\alpha}-\tilde{e}_{s\alpha}\\ -K_2\tilde{i}_{s\beta}-\tilde{e}_{s\beta}\end{bmatrix} \tag{3.7}$$

Using a disturbance observer to estimate the back-EMF components $\hat{e}_{s\alpha}, \hat{e}_{s\beta}$, which can be seen as slowly variable disturbances in the electrical equations gives:

For a nonlinear system, the existence of Lyapunov functions is a sufficient condition for asymptotic stability. A Lyapunov function V is a positive definite function and has a Lie-derivative $\dot{V}$, which is negative definite.

A candidate for a Lyapunov function is: $V=\frac{1}{2}(\tilde{i}_{s\alpha}{}^2+\tilde{i}_{s\beta}{}^2)\geq 0$ (3.8)

$$\begin{aligned}\dot{V}&=-\frac{R_s}{L}(\tilde{i}_{s\alpha}^2+\tilde{i}_{s\beta}^2)-\frac{K_1}{L}\tilde{i}_{s\alpha}^2-\frac{K_2}{L}\tilde{i}_{s\beta}^2+\frac{\tilde{i}_{s\alpha}\tilde{e}_{s\alpha}}{L}+\frac{\tilde{i}_{s\beta}\tilde{e}_{s\beta}}{L}\\ \dot{V}&\leq-\frac{R_s}{L}(\tilde{i}_{s\alpha}^2+\tilde{i}_{s\beta}^2)-\frac{1}{L}\left(K_1\tilde{i}_{s\alpha}^2-\tilde{e}_{s\alpha}\tilde{i}_{s\alpha}\right)-\frac{1}{L}\left(K_2\tilde{i}_{s\beta}^2-\tilde{e}_{s\beta}\tilde{i}_{s\beta}\right)\end{aligned} \tag{3.9}$$

$-\frac{R_s}{L}(\tilde{x}_1^2+\tilde{x}_2^2)<0$ and $\dot{V}\leq 0$ if $\left(K_1\tilde{i}_{s\alpha}^2-\tilde{e}_{s\alpha}\tilde{i}_{s\alpha}\right)>0$, $\left(K_2\tilde{i}_{s\beta}^2-\tilde{e}_{s\beta}\tilde{i}_{s\beta}\right)>0$

It yields: $\dot{V}\leq 0$ if $\boxed{\{K_1,K_2\}>\max\left(|\tilde{e}_{s\alpha}|,|\tilde{e}_{s\beta}|\right)}$

The stability is ensured by the choice of K_1, K_2 which define the convergence dynamics. The observer gains K_1, K_2 must be tuned properly according to (3.7) to have an accurate estimation. The current observer is then asymptotically stable and the estimation error will converge to a minimal value while $\dot{V}<0$. This last stability analysis defines the setting range for the gain.

3.2.3 High-Frequency Signal injection

The technique consists in injecting either a pulse or a sinusoidal test signal in order to be able to track the existing magnetic saliency without introducing torque ripples. It makes position estimation possible without requiring machine model by using magnetic saliencies.

There are several HF injection methods found in the literature and they can be classified into (α,β) frame rotating injection, (d,q) frame pulsating injection and (d,q) frame rotating injection [Jan1995, Hol2006, Sil2006].

The position estimation is derived from a high frequency current injection by using three filters (a low-pass Filter (LPF) a high pass filter (HPF) and a band pass-filter (BPF). The most common approach is to superimpose a HF voltage carrier on the fundamental voltage supply. The rotor position is then extracted from the resulting HF current components as shown in figure 3.2. The frequency of the injected voltage carrier, w_i, should be high enough to ensure sufficient spectral separation between the excitation and the fundamental supply to reduce the requirements of the band-pass filters [Ari2008]. The frequency is usually set in a range 10 times higher than the maximum fundamental frequency and 10 times lower than the power converter switching frequency.

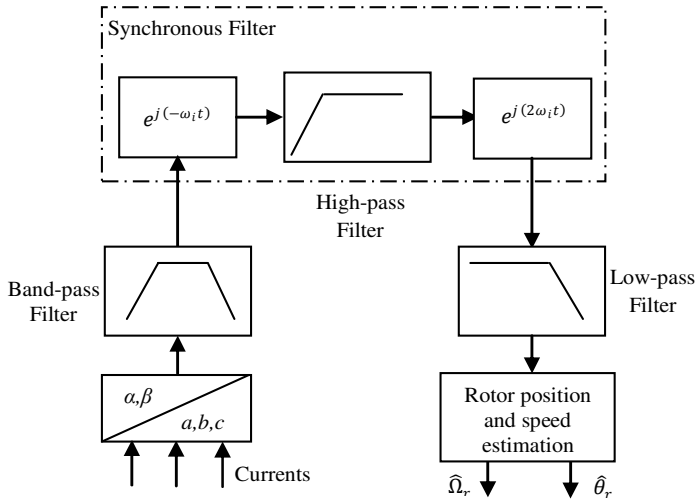

Figure 3.2 Block diagram of HF current demodulation for position estimation

Up to now, it is recognized to be the best estimator at very low speed and standstill [Gong2013, Man2013]. However, this method induces extra losses and its speed range is limited.

3.3 New Estimator based on a Differential Algebraic Approach

The choice of the algebraic approach for the position/speed estimation is well suited because it has strong abilities in dealing with nonlinearities. Indeed, its effectiveness in the control and the observation of electromechanical systems has already been proved through many works [Sir1992, Menh2011].

3.3.1 Observation Principle

The concept of observability aims to say if it is possible to find the internal state of a dynamical system when a set of inputs and outputs data is available. Observability is a linear concept in the sense that a nonlinear system is observable if and only if, its linearized tangent is so. For nonlinear systems, the differential geometric approach leads to the well-known rank criterion where the observability is defined by Lie-derivatives theory [Her1977]. In addition, while the observability of linear systems is well established, the observability of a nonlinear system is not a sufficient condition for the existence of an observer and the definition of nonlinear observability is still an active research field [Han2009].

The main point of the differential algebraic approach of observation, recalled in [Fli1991], is that a quantity z, of a system is observable with respect to some other one w if each component of z is a solution of an algebraic equation with coefficients eventually depending on w and a number of its finite time derivative. Globally, general systems are described with the differential algebraic approach in with

$$\begin{cases} R_i(w, z, \zeta) = 0, i \in \{1,2,..., L\} \\ S(w, z, \zeta) \neq 0, \end{cases} \tag{3.10}$$

Where the R_i and S are polynomials in w, z, ζ and their derivatives and L is a finite number. The variable w stands for the data (in the classical observation problem, w is (u, y) the input and the output), z is the variable to be observed, and ζ is an extra variable, which may be present in the system's description ($x = (z, \zeta)$). The algebraic observability for (3.10) means that the whole differential information is contained in $k<w>$ [Diop2001] where k is a differential field.

The nonlinear system is assumed to be a set χ of trajectories $(\bar{u}, \bar{x}, \bar{y})$ satisfying the equation

(2.6) in some affine space U_m x U_n x U_p where U is the function space where the input u, the state x, and the output y take their values. We have m actuators for the system, n state variables and p measured outputs. The coefficients of the system's equation in (2.6) are time variable and are supposed to be in a differential field k. The above mentioned function space U over which the system variables take their values is here a differential algebraic closure $\bar{k}$ of k. A more general definition of (2.6) where f and h are rational functions of u and x with coefficients in some differential field k can be written as:

$$\begin{cases} \dot{x}_i = \dfrac{p_i(u,x)}{q_i(u,x)} (1 \le i \le n) \\ y_i = \dfrac{r_i(u,x)}{g_j(u,x)} (1 \le i \le p) \end{cases} \tag{3.11}$$

Where p_i, q_i, r_i and g_i are differential polynomials of finite order in x with coefficients in k.
The system is observable with respect to u and y if each component x_i of the state vector is algebraic over the differential field extension of k generated by the data u and y.The observability condition for (3.11) can then be written as: $x_i = \dfrac{l_i(u,y)}{s_i(u,y)}$ where l_i and s_i are differential polynomials with coefficients in k.

3.3.2 Differential Algebraic Estimation for PMSM

The PMSM model is a combination of a structure and a set of parameters. It is written in the standard (d,q) synchronous rotating reference frame as follows:

$$\frac{d}{dt}\begin{bmatrix} x_1 \\ x_2 \end{bmatrix} = \begin{bmatrix} -\dfrac{R_s}{L_d} & \dfrac{L_q}{L_d}\omega \\ -\dfrac{L_d}{L_q}\omega & -\dfrac{R_s}{L_q} \end{bmatrix} \begin{bmatrix} x_1 \\ x_2 \end{bmatrix} + \begin{bmatrix} \dfrac{\cos(\theta)}{L_d} & \dfrac{\sin(\theta)}{L_d} \\ -\dfrac{\sin(\theta)}{L_q} & \dfrac{\cos(\theta)}{L_q} \end{bmatrix} u + \begin{bmatrix} 0 \\ -\dfrac{\phi}{L_q} \end{bmatrix} \omega \tag{3.12a}$$

$$y = \begin{bmatrix} \cos(\theta) & -\sin(\theta) \\ \sin(\theta) & \cos(\theta) \end{bmatrix} \begin{bmatrix} x_1 \\ x_2 \end{bmatrix} \tag{3.12b}$$

With $x = [x_1, x_2]^T = [i_{sd}, i_{sq}]^T$, $y = [y_1, y_2]^T = [i_{s\alpha}, i_{s\beta}]^T$ $u = [u_1, u_2]^T = [v_{s\alpha}, v_{s\beta}]^T$

This equation contains transcendental functions (*sin* and *cos*) which do not satisfy the conditions of an algebraic function. However, it can be made algebraic using a coordinate change with $x_3 = \cos\theta$ and $x_4 = \sin\theta$. This will transform (3.12a) into a four-order system. For sake of simplicity, the system notation described in (3.12a) and (3.12b) is kept.

Notice that it's very important to take the outputs in the (α,β) frame because the sensors measure the currents in the (a, b, c) natural machine reference frame before being transformed in (α,β) by Concordia transformation. If the outputs are in the (d,q) frame, the position (which is estimated from these currents) will be required to compute the outputs with Park Transformation [Wang2005]. This may lead to an algebraic loop and eventually propagate a position error.

For the algebraic theory, referring to [Diop2001a], θ is observable if $\theta = \frac{l(u,\dot{u},y,\dot{y},...)}{q(u,\dot{u},y,\dot{y},...)}$

Denoting $\dot{y} = \frac{d}{dt}y$ and deriving (3.12b) leads to:

$$\begin{cases} L_d(\dot{y}_1\cos\theta + \dot{y}_2\sin\theta) = -\omega L_d x_2 + L_d\dot{x}_1 \\ L_q(\dot{y}_1\sin\theta - \dot{y}_2\cos\theta) = -\omega L_q x_1 - L_q\dot{x}_2 \end{cases} \tag{3.13}$$

Rewriting (3.12a) gives:

$$\begin{cases} L_d\dot{x}_1 = -R_s x_1 + \omega L_q x_2 + u_1\cos\theta + u_2\sin\theta \\ L_q\dot{x}_2 = -R_s x_2 - \omega L_d x_1 - u_1\sin\theta + u_2\cos\theta - \phi\omega \end{cases} \tag{3.14}$$

Combining (3.13) and (3.14) gives:

$$\begin{aligned} \dot{y}_1(L_d\cos^2\theta + L_q\sin^2\theta) + (L_d - L_q)\frac{\dot{y}_2}{2}\sin 2\theta &= -R_s y_1 + u_1 + \phi\omega\sin\theta + \omega(L_d - L_q)(x_1\sin\theta - x_2\cos\theta) \\ \dot{y}_2(L_q\cos^2\theta + L_d\sin^2\theta) + (L_d - L_q)\frac{\dot{y}_1}{2}\sin 2\theta &= -R_s y_2 + u_2 - \phi\omega\cos\theta - \omega(L_d - L_q)(x_1\cos\theta + x_2\sin\theta) \end{aligned} \tag{3.15}$$

If $L=L_d=L_q$ (case of (SPMSM)) then $\tan\theta$ is rationally observable with:

$$\tan\theta = \left(\frac{\dot{y}_1 L + R_S y_1 - u_1}{-\dot{y}_2 L - R_S y_2 + u_2}\right) \tag{3.16}$$

The observability of θ is then established for a non-salient PMSM. Unlike other results on the observability of SPMSM [Zal2010] where the key condition is based on the speed (the system is unobservable if the speed is null), two results can be pointed out:

- ✓ The observability at low speed is obtained, provided that the outputs' derivatives are available,
- ✓ The observability of the position is not speed dependant.

Let's notice that the same study can be extended to a salient PMSM. The entire PMSM model described by (3.12) is algebraically observable since given the knowledge of (ω, θ), the states i_{sd}, i_{sq} are algebraically observable.

3.3.2.1 Speed/position Estimator Synthesis

In the following, upper script ^ refers to estimated variables. Indeed this technique has already been successfully used in [Men2006] for induction machines using a mathematical model written in space vector form [Leo2001]. The objective is here to apply it for a PMSM to find the dynamic of the position $\dot{\theta} = f(\theta, u, \dot{u}, y, \dot{y})$ as a function of the input *u*, the output *y* and their derivatives as described in [Diao2014].

From (3.13), we have: $\hat{\omega} = \dot{\hat{\theta}} = \dfrac{\sin\hat{\theta}(L_q \dot{y}_1 + R_s y_1 - u_1) + \cos\hat{\theta}(-L_q \dot{y}_2 - R_s y_2 + u_2)}{(L_d - L_q)(y_1 \cos\hat{\theta} + y_2 \sin\hat{\theta}) + \phi}$ (3.17)

With no loss of generality and for simplicity, the estimator is written for a non-salient PMSM ($L = L_d = L_q$):

$$\begin{cases} \hat{\omega} = \dot{\hat{\theta}} = \dfrac{\sin\hat{\theta}(L\dot{y}_1 + R_s y_1 - u_1) + \cos\hat{\theta}(-L\dot{y}_2 - R_s y_2 + u_2)}{\phi} \\ \hat{\theta} = \arctan\left(\dfrac{\dot{y}_1 L + R_S y_1 - u_1}{-\dot{y}_2 L - R_S y_2 + u_2}\right) \end{cases} \quad (3.18)$$

The main point here is that no assumption on the mechanical dynamics for the estimator model is required (i.e. doesn't need to insert $\dot{\omega} = 0$ in the estimator model). Figure 3.3 shows the differential algebraic speed/position estimator in the PMSM drive. Sensor measurements (current and position/speed) associated to the control reference (torque or speed) are the inputs of the controller.

The controller drives the power electronic inverter in order to feed the machine with the appropriate voltages. The goal of the controller is to achieve an effective operation over a wide range of the torque-speed plane. Thus, a closed loop control is necessary.

The Current Control Loop (CCL) ensures the tracking of the current references computed from the torque/speed reference and the machine electrical parameters.

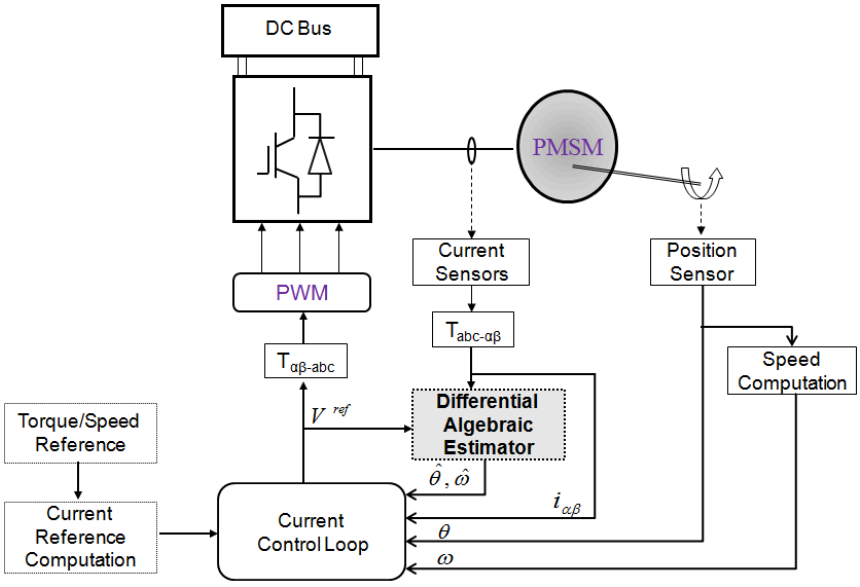

Figure 3.3 PMSM drive with the differential algebraic estimator

To achieve the estimation, derivative of currents are required. They can be determined with backward finite difference approximations.

Given a function g_i, its first order derivative is: $\dot{g}_i = \frac{g_i - g_{i-1}}{T_e}$ where T_e is the sampling period.

3.3.2.2 Stability Analysis

First, the estimation error is defined for $L=L_d=L_q$ by: $\tilde{\theta} = \hat{\theta} - \theta$

$$\dot{\tilde{\theta}} = \frac{(L\dot{y}_1 + R_s y_1 - u_1)(\sin\hat{\theta} - \sin\theta) + (-L\dot{y}_2 - R_s y_2 + u_2)(\cos\hat{\theta} - \cos\theta)}{\phi} \tag{3.19}$$

The voltages can be computed as follows using (α,β) coordinates [Ezz2011]:

$u_1 = L\dot{y}_1 + R_s y_1 - \omega\phi\sin\theta$, $u_2 = L\dot{y}_2 + R_s y_2 + \omega\phi\cos\theta$

and then $\dot{\tilde{\theta}} = \omega\sin\theta(\sin\hat{\theta} - \sin\theta) + \omega\cos\theta(\cos\hat{\theta} - \cos\theta) = \omega(\cos\tilde{\theta} - 1)$

For a non-linear system, the existence of Lyapunov functions is a sufficient condition for asymptotic stability. A Lyapunov function V is a positive definite function and has a Lie-derivative $\dot{V}$ that is negative definite.

For $\omega > 0$, $V(\tilde{\theta}) = \frac{\tilde{\theta}^2}{2}$,

⇨ $\dot{V}(\tilde{\theta}) = \omega(\cos\tilde{\theta} - 1)(\tilde{\theta})$ and $\omega(\cos\tilde{\theta} - 1) < 0$

Assuming the position estimation error $\tilde{\theta}$ being within [0,2π], $\dot{V}(\tilde{\theta}) \leq 0$.

To prove global asymptotic stability, the Barbalat's lemma is used [Raf2008]. We need $\dot{V}(\tilde{\theta})$ being uniformly continuous. Then $\ddot{V}(\tilde{\theta})$ must be bounded and using $\omega, \tilde{\theta}, \dot{\tilde{\theta}}, \sin(\tilde{\theta}), \cos(\tilde{\theta})$ bounded gives the global asymptotic stability: $\ddot{V}(\tilde{\theta}) = \omega\dot{\tilde{\theta}}((\cos(\tilde{\theta}) - \tilde{\theta}\sin(\tilde{\theta}) - 1)$.

For $\omega < 0$, the linearization around the origin $\tilde{\theta} = 0$ yields $\dot{\tilde{\theta}} = 0$ which is just stable.

So the observer is then globally asymptotically stable for a positive speed and stable for a negative speed. Although the nonlinear estimator ensures a global convergence for $\omega > 0$, the initial position value θ_0 can also be determined as follows:

$$\dot{\hat{\theta}} = f(\hat{\theta}, u, y, \dot{y}, R_s, L_d, L_q, \phi) = 0 \quad \Leftrightarrow \quad (R_s y_1 + L_q \dot{y}_1 - u_1)\tan\theta_0 = R_s y_2 + L_q \dot{y}_2 - u_2$$

$$\theta_0 = \arctan\left(\frac{R_s y_2 + L\dot{y}_2 - u_2}{R_s y_1 + L\dot{y}_1 - u_1}\right)\Bigg|_{t=0} \tag{3.20}$$

θ_0 is an equilibrium point for the position dynamic. Starting from this point, local convergence of the estimation can be ensured for $\omega < 0$.
Once the nonlinear estimator designed and its stability domain checked, the experimental results are now presented.

3.3.3 Experimental Position/Speed Estimation results

The PMSM parameters and the description of the test bench are given in Annex 1. The switching frequency of the inverter is 20 kHz. The current control algorithm and the speed control are carried out every 100 μs.

3.3.3.1 Operation with the sensor

The position sensor is used for the control and the estimator is compared to the measured position for different operating points. The tests start with the low speed range. The performances of the algebraic estimator speed and position tracking capabilities are evaluated in Figure 3.4 from 0 to 500 mechanical rpm that represents 4% of the maximum speed equal to 12000 rpm.

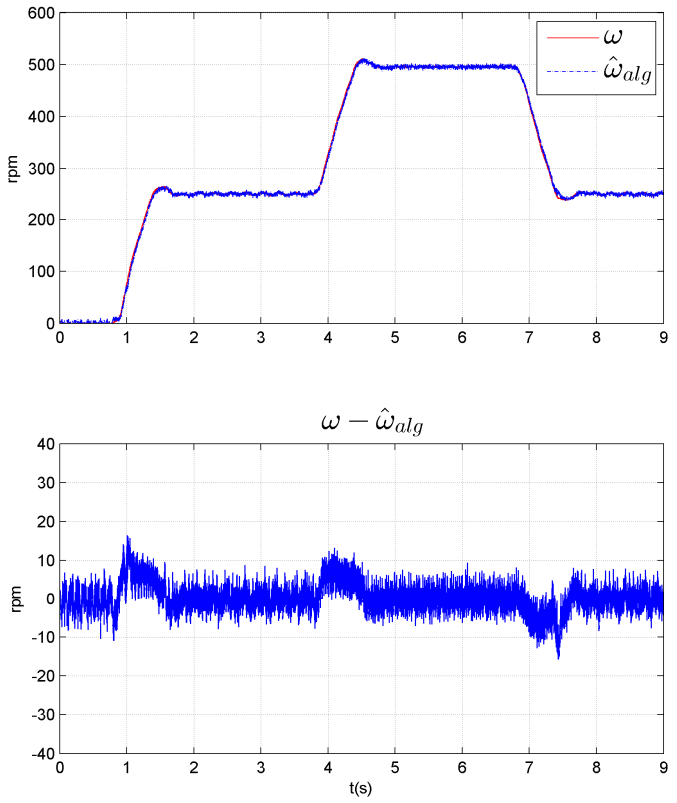

a) Speed Estimation

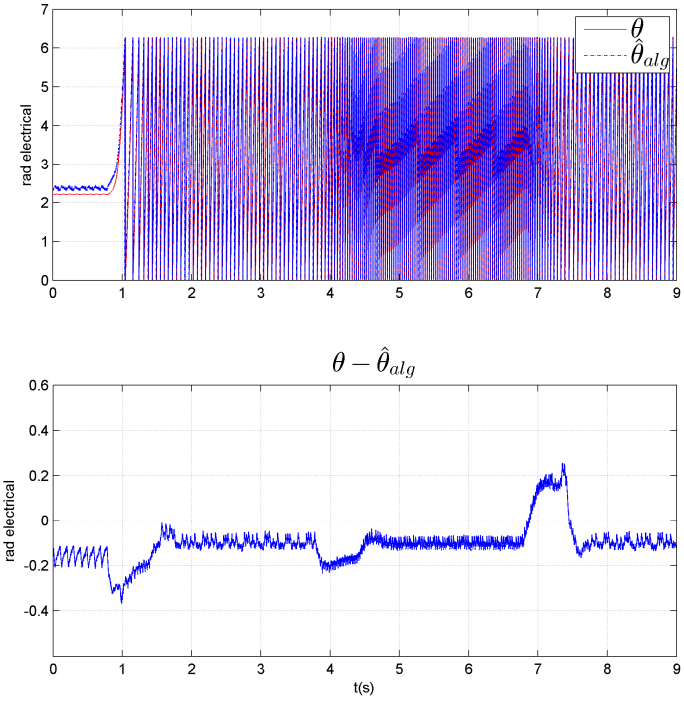

b) Position Estimation

Figure 3.4 Differential algebraic estimator evaluation in sensor operation in low speed range

The average speed estimation error at steady state is almost zero and the maximum speed transient error is approximately 15 rpm. The position error is near -0.1 electrical radians (0.025 mechanical radian or 1.45 mechanical degrees). These results are satisfactory for our

application because usually mechanical position estimation errors below 5 degrees are acceptable in automotive industry. A very low speed operation is illustrated in Figure 3.5.

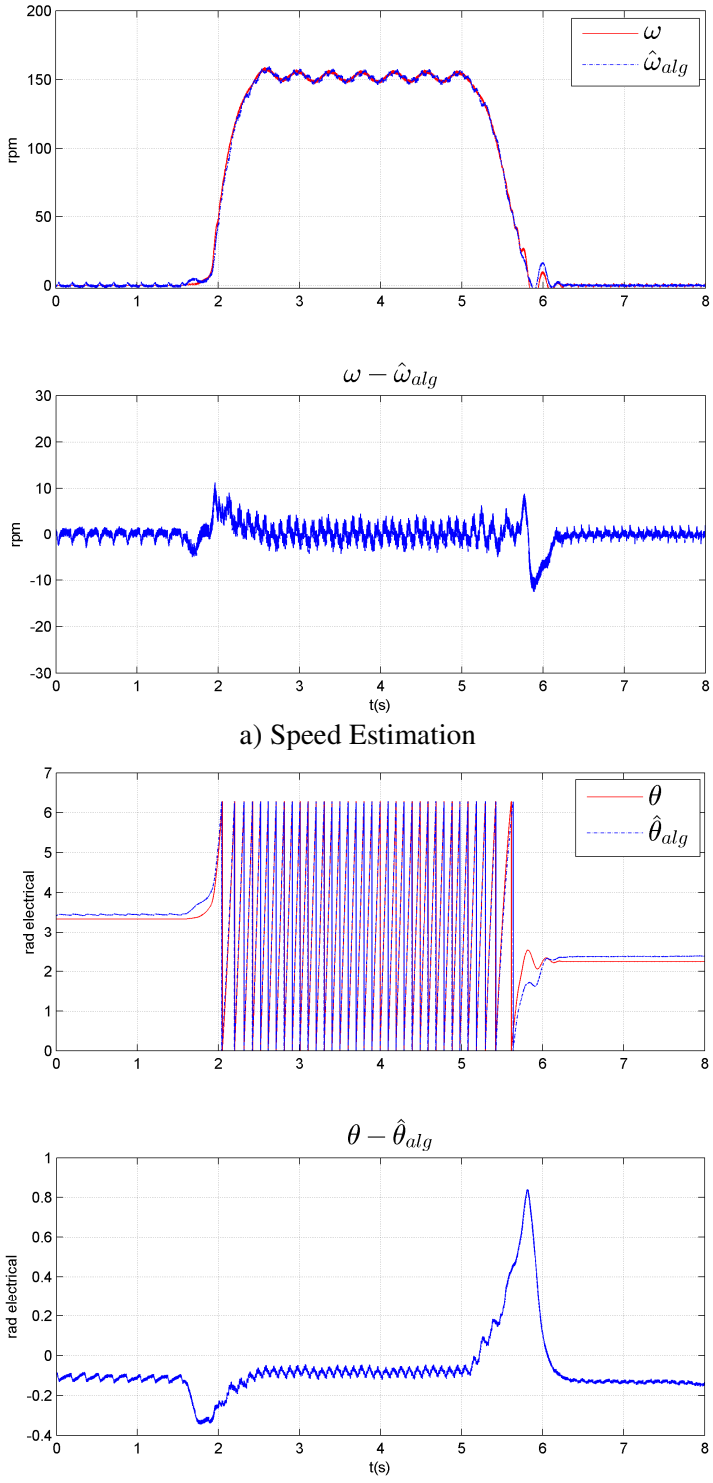

a) Speed Estimation

b) Position Estimation

Figure 3.5 Differential algebraic estimator evaluation in sensor operation at very low speed

The estimator exhibits also good tracking performances for an operation between 0 and 150 rpm. This speed represents 1/20 of the nominal speed (electrical machine with a nominal speed of 3000 rpm and a maximal speed of 12000 rpm).

Stability Tests:

The stability of the estimator is now evaluated. An equilibrium point is asymptotically stable when all nearby trajectories converge to the equilibrium point in large time. When there is more than one equilibrium point in a system (for e.g. systems with nonzero initial conditions), global stability needs to be studied. For the estimator, and choosing an equilibrium point corresponding to a null estimation error, we must ensure that for any initial position error, the estimator will converge to the real position in finite time. This is a strong property because most of the observers only guarantee a local stability. Figure 3.6a shows the convergence of the estimation with an initial position error of *0.9* electrical radians. The error quickly decreases to *-0.12* radians while the transient error of the speed estimation (Figure 3.6b) is 20 rpm.

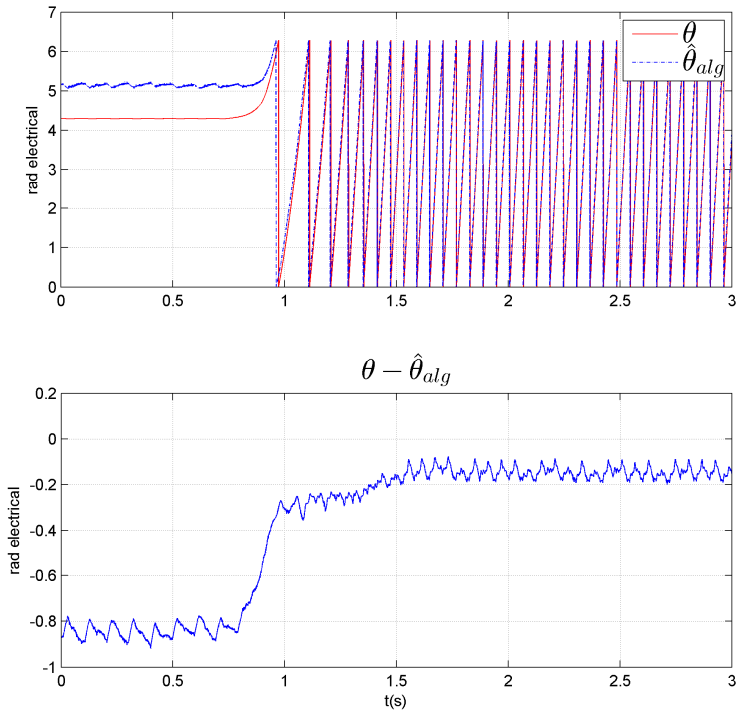

a) Position estimation

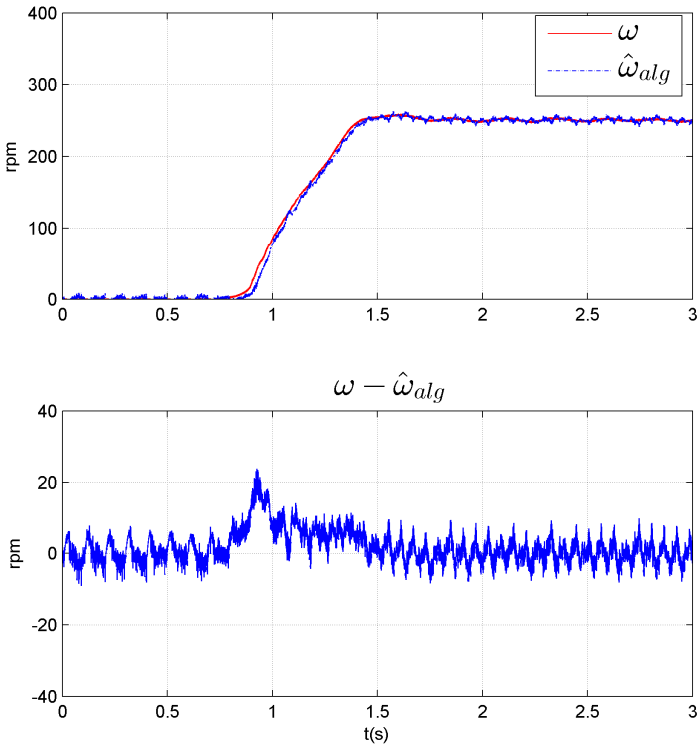

b) Speed estimation

Figure 3.6 Differential algebraic estimator in sensor operation with an initial error of *0.9* rad

The evaluation results with a higher initial error (*3* radians which is the maximal error feasible.) are displayed in Figure 3.7. The estimator converges also to a small error (*-0.08* radian) with an overshoot in the speed estimation (Figure 3.7b).

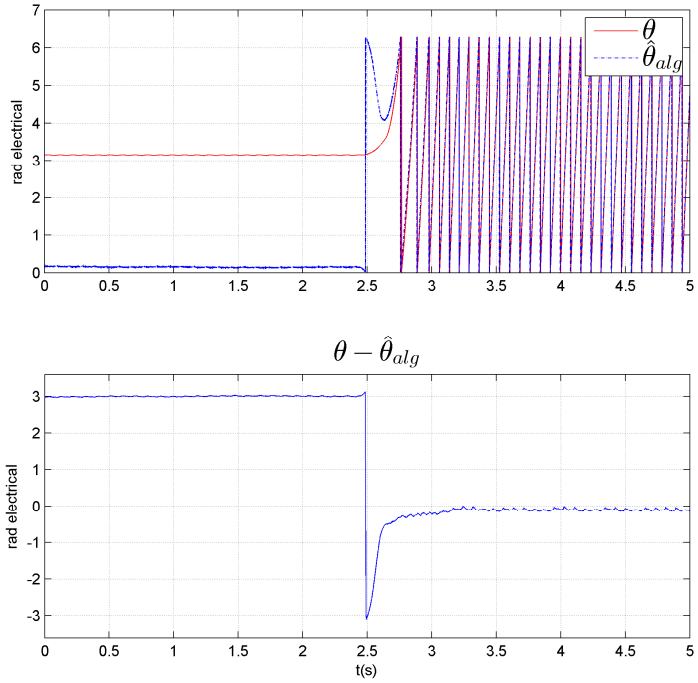

a) Position estimation

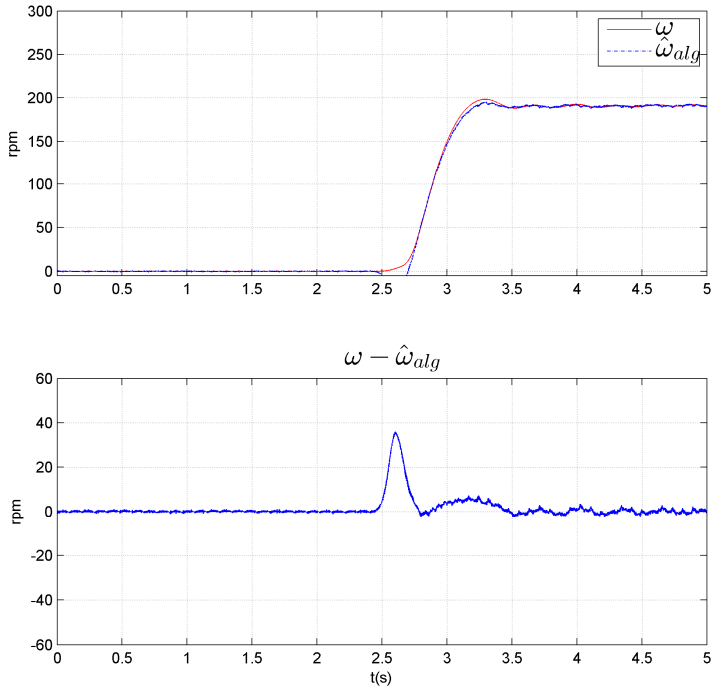

b) Speed estimation

Figure 3.7 Differential algebraic estimator in sensor operation with an initial error of *3* rad

Now the case of the reversal speed is studied in Figure 3.8. The position error at steady state is -0.15 rad. However, the transient error is very high (*1.3 rad*).

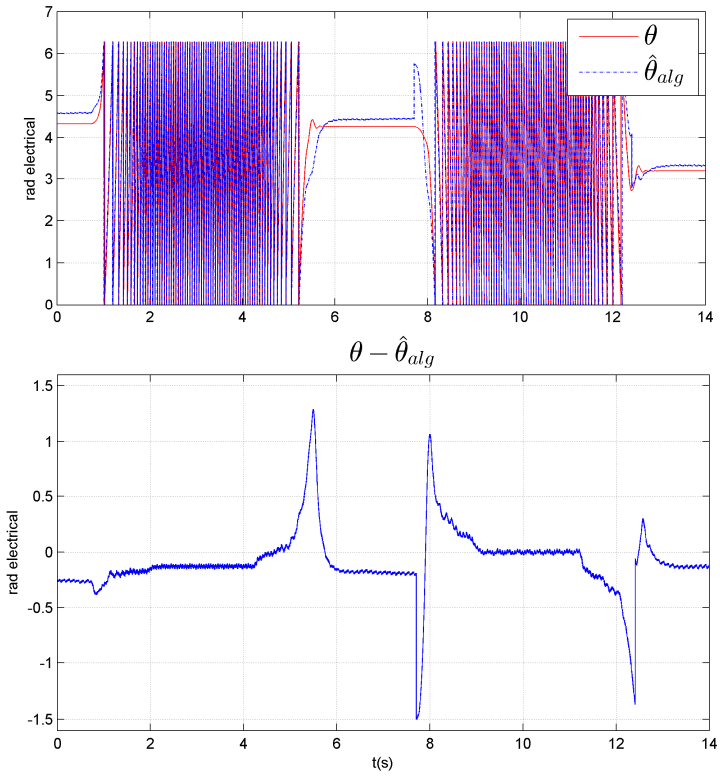

a) Position estimation

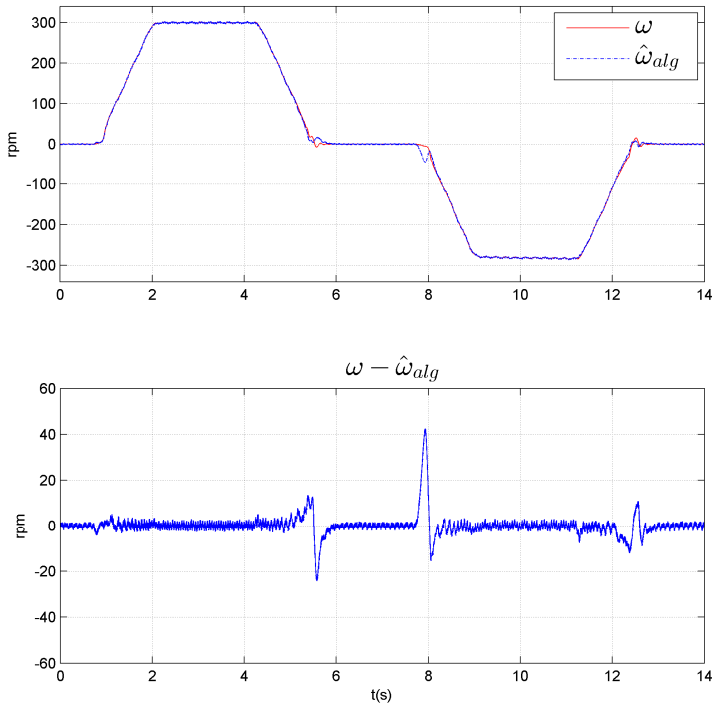

b) Speed estimation

Figure 3.8 Differential algebraic estimator in sensor operation under speed reverse

The impact of a load variation of 25% in steady state is also studied. This is done by imposing the speed with the Asynchronous Machine and the torque through the PMSM control. In Figure 3.9a, the q axis current performance is displayed with a step change at t=3.5s from 4 to 5*A* representing 16% of the nominal current (i_{qnom} = 30A).

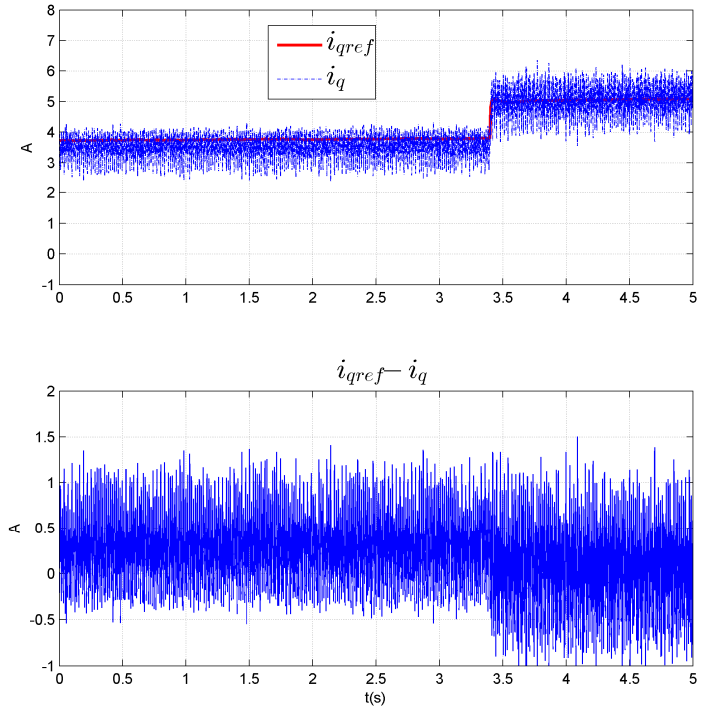

a) *q* axis current

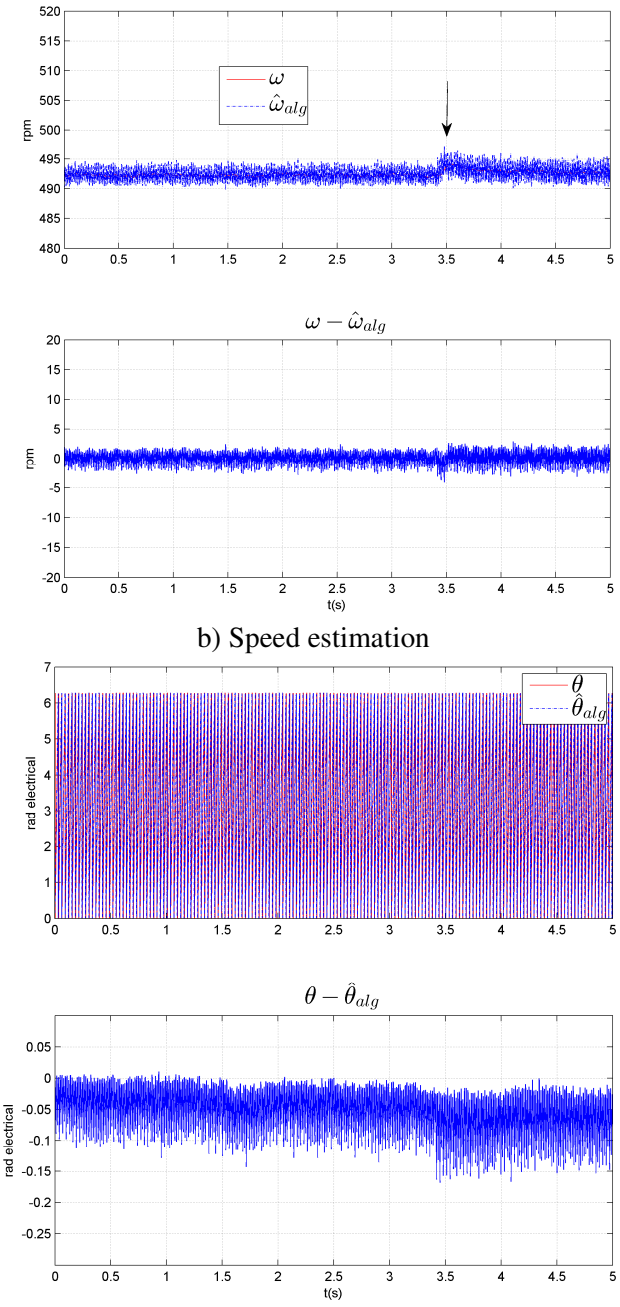

b) Speed estimation

c) Position estimation

Figure 3.9 Differential algebraic estimator in sensor operation: robustness to load torque variation

The speed estimation (Figure 3.9b) error remains very low (below 5 rpm corresponding roughly to 1% of the steady state speed) while higher ripples on the position error are noticed with an error still centered on -0.07 electrical radian (Figure 3.9c).

3.3.3.2 Sensorless Operation

The position/speed estimator output is now used for the control and the position sensor output is used solely for comparison purpose. Figure 3.10 shows the performances of the estimator in sensorless operation in the very low speed range.

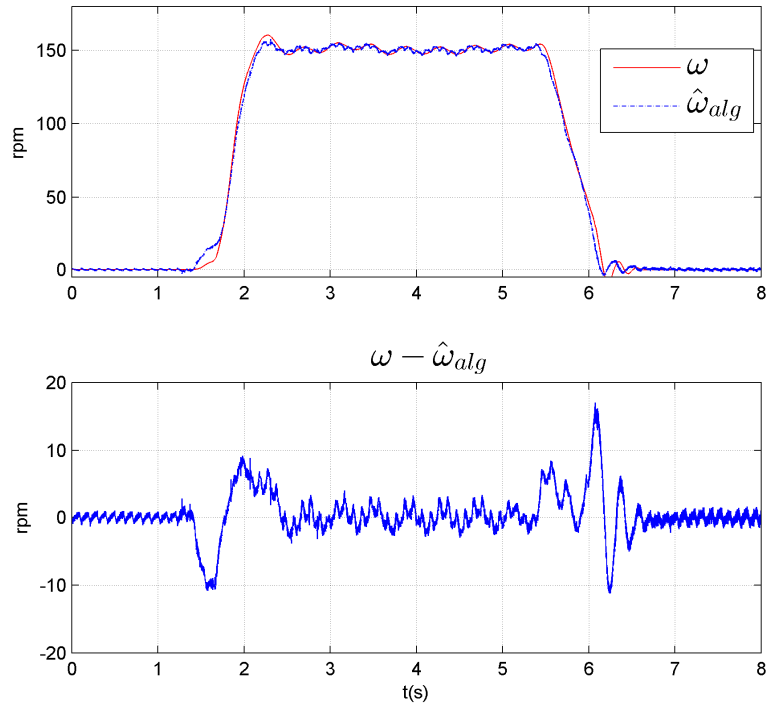

a) Speed Estimation

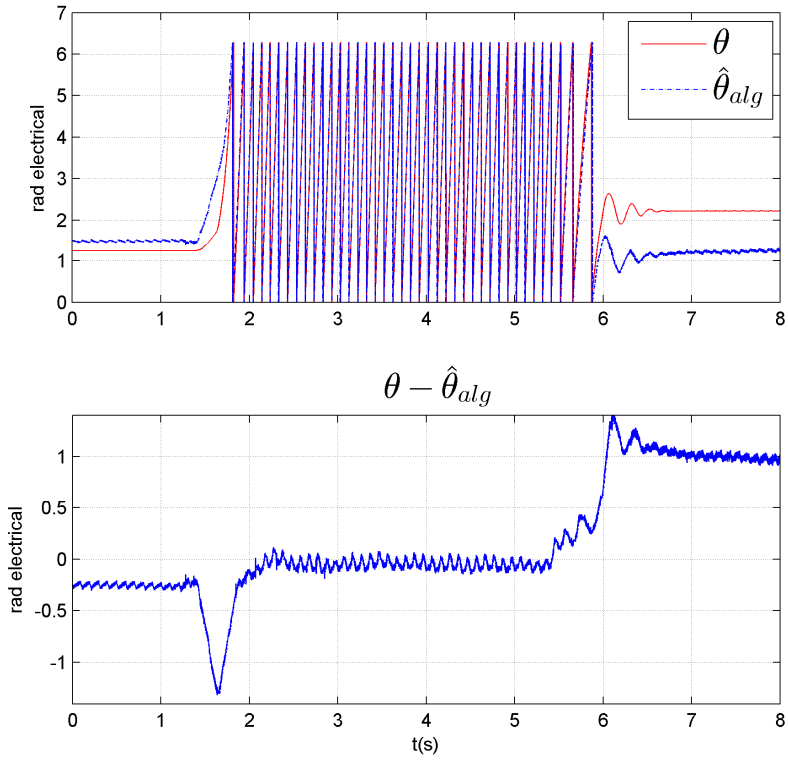

b) Position Estimation

Figure 3.10 Differential algebraic estimator in sensorless operation

In steady state, the speed estimation error is almost zero and the position estimation error is equal to *-0.15* radians (Figure 3.10b). During the transients, the maximal speed estimation error is equal to 10 rpm and the maximal position error is equal to *1.5 electrical radian (0.375*

mechanical radian or 21.5 mechanical degrees) radians. Compared to the results obtained in sensor operation at low speed (displayed in figure 3.5), the sensorless drive performances are satisfactory in steady state but the transients errors are higher particularly for the position estimation.

Despite the fact that the currents measured by the Analog-to-Digital Converters (ADC) are synchronized with the PWM, the current sensors are not very accurate (number of turns around sensor too small) and the dead-time effects of the voltage inverter are not compensated. Therefore these errors can be considered as the highest and the estimation errors can then be improved. In ([Nah2007]) the impact of the inverter imperfections on the estimation accuracy is pointed and the compensation of dead-time is found to be helpful for the estimation at very low speed.

The stability is also tested in sensorless control with an initial estimator error of 3 rad (Figure 3.11) which is the maximal error feasible.

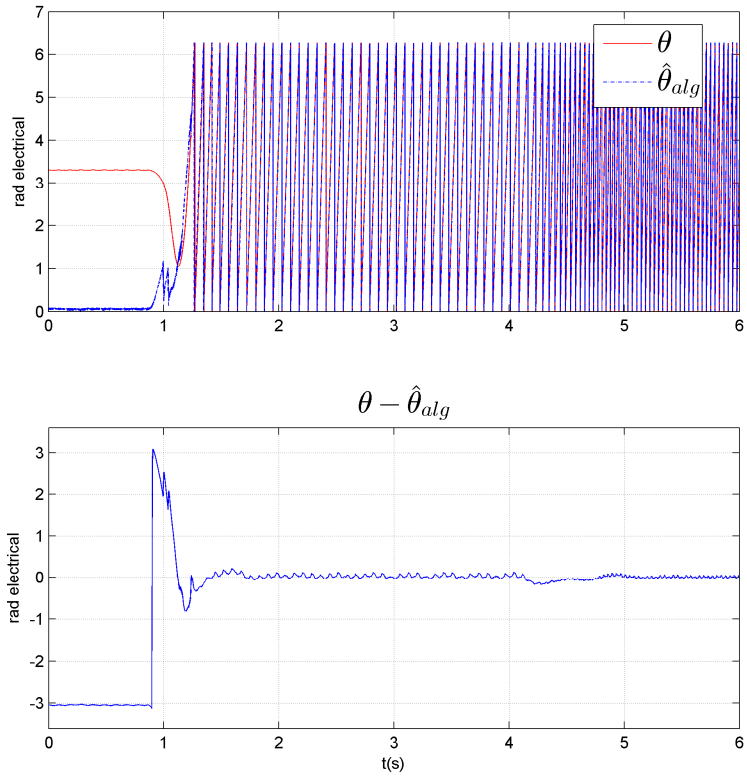

a) Position estimation

The position estimation compensates the initial error position in Figure 3.11a and converges to an error of *0.025* radians. However, a harder start with an overshoot of 55 rpm (figure 3.11b) for the speed is noticed. This can also be observed in the *q* axis current transient (which is computed from the estimated position) in Figure 3.11c with a peak value more than 20 times higher than the steady state value!

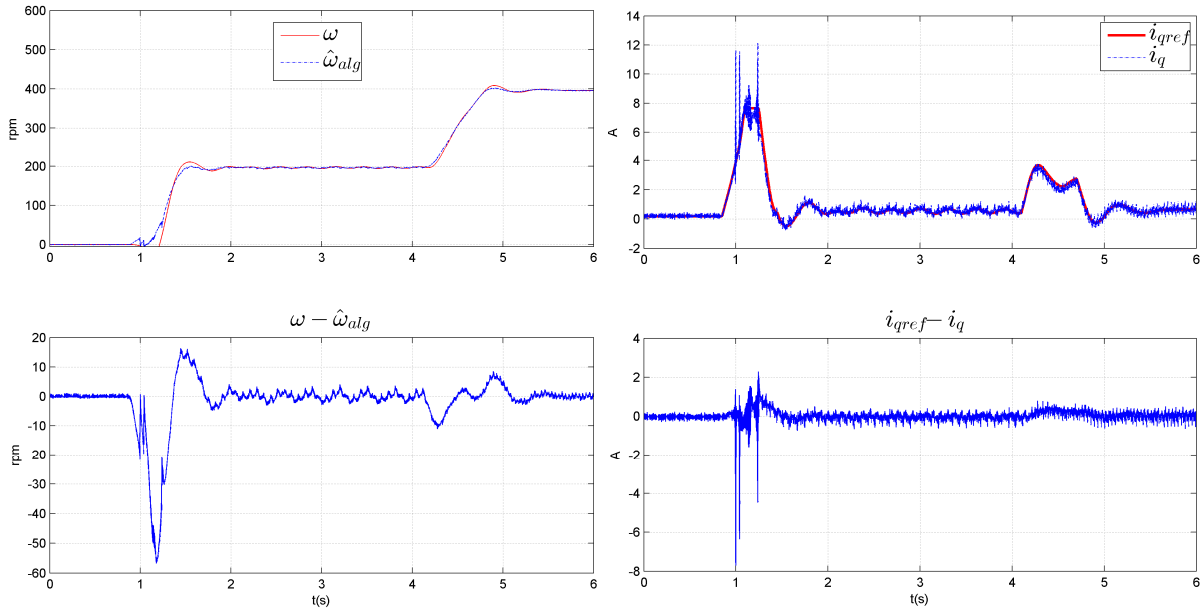

b) Speed estimation c) q axis current

Figure 3.11 Differential algebraic estimator in sensorless operation with an initial error of 3 rad

The algebraic estimator is also evaluated at medium speed (Figure 3.12).

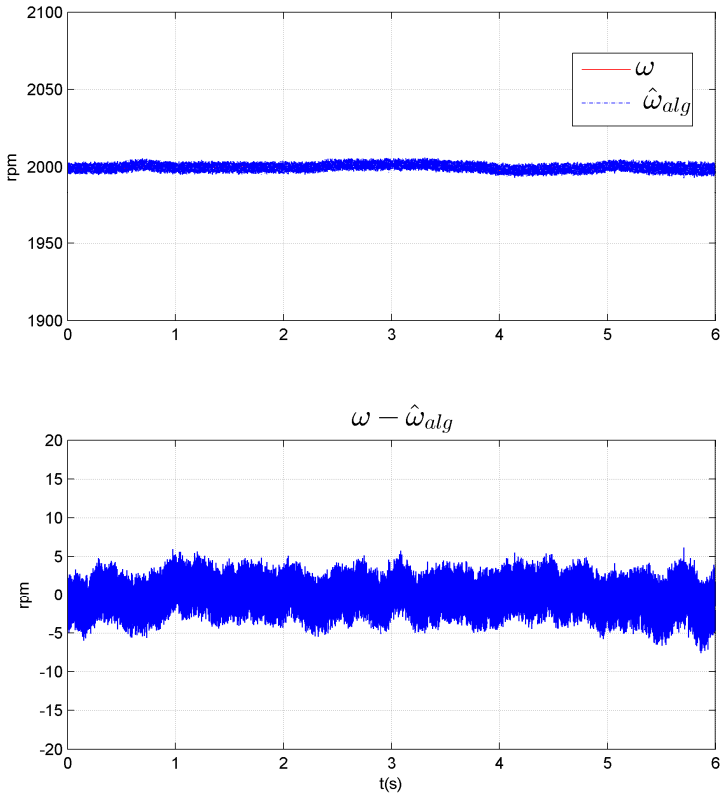

a) Speed Estimation

The behavior of the q axis current component is also acceptable (Figure 3.12b) despite the increase of the ripples.

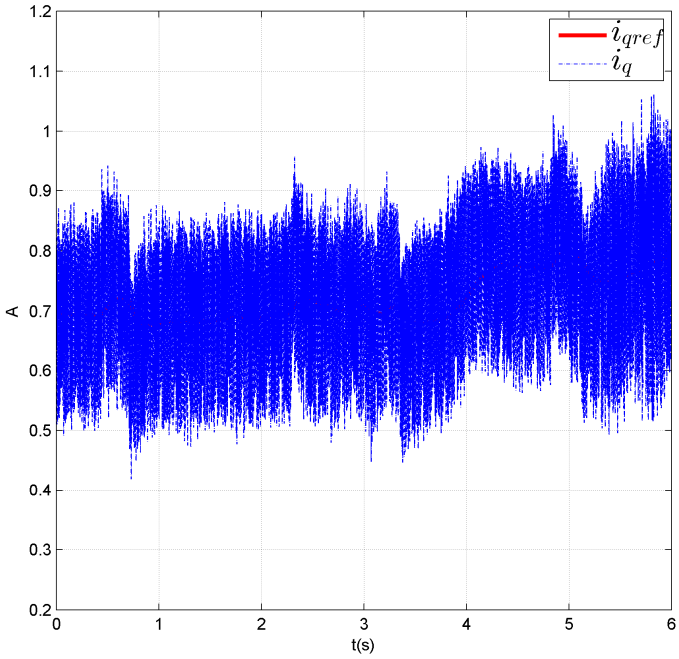

b) q axis current

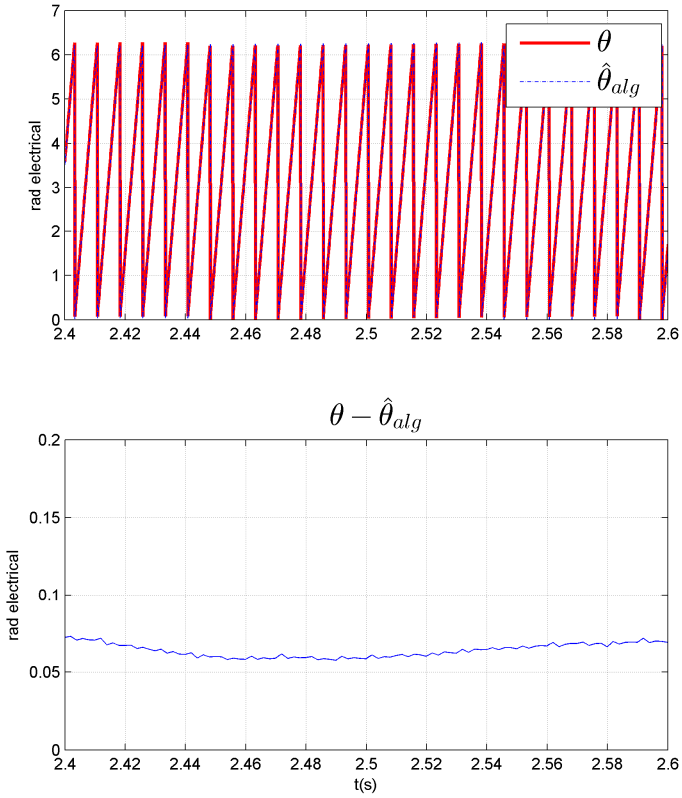

c) Position Estimation

Figure 3.12 Differential algebraic estimator in sensorless operation in medium speed range

In figure 3.12c, the results for the position are pointed out in a reduced time range so as to have a better view of the tracking. The position error is of 0.075 electrical rad which is still satisfactory.

Then, the following profile from 0 to 2000rpm is considered in sensorless mode (Figure 3.13).

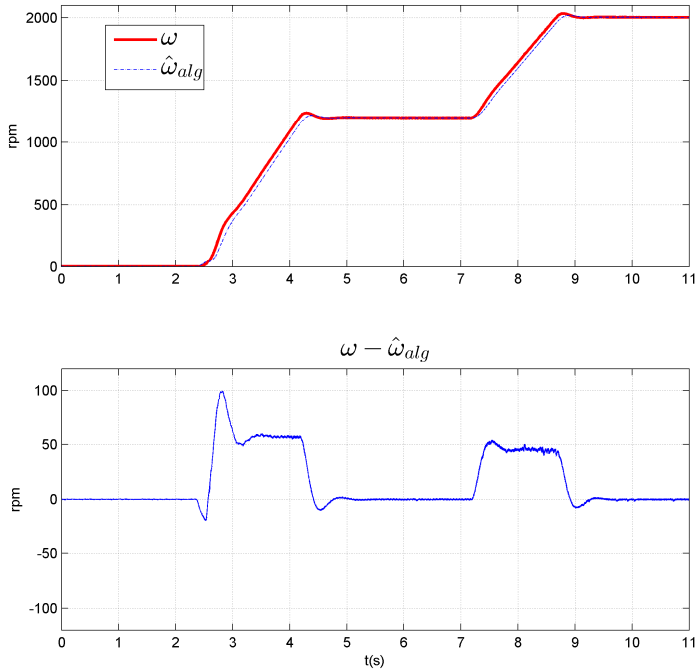

a) Speed Estimation

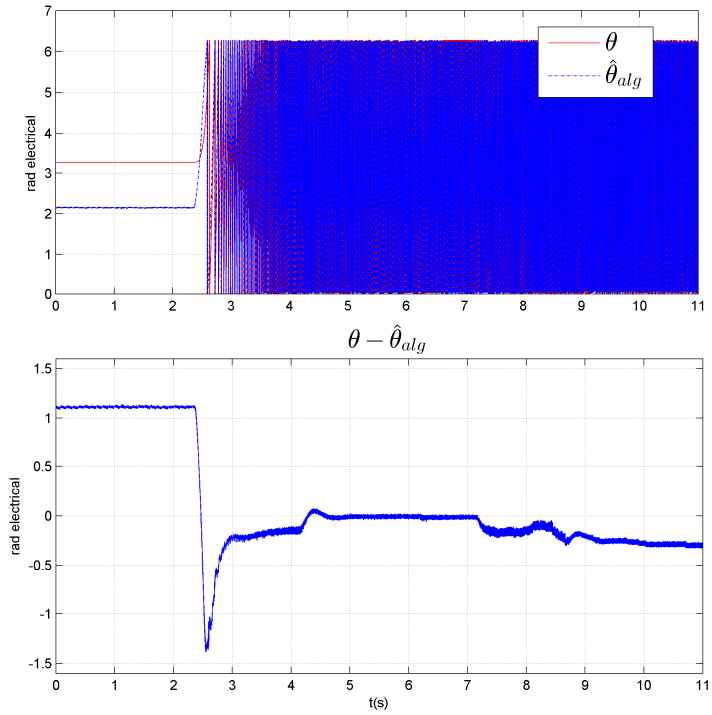

b) Position Estimation

Figure 3.13 Differential algebraic estimator in sensorless from 0 to 2000 rpm mechanical

The errors at steady state are respectively -0.05 rad (at 1400 rpm) and -0.3 rad (at 2000 rpm). Now the impact of a load variation is studied. Figure 3.14 illustrates with experimental results the estimator performances with a load torque variation in steady state.

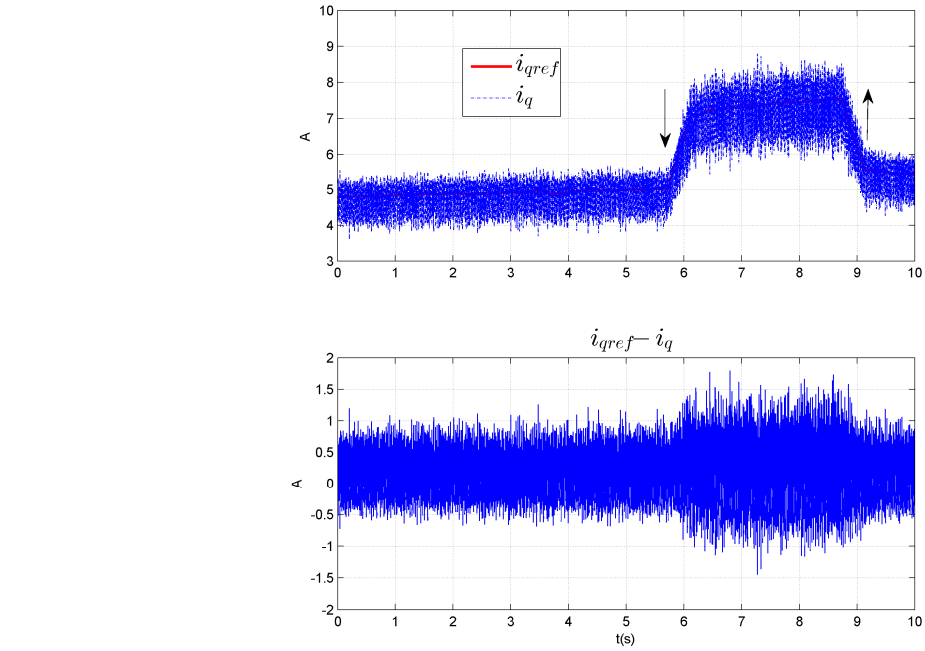

a) q axis current

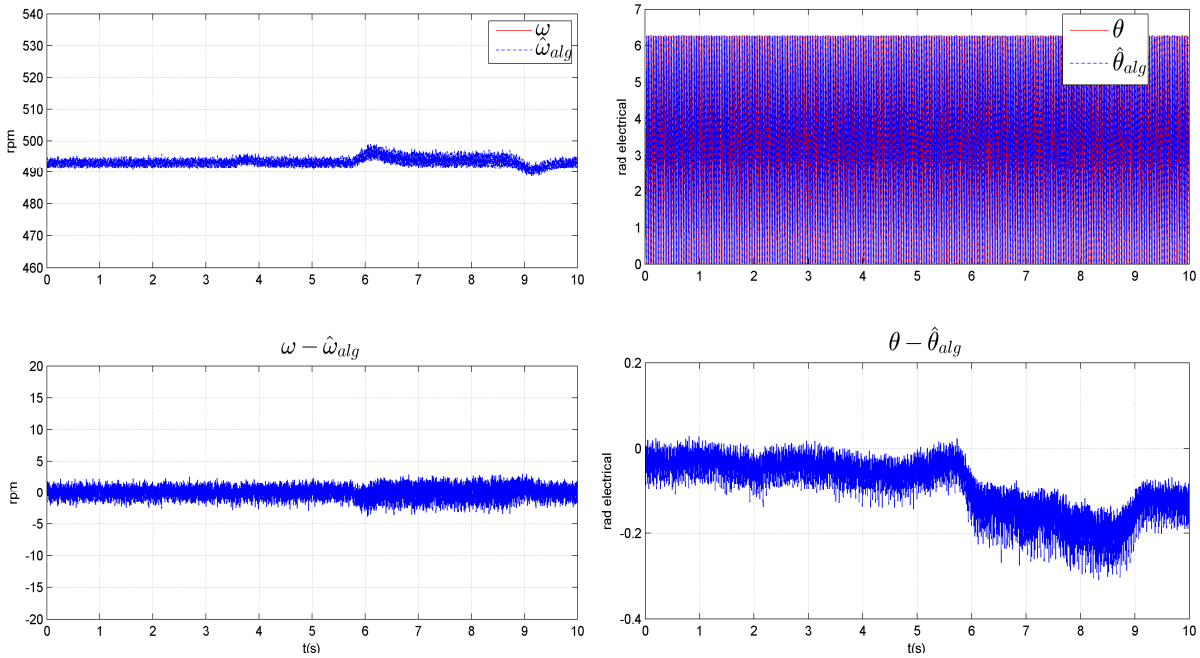

b) Speed Estimation Position Estimation

Figure 3.14 Differential algebraic estimator in sensorless operation with load torque variation

In the right column of Figure 3.14b, the position error increases to 0.2 rad at the load variation occurrence; this corresponds to a 3 mechanical degrees error. However, this variation is still acceptable and the whole drive is under control despite the additional oscillations in the *q* axis current (Figure 3.14a).

3.3.3.3 Robustness issues

The estimator is sensitive to the machine parameters and the current measurements. Experimental tests are performed to evaluate the robustness of the estimator to the stator resistance and inductance variations on the whole operating range. An analytical study is derived to support the evaluation of the robustness.

Given the expression of the estimator in (3.18), the resistance and the inductance appear only in the numerator called *N*: $N = \sin\hat{\theta}(L_q\dot{y}_1 + R_s y_1 - u_1) + \cos\hat{\theta}(-L\dot{y}_2 - R_s y_2 + u_2)$

This numerator is now rewritten in the case of a variation of *L* by N_1 and by N_2 for a variation of R_s.

$N_1 = \sin\hat{\theta}(L^*\dot{y}_1 + R_s y_1 - u_1) + \cos\hat{\theta}(-L^*\dot{y}_2 - R_s y_2 + u_2)$,

$N_2 = \sin\hat{\theta}(L\dot{y}_1 + R_s^* y_1 - u_1) + \cos\hat{\theta}(-L\ \dot{y}_2 - R_s^* y_2 + u_2)$

L^* and R_s^* stands for the actual parameters. The estimation error is then defined respectively for *L* and R_s variation by:

$$\varepsilon_L = (L - L^*)(\dot{y}_1\sin\hat{\theta} - \dot{y}_2\cos\hat{\theta}), \varepsilon_{R_s} = (R_s - R_s^*)(y_1\sin\hat{\theta} - y_2\cos\hat{\theta}) \quad (3.21)$$

Using $\left|\sin\hat{\theta} - \cos\hat{\theta}\right| \le \sqrt{2}$ and $\left|\dot{y}_1\right| = \left|\omega y_1\right|$ leads to:

$$\left|\varepsilon_{L_q}\right| \le \sqrt{2}\left|L - L^*\right|\left|\omega y_1\right|, \left|\varepsilon_{R_s}\right| \le \sqrt{2}\left|R_s - R_s^*\right|\left|y_1\right| \quad (3.22)$$

Considering a 40 % inductance error and the unit of *L*, the error is $\left|\varepsilon_L\right| \le \sqrt{2} * 2.4e^{-3}\left|\omega y_1\right|$ and for a resistance variation of 50 % $\left|\varepsilon_{R_s}\right| \le \sqrt{2} * 0.168\left|y_1\right|$.

From this, the robustness with respect to the parameters variation is now evaluated (Figure 3.15 and Figure 3.16 for the resistance, Figure 3.17 and Figure 3.18 for the inductances). The parameter errors are inserted in the control loop by modifying their default values and the behavior of the estimator is observed.

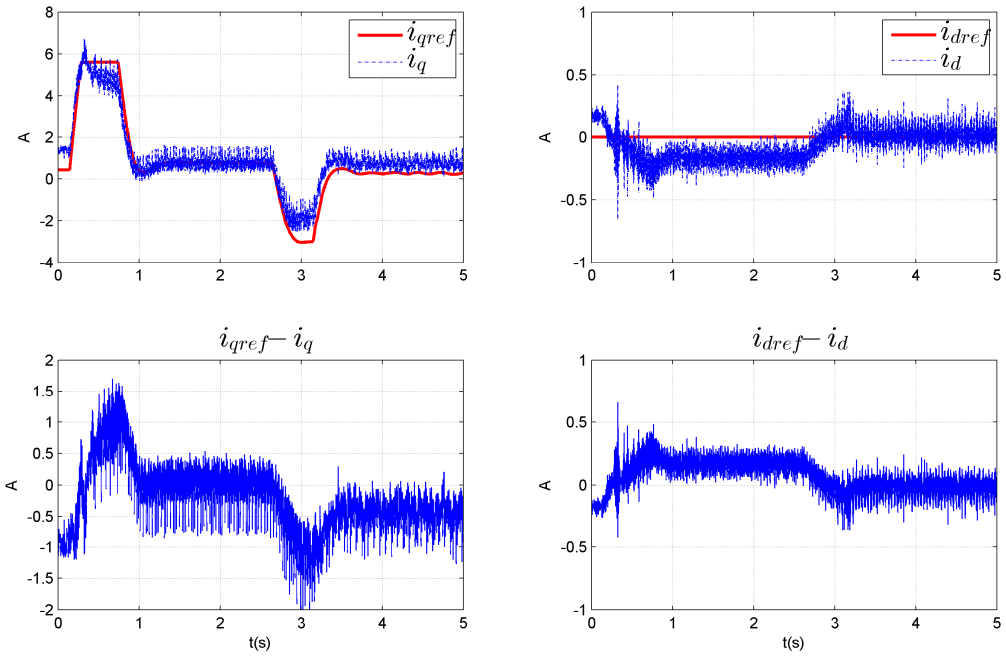

a) d,q axis currents under R_s variation (-50%)

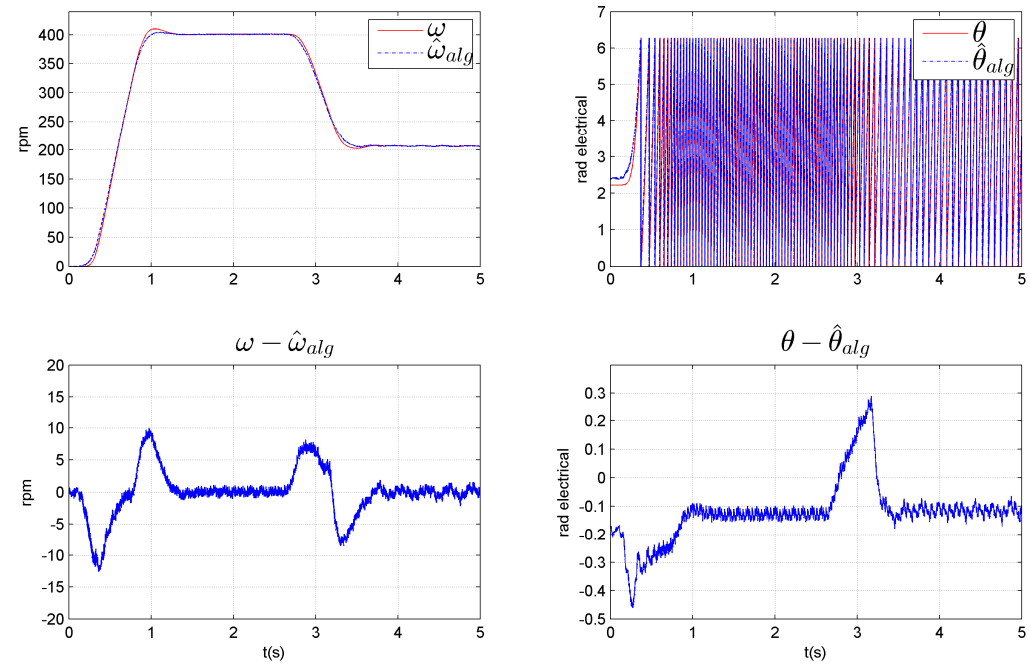

b) Speed and Position estimation under R_s variation (-50%)

Figure 3.15 Differential algebraic estimator robustness evaluation in sensorless operation (-50% R_s)

The first point is the robustness of the control with respect to the parameter variation (R_s, L). The tracking of the d,q currents is maintained with as expected a steady state error under R_s variation. In fact the static gain of the closed loop is strongly related to R_s.

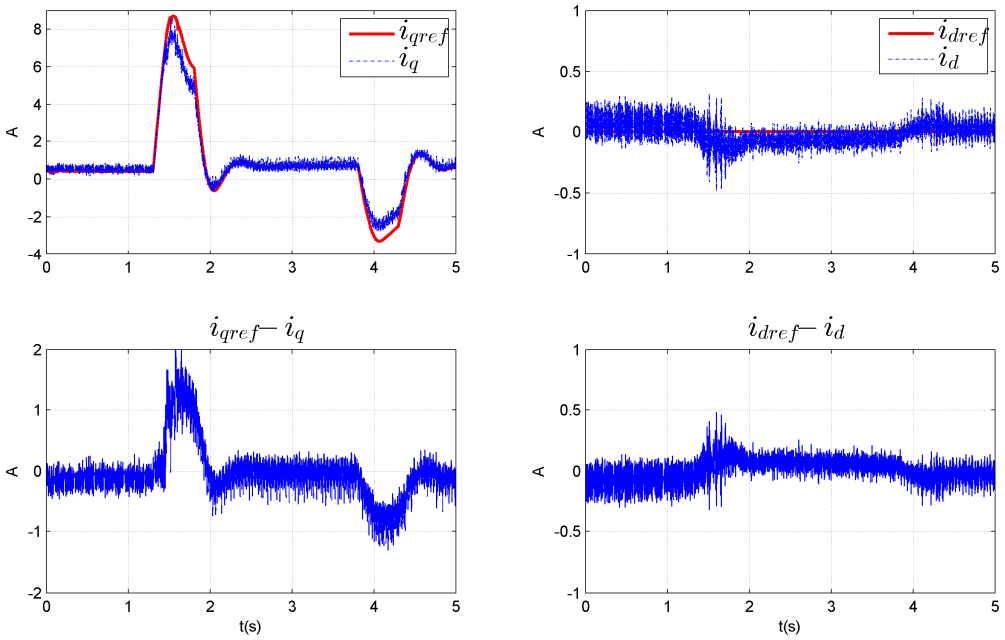

a) *d* and *q* axis currents under R_s variation (+50%)

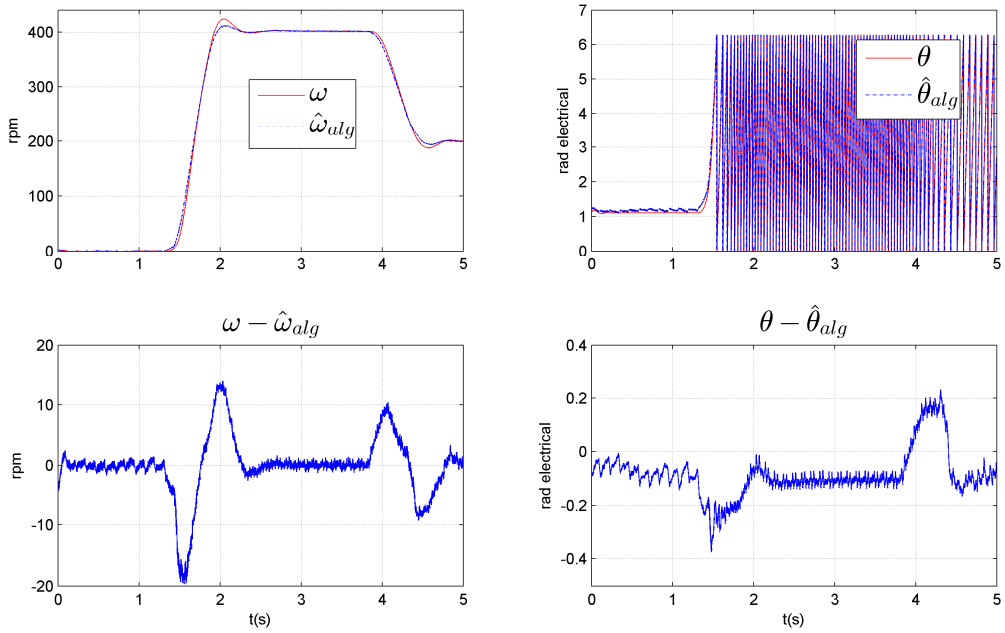

b) Speed and Position estimation error under R_s variation (+50%)

Figure 3.16 Differential algebraic estimator robustness evaluation in sensorless operation (+50% R_s)

For these experimental results, we have at steady state $|y_1| = |y_2| \approx 1$. Then the experimental results must verify for the steady state operation: $|\varepsilon_L| \leq 0.5, |\varepsilon_{R_s}| \leq 0.24$ and the speed estimation error is almost zero at steady state.

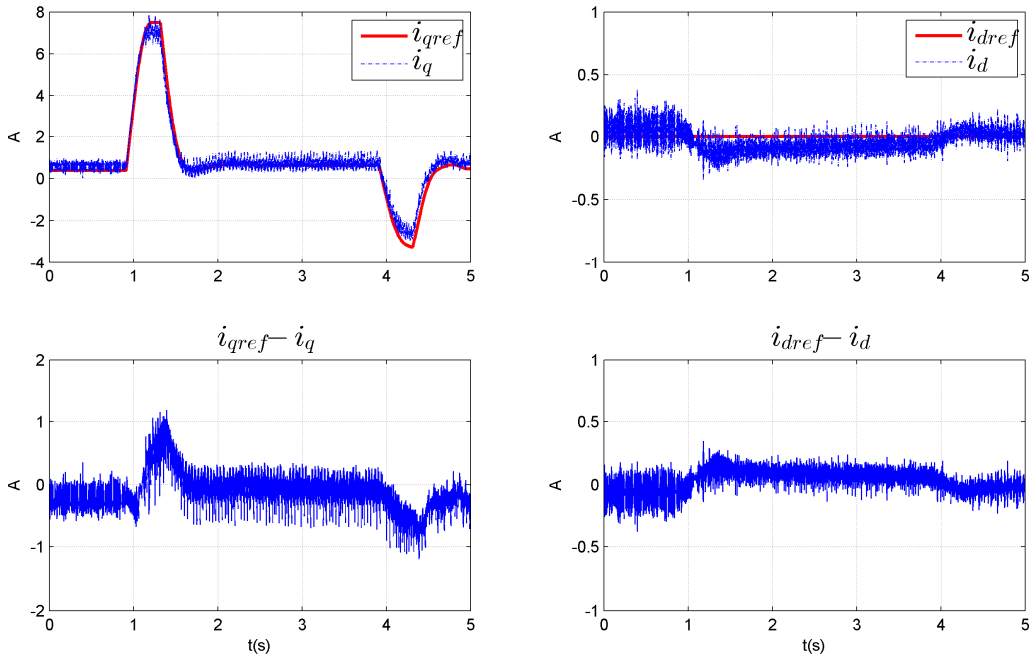

a) *d* and *q* axis currents with *L* variation (-50%)

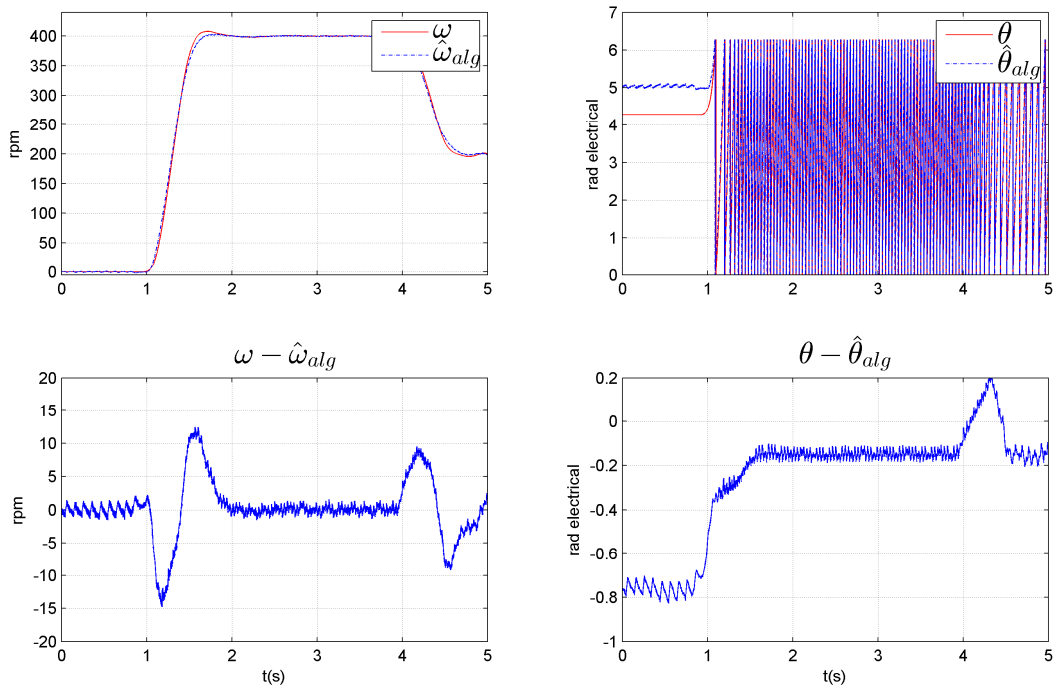

b) Speed and Position estimation error under *L* variation (-50%)

Figure 3.17 Differential algebraic estimator robustness evaluation in sensorless operation (-50% *L*)

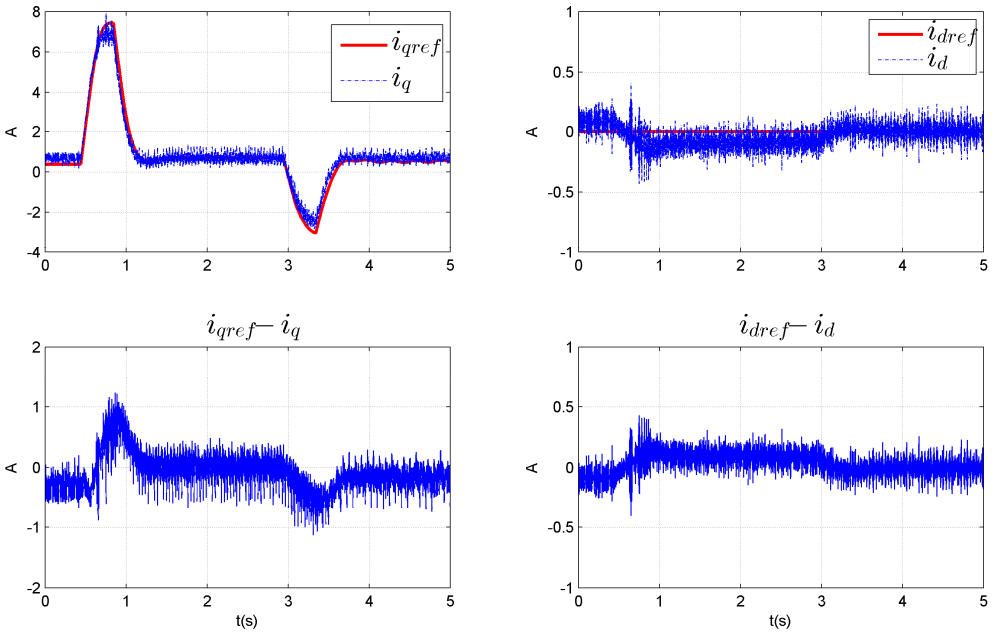

a) *d,q* axis currents under *L* variation (+50%)

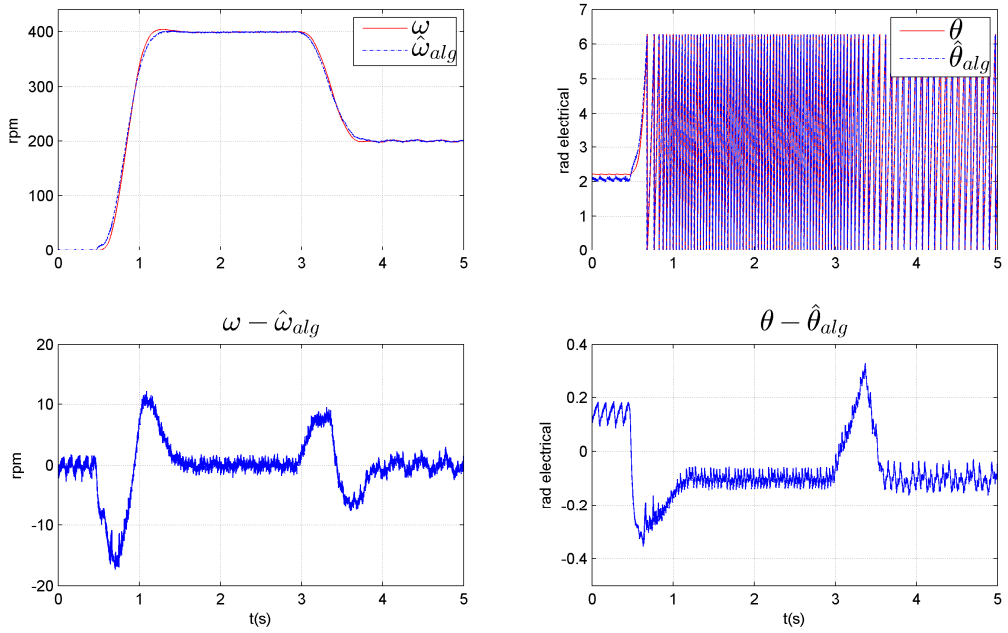

b) Speed and Position estimation error under *L* variation (+50%)

Figure 3.18 Differential algebraic estimator robustness evaluation in sensorless operation (+50% *L*)

In Figure 3.15b and 3.16b at steady state, the position estimation error is inferior to $|\varepsilon_{R_s}|$ for the variation of the resistance. In Figures 3.17b and 3.18b, the position estimation error is inferior to $|\varepsilon_L|$ under the variation of the inductance.

To conclude, the position errors (inferior to 0.2 electrical radians in steady state corresponding to 3 mechanical degrees) are in the acceptable ranges for automobile applications, which target generally a 5% position error (0.31 electrical radians) [Liu2003].

3.3.4 Comparison of the three estimators

In this paragraph, a brief experimental comparison of the three estimators (EKF, Back-emf and differential algebraic) is proposed. They are implemented on the same test bench and evaluated under the same conditions (i_q = 1A in steady state). The estimated positions and speeds are compared to the measurements. The estimation errors will be computed and compared.

The algebraic estimator based on a straight analytical expression has a lower algorithmic cost compared to EKF and back-emf observer and is more suitable for embedded applications. Position estimation based on back-emf technique is known to have poor performances at low speed because the magnitude of the back-emf voltage is proportional to the speed. EKF is much more appropriated for nonlinear systems that involve very noisy measurements and appears to be a viable candidate provided a good knowledge of initial conditions [Aug2013].

The comparison starts with the low speed case (around 12% of the nominal speed and 3% of the maximal speed). The results are displayed in Figure 3.19.

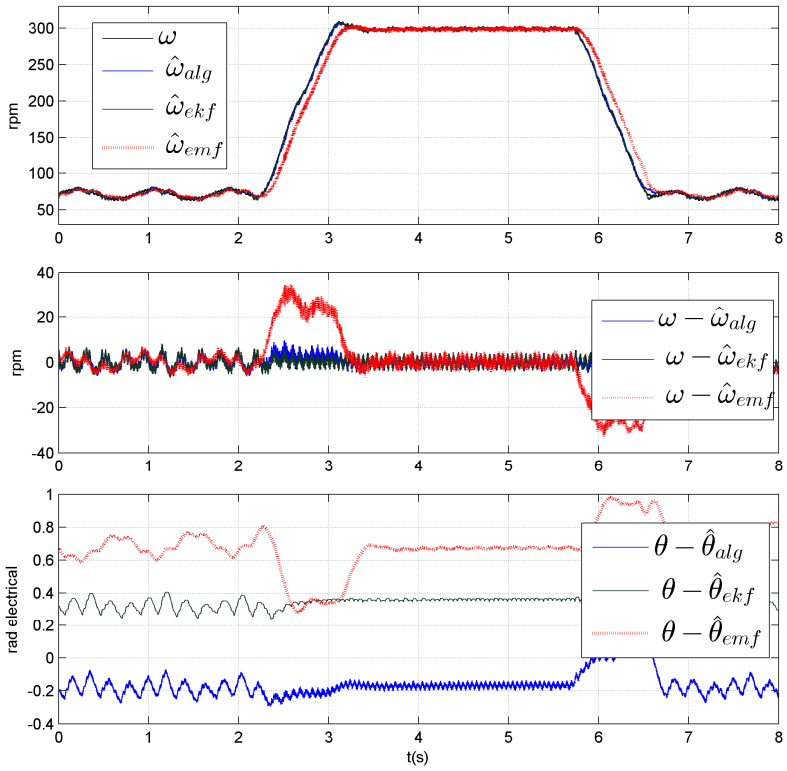

a) Very low speed operation

From 50 to 300 rpm, the steady state algebraic position error is near -0.2 rad while the error

for EKF is equal to 0.4 and 0.7 for the back-EMF (Figure 3.19a).

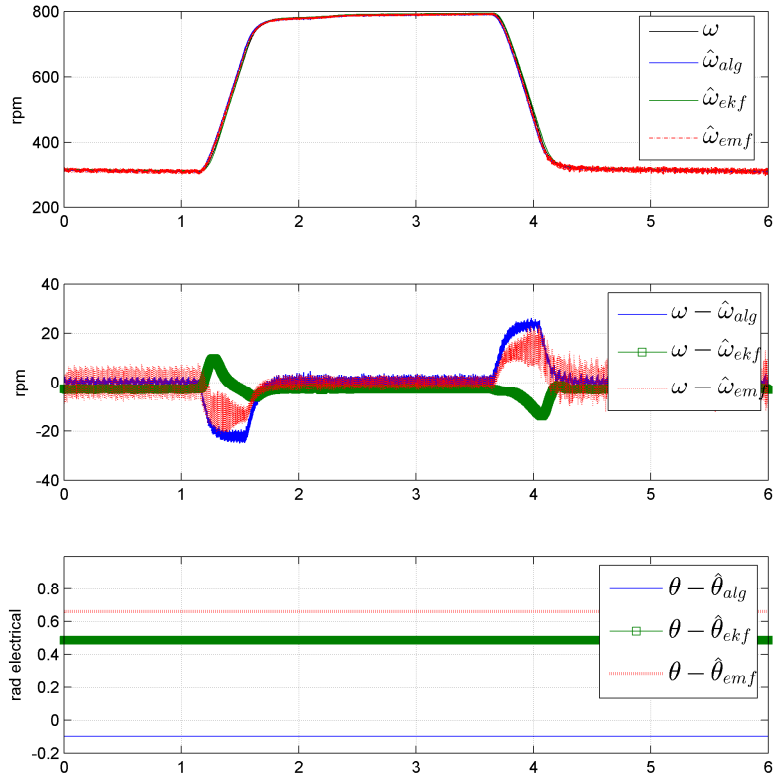

b) Low speed operation

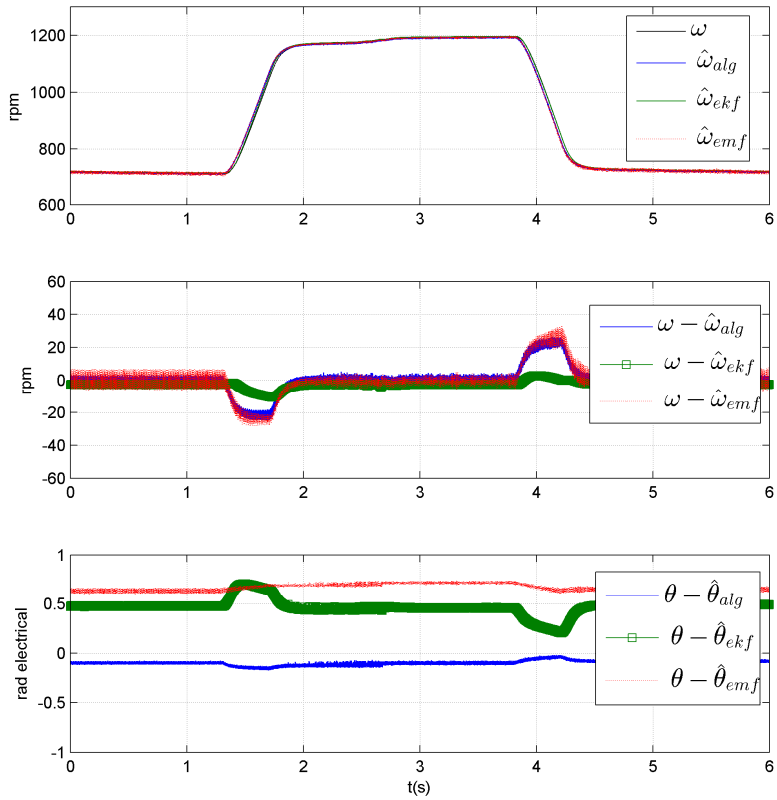

c) Medium speed operation

Figure 3.19 Comparison of the Estimators

From 300 to 800 rpm, the algebraic position error at steady state is near -0.15 rad while the error for EKF is equal to 0.5 and 0.7 for the back-EMF (Figure 3.19b). As expected, Back-EMF estimation is less accurate at low speed and the EKF could be improved with a better tuning of the initial conditions, which is hard and hazardous. The same trend is noticed between 700 and 1200 rpm (Figure 3.19c).

The variation of the different position estimation errors with respect to the speed is shown in Figure 3.20.

Figure 3.20 Evolution of the Electrical Position Estimation errors

The experimental results are summarized in the following table (Table 3.1). From this non-exhaustive study, in every speed range (low, medium), there is one efficient estimator. Despite the absence of comparative tests at high speed, one can recall the good ability of EKF and the Back-emf observer which has already been proved in this speed range according to the literature.

Table 3.1: Comparison of the Estimators

	Implementation	Accuracy	Robustness
Extended Kalman Filter	Hard	Very good	Very robust
Back-emf observer	Easy	Good	Robust
Differential algebraic estimator	Very easy	Very Good	Robust

Therefore one can conclude that for sensorless operation or mechanical sensor monitoring for FTC on a wide speed range, two estimators can be combined with the sensor for diagnosis purposes or for ensuring the continuity of operation. It is a fact that EKF can have a better accuracy with a better tuning of the initial values and by adding a load torque observation [Akr2010]. Doing so, it becomes the most accurate observer but the implementation cost will be higher and up to now, we didn't find an efficient tool to correctly initialize the EKF in position/speed estimation. In annex 4, the characteristics of the estimators (EKF and the algebraic estimator) are compared experimentally with criteria such as the convergence and the accuracy of the regulators in sensorless mode.

3.4 Position /Speed Sensor Fault Detection, Isolation and Reconfiguration

3.4.1 Sensor Fault Enabling based on observers

In order to detect and diagnose a sensor fault, safety rules recommend having at least three measurements of the same information, including two with uncorrelated sources [Ise2006].
In our case, the FTC strategy is based on the combination of two analytical redundant virtual sensors (the algebraic estimator and the EKF) with the mechanical sensor. When reconfiguring the control, the selection of the position and the speed is done through a voting algorithm (Figure 3.21).

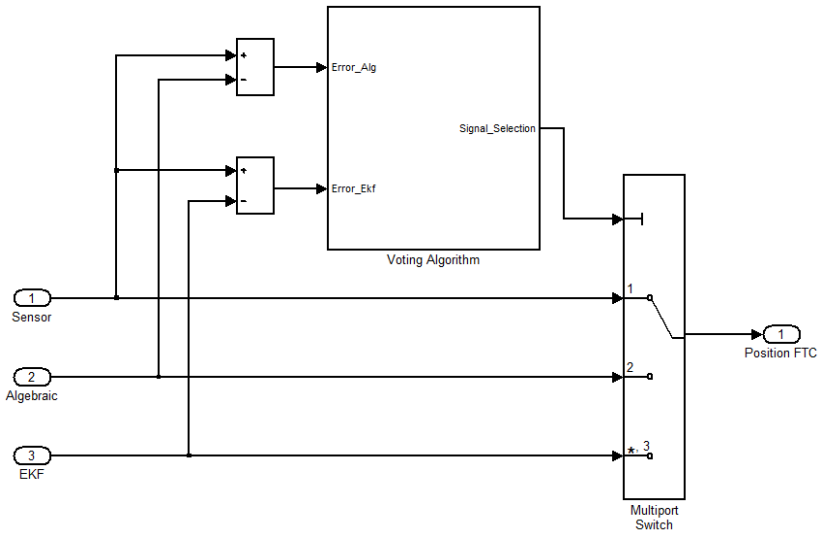

Figure 3.21 Position Sensor FTC

Several voting algorithms have been widely used for FDI [Ven2003]. In our case, the majority voting algorithm has been chosen. The schematic diagram is displayed in Figure 3.22.

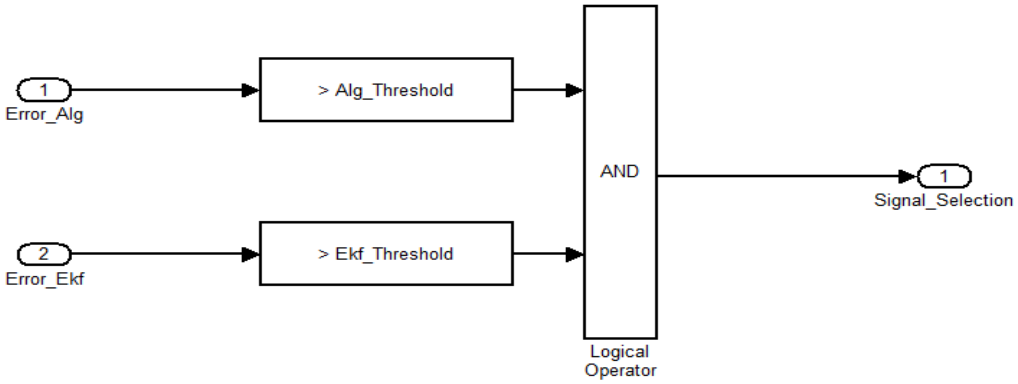

Figure 3.22 Voting Algorithm

A fault is detected when the estimation errors (difference between the sensor output and the estimator's outputs) Error_Alg and Error_Ekf are superior to the predefined thresholds. At this level, a challenging issue is the choice of the detection threshold (two thresholds need to be settled for the algebraic estimator and for the EKF).

Indeed, as noticed in the previous paragraph (Figure 3.20), the accuracy of the observers is variable. It is then necessary to have an adaptive threshold to mitigate this problem.
Our proposal is to store the estimation errors in a lookup table (variation of the position error depending on the speed provided by the data plotted in Figure 3.20). These errors will be used as inputs to calculate the threshold. The voting algorithm is then modified as shown in Figure 3.23. In the following experimental results, different kind of sensor faults will be considered: offset, gain error and complete loss of information. These faults may come from the encoder signal conditioning or from a counting error in the processing block (Annex 5).

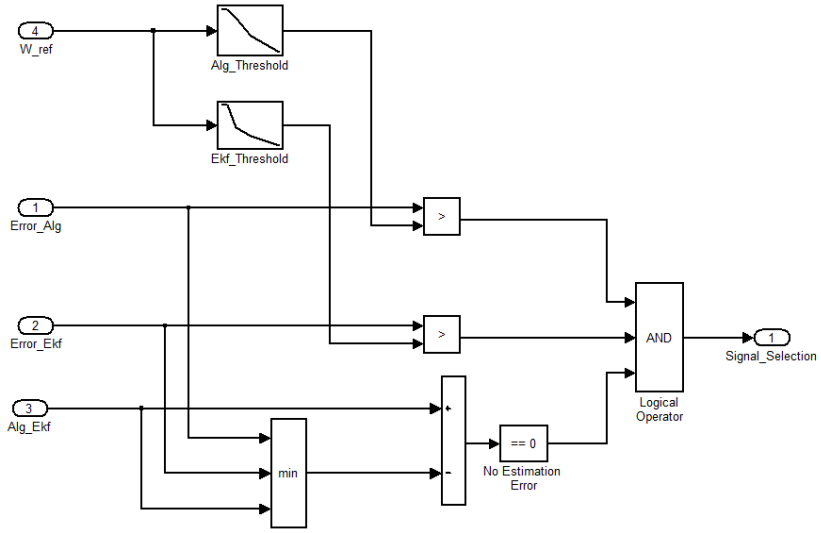

Figure 3.23 Voting Algorithm with adaptive thresholds

3.4.2 Experimental Results

The Fault Detection and Isolation (FDI) unit is firstly tested with an abrupt sensor fault in no load condition (offset of 0.4 electrical rad between t=3.13s and t=8.13s) as shown in Figure 3.24. After numerous experimental trials, it was found that for electrical position errors lower than 0.4 radian, the controllers were robust enough to cope with the fault. Beyond this value undesirable effects arise and the fault detection becomes mandatory.

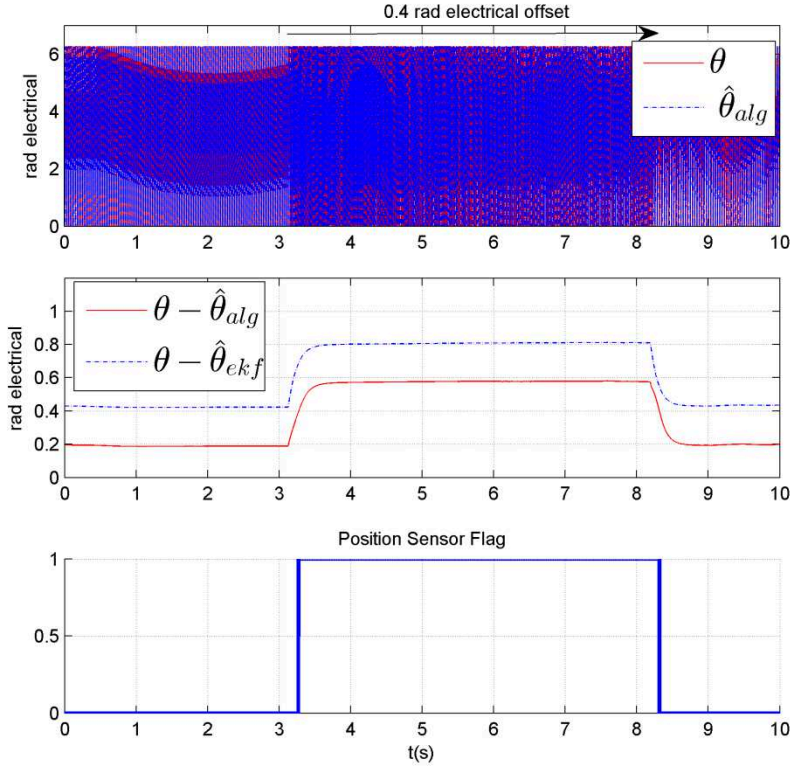

a) Position estimation

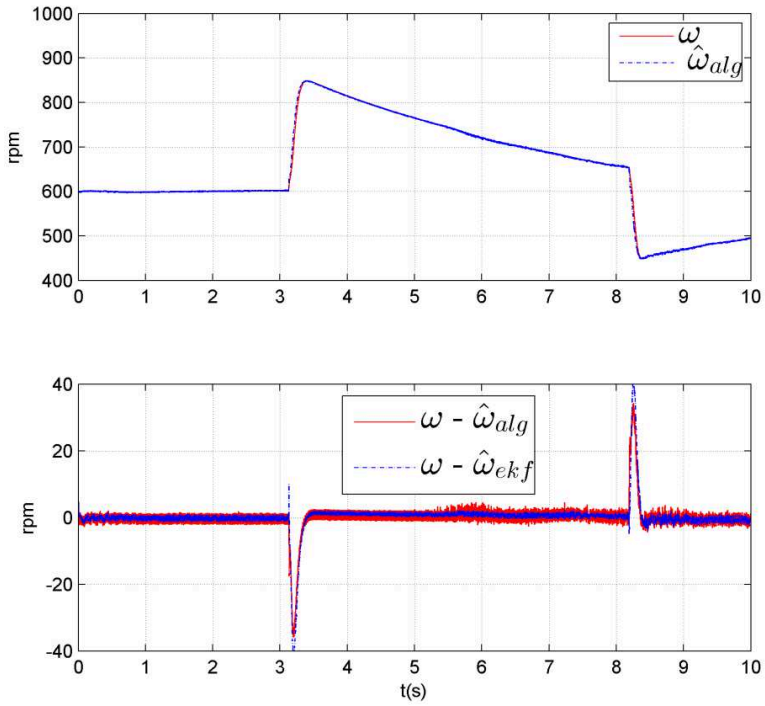

b) Speed Estimation

Figure 3.24 Abrupt sensor fault detection

The threshold is settled at 0.25 for the algebraic estimator and 0.45 for the EKF according to the evolution of the position estimation errors (Figure 3.24).The fault is detected after 0.08 s and as no action is taken, the consequence is the loss of the speed control during the offset (Figure 3.24b). Then it is essential to setup a reconfiguration strategy. Now the case of the Fault Reconfiguration in load condition after a sensor outage is evaluated. The results are displayed in Figure 3.25.

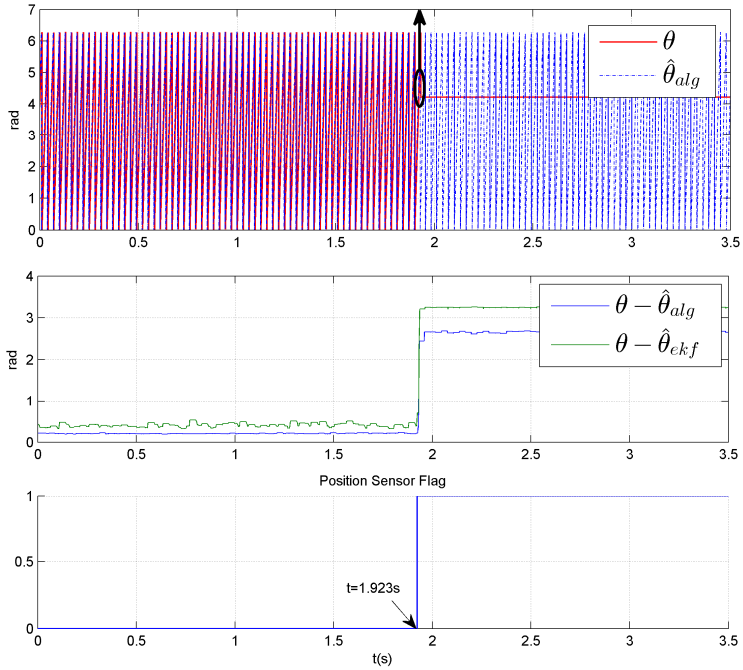

a) Position Estimation and Flag

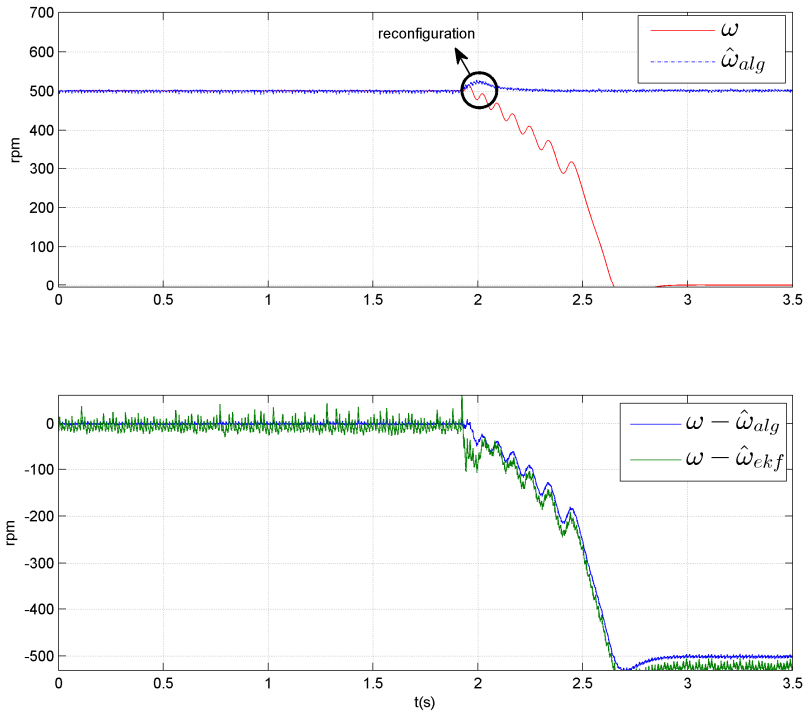

b) Speed Control

The fault is detected as proved with the flag variation in the third plot of Figure 3.25a. The measured speed vanishes after the fault while the speed given by the algebraic estimator is used to continue the operation as shown in Figure 3.25b.

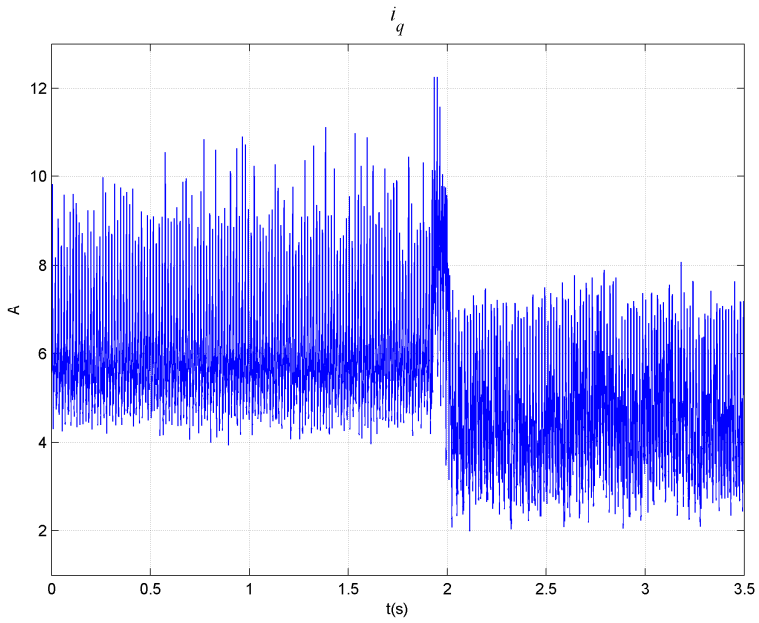

c) i_q current variation

Figure 3.25 Fault Reconfiguration after a sensor outage

Before the fault, the i_q average current was 5.5 A (figure 3.25c). After the fault, it decreases to 4.5 A. This can be explained by the estimation error which leads to a difference between the actual *d,q* currents (in the equivalent machine windings) and the computed *d,q* currents from the Park transformation. Nonetheless, the speed reference at steady state (500 rpm) is still reached and the speed kept under control.

Finally, the case of a slowly growing fault is studied. A typical example of a gradual position sensor fault is a drift due to the inverter switching, which disturbs the position measurement as the speed increases. Figure 3.26 illustrates this case. The current controllers manage to maintain the reference tracking capability despite the fault by modifying the voltage references to compensate the position error. However, the voltages are limited by the DC bus voltage set to 150V in this case (at the reconfiguration moment in Figure 3.26d (t=50.55s), we get closer to the saturation level: $|V_s| = \sqrt{\frac{2}{3}(U_d^2 + U_q^2)}$).

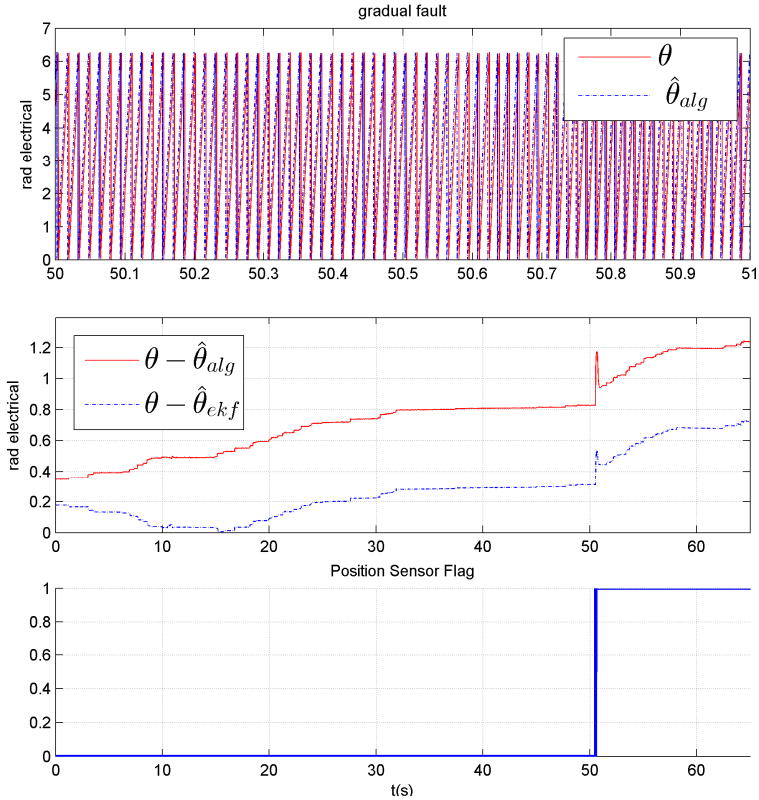

a) Position Estimation and Fault detection

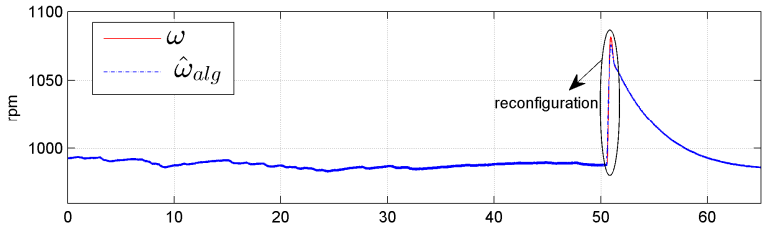

b) Speed Control under a gradual offset

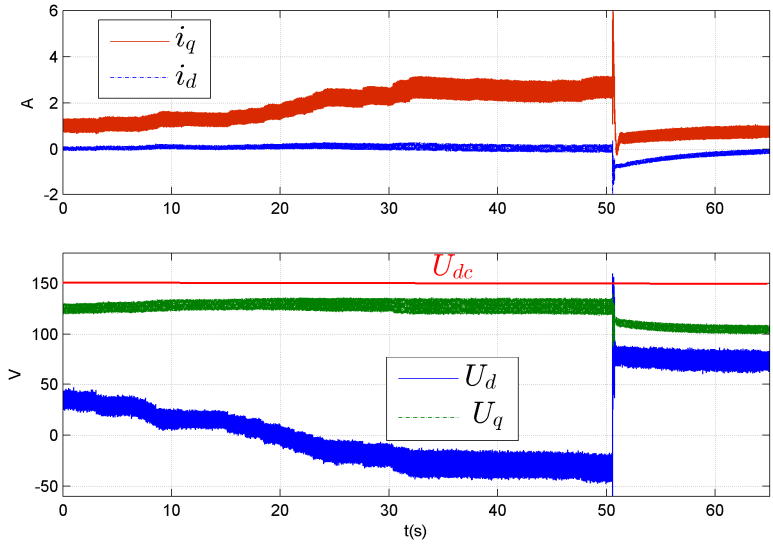

c) *dq* currents and voltages

As a consequence, the position sensor offset induces a bias in *dq* currents. After the reconfiguration, the position estimated by the algebraic estimator is used in the control instead of the measured position. We can notice that the drive remains under control. The flux and torque current components retrieve almost the values as before the beginning of the position sensor drift. Then the behavior of the control during the reconfiguration is highlighted (Figure 3.26c). For a growing fault, the detection time is strongly linked to the fault growth rate (Figure 3.26a).The measured speed (Figure 3.26b) is weakly affected because speed measurement can deal with a position offset (the derivative action cancels the offset).

The fault could be detected earlier considering the large distance between $\theta - \widehat{\theta}_{alg}$ and $\theta - \widehat{\theta}_{ekf}$ (in Figure 3.26a starting from t=10s, the distance exceeds 5 rad).

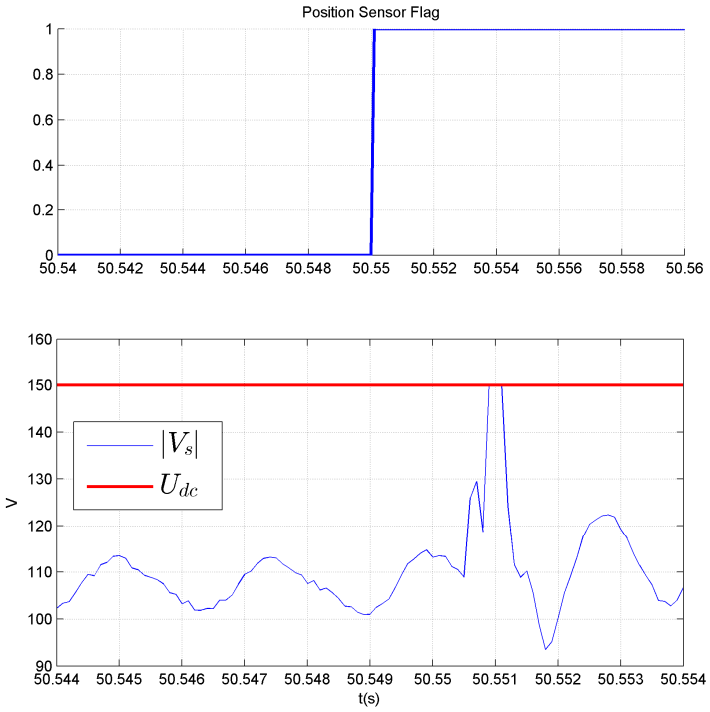

d) Zoom at the reconfiguration time

Figure 3.26 Fault Tolerant Control under a gradual offset

To use effectively the distance between $\hat{\theta}_{alg}$ and $\hat{\theta}_{ekf}$, the two following variables are defined:

$$\varepsilon_1 = \left\| \theta - \hat{\theta}_{alg} \right| - \left| \theta - \hat{\theta}_{ekf} \right\| \ , \ \varepsilon_2 = \left| \hat{\theta}_{alg} - \hat{\theta}_{ekf} \right|$$

The relation between ε_1 and ε_2 is the well-known triangle inequality theorem:

$$\left\| \theta - \hat{\theta}_{alg} \right| - \left| \theta - \hat{\theta}_{ekf} \right\| \le \left| \hat{\theta}_{ekf} - \hat{\theta}_{alg} \right| \Leftrightarrow \varepsilon_1 \le \varepsilon_2 \qquad (3.23)$$

Then, by adding this condition to the detection, a new voting algorithm is defined (Figure 3.27).

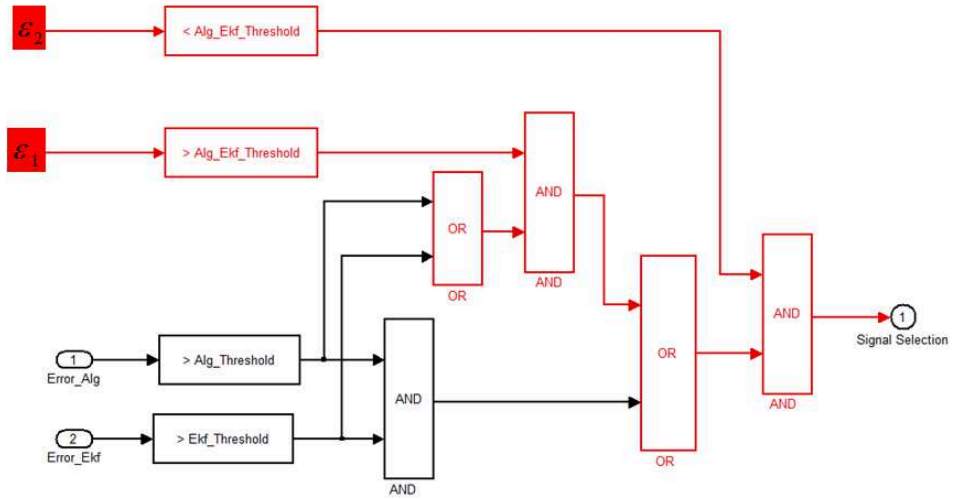

Figure 3.27 New voting algorithm

Figure 3.28 illustrates the behavior of ε_1 and ε_2 under a position sensor fault with a drift due to the inverter switching. The first remark is that ε_2 is uncorrelated from the measured position θ. In healthy mode, ε_1 is far away from ε_2 and at the fault occurrence (starting from 1400 rpm, the position measurement process is no more able to handle inverter imperfection), ε_1 gets closer to ε_2.

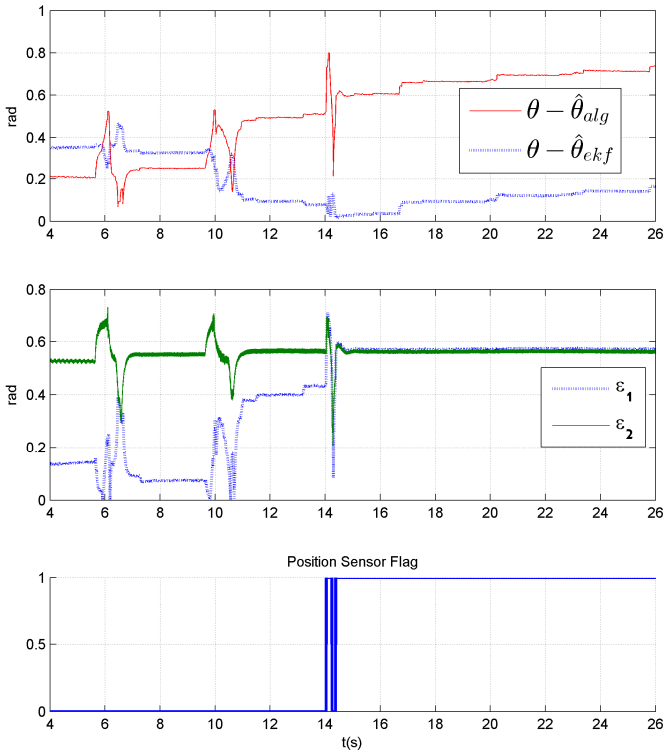

a) Position Estimation error and Flag

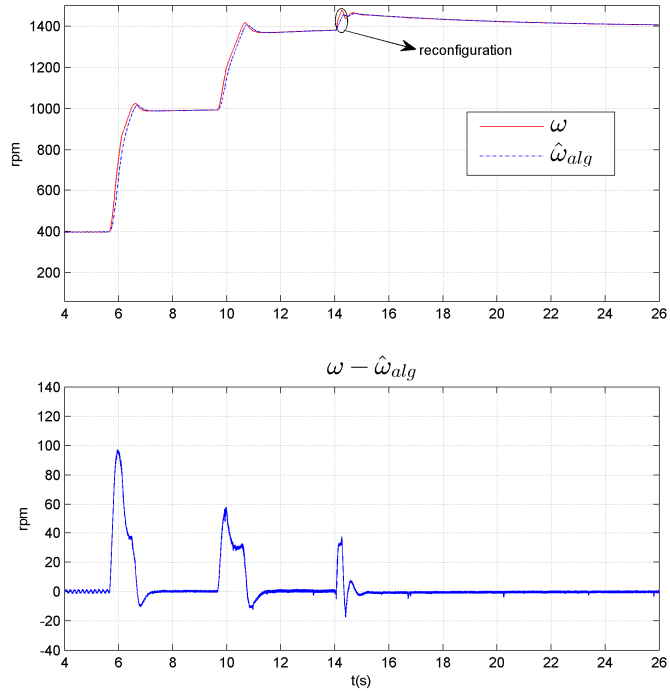

b) Speed Estimation

Figure 3.28 Fault Tolerant Control under a gradual offset with improved FDI

In Figure 3.28a, because the estimations are good, ε_2 remains constant. However, due to the position sensor error, ε_1 varies significantly from t=11s.

Using the new voting algorithm where this time the bias is manually inserted, in load condition, the results displayed in Figure 3.29a are obtained.

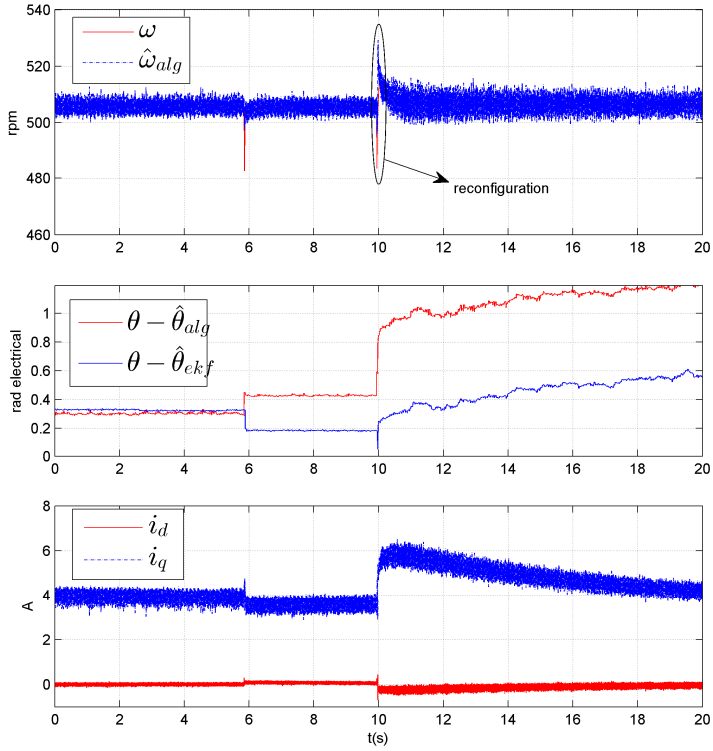

a) Speed and Position Estimation errors

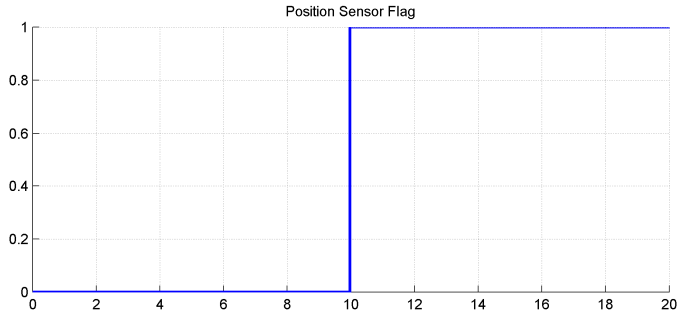

b) Position sensor flag

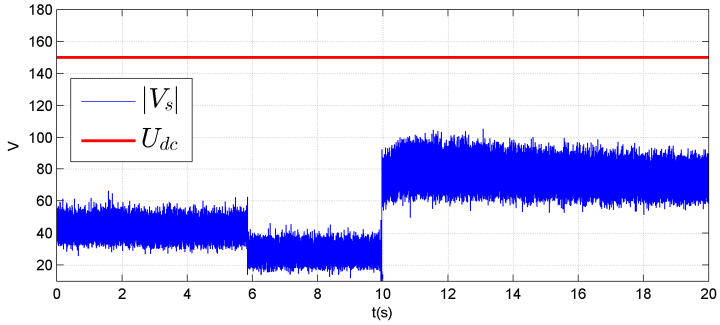

c) Reference voltage

Figure 3.29 Fault Tolerant Control under additive random position sensor offsets

At t=5.8s, a first small offset is inserted but its magnitude is not high enough to be detected. The offset is increased at t=10s. The accumulation of the two bias leads to the detection with the flag displayed in Figure 3.29b. Moreover, the variation of the reference voltages is acceptable. The modulus of control voltages is below the DC bus voltage as displayed in Figure 3.29c.

A 10% position sensor gain error is inserted at t=1.3832s and the results are shown in Figure 3.30. The fault is detected after 0.0378s (Figure 3.30a). In addition, for a gain sensor error, the magnitude of the estimation error is very useful to enable the detection.

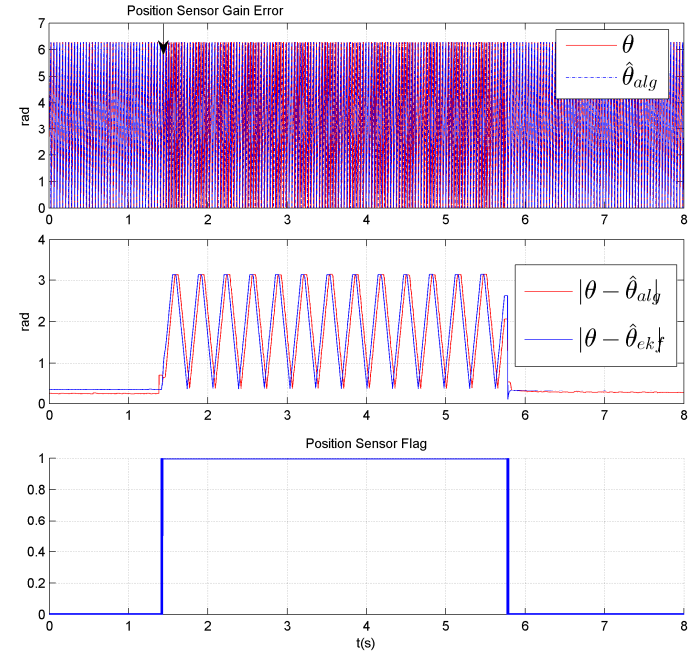

a) Position Estimation error and Flag

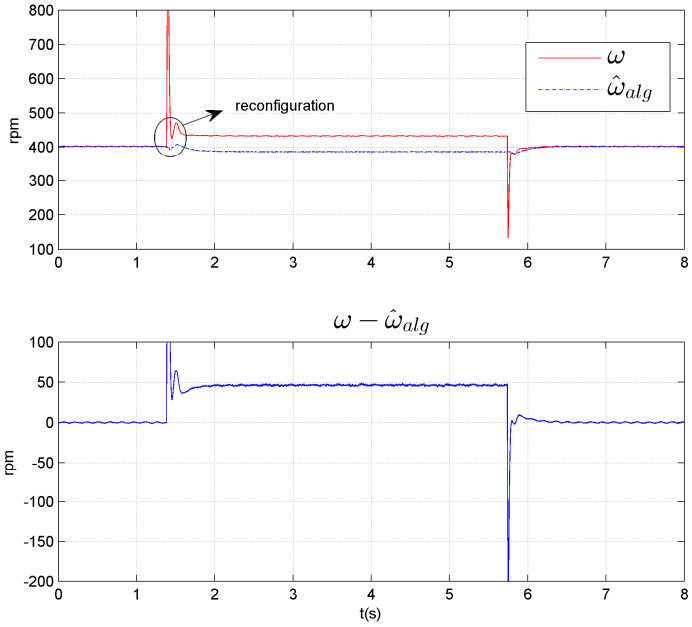

b) Speed Estimation

Figure 3.30 Fault Tolerant Control under Gain Position sensor error

The reference speed is 400 rpm and thanks to the reconfiguration, the speed is maintained close to its reference with an error of 12 rpm (3% in steady state) as highlighted in Figure 3.30b.

Now, in order to justify the use of two estimators instead of one for the detection, the case where the operating conditions may lead to wrong estimations is under study. Logically, the estimation errors could get out of bounds but the fault should not be detected because the position sensor is healthy. This type of error is the root cause of the false alarms when using observers in FDI. This case is emulated by inserting a bias of 2.5 A in the A-phase current sensor (that is a 65% error in Figure 3.31a) at t=3.22s. Using the closeness between the EKF and the algebraic estimator, the detection has been avoided (flag remains null in Figure 3.31b). Obviously, if the FDI relied only on one estimator, this situation would not be handled.

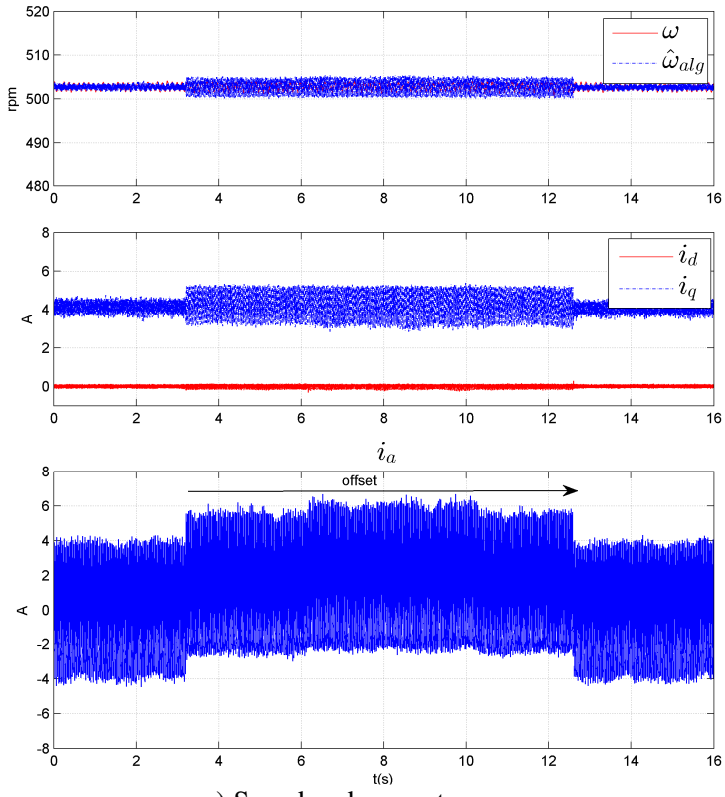

a) Speed and currents

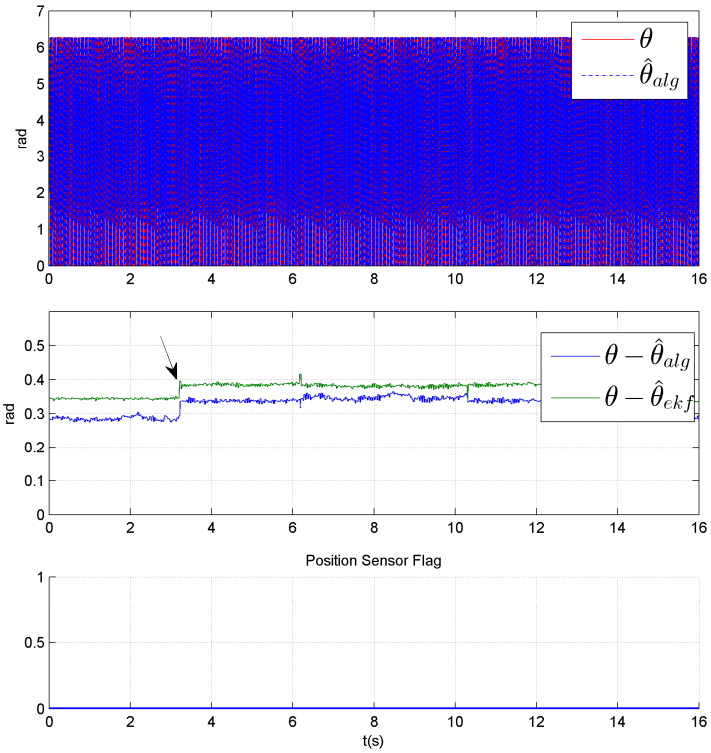

b) Position Estimation and Flag

Figure 3.31 Fault Tolerant Control under harsh current sensor fault

What about a gradual offset in load condition? This case can be troublesome when the reference voltages are close to the saturation level. In the last example (Figure 3.26), we observe that the reconfiguration generates an over-voltage and in high load condition, this can induce a loss of control if the switching between the sensor and the estimator is not properly managed.

3.5 Conclusion

This chapter has presented a position sensor FTC for a PMSM drive. A virtual sensor based on a differential algebraic approach has been developed to estimating the position and the speed. The main advantages are its simplicity (a one-dimension model) and that the position observability is not speed dependant. In addition, the observability at low speed is obtained provided that the currents and the voltages are available. Moreover, an analytical study of the robustness with respect to the parameters has been done and experimental results have confirmed the robustness to parameter variation. The behavior of the estimator in presence of load torque variation is also good. Finally, this estimator has been compared to the other methods (EKF, Back-EMF).

Experimental results have shown the effectiveness of the technique and its combination with the EKF for FTC has provided good results. The efficiency of the FTC scheme has been evaluated and the requirement of two estimators for the diagnosis illustrated.

The main contributions can be summarized as follows:

- Development of a simple method for position and speed estimation that can be accurate on the whole speed range and especially at very low speed.
- For implementation issues, the method is also cost effective in terms of execution time and robust to parameter variations and current measurement errors.
- Position Sensor Fault Tolerant Control performed involving the algebraic estimator and the EKF.

In the next chapter, the diagnosis of the three phase currents sensors and the DC link voltage sensor will be studied.

REFERENCES

[Aug2013] **Industrial Applications of the Kalman Filter: A Review,** Auger F., Guerrero J., Hilairet M, Monmasson E., Orlowska-Kowalska T. and Katsura S.; *IEEE Trans. on Industrial Electronics*, vol. 60, n°. 12, pp. 5458-5471, December 2013

[Akr2011] **Design of a Fault-Tolerant Controller Based on Observers for a PMSM drive**, Akrad A., Diallo D., Hilairet M., *IEEE Transactions on Industrial Electronics,* vol.58, n°4, pp. 1416-1427, April 2011

[Ari2008] **Angle estimation for Sensorless Field Oriented Control with Matrix Converters and Surface Mount Permanent Magnet Synchronous Machines**, Arias, A.; Ortega, C.; Pou, J.; Gonzalez, D.; Balcells, J., *Power Electronics Specialists Conference,* pp.3659-3664, 15-19 June 2008

[Ben2007] **Advanced Fault-Tolerant Control of Induction-Motor Drives for EV/HEV Traction Applications: From Conventional to Modern and Intelligent Control Techniques**, Benbouzid M.E.H., Diallo, D., Zeraoulia, M.; *IEEE Transactions on Vehicular Technology,* vol.56, n°2, pp.519-528, March 2007

[Hol1996] **Methods for speed sensorless control of AC drives**, Holtz J., *Sensorless Control of AC Motor Drives, Piscataway, NJ, IEEE Press,* 1996

[Bar2013] **Resolver vs Encoder**, D. Barnett; *Tutorials,* 2013

[Bat2005] **Electric Propulsion With Sensorless Permanent Magnet Synchronous Motor: Implementation and Performance**, Batzel, T.D. and Lee, K.Y.; *IEEE Transactions on Energy Conversion,* vol.20, n°3, pp. 575-583, Sept. 2005

[Bol2011] **Sensorless Control of IPM Motors in the Low-Speed Range and at Standstill by HF Injection and DFT Processing**, Bolognani, S.; Calligaro, S.; Petrella, R.; Tursini, M., *IEEE Transactions on Industry Applications,* vol.47, n°1, pp.96-104, Jan.-Feb. 2011

[Bou2005] **Implementation and experimental investigation of sensorless speed control with initial rotor position estimation for interior permanent magnet synchronous motor drive**, Boussak, M.; *IEEE Transactions on Power Electronics,* vol. 20, n°6, pp. 1413-1422, Nov. 2005

[Chen2003] **An extended electromotive force model for sensorless control of interior permanent magnet synchronous motors**, Z. Chen, M. Tomita, S. Doki, and S. Okuma, *IEEE Transactions on Industrial Electronics*, vol. 50, no. 2, pp. 288–295, Apr. 2003.

[Diao2014] **A Differential Algebraic Estimator for Sensorless Permanent-Magnet Synchronous Machine Drive**, Diao, S.; Diallo, D.; Makni, Z.; Marchand, C.; Bisson, J.-F., *IEEE Transactions on Energy Conversion,* to be published in 2014

[Diop2001a] **The algebraic theory of nonlinear observability revisited**, S. Diop, *Proceedings of the 40th IEEE Conference on Decision and Control,* vol.3, pp. 2550-2555, 2001

[Ezz2011] **Sensorless nonlinear control of a permanent magnet synchronous motor**, Ezzat M., *Phd thesis, Institut de Recherche en Communications et en Cybernétique de Nantes,* Sept. 2011

[Fli1991] **On Nonlinear observability** , M. Fliess, S. Diop, *Proceedings of the European Control Conference*, Hermès, Paris, pp. 152-157, 1991

[Gong2013] **Robust Initial Rotor Position Estimation of Permanent-Magnet Brushless AC Machines With Carrier-Signal-Injection-Based Sensorless Control**, Gong, L.M.; Zhu, Z.Q., *IEEE Transactions on Industry Applications,* vol. 49, n°6, pp. 2602-2609, Nov. 2013

[Han2009] **On the "Uniform" Observability of Discrete-Time Nonlinear Systems** , S. Hanba, *IEEE Transactions on Automatic Control,* vol. 54, n°8, pp. 1925-1928, Aug. 2009

[Hen2011] **PMSM Identification for Automotive Applications: Cancellation of Position Sensor Errors**, N. Henwood; J. Malaize; L. Praly, *37th Annual Conference on IEEE Industrial Electronics Society IECON,* pp.687,692, 2011

[Hol2006] **Sensorless Control of Induction Machines; With or Without Signal Injection?,** J. Holtz, *IEEE Transactions on Industrial Electronics,,* vol. 53, pp. 7-30, 2006.

[Ise2006] **Fault tolerant sensors for vehicle dynamics control**, Unger, I; Isermann, Rolf, American Control Conference, June 2006

[Jan1995] **Transducerless position and velocity estimation in induction and salient AC machines**, P. L. Jansen and R. D. Lorenz, *IEEE Trans. Industrial Applications*, vol.31, no.2, pp. 240-247, Mar./Apr.1995.

[Jan2013] **Load torque estimation for sensorless PMSM drive with output filter fed by PWM converter**, D. Janiszewski, *39th Annual Conference of the IEEE Industrial Electronics Society* IECON, pp. 2953 - 2959, 2013

[Lep2003] **Motor control sensor feedback circuits**, J. Lepkowski, Microchip technology Incorporations , AN894 - 2003

[Lar2008] **Methodological insights for online estimation of induction motor parameters**, E. Laroche, E. Sedda, and C. Durieu, *IEEE Trans. Control Syst. Technol.*, vol. 16, no. 5, pp. 1021–1028, Sep. 2008.

[Liu2003] **Position Sensor Error Analysis for EPS Motor Drive**, G. Liu, A. Kurnia, R. De Larminat and S. J. Rotter, *International Electric Machines & Drives Conference (IEMDC), IEEE,* pp. 249 – 254, 2003

[Man2013] **Improved rotor position estimation of salient-pole PMSM using high frequency carrier signal injection**, O. Mansouri-Toudert, H. Zeroug, F. Auger, A. Chibah, *IEEE International Conference on Mechatronics* (ICM), Vicenza, pp.761 – 767, Feb. 27-Mar.1, 2013.

[Men2006] **A differential-algebraic approach to speed estimation in an induction motor** , Mengwei Li, J. Chiasson , M. Bodson, M. Tolbert , *IEEE Transactions on automatic control,* vol. 51, n°7, pp. 1172-1177, 2006

[Menh2011]**Algebraic nonlinear estimation and flatness-based lateral/longitudinal control for automotive vehicles**, L.Menhour, B. d'Andrea-Novel, C. Boussard, M. Fliess, *IEEE 14th International Conference on Intelligent Transportation Systems (ITSC)***,** pp.463,468, 5-7 Oct. 2011

[Nah2007] **Back EMF Estimation-Based Sensorless Control of PMSM: Robustness With Respect to Measurement Errors and Inverter Irregularities**, Nahid-Mobarakeh, B.; Meibody-Tabar, F.; Sargos, Francois-Michel, *IEEE Transactions on Industry Applications,* vol.43, n°2, pp.485-494, March-April 2007

[Raf2008] **Simultaneous observer based sensor diagnosis and speed estimation of Unmanned Aerial Vehicle**, Rafaralahy, H.; Richard, E.; Boutayeb, M.; Zasadzinski, M., *Conference on Decision and Control,* pp.2938,2943, 9-11 Dec. 2008

[Sar2012] **Sensorless Control of PM Synchronous Machines by Physics-Based EMF Observer**, Sarikhani A., Mohammed, O.A.;, *IEEE Transactions on Energy Conversion,* vol. 27, n°4, pp. 1009-1017, Dec. 2012

[Sil2006] **Hybrid Rotor Position Observer for Wide Speed-Range Sensorless PM Motor Drives Including Zero Speed**, C. Silva, G. M. Asher, M. Sumner, *IEEE Transactions on Industrial Electronics,* vol. 53, pp. 373-378, 2006

[Sir1992] **The differential algebraic approach in nonlinear dynamical feedback controlled landing maneuvers,** Sira-Ramirez, H., *IEEE Transactions on Automatic Control,* vol.37, no.4, pp.518-524, April 1992

[Vac2013] **AC Drive Observability Analysis**, Vaclavek, P. ; Blaha, P. ; Herman, I., *IEEE Transactions on Industrial Electronics,* vol.60, no.8, pp.3047,3059, 2013

[Ven2003] **A review of process fault detection and diagnosis**, V. Venkatasubramanian, R. Rengaswamy, N. Kavuri, K.Yin, *Computer and Chemical Engineering* 27, 327-346, 2003

[Wang2005] **Differential algebraic observer based nonlinear control of permanent magnet synchronous motor**, Wang, J.; T. Li; K. M. Tsang, et al., *Proceedings of the CSEE,* vol. 2, n° 25, pp. 87-92, 2005

[Wan2011] **Analysis of influence on back-EMF based sensorless control of PMSM due to parameter variations and measurement errors**, Wang Z., Lu K., Ye Y., Jin Y., Hong W., *International Conference on Electrical Machines and Systems (ICEMS),* pp.1-6, 20-23 Aug. 2011

[Zhu2011] **Investigation of Effectiveness of Sensorless Operation in Carrier-Signal-Injection-Based Sensorless-Control Methods,** Zhu, Z.Q.; Gong, L.M;, *IEEE Transactions on Industrial Electronics,* vol. 58, n°8, pp. 3431-3439, Aug. 2011

[Zal2010] **Synchronous Motor Observability Study and an Improved Zero-speed Position Estimation Design**, Zaltni D. ; Ghanes M., Barbot J-P., Naceur A., *IEEE Conference on Decision and Control,* Atlanta, 2010

Chapter IV: Diagnosis of Phase currents and DC-Link voltage sensors

4.1 Needs on phase currents sensors and DC link voltage sensor diagnosis

4.1.1 Current Sensor fault origins and consequences

Current sensors are generally used for the control, the supervision, and or the monitoring of electrical drives. For the control, they are used to measure the currents flowing from the power converter in the electrical machine windings. When used for supervision due to safety request (for e.g. in the starter-alternator system StARS of Valeo), they are placed in series with the power electronic system's protection.

Obviously in both cases, faults or failure of the sensor are not acceptable and the most common approach is to implement hardware redundancy and the associated signal management. However the new trend is to reduce the number of components and implement virtual sensors in the already embedded digital control circuit. Benefits are the reduction of the overall cost in the long term, the decrease of the fault rate and a more flexible design. However the safety requirements are still to be fulfilled with the continuity of operation and the level of performances.

The common current sensing solutions are: Hall-effect sensors, Current transformer, Current shunt and Rogowski coil. Hall-effect sensors are widely used for the control of electrical drives used in automotive systems [Por2007].

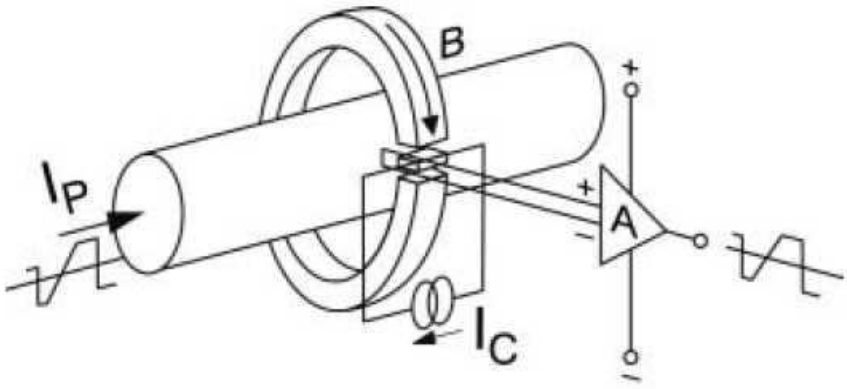

Figure 4.1 Open-loop Hall-Effect [Por2007]

In the Hall-effect current sensor, the output is a voltage proportional to the sensed current (Figure 4.1). Since the control is digital, an associated electronic ensures the Analog to Digital Conversion (ADC). During the acquisition, the output of the Hall device is then signal

conditioned to provide an exact representation of the primary current at the output. This ensures the filtering of the signal while adjusting the gain measurement. The performances of the current sensing can be affected by the interferences caused by the environment, the Joule losses and the signal cable length.

In SOFRACI project, three Hall-effect sensors are used (one per phase). This is due to the fact that the phases are physically and magnetically decoupled. Therefore the usual balance equation used to deduce the third phase current from two measurements does not hold any longer as a zero sequence current can take place. The 3 Hall Effect LEM transducers used (LEM LA 55-P) can measure AC currents up to 50 A with a bandwidth of 200 kHz , an accuracy of ±0.65% and an ambient temperature ranging from -40° to 85°C.

The different types of measurement errors for a Hall-Effect transducer that may come from the properties of the materials or from the temperature variation are an electric offset, a magnetic offset, sensitivity or a gain error and a linearity error.

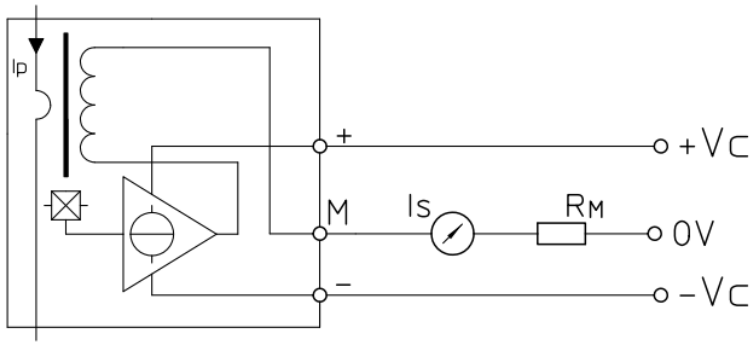

Figure 4.2 Connection of LEM Current Transducer

In Figure 4.2, a failure of the supply voltage V_c or disconnection due to excessive vibrations can lead to a complete outage of the current sensor. Also, in automotive systems, the current sensors are nested in an Electronic Control Unit (ECU) located in an environment which ambient temperature can range from 10° to 80°C and can even raises in critical mode up to 110°. So, in this harsh environment, one of the consequences could be the occurrence of significant offsets in the current measurement. In addition, during the conversion performed by the analog to digital converter (ADC), gain errors could also arise.

So in the following, these two types of current sensor fault (a gain error and an offset (abrupt of gradual)) will be under consideration for fault detection and isolation purposes. The total loss of information (sensor complete outage) due for example to a power failure in the acquisition chain will also be considered.

In real time operation, the faults will be emulated by modifying the sensor actual output through the digital interface.

4.1.2 DC Voltage measurement

In electrical drives control, the DC link voltage is measured across the electrolytic capacitor, which acts as an energy storage device. It's the electrical connection between the primary energy source (battery e.g.) and the DC/AC power converter. As a consequence the measured voltage is key information for the computation of the PWM duty cycles and the saturation level of the control voltages. Different methods are used to perform a DC voltage sensing.

A Varistor V661BA60 is used for the DC voltage measurement. Varistors are designed to provide surge protection for motor controls and power supplies and their voltage sensing property is derived from the highly nonlinear current voltage characteristics [Lit]. Unpredictable disconnection and faults in the digital electronic acquisition chain can also affect the measure of the DC-link voltage.

4.1.3 Existing methods based on state observers and signal processing techniques

At the occurrence of a current sensor fault, we are looking for a deviation of the faulty phase current [Abd2010] and the main task is to spot quickly this variation so as to ensure an efficient diagnosis. The severity of the distortion from normal waveform depends mainly on the type of fault. For embedded applications, one of the main concerns is to find a FDI that:

- is easy to tune and that can be nested easily in an existing control,
- uses already available measurements,
- has a low algorithmic cost.

Among the fault detection and diagnosis problem formulation methods, physical-based models and history-based models are the most suitable. As shown in Figure 4.3, different tools are available. There have been in the literature many works in the field of current sensor fault detection and isolation (FDI) in electrical drives [Ben2007, Jeo2005,Wel2004].

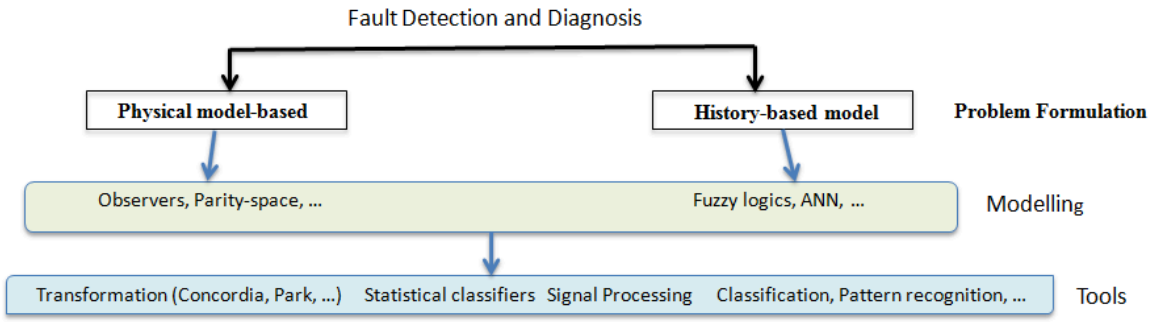

Figure 4.3 Simplified scheme of the FDD approaches

Generally, as physical models are available, model-based methods are the most suitable. Among the methods relying on mathematical models, those based on state observer and space parity have been successfully applied in electrical drives [Ise2011, DeP2001, Chen1999]. This approach is used in ([Rot2009, Lee2011, Diao2013]) to diagnose a phase current sensor fault. The method is based on the computation of residuals as the difference between the actual process behavior and the reference one described by its mathematical-based model. The decision whether there is a fault or no is made based on the analysis of the residuals. However, the main drawback of model-based methods is their sensitivity to the model accuracy, the parameter variations and the uncertainties that may lead to false alarms or misdetections.

An alternative is the use of a single current sensor in the DC to estimate the phase currents [Jia2010] but its applicability is made difficult as it requires the phase voltages measurements, which is uncommon and not cost effective.

With the development of the computational capability of embedded electronic circuits, signal processing techniques have spread into the fault diagnosis community. They rely on a nonparametric approach and therefore are independent of the electrical machine parameters as well as providing very quick fault detection. However, when used in a closed loop system (i.e. a control loop based on phase current measurements), the isolation step could be tricky because the fault has spread in the other phases owing the Clarke/Park Transformation of the closed loop. They have shown their effectiveness in the diagnosis of electrical machines (short circuit, bearings, broken rotor bars, …) even if there are still some issues on the time windowing, the computational burden, the stationarity and the ageing effects. They have also

been used to diagnose current sensors used for the monitoring and the supervision of power electronics devices ([Gal2010, Fre2014]).

As for the DC link voltage sensor diagnosis, an observer can be an efficient back-up solution in case of failure to ensure the continuity of the operation with acceptable performance ([Ohn2004]). One can also estimate the equivalent series resistance (ESR) of the dc-link electrolytic capacitor like in [Xin2013] to monitor the capacitor voltage. Voltage sensorless control method has also been applied in [Yip2003] where a single current sensor is used to measure the inductor current and then give the inductor voltage. Detecting the fault with a power balance equation has also been tested but its operating range is very limited (tests at standstill).

In the following, two alternatives to the current sensor FDI will be developed and validated experimentally. The first one is a model-based estimation of the current residuals dynamics in the stationary reference frame with a differential algebraic approach.

The second one is also model-based with an analysis of the current waveforms in the synchronous rotating reference frame in which the field-oriented control is usually built.

In the last section of the chapter, we will develop a DC link voltage estimator using the phase currents and the duty cycles. The experimental results will be presented in a DC link voltage sensor diagnosis scheme.

4.2 Phase Current Sensors Fault Detection and Isolation

4.2.1 Diagnosis with an algebraic fault estimator in the Stationary Frame

The method is based on a differential algebraic estimation of the faults dynamics in the stationary reference frame [Ibr2003]. As said above, observer-based FDI has some drawbacks. First, it requires fulfilling the observability condition for the entire state variables. Secondly, it is difficult to synthesize a robust observer with respect to disturbances, which are not considered as faults (e.g. torque variation).

Therefore this method proposes an alternative based on the estimation of the current residuals dynamics in the stationary reference frame with a differential algebraic approach. This reference frame is chosen because the current measurement takes place in the natural three-phase reference.

We assume a single sensor failure during motor operation. This is a practical assumption since the probability of two simultaneous sensor faults is very low.

4.2.1.1 Design and Simulation Results

Fault estimator

The algebraic approach of diagnosis tends to establish if a fault represented by a state variable is observable or not. To do so, the fault variable is reconstructed through the design of estimators represented by differential-algebraic equations.

The system diagnosis problem is then to detect, identify, and estimate the fault by processing the control data and the available outputs. According to [Diop2001b], a fault f_i is observable with respect to u the inputs and y the outputs if each component f_i is algebraic over the differential field extension of k generated by u and y.

Using the mathematical model of the PMSM, let us assume that the outputs of the sensors in the stationary (α,β) reference frame have an error defined by $f = (f_\alpha, f_\beta)$:

$$\begin{bmatrix} f_\alpha \\ f_\beta \end{bmatrix} = y_m - \begin{bmatrix} \cos\theta & -\sin\theta \\ \sin\theta & \cos\theta \end{bmatrix} \begin{bmatrix} x_1 \\ x_2 \end{bmatrix} \tag{4.1}$$

The lower script m stands for the measured values, x_1, x_2 for the dq currents. Deriving (4.1) yields:

$$\begin{aligned} \dot{f}_\alpha &= \dot{y}_{1m} - \dot{y}_1 = \dot{y}_{1m} - \dot{x}_1\cos\theta + \dot{x}_2\sin\theta + \omega y_2 \\ \dot{f}_\beta &= \dot{y}_{2m} - \dot{y}_2 = \dot{y}_{2m} - \dot{x}_2\cos\theta - \dot{x}_1\sin\theta - \omega y_1 \end{aligned} \tag{4.2}$$

Now the dynamics of the currents $\dot{x}_1, \dot{x}_2$ (eq. 2.14a) are replaced by their expressions according to (4.2):

$$\begin{aligned} &L_d L_q \dot{f}_\alpha = L_d L_q \dot{y}_{1m} + L_q \omega y_2 (L_d - L_q) + R_s y_1 L_d + u_2 (L_d - L_q) \cos\theta \sin\theta \\ &- u_1 (L_d \sin^2\theta + L_q \cos^2\theta) - L_d \phi\omega \sin\theta + R_s (L_d - L_q) x_1 \cos\theta \\ &L_d L_q \dot{f}_\beta = L_d L_q \dot{y}_{2m} + L_q \omega y_1 (L_q - L_d) + R_s y_2 L_d + u_1 (L_d - L_q) \cos\theta \sin\theta \\ &- u_2 (L_q \sin^2\theta + L_d \cos^2\theta) + L_d \phi\omega \cos\theta + R_s (L_q - L_d) x_1 \sin\theta \end{aligned} \tag{4.3}$$

Then replacing $[y_1, y_2]$ by $[y_{1m} - f_\alpha, y_{2m} - f_\beta]$ gives

$$\begin{aligned} \dot{f}_\alpha &= -\frac{R_s}{L_q} f_\alpha + \frac{R_s}{L_q} y_{1m} + \omega \frac{(L_d - L_q)}{L_d} (y_{2m} - f_\beta) - \frac{\phi\omega \sin\theta}{L_q} + u_2 \frac{(L_d - L_q)}{L_d L_q} \cos\theta \sin\theta - \frac{u_1}{L_d L_q} (L_d \sin^2\theta + L_q \cos^2\theta) + \dot{y}_{1m} \\ \dot{f}_\beta &= -\frac{R_s}{L_q} f_\beta + \frac{R_s}{L_q} y_{2m} + \omega \frac{(L_q - L_d)}{L_d} (y_{1m} - f_\alpha) + \frac{\phi\omega \cos\theta}{L_q} + u_1 \frac{(L_d - L_q)}{L_d L_q} \cos\theta \sin\theta - \frac{u_2}{L_d L_q} (L_q \sin^2\theta + L_d \cos^2\theta) + \dot{y}_{2m} \end{aligned} \tag{4.4}$$

The implementation for a salient PMSM is complicated because cross terms need to be inserted.

In the case of $L_d = L_q$, the fault estimator is:

$$\begin{cases} \dot{f}_\alpha = -\dfrac{R_s}{L} f_\alpha + \dfrac{R_s}{L} y_{1m} - \dfrac{\phi\omega \sin\theta}{L} - \dfrac{u_1}{L} + \dot{y}_{1m} \\ \dot{f}_\beta = -\dfrac{R_s}{L} f_\beta + \dfrac{R_s}{L} y_{2m} + \dfrac{\phi\omega \cos\theta}{L} - \dfrac{u_2}{L} + \dot{y}_{2m} \end{cases} \tag{4.5}$$

Figure 4.4 represents a schematic diagram of the fault estimator.

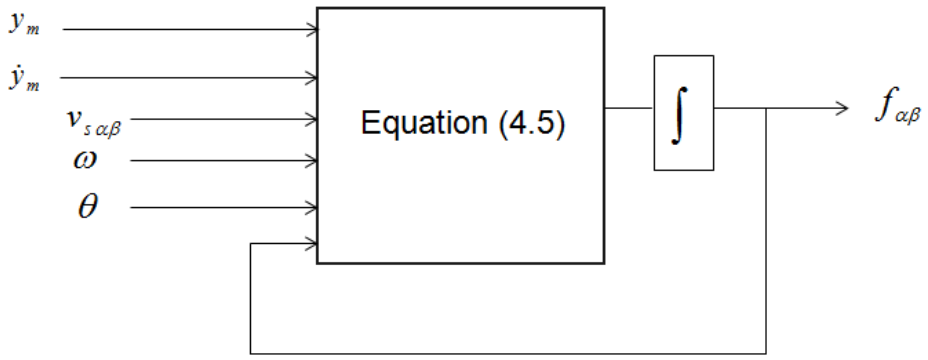

Figure 4.4 Algebraic Fault Estimator implementation

Fault modeling

The current sensor with the fault is modeled as: $i_m = G_i i_r + \Delta i$ where G_i is the sensor gain, which is equal to one in the healthy mode and Δi is the offset value that is null in healthy mode. i_m is the measured current and i_r is the actual current flowing in the machine windings. The virtual healthy currents in the fixed frame are represented by $i_{h,\alpha\beta}$ and $i_m^{'}$ stand for the measured currents in this frame. The residuals are given by: $r_{0,\alpha\beta} = i_m^{'} - i_{h,\alpha\beta}$ (see Table 4.1).

The main features are the residuals in the (α,β) reference frame. We first notice that a fault in the phase A sensor only affects the α-component. We can also notice that the vectors of residuals have opposite signs if the fault occurs in the phase B sensor or the phase C sensor.

Based on these remarks, the fault detection and isolation can be summarized as follows:

- $|f_\alpha| > thr$ and $|f_\beta| < thr$ => phase A sensor is faulty
- $f_\alpha > thr$ and $f_\beta > thr$ *and* $f_\beta * f_\alpha < 0$ => phase B sensor is faulty
- $f_\alpha > thr$ and $f_\beta > thr$ *and* $f_\beta * f_\alpha > 0$ => phase C sensor is faulty

Where *thr* is the threshold.

TABLE 4.1: CURRENT SENSOR RESIDUALS IN STATIONARY FRAME

Offset in phase A	Offset in phase B	Offset in phase C
$\begin{bmatrix} r_0 \\ r_\alpha \\ r_\beta \end{bmatrix} = \sqrt{\frac{2}{3}} \begin{bmatrix} \Delta i_a \\ \Delta i_a \\ 0 \end{bmatrix}$	$\begin{bmatrix} r_0 \\ r_\alpha \\ r_\beta \end{bmatrix} = \sqrt{\frac{2}{3}} \begin{bmatrix} \Delta i_b \\ \frac{-\Delta i_b}{2} \\ \frac{\sqrt{3}\Delta i_b}{2} \end{bmatrix}$	$\begin{bmatrix} r_0 \\ r_\alpha \\ r_\beta \end{bmatrix} = \sqrt{\frac{2}{3}} \begin{bmatrix} \Delta i_c \\ \frac{-\Delta i_c}{2} \\ -\frac{\sqrt{3}\Delta i_c}{2} \end{bmatrix}$
Gain error in phase A	Gain error in phase B	Gain error in phase C
$\begin{bmatrix} r_0 \\ r_\alpha \\ r_\beta \end{bmatrix} = \sqrt{\frac{2}{3}} \begin{bmatrix} (G_a - 1) i_a \\ (G_a - 1) i_a \\ 0 \end{bmatrix}$	$\begin{bmatrix} r_0 \\ r_\alpha \\ r_\beta \end{bmatrix} = \sqrt{\frac{2}{3}} \begin{bmatrix} (G_b - 1) i_b \\ \frac{-(G_b - 1) i_b}{2} \\ \frac{\sqrt{3}(G_b - 1) i_b}{2} \end{bmatrix}$	$\begin{bmatrix} r_0 \\ r_\alpha \\ r_\beta \end{bmatrix} = \sqrt{\frac{2}{3}} \begin{bmatrix} (G_c - 1) i_c \\ \frac{-(G_c - 1) i_c}{2} \\ \frac{-\sqrt{3}(G_c - 1) i_c}{2} \end{bmatrix}$

One of the issues is to estimate accurately the actual residuals (r_α and r_β) with the algebraic estimator variables (f_α and f_β).

Offset fault

In the following figures, simulation results are presented with an offset fault type Δi=-1A inserted in phase B (Figure 4.5), in phase C (Figure 4.6) and in phase A (Figure 4.7) respectively for different operating points. The fault on the B-phase sensor fault stands for a no load condition (very low current magnitude) with a value of the phase current at 1.6A in steady state. At fault appearance, one can see for a B-phase sensor fault that the estimator's outputs converge to $f_\alpha = 0.4$ and $f_\beta = -0.72$.

For a C-phase sensor fault and in load condition (20% of the nominal current), in steady state, f_α = 0.4 and f_β = 0.72. Lastly, for the A-phase sensor fault, we operate at 1/3 of the nominal current. We notice that only the α component of the estimator is affected with f_α = -0.9.

By setting thresholds values for f_α, f_β, the sensor fault detection can be done.

The following step is the isolation which is achieved using the sign of the fault variables and the threshold test result.

For all the three cases, the fault estimator is robust to the current transients during the start. That can be seen as an ability to distinguish a phase current fault from a torque variation.

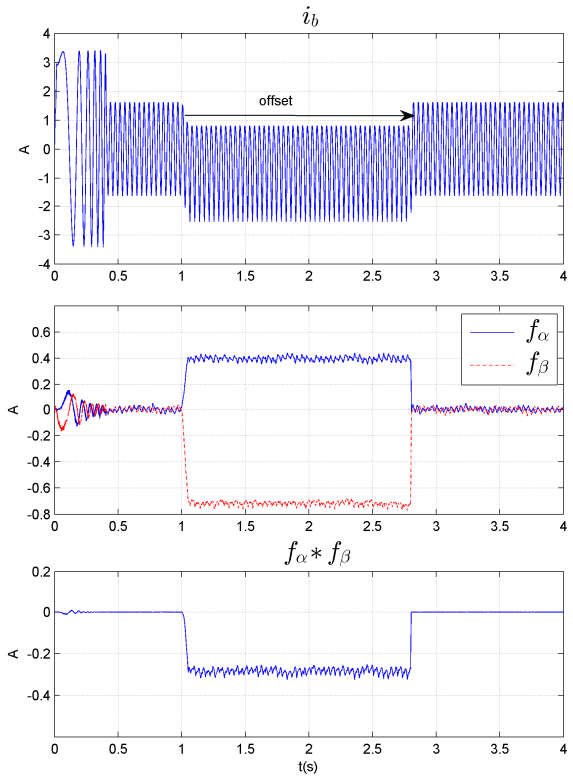

Figure 4.5 Offset Fault Simulation in phase B

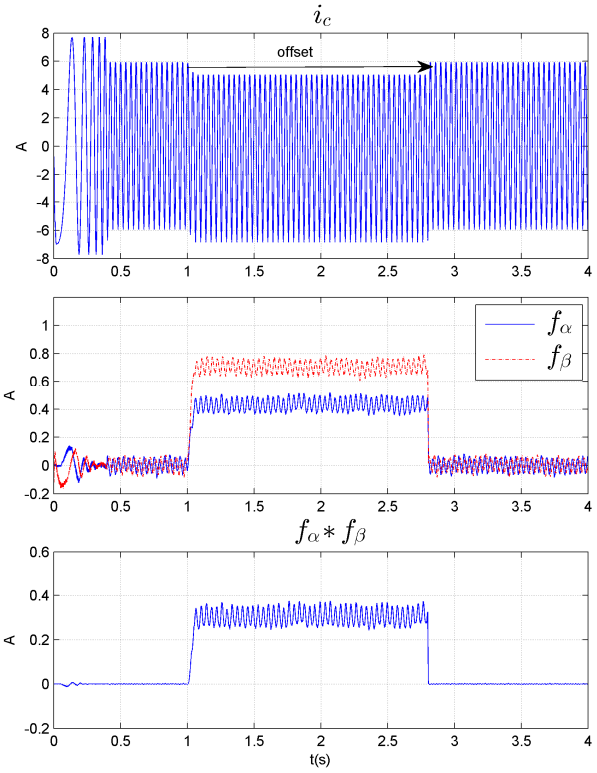

Figure 4.6 Offset Fault Simulation in phase C

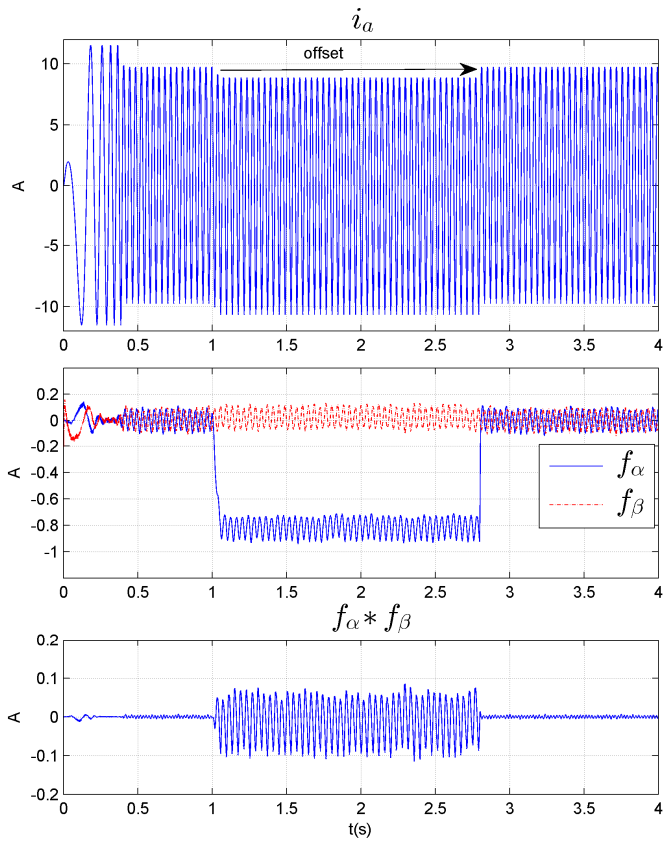

Figure 4.7 Offset Fault Simulation in phase A

To set a good threshold level, we are interested by the variation in healthy mode of $f_{\alpha\beta}$ magnitude with the mechanical speed shown in Figure 4.8.

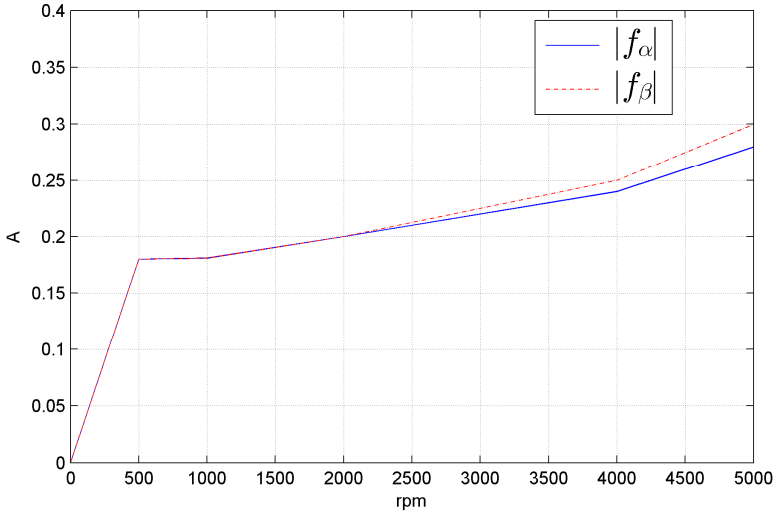

Figure 4.8 Residuals estimation in the (α,β) reference frame

The previous simulation results have shown that the fault estimator accuracy is invariant because the same offset in the current measurement for different operating points has led to the

same estimated values. The comparison to the actual residuals r_α, r_β with an offset Δ_i =-1 for each phase gives:

- for B and C phase sensor fault ;

$|r_\alpha| = 0.4082, |f_\alpha| = 0.4$ and

$|r_\beta| = 0.707, |f_\beta| = 0.72$; the estimation error is nearly 2%.

- For a A phase sensor fault ;

$|r_\alpha| = 0.816,\ |f_\alpha| = 0.85$ with an estimation error nearly 4%.

Gain fault

The case of a gain sensor fault is now studied. The expressions of the residuals are now:

$$\begin{bmatrix} f_\alpha \\ f_\beta \end{bmatrix} = y_m - \begin{bmatrix} \cos(\theta) & -\sin(\theta) \\ \sin(\theta) & \cos(\theta) \end{bmatrix} \begin{bmatrix} x_1 \\ x_2 \end{bmatrix} = (G_i - 1) \begin{bmatrix} \cos(\theta) & -\sin(\theta) \\ \sin(\theta) & \cos(\theta) \end{bmatrix} \begin{bmatrix} x_1 \\ x_2 \end{bmatrix} \quad (4.6)$$

$\begin{bmatrix} f_\alpha \\ f_\beta \end{bmatrix} = (G_i - 1) \begin{bmatrix} y_{1m} \\ y_{2m} \end{bmatrix}$ where G_i is the sensor gain.

Then (4.5) holds for the current sensor gain fault dynamic estimation. In the simulation results (Figures 4.9, 4.10 and 4.11), the gain fault (with G_i = 1.6) is introduced for 1.8s from t =1s.

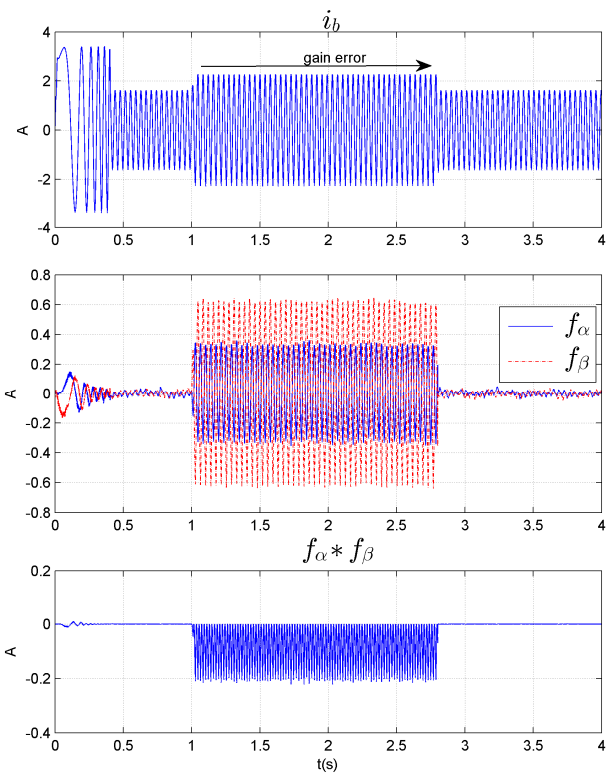

Figure 4.9 Gain Sensor Fault (phase B)

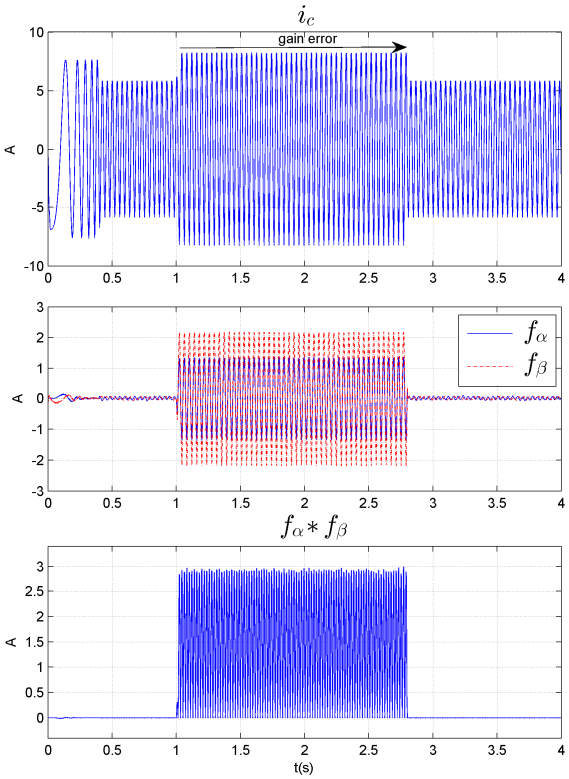

Figure 4.10 Gain Sensor Fault (phase C)

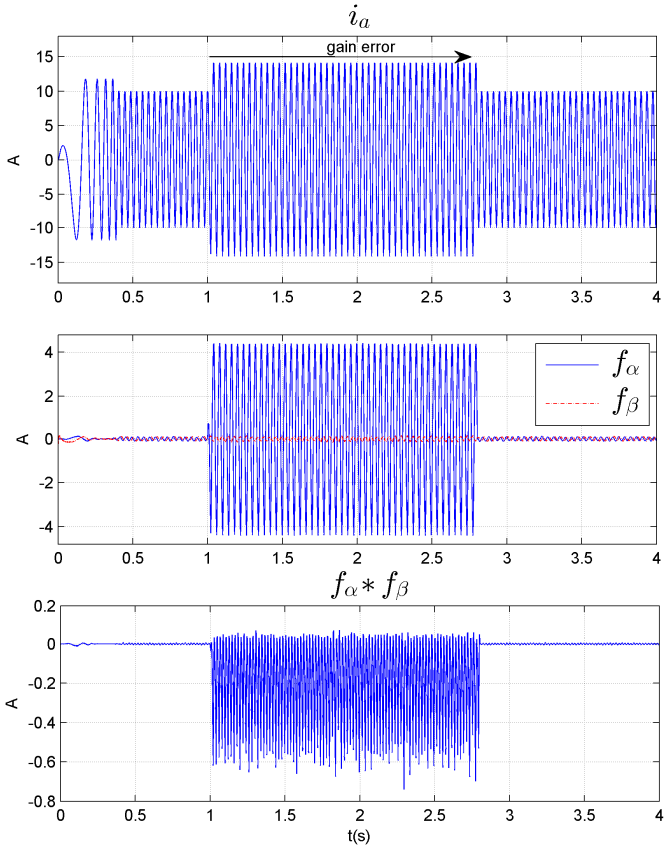

Figure 4.11 Gain Sensor Fault in phase A

According to Table 4.1 with G_i=1.6 and to the operating cases listed above, we have:

$|r_\alpha| = 4.8, r_\beta = 0$ and $|f_\alpha| = 4.4, |f_\beta| = 0.2$ for the A phase sensor fault,

$|r_\alpha| = 0.41, |r_\beta| = 0.72$ and $|f_\alpha| = 0.38, |f_\beta| = 0.62$ for the B phase sensor fault

$|r_\alpha| = 1.38, |r_\beta| = 2.37$ and $|f_\alpha| = 1.34, |f_\beta| = 2.18$ for the C phase sensor fault.

The estimated residuals are in the same ranges than the actual ones with a maximal error of 14%.

However, because the residuals f_α and f_β are sinusoidal for a gain sensor fault, one may compute their magnitude to detect the A-phase sensor fault (Figure 4.11). For the remaining phases, the sign of the product $f_\alpha * f_\beta$ is sufficient to enable the detection.

The complete FDI structure implemented in the control unit is presented in Figure 4.12. Enable_Fault_A, Enable_Fault_B and Enable_Fault_C are three logic signals which raise a flag when a sensor fault occurs in the corresponding phase.

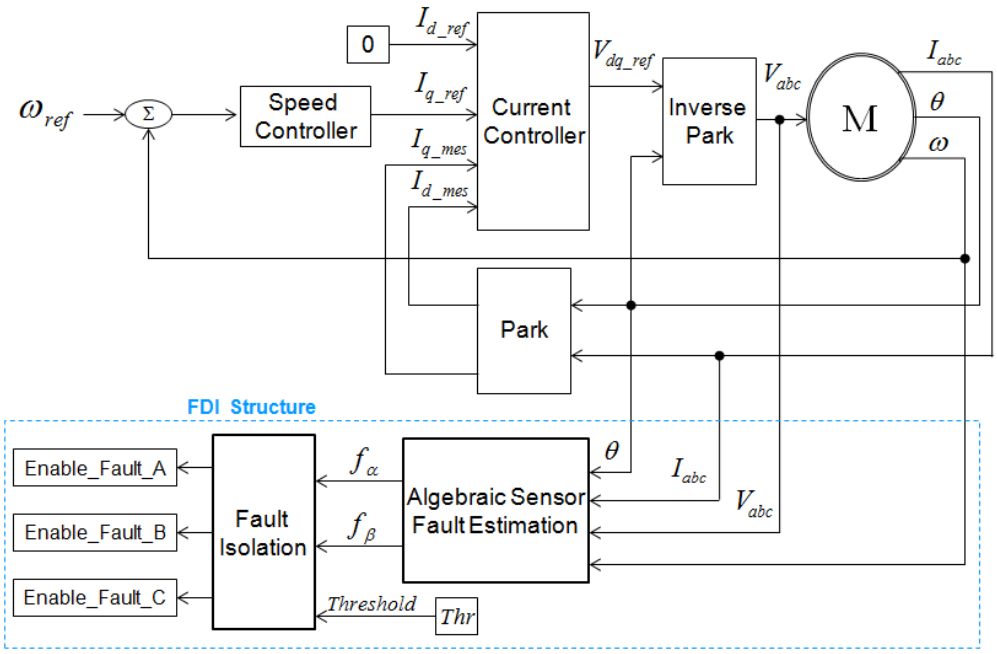

Figure 4.12 Fault Estimator based FDI Scheme

4.2.1.2 Experimental Results in FDI scheme

For these experimental tests, the faults are introduced by multiplying the output of the sensor by a constant (gain error) or by adding a constant to the output (offset).

As for the simulation an offset of -**1A** is inserted experimentally in real time operation in the C phase measured current at t=1.1826 s. This fault represents **16%** of the phase current magnitude at steady state. Figure 4.13 shows experimental results of the differential algebraic fault estimator in the fixed frame with a threshold set at **0.3**. Despite the ripples and the noises, the estimation errors are acceptable:

$$\left|r_\alpha\right| = 0.42, \left\langle f_\alpha \right\rangle = 0.4$$

$$\left|r_\beta\right| = 0.707, \left\langle f_\beta \right\rangle = 0.72$$

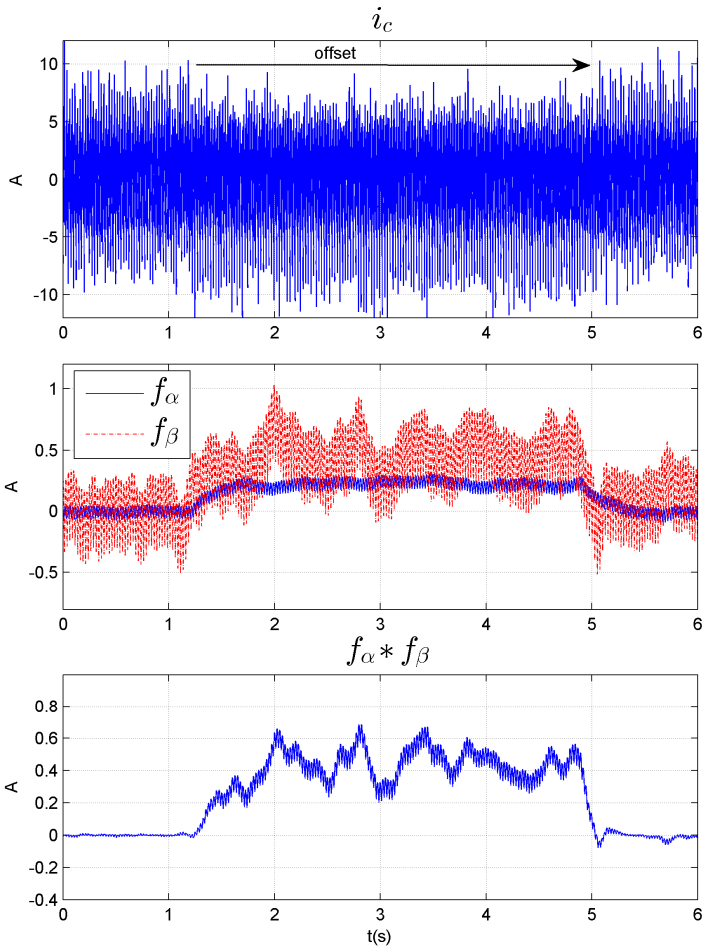

Figure 4.13 Residuals estimation in the (α,β) reference frame (experimentation)

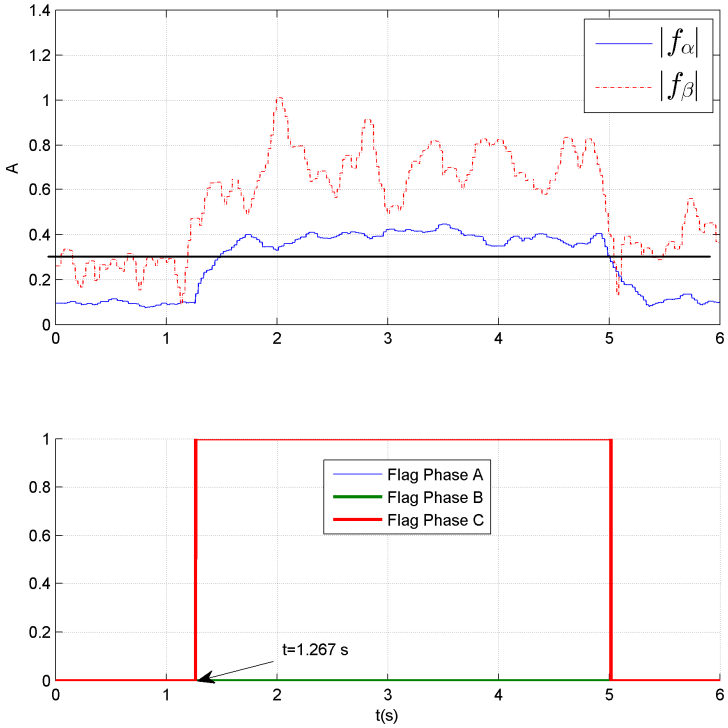

Figure 4.14 Flags for enabling offset detection

At the sensor fault appearance (t = 1.1826s), f_α and f_β increase and become superior to **0.3**. Moreover, f_α and f_β have the same sign. According to the fault isolation process, a phase C current sensor fault is diagnosed with a detection time duration Δt=0.085s (Figure 4.14). As expected, we notice an accentuation of the ripples after the fault in the q axis currents, which have no impact on the motor speed (Figure 4.15).

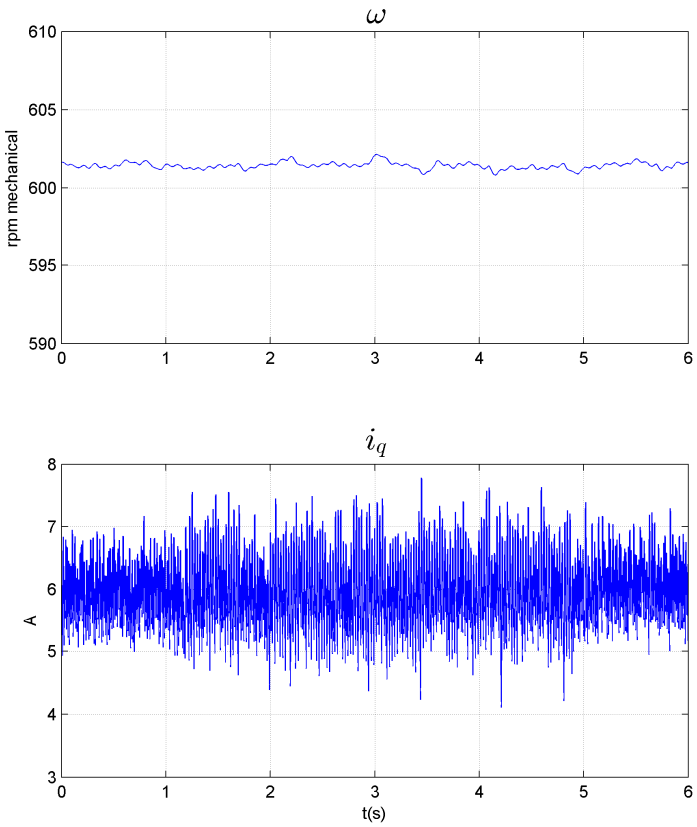

Figure 4.15 Mechanical Speed and q-axis current

The same offset representing a 12% error at steady state in the A current sensor is inserted at t= 1.205s (0.5 A). With the noise, the offset is barely visible (Figure 4.16) and the expected errors are ($|r_\alpha| = 0.408, |r_\beta| = 0$). The fault estimation is good with the results in Figure 4.17 $|f_\alpha| = 0.48$, $|f_\beta| = 0$.

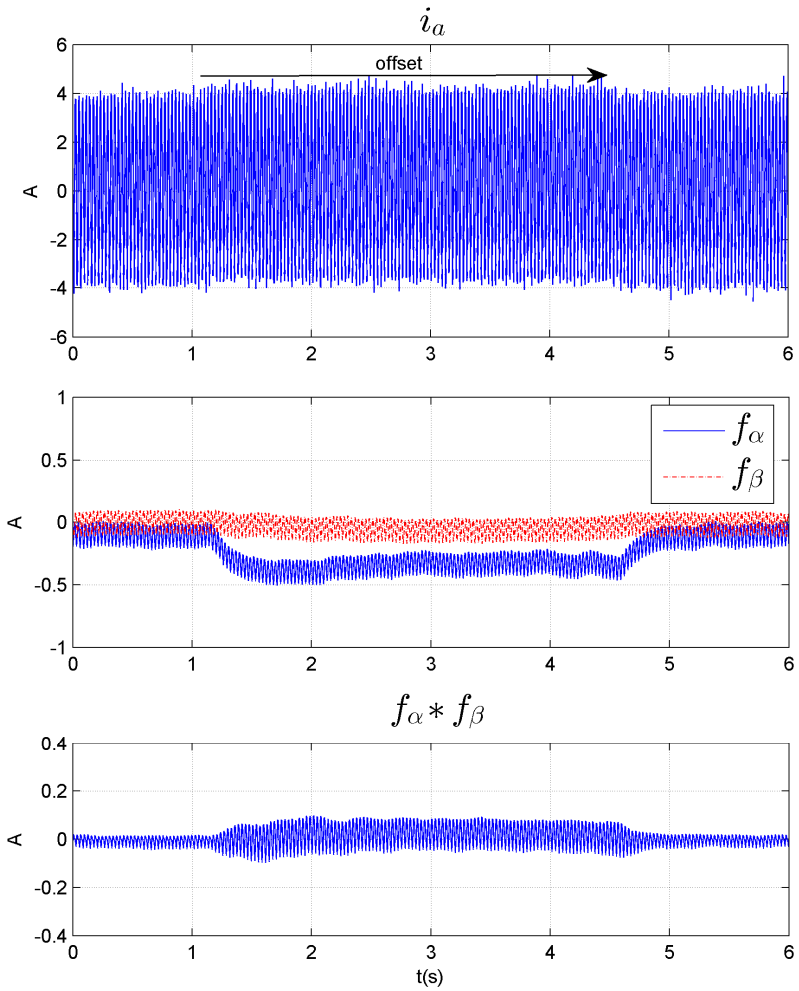

Figure 4.16 Residuals estimation in the (α,β) reference frame

The detection of the A-phase current sensor fault is done after 0.11s (Figure 4.17). This case is interesting because the fault doesn't have an immediate and significant impact on the torque and the speed but one can however think about the usefulness of detecting this kind of small (incipient) fault. In fact, the *q* axis current slightly increases during the fault (Figure 4.18) therefore increasing the joule losses and eventually the temperature. In the long term, this fault if undetected can lead to failure.

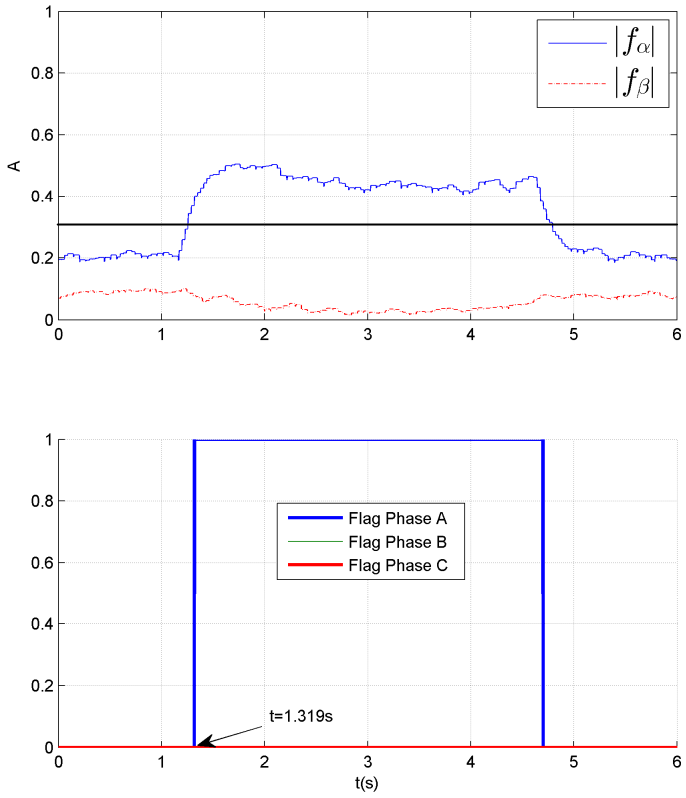

Figure 4.17 Flags for enabling offset detection

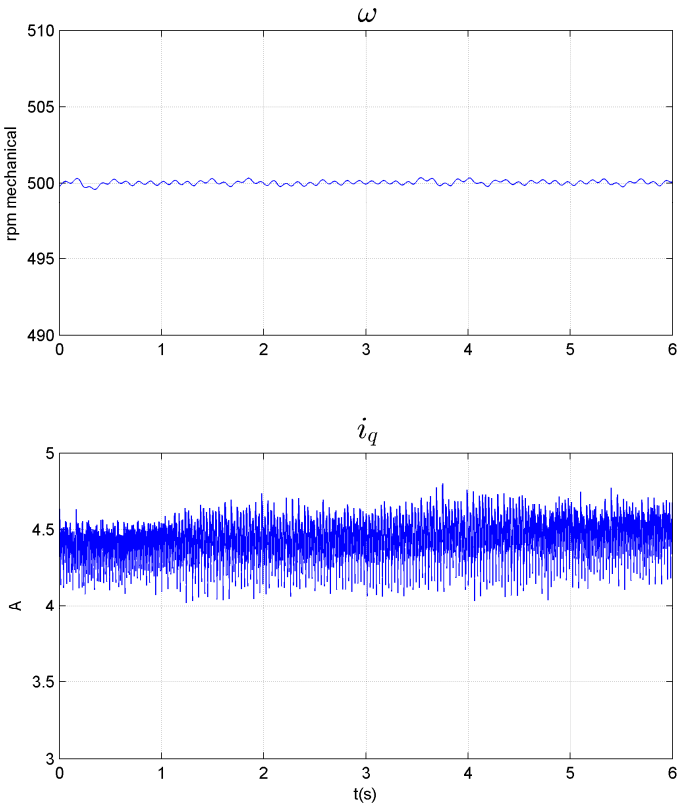

Figure 4.18 Mechanical Speed and q-axis current

From these two experimental tests, there is a situation that needs to be carefully studied. Indeed, the level of the sensor fault compensated by the control is unspecified.

Generally, the regulators reject disturbances like sensor errors with variable performances. For e.g., a RST controller has a better disturbance rejection than a PI controller [Gan2009]. And so, defining this rate of error compensation of the control could be very helpful to design efficient sensor fault detection level and avoid diagnosing faults without important effects.

The results of a gain sensor error (in phase B at t=2.23s) are displayed in Figure 4.19 with G_i =1.6.

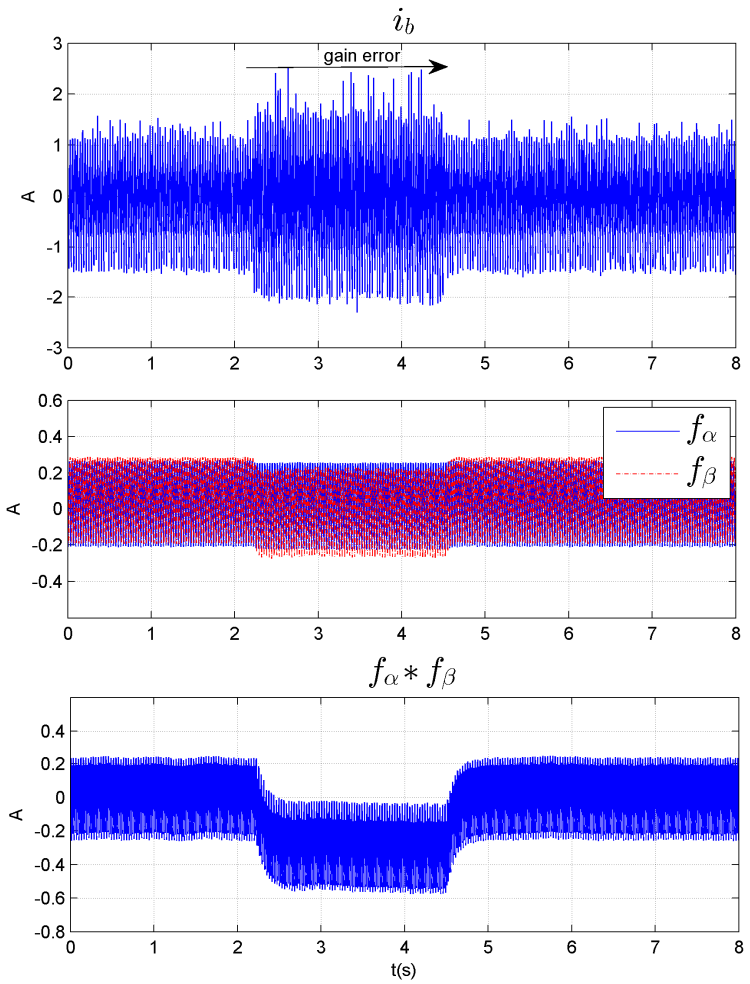

Figure 4.19 Residuals estimation in the (α,β) reference frame

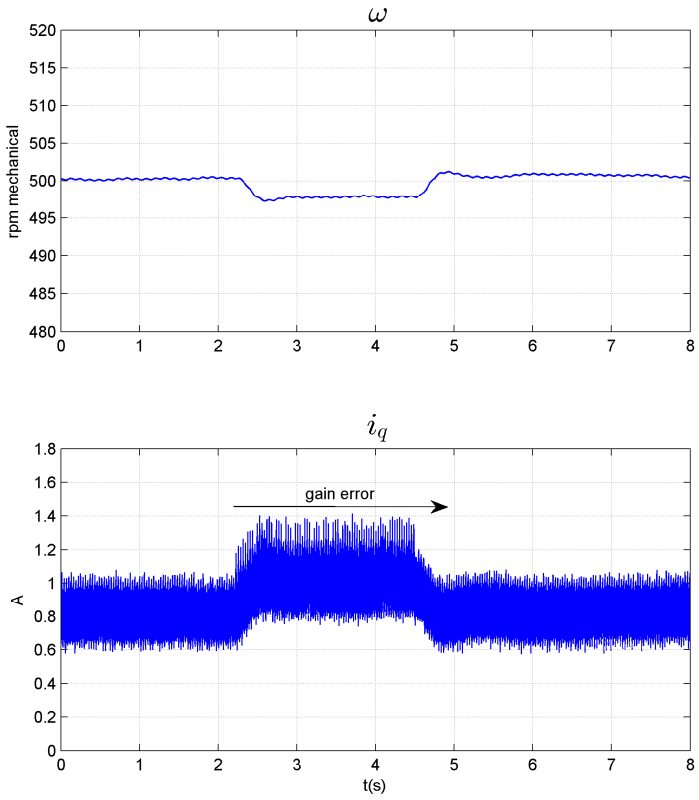

Figure 4.20 Electrical Speed and q-axis current

Speed variation and q-axis current variation during the sensor fault are shown in Figure 4.20. The sign of $f_\beta * f_\alpha$ being negative in Figure 4.19, a flag could be raised for B-phase sensor but due to the threshold setting and the detection rules, the fault is undetectable (Figure 4.21).

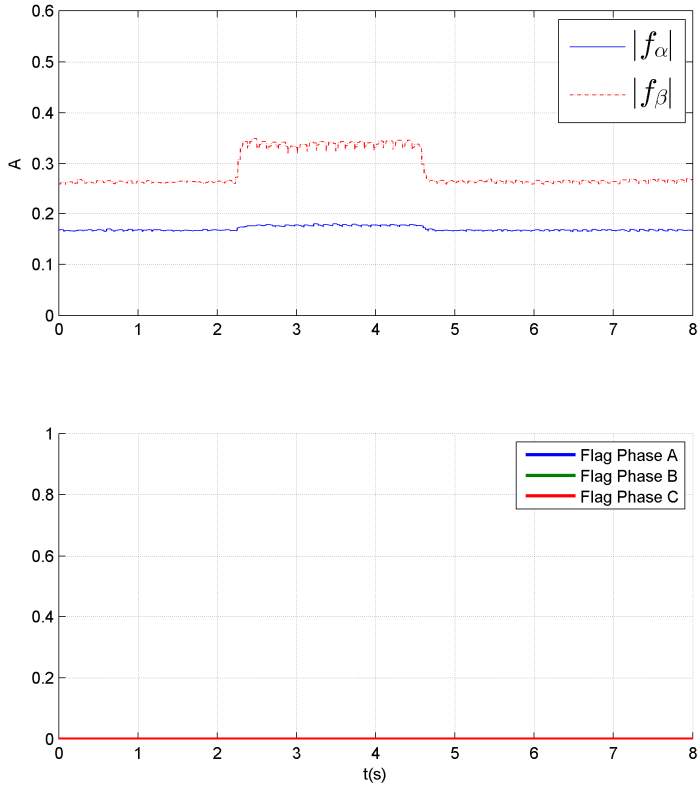

Figure 4.21 Flags for enabling gain fault detection

Partial Conclusion

The algebraic approach of nonlinear diagnosis has been used to detect and isolate current sensor fault in a Permanent Magnet Synchronous Machine (PMSM) drive. The approach is based on a differential algebraic estimation of the faults dynamics in the stationary reference frame. The cases of an offset sensor fault and a gain sensor fault have been studied and a complete FDI structure has been proposed. More experiments are required to tune efficiently the fault detector for all the operating points. However simulation and experimental results have shown the effectiveness of the method.

4.2.2 Current vector analysis for Fault Detection and Diagnosis

4.2.2.1 Current residuals analysis in the (d,q) frame

Signal processing methods have been successfully applied for the diagnosis of current sensors but suffer from a lack of information for fault identification. The main idea comes from the analysis of the behavior of the *d,q* currents in presence of sensor fault.

For this purpose, a detection scheme based on the analysis of the currents waveform in the rotating (*d,q*) frame is synthesized. It uses only the phase currents, the position/speed to detect and isolate the faulty current sensor.

The waveform analysis of the currents in the rotating frame is now detailed. We first give the equations of the currents in the natural frame (*a, b, c*) and in the (*d,q)* frame in healthy mode:

$$\begin{aligned} i_{a,h} &= I\sin(\theta) \\ i_{b,h} &= I\sin(\theta-\frac{2\pi}{3}) \\ i_{c,h} &= I\sin(\theta+\frac{2\pi}{3}) \end{aligned} \quad , \quad \begin{bmatrix} i_{0,h} \\ i_{d,h} \\ i_{q,h} \end{bmatrix} = \sqrt{\frac{2}{3}} \begin{bmatrix} \frac{1}{\sqrt{2}} & \frac{1}{\sqrt{2}} & \frac{1}{\sqrt{2}} \\ \cos\theta & \cos(\theta-\frac{2\pi}{3}) & \cos(\theta+\frac{2\pi}{3}) \\ -\sin\theta & -\sin(\theta-\frac{2\pi}{3}) & -\sin(\theta+\frac{2\pi}{3}) \end{bmatrix} \begin{bmatrix} i_a \\ i_b \\ i_c \end{bmatrix} \qquad (4.7)$$

The lower script *h* stands for the variables in healthy mode. Then, the sensor fault is modeled considering two cases: offset and gain fault.

A- Offset

$i_{am} = i_{a,h} + \Delta i_a$, $i_{bm} = i_{b,h} + \Delta i_b$, $i_{cm} = i_{c,h} + \Delta i_c$ where Δi_a, Δi_b and Δi_c are the offset in phase A, B and C respectively. i_{am}, i_{bm} *and* i_{cm} are the measured currents in phase A, B and C.

Let us assume an offset in phase A, the *d,q* currents become:

$$\begin{cases} i_{dm} = \sqrt{\frac{2}{3}}(i_a \cos(\theta) + \Delta i_a \cos(\theta) + i_b \cos(\theta - \frac{2\pi}{3}) + i_c \cos(\theta + \frac{2\pi}{3})) \\ i_{qm} = \sqrt{\frac{2}{3}}(-i_a \sin(\theta) - \Delta i_a \sin(\theta) - i_b \sin(\theta - \frac{2\pi}{3}) - i_c \sin(\theta + \frac{2\pi}{3})) \end{cases} \quad (4.8)$$

If we compute the residuals $\tilde{i}_d = i_{d,h} - i_{dm}$ and $\tilde{i}_q = i_{q,h} - i_{dm}$, we have the following expressions:

$$\begin{cases} \tilde{i}_d = \sqrt{\frac{2}{3}} \cos(\theta) \Delta i_a \\ \tilde{i}_q = -\sqrt{\frac{2}{3}} \sin(\theta) \Delta i_a \end{cases}$$

Analogously, the same calculation is performed for B and C phases. Finally, it yields:

$$\begin{matrix} PhaseB \\ \begin{cases} \tilde{i}_d = \sqrt{\frac{2}{3}} \cos(\theta - \frac{2\pi}{3}) \Delta i_b \\ \tilde{i}_q = -\sqrt{\frac{2}{3}} \sin(\theta - \frac{2\pi}{3}) \Delta i_b \end{cases} \end{matrix} , \begin{matrix} PhaseC \\ \begin{cases} \tilde{i}_d = \sqrt{\frac{2}{3}} \cos(\theta + \frac{2\pi}{3}) \Delta i_c \\ \tilde{i}_q = -\sqrt{\frac{2}{3}} \sin(\theta + \frac{2\pi}{3}) \Delta i_c \end{cases} \end{matrix} \quad (4.9)$$

As it can be noticed in these expressions, when an offset arises in one of the three phase current sensors, a sinusoidal component at the electrical frequency $\tilde{i}_{d,q}$ is added to the continuous *d,q* currents in steady state. Moreover the amplitude of the residuals is proportional to the fault amplitude.

If we define θ_{res} such as $\theta_{res} = \arctan(-\frac{\tilde{i}_q}{\tilde{i}_d})$ and $\omega_{res} = \frac{d}{dt}\theta_{res} = \omega$, the comparison to the electrical position θ allows the isolation and the comparison to the electrical frequency gives the fault type.

PhaseA	*PhaseB*	*PhaseC*
$\theta_{res} = \theta$	$\theta_{res} = \theta - \frac{2\pi}{3}$	$\theta_{res} = \theta + \frac{2\pi}{3}$

B- Gain Sensor fault

We assume that the measured currents are written as:

$i_{am} = G_a I \sin\theta$, $i_{bm} = G_b I \sin(\theta - \frac{2\pi}{3})$, $i_{cm} = G_c I \sin(\theta + \frac{2\pi}{3})$ where G_a, G_b and G_c are the sensors' gains on phase A, B and C respectively. In healthy mode, $G_a = G_b = G_c = 1$.

If we assume a gain fault in sensor A, the (d,q) currents are:

$$\begin{cases} i_{dm} = \sqrt{\frac{2}{3}}(i_a \cos(\theta) + i_b \cos(\theta - \frac{2\pi}{3}) + i_c \cos(\theta + \frac{2\pi}{3})) + \sqrt{\frac{1}{6}}(G_a - 1) I \sin(2\theta) \\ i_{qm} = \sqrt{\frac{2}{3}}(-i_a \sin(\theta) - i_b \sin(\theta - \frac{2\pi}{3}) - i_c \sin(\theta + \frac{2\pi}{3})) - \sqrt{\frac{1}{6}}(G_a - 1) I (1 + \cos(2\theta)) \end{cases} \quad (4.10)$$

Computing the residuals $\tilde{i}_d = i_{d,h} - i_{dm}$ and $\tilde{i}_q = i_{q,h} - i_{qm}$, we obtain:

$$\begin{cases} \tilde{i}_d = \sqrt{\frac{1}{6}}(G_a - 1) I \sin(2\theta) \\ \tilde{i}_q = -\sqrt{\frac{1}{6}}(G_a - 1) I (1 + \cos(2\theta)) \end{cases} \quad (4.11)$$

Analogously, the same calculation is performed for B and C phases and yields to:

PhaseB

$$\begin{cases} \tilde{i}_d = \sqrt{\frac{1}{6}}(G_b - 1) I \sin(2\theta - \frac{4\pi}{3}) \\ \tilde{i}_q = -\sqrt{\frac{1}{6}}(G_b - 1) I (1 + \cos(2\theta - \frac{4\pi}{3})) \end{cases}$$

PhaseC

$$\begin{cases} \tilde{i}_d = \sqrt{\frac{1}{6}}(G_c - 1) I \sin(2\theta + \frac{4\pi}{3}) \\ \tilde{i}_q = -\sqrt{\frac{1}{6}}(G_c - 1) I (1 + \cos(2\theta + \frac{4\pi}{3})) \end{cases}$$

At fault occurrence, a sinusoidal component at twice the electrical frequency appears in the (d,q) currents with an amplitude proportional to the fault amplitude. The fault type is identified with the computation of the estimated frequency ($\omega_{res} = \frac{d}{dt}\theta_{res} = 2\omega$) and the isolation is based on the estimated angle computation using $\arctan(-\frac{\tilde{i}_q}{\tilde{i}_d})$.

The methodology is finally summarized in Figure 4.22.

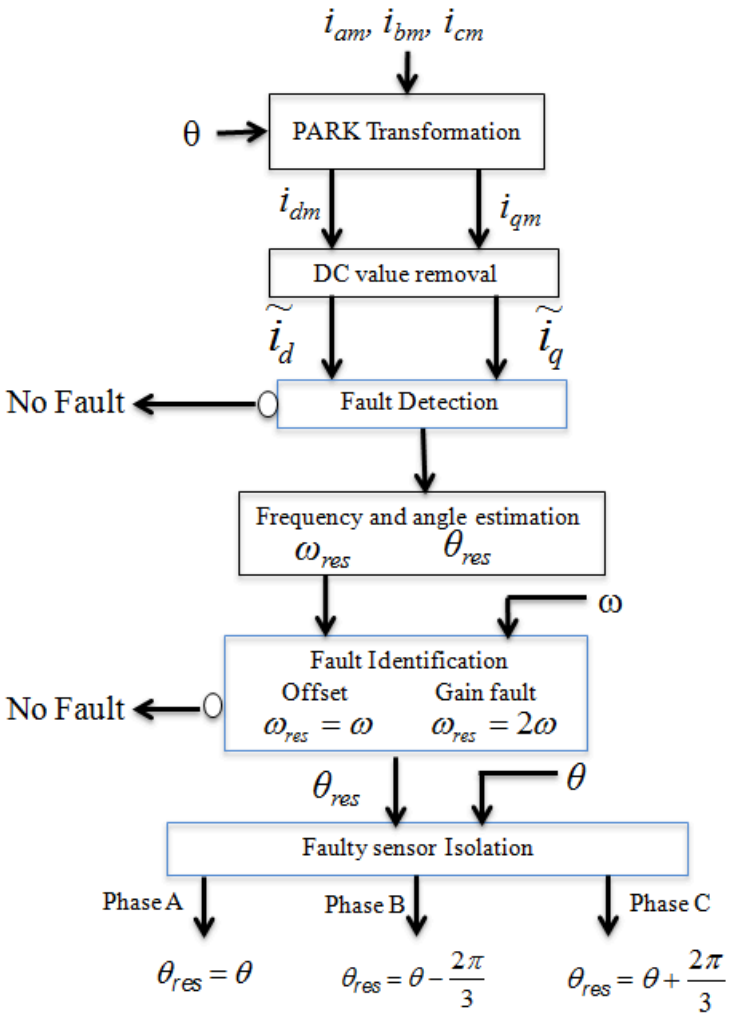

Figure 4.22 Current residual analysis for current sensor fault diagnosis

To achieve the first step (find a sinusoidal component), if we recall that in healthy steady state, currents in the (d,q) reference frame are DC components, a high pass filter could be used to remove the DC part. However, this idea is not well suited because in a variable speed drive, the filter design is more tedious as it would be necessary to have a variable cutoff frequency. Another method is to compute the difference between the (d,q) currents and their respective mean values computed in a time finite window.

For a fault current sensor, the sinusoidal component appears at single or twice the fundamental frequency depending whether it is an offset or a gain fault respectively. Therefore, by applying a rotation $e^{-j\omega t}$ to the single frequency of the sinusoidal component, we can discriminate the fault type.

In the following the simulation and the experimental results of this method are presented.

4.2.2.2 Simulation Results

An offset of 1A is inserted at t=1.2s in the B-phase sensor. Figure 4.23 shows the variation of *dq* currents at the fault apparition.

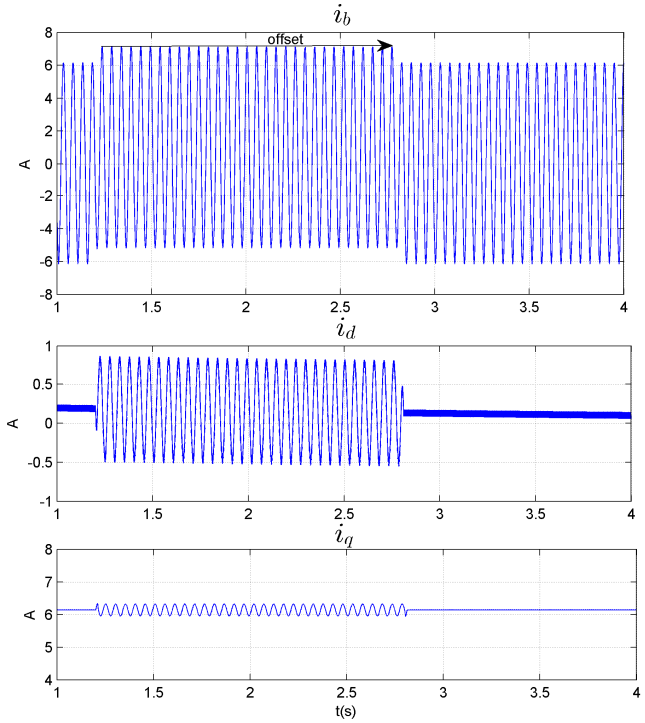

a)

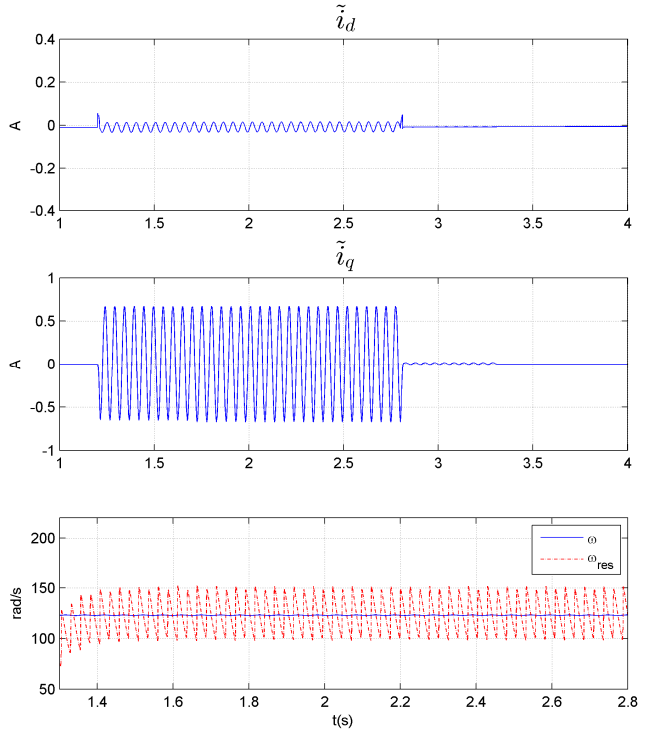

b)

Figure 4.23 Current sensor fault detection with a waveform analysis in B-phase

We see in Figure 4.23a an additional sinusoidal component at the fault apparition in the (*dq*) currents waveforms. This is the information on which the fault detection and diagnosis is based on. In fact the advantage of this method is its ability to distinguish a sensor gain fault from a sensor offset fault thanks to the frequency of this additive component. The isolation is highlighted with the flags in Figure 4.24.

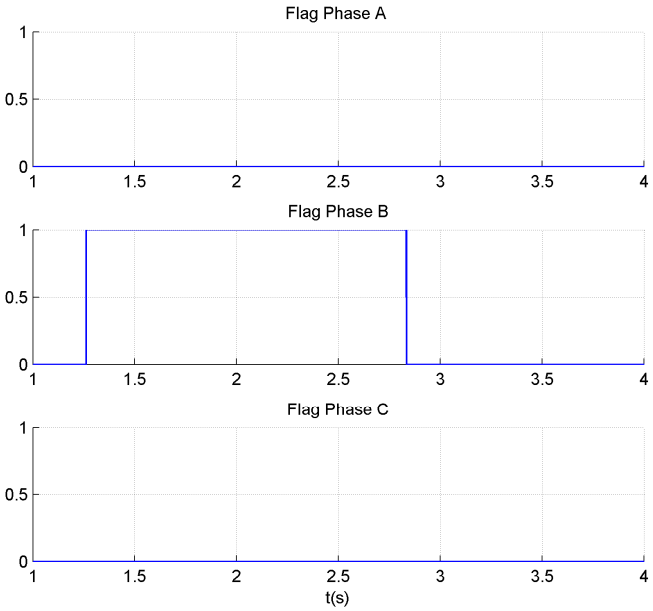

Figure 4.24 Flags in simulation for an offset

The case of a gain sensor fault is studied in Figure 4.25a with a gain error inserted at t=2.01s with G_c = 1.6. The additional sinusoidal component frequency is estimated (see last plot in figure 4.25b). It clearly indicates a gain sensor fault type.

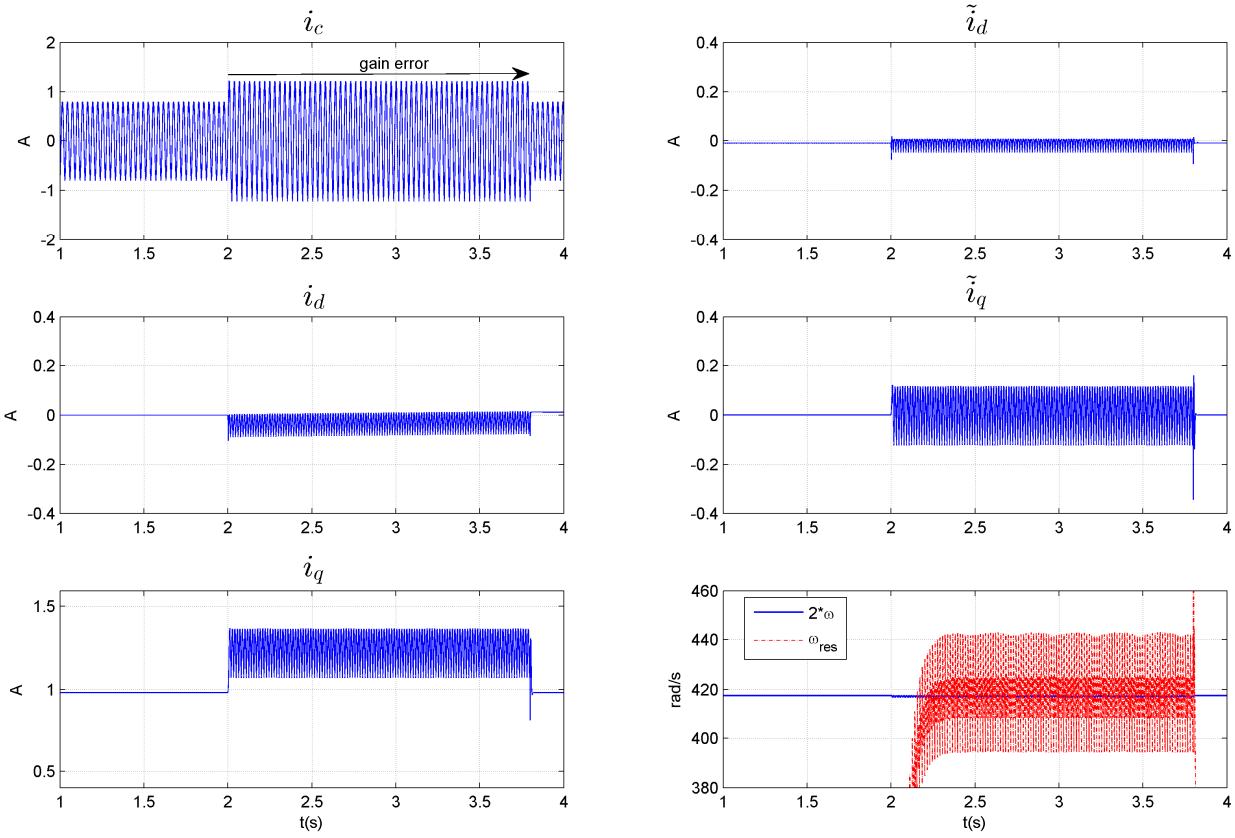

a) b)

Figure 4.25 Current sensor fault detection with a waveform analysis in C-phase (simulation)

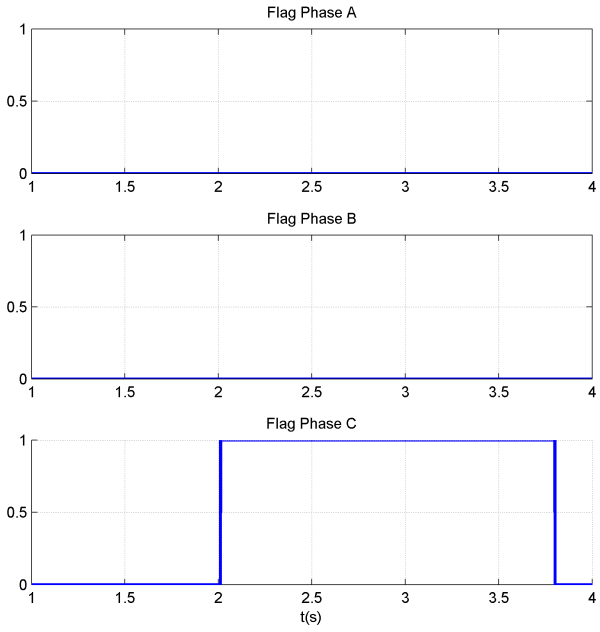

Figure 4.26 Flags in simulation for a gain fault

The fault isolation is confirmed in figure 4.26 with the flags.

4.2.2.3 Experimental results

The experimental results plotted in Figures 4.27a show the behavior of the fault detection method with an offset Δi=1A injected at t=2.83s in phase B. This fault injected represents around a 16% error at steady state (the current magnitude is 5A).

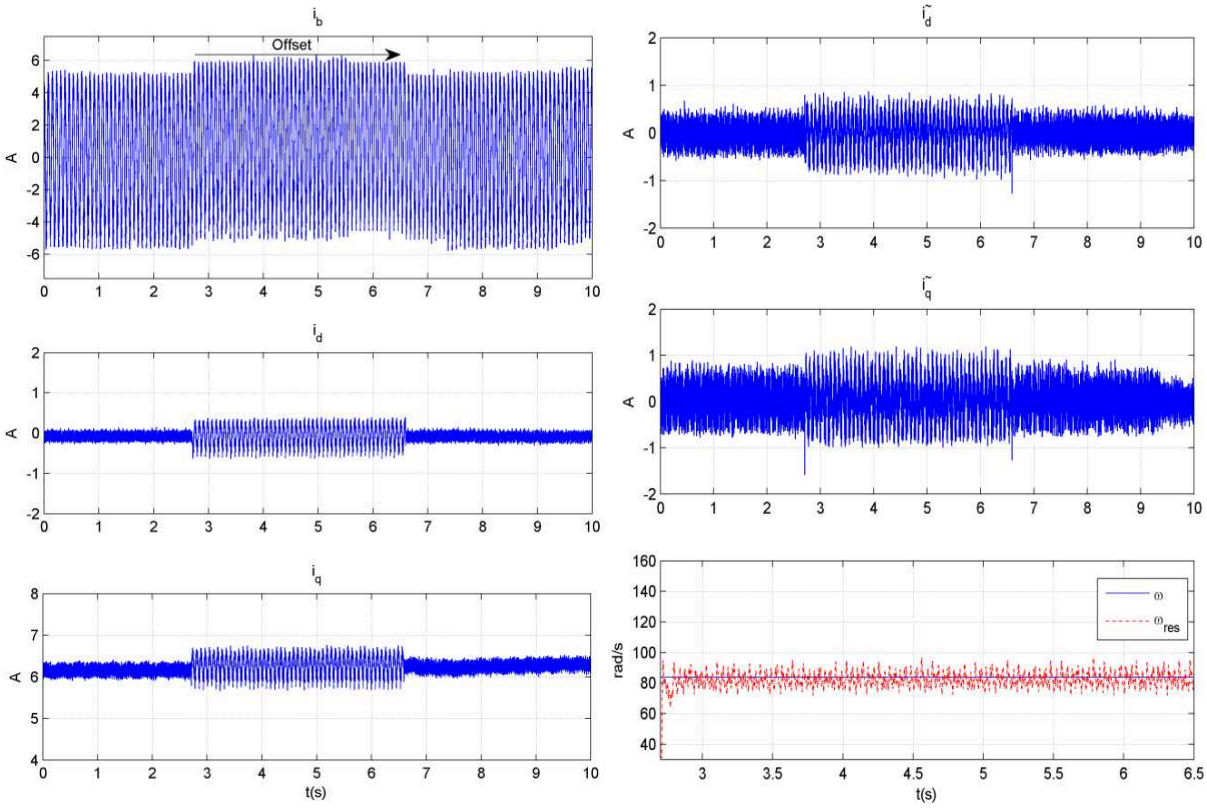

a) b)

Figure 4.27 B Sensor Fault Detection

The sinusoidal residual estimated frequency is equal to the electrical frequency during the sensor fault as expected (Figure 4.27b). The fault detection is confirmed in Figure 4.28 with the flag raising at t=2.93s. The detection time duration Δt = 0.01s. However, in absence of faults, $\tilde{i}_{dq}$ is not null and a threshold needs to be settled and two cases are possible. If the chosen threshold is too high, we could potentially have a misdetection of certain faults. Otherwise if the chosen threshold is too small, in the diagram of the Figure 4.22, we could validate the step of fault detection but the process would stop at the frequency test.

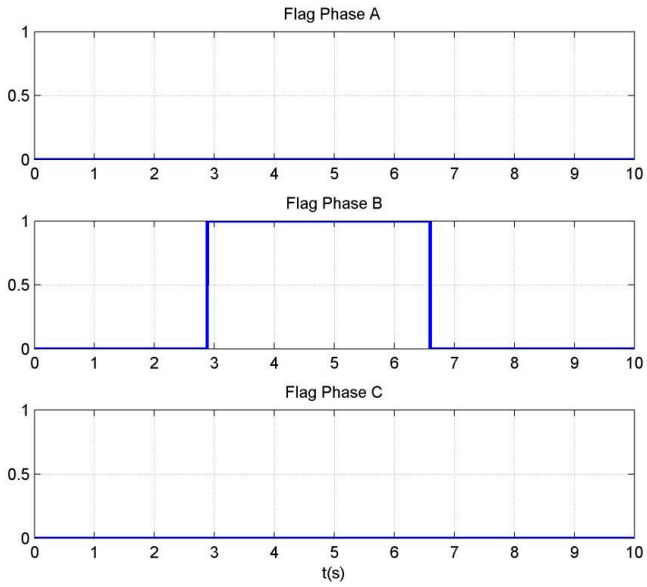

Figure 4.28 Flags of *B* Sensor Fault Detection (offset)

Now we are interested by the detection time. At each calculation sample t_k, an average value of i_{dq} current is computed as follows: $< i_{dq} > (t_k) = \frac{1}{N}\sum_{k=1}^{N} i_{dq}(t_k - kT_e)$ where T_e is the sampling period. Then $\tilde{i}_{dq}$ residual is calculated: $\tilde{i}_{dq} = i_{dq}(t_k) - < i_{dq} > (t_k)$. For the experimental tests, we have set N =500.

The case of a gain sensor fault is now studied in the following figures. The experimental results plotted in Figure 4.29a show the behavior of the detection method with a gain sensor error G_a=1.6 injected at time t=2.3s in phase A. A sinusoidal component $\tilde{i}_{d,q}$ is superimposed to the continuous *d,q* currents at twice the electrical frequency ($\omega_{res} = 2\omega$) as shown in Figure 4.29b, last plot). The detection time duration is Δt = 0.012s (Figure 4.30).

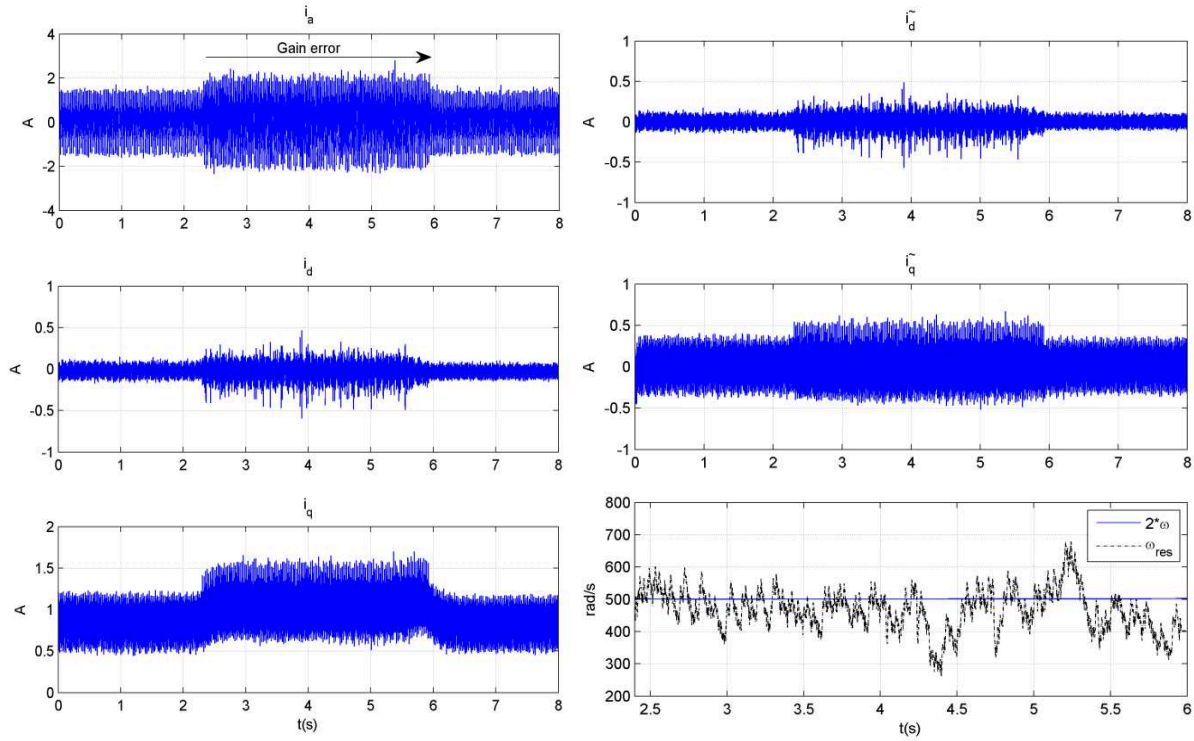

a) b)

Figure 4.29 Experimental results of Phase A Gain Sensor Fault Detection

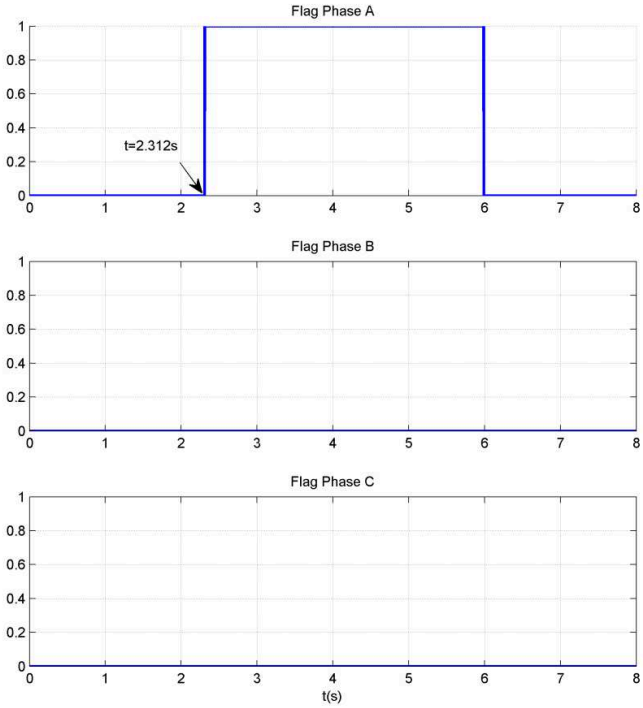

Figure 4.30 Flags of phase *A* Sensor Fault Detection

In the following the case of a current sensor outage (B-phase) is illustrated.

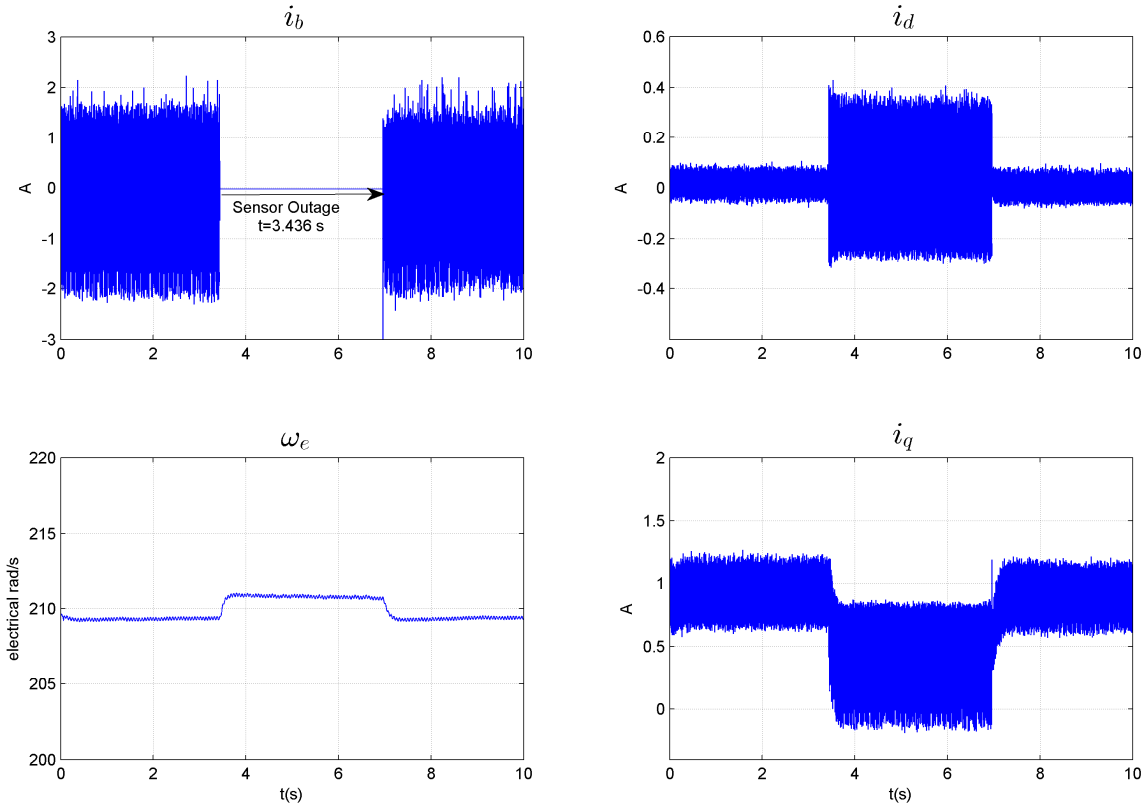

Figure 4.31 Current and Speed in case of current sensor outage

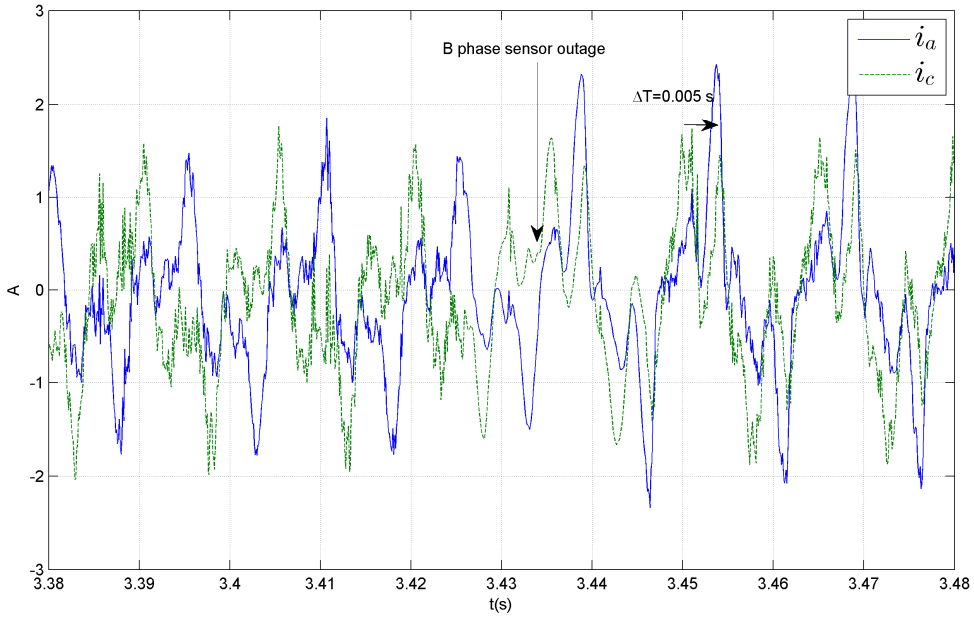

Figure 4.32 Phase shift between A and C phases at B sensor outage

At t=3.436s the current sensor output of the B phase is forced to zero as displayed in the upper left plot of Figure 4.31. As a consequence, it appears a phase displacement of 60º between i_a and i_c (Figure 4.32: ΔT=0.005s with ω_e = 209.4 rad/s). Under these conditions, the system efficiency is reduced and oscillations at twice the fundamental frequency appear in the *d,q* currents (Figure 4.31).

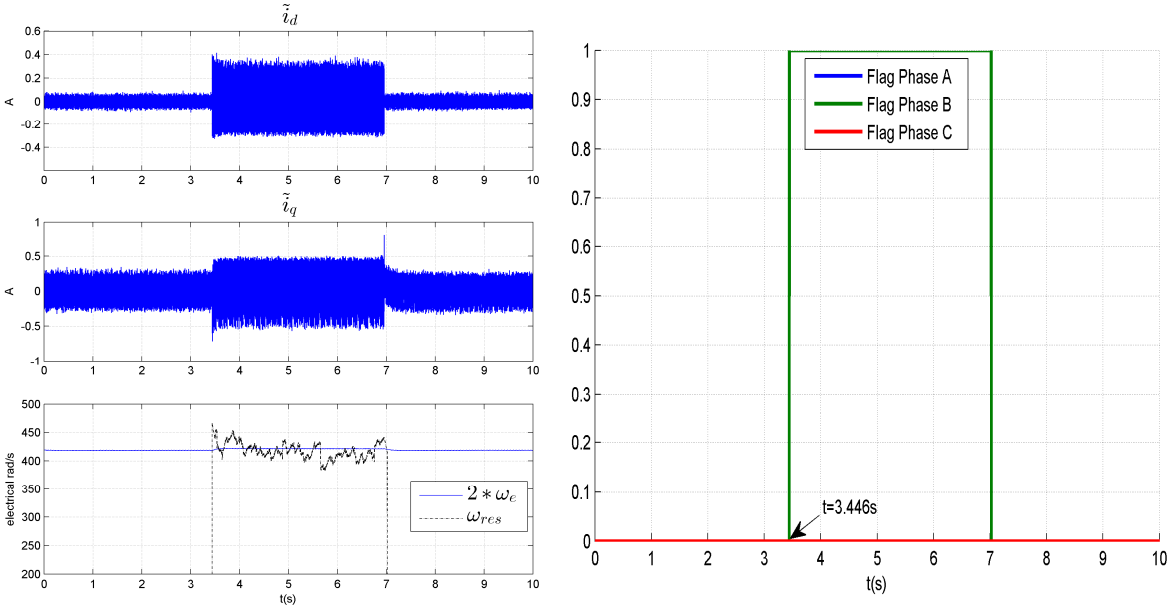

a) *dq* currents, estimated frequency b) Flags

Figure 4.33 FDI in case of current sensor outage

The fault is detected and isolated in two periods (Δt_1 = 0.01s) despite the closed-loop action (Figure 4.33).

Partial Conclusion

The current sensor fault detection based on a waveform analysis has a high ability for fault detection. This method also exhibits a good capability for fault identification and isolation thanks to the estimated electrical frequency and angle. Finally, it is robust thanks to the use of a nonparametric approach independent of the machine electrical model.

As we have proposed two methods, we are interested in comparing their performances in terms of detection time duration and current level for the same operating points.

Naturally, for a relevant comparison, the tests should be performed in the whole torque / speed plane. However, due to time constraints, we choose to do it in the operating point given in Figure 4.34 with an offset of **-0.8** A (corresponding to a 60% error) inserted at t=3.045s in Phase C.

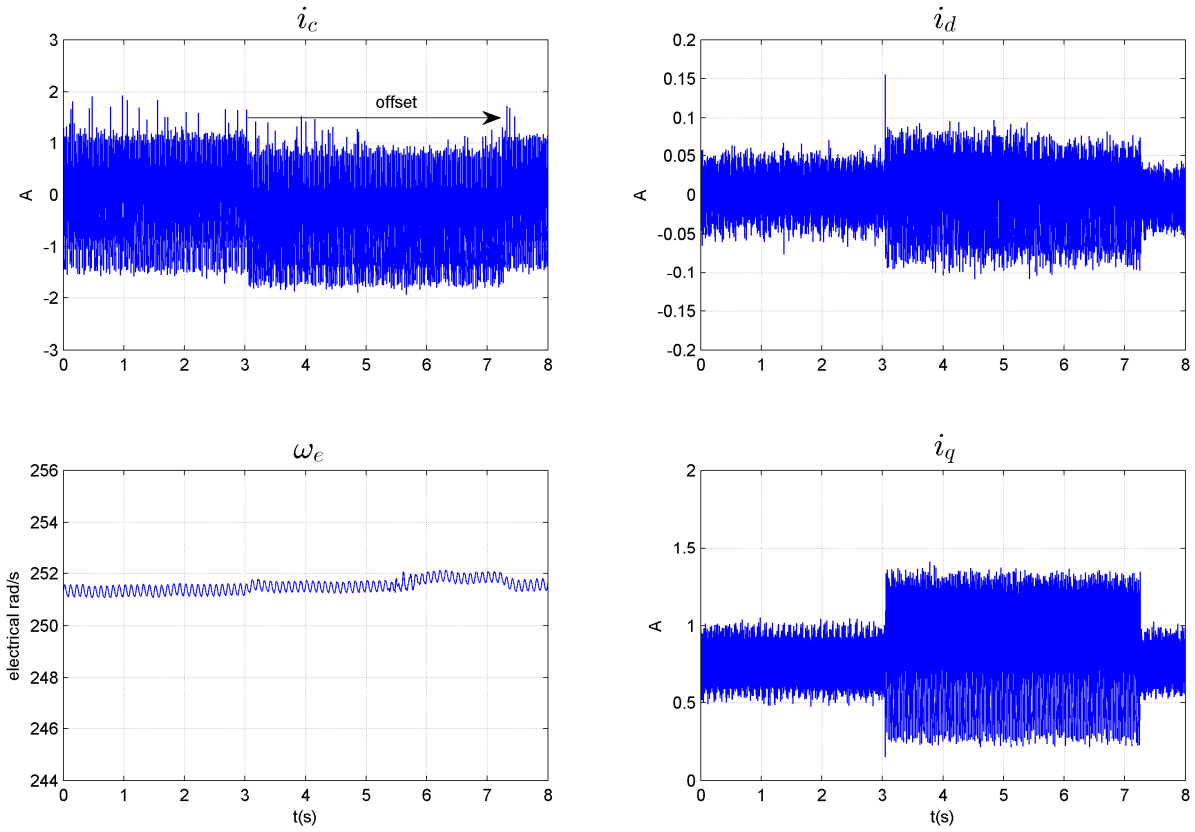

a) Phase C current and speed

b) *d,q* currents

Figure 4.34 Offset in phase C current sensor

The current vector analysis in the rotating frame is first applied to evaluate its detection capability. The results are presented in Figure 4.35.

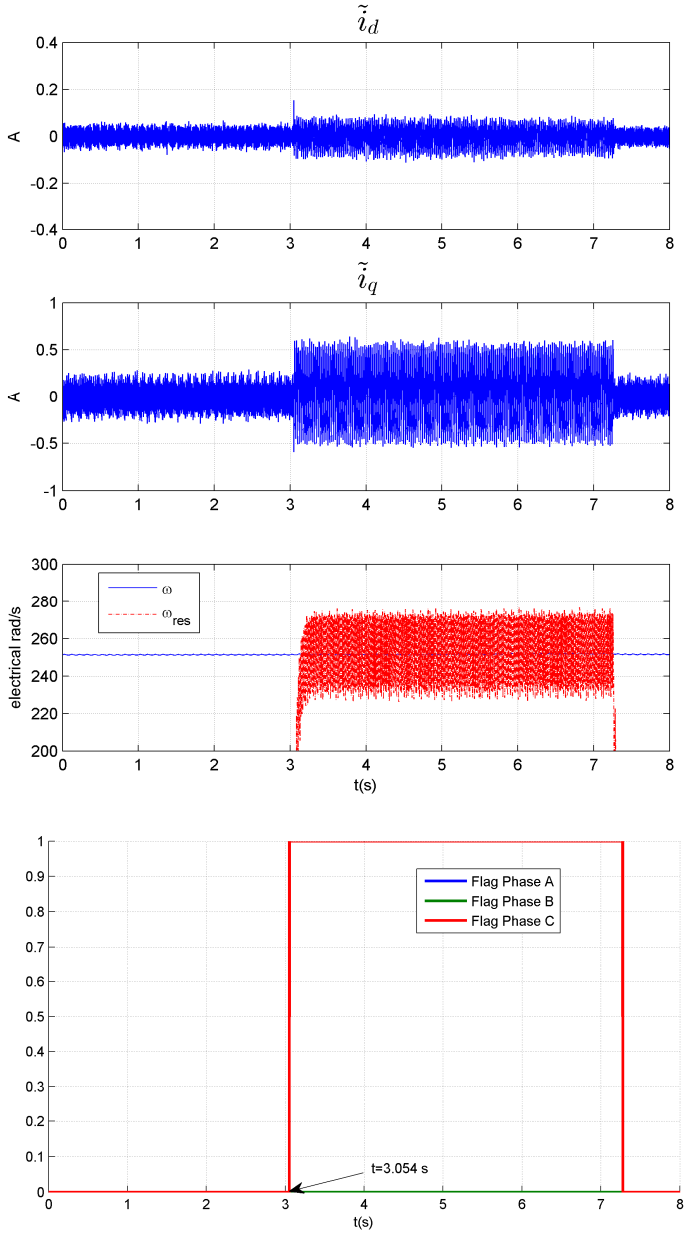

Figure 4.35 Current vector analysis for Fault Detection and Isolation

The same data are used with the algebraic estimator for fault diagnosis. The results are presented in figure 4.36.

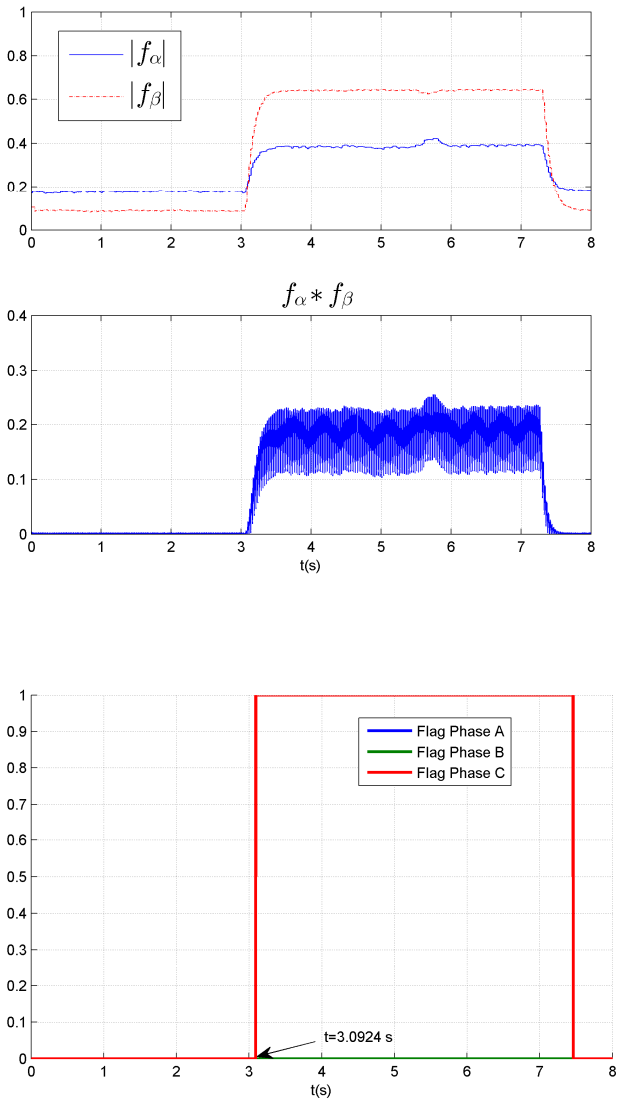

Figure 4.36 Algebraic estimator for Fault Detection and Isolation

We have two detection durations: Δt_1 = 0.01s for the *dq* method (Figure 4.35) and Δt_2 = 0.047s for the algebraic method (Figure 4.36). The main result is the fact that the waveform analysis method has a better detection time than the algebraic approach of diagnosis.

4.3 Observer for the DC link voltage

Actually, when the DC voltage sensor fails, the output of the Current Control Loop is modified and the PWM signal increases or decreases (positive offset/gain or negative offset/gain) to maintain the requested torque/speed. This may affect the energy management and also reduce the acceleration capabilities. To avoid these undesirable consequences on the performances or possibly on the security, a virtual redundancy should be implemented to monitor the sensor. Then we are interested by the estimation of the DC link voltage using the phase currents and the duty cycles. Firstly, the Kirchhoff law at the capacitor output is written. Then, using the voltage equation at the machine gates, a second-order system is defined according to Figure 4.37.

$$i = C\frac{dU_{dc}}{dt} = i_{DC/DC} - i_{DC/AC}, i_{DC/AC} = \sum_{j=1}^{3} i_j \alpha_j \,, \tag{4.12}$$

The A-phase voltage can be written as: $v_a = \alpha_1 U_{DC}$ where the α_j are the three half bridge control signals and i_j the phase currents. $i_{DC/DC}$ is the output current of the DC source.

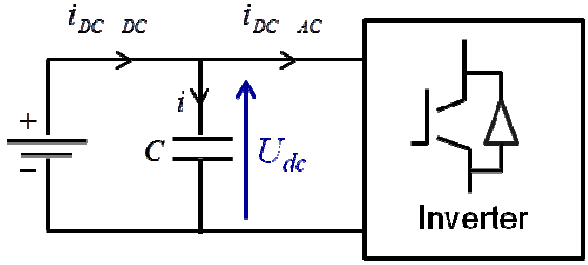

Figure 4.37 Supply of the inverter by the DC voltage bus

The dynamic of the DC link voltage and the A-phase current can be written in a state space model as follows with e_a the A-phase emf:

$$\begin{aligned} C\frac{dU_{dc}}{dt} &= i_{DC/DC} - \alpha_1 i_a - \alpha_2 i_b - \alpha_3 i_c \\ L_a\frac{di_a}{dt} &= -R_s i_a + v_a - e_a = -R_s i_a + \alpha_1 U_{dc} + \phi\omega\sin\theta \end{aligned} \tag{4.13}$$

From this, the observer is synthesized:

$$\begin{aligned} \frac{d\hat{U}_{dc}}{dt} &= \frac{1}{C}(i_{DC/DC} - \alpha_1\hat{i}_a - \alpha_2 i_b - \alpha_3 i_c) + M_1(i_a - \hat{i}_a) \\ \frac{d\hat{i}_a}{dt} &= \frac{1}{L_a}(-R_s\hat{i}_a + \hat{U}_{dc}\alpha_1 - \phi\omega\sin\theta) + M_2(i_a - \hat{i}_a) \end{aligned} \tag{4.14}$$

Phase current estimation is used to correct the DC-link voltage estimation and compensate model uncertainties. The tuning of M_1 and M_2 must be done according to the stability criterion. We first define the estimation error: $\varepsilon_1 = i_a - \hat{i}_a, \varepsilon_2 = U_{DC} - \hat{U}_{DC}$. Then the dynamic of the estimation error is given by:

$$\begin{aligned}\dot{\varepsilon}_1 &= -\frac{R_s}{L_a}\varepsilon_1 + \frac{\alpha_1}{L_a}\varepsilon_2 - M_2\varepsilon_1 = -(\frac{R_s}{L_a} + M_2)\varepsilon_1 + \frac{\alpha_1}{L_a}\varepsilon_2 \\ \dot{\varepsilon}_2 &= \frac{\alpha_1}{C}\varepsilon_1 - M_1\varepsilon_1 = (\frac{\alpha_1}{C} - M_1)\varepsilon_1\end{aligned} \tag{4.15}$$

Assuming the following Lyapunov function: $V = \frac{1}{2}(\varepsilon_1^2 + \varepsilon_2^2) > 0$, $\dot{V} = \varepsilon_1\dot{\varepsilon}_1 + \varepsilon_2\dot{\varepsilon}_2$

$$\begin{aligned}\dot{V} &= -(\frac{R_s}{L_a} + M_2)\varepsilon_1^2 + \varepsilon_1\varepsilon_2(\frac{\alpha_1}{L_a}) + \varepsilon_1\varepsilon_2(\frac{\alpha_1}{C} - M_1) \\ \dot{V} &= -(\frac{R_s}{L_a} + M_2)\varepsilon_1^2 + \varepsilon_1\varepsilon_2(\alpha_1(\frac{1}{L_a} + \frac{1}{C}) - M_1)\end{aligned} \tag{4.16}$$

Choosing $M_1 = \alpha_1(\frac{1}{L_a} + \frac{1}{C})$ yields to $\dot{V} = -(\frac{R_s}{L_a} + K_2)\varepsilon_1^2 \le 0$ if $M_2 > 0$. So $\dot{V} \le 0$ and the closed loop system is then asymptotically stable with $M_1 = \alpha_1(\frac{1}{L_a} + \frac{1}{C}), M_2 > 0$.

Figure 4.38 shows the experimental results of the nonlinear observer. We notify that for the following tests, the system is controlled in open-loop.

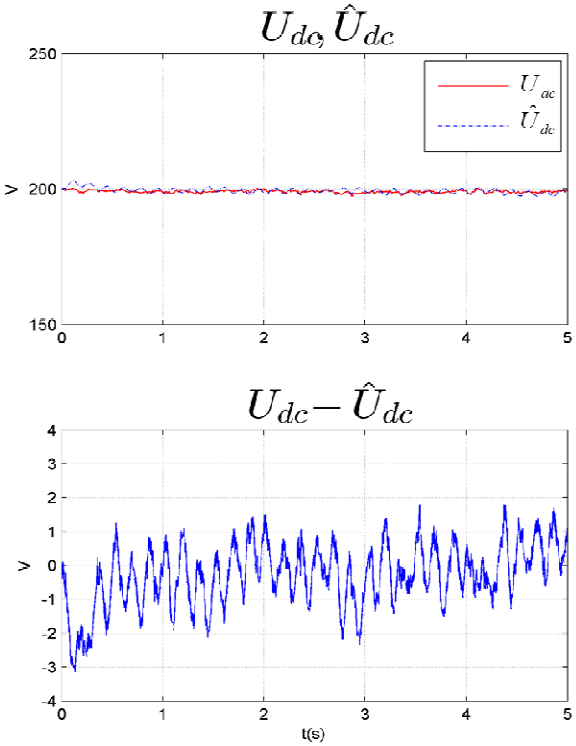

Figure 4.38 DC link voltage estimation

The estimation error is around 1.5%. The observer is then evaluated at the same operating point during a sensor fault. An abrupt offset of 20 V representing 10% of the real value is introduced at t=2.83 s. As displayed in figure 4.39, the estimation error increases significantly enabling the fault detection.

In the same time, the amplitude of the measured currents (lower plot in figure 4.39) decreases significantly. This is due to the fact that by over-measuring the DC voltage, the current control loops generate higher duty cycles for the reference speed trajectory.

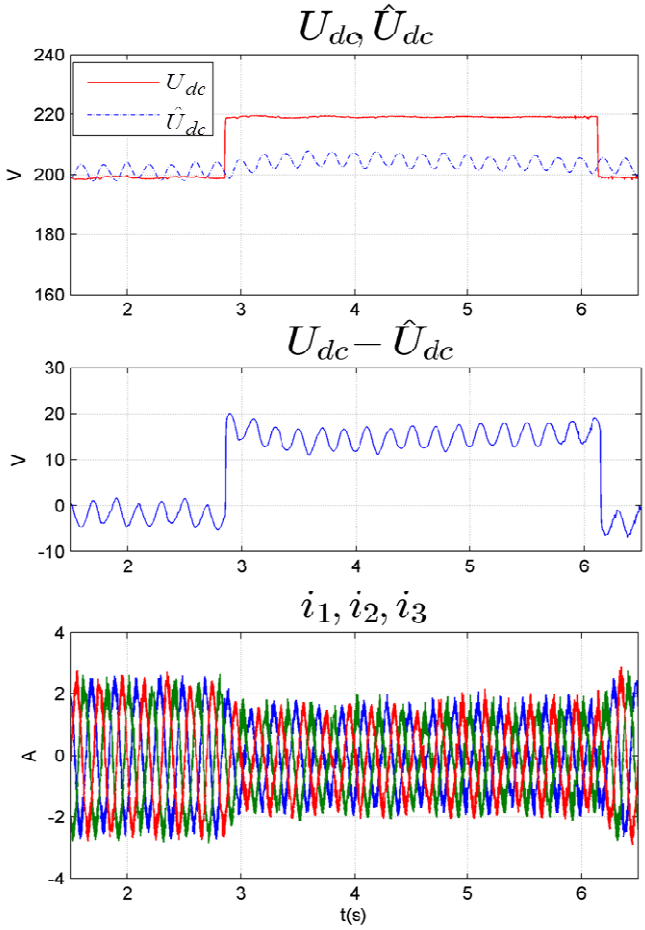

Figure 4.39 DC link voltage estimation during a sensor fault

Consequently, setting a threshold at *10 V,* which means that an error of 5% on the nominal voltage is tolerated, a DC voltage sensor fault is detected in Figure 4.40 with a detection time duration Δt=0.058s.

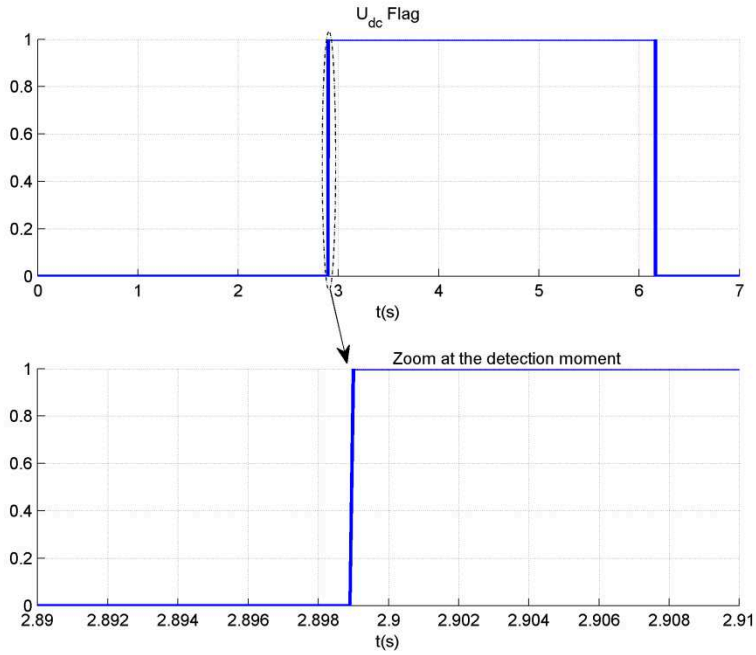

Figure 4.40 DC voltage sensor flag

At this level, the Fault Detection is not fully achieved. As said in Chapter 3, it is necessary to have at least three measurements of the same information. In our case, we only have a DC link voltage measurement and its estimation. So, another source is requested for a complete Fault Detection. Facing the difficulty of designing a second observer for the DC voltage, we could use the results of the current sensors FDI. Indeed, we know that the root cause of estimation error comes from the validity of the inputs data. In our case, the inputs are the control signals and the phase current measurements.

So, to prevent false alarms, we can combine the flags of the current sensor FD with the DC voltage sensor flag. Doing so, we will avoid enabling a DC voltage sensor FD during a phase current sensor outage.

Another way is to use an additional correction state using B-phase current in equation (4.14). Then, the DC voltage will be estimated with a correction step involving two phase currents sensors. However, it will transform the initial system into a four order system and then increases the algorithmic cost.

The last step of the fault tolerant control is the reconfiguration of the strategy. For a DC link voltage sensor fault, the nonlinear observer could take over to ensure continuity of the operation.

4.4 Conclusion

This chapter was dedicated to the development of current and DC-link voltage sensors fault detection and isolation in the powertrain of an electric vehicle. For the currents, two methods have been presented to detect and isolate current sensor fault. The first one is based on a differential algebraic estimation of the faults dynamics in the stationary reference frame.

Because the method is parametric, the robustness issues against motor parameter variations should be addressed. However this estimator is a dynamic system and therefore its performances (convergence rate, estimated residuals) are useful means for maintenance and prognosis. The first experimental results are promising and further studies on the threshold setting must enhance the detection capability.

The second one is based on the current waveform analysis of the currents in the (d,q) synchronous rotating reference frame. This non-parametric method is more straightforward as it is based on variables already available in the control loops. Due to its structure, this method is more robust to false alarms. However there is also a threshold issue particularly due to environmental perturbations. The first experimental results are very promising and the detection time duration is shorter than the first method's one.

Finally, for the DC-link voltage sensor, an observer has been developed and experimentally evaluated. The first results are encouraging as the estimated value can be used for monitoring purposes and eventually as a redundant sensor for fault tolerant purposes.

References

[Abd2010] **Electrical drive service continuity for an induction machine fed by stator and rotor in presence of sensor faults**, M. Abdellatif, *PhD thesis*, *INP Toulouse,* Apr 2010

[Bag2005] **Sensor fault detection for fault tolerant vector controlled induction machine**, L. Baghli, P. Poure, A. Rezzoug, *in Proceedings of European Conference on Power Electronics and Applications*, pp. 1–10, 2005

[Ben2007] **Advanced Fault-Tolerant Control of Induction-Motor Drives for EV/HEV Traction Applications: From Conventional to Modern and Intelligent Control Techniques**, M.E.H. Benbouzid, D. Diallo, M. Zeraoulia, *IEEE Transactions on Vehicular Technology,* vol.56, n°.2, pp.519-528, March 2007

[Bou2013] **Combined Signal and Model-Based Sensor Fault Diagnosis for a Doubly Fed Induction Generator**, B. Boulkroune, M. Gálvez-Carrillo, M. Kinnaert, *IEEE Transactions on Control Systems Technology*, vol.21, no.5, pp.1771,1783, Sept. 2013

[Chen1999] **Robust model-based fault diagnosis for dynamic systems**, J. Chen, R. Patton, *Kluwer Academic*, Boston, 1999.

[DeP2001] **A geometric approach to nonlinear fault detection and isolation**,C. De Persis, A. Isidori, *IEEE Transactions on Automatic Control*, pp 853–865, 2001.

[Diao2013] **Sensor Fault Diagnosis for Improving the Availability of Electrical Drives,** S. Diao, D. Diallo, Z. Makni, C. Marchand, J.F. Bisson , *Proceedings of the 39th Conference on IEEE Industrial Electronics Society (IECON)*, pp.3108-3113, Vienne, AT, November 2013

[Diop2001b] **On an algebraic and differential approach of nonlinear systems diagnosis**, S. Diop, R. Martinez-Guerra, *Proceedings of the 40th IEEE Conference on Decision and Control*, vol.1, pp.585-589 vol.1, 2001

[Fre2014] **New Approach for Current Sensor Fault Diagnosis in PMSG Drives for Wind Energy Conversion Systems**, N. M. A. Freire, J. Estima, A. J. M. Cardoso, *IEEE Transactions on Industry Applications* , Mar 2014

[Gal2010] **Sensor fault detection and isolation in three-phase systems using a signal-based approach**, M. Gálvez-Carrillo, M. Kinnaert, *IET Control Theory & Applications*, vol.4, no.9, pp.1838-1848, September 2010

[Gan2009] **Comparison of different control; strategy based on pole placement for cascaded multilevel inverter based dynamic voltage restorer**, S.N.V. Ganesh, K. Ramesh Reddy, B.V. Shankar, *Journal of Electric Systems*, 6 (1), March 2009

[Ise2011] **Fault Diagnosis Applications: Model Based Condition Monitoring, Actuators, Drives, Machinery, Plants, Sensors, and Fault tolerant Systems**, R. Isermann, *Springer, 1st Edition*, 2011.

[Ibr2003] **Online exact differentiation and notion of asymptotic algebraic observers**, S. Ibrir, *IEEE Transactions on Automatic Control,* vol.48, no. 11, pp. 2055 – 2060, 2003

[Jeo2005] **Fault detection and fault-tolerant control of interior permanent-magnet motor drive system for electric vehicle**, Y. Jeong, S. Sul, S. Schulz, and N. Patel, *IEEE Transactions on Industrial Applications Industrial Electronics,* vol. 41, no. 1, pp. 46–51, Jan./Feb. 2005.

[Jia2010] **Current reconstruction techniques for survivable three-phase PWM converters**, W. Jiang and B. Fahimi, *IEEE Transactions on Power Electronics*, vol. 25, no. 1, pp.188 -193 2010

[Lee2011] **Current sensor fault detection and isolation of the driving motor for an in-wheel motor drive vehicle**, B.Lee, N.Jeon, H. Lee, *International conference on Control, Automation and Systems (ICCAS)*, pp.486,491, 26-29, Oct. 2011

[Lit] **http://www.littelfuse.com/products/varistors/industrial-high-energy/ba/v661ba60.aspx**

[Mei2011] **Fault detection, isolation and control reconfiguration of three-phase PMSM drives**, F. Meinguet, X. Kestelyn, E. Semail, J. Gyselinck, *IEEE International Symposium on Industrial Electronics (ISIE)*, pp.2091-2096, 27-30 June 2011

[Naja2011] **Detection and Isolation of Speed, DC-link voltage and current sensor faults based on an adaptive Observer in Induction Motor Drives**, T. A. Najafabadi, F. R. Salmasi, P. Jabehdar-Maralani, *IEEE Transactions on Industrial Electronics*, vol. 58, n°5, pp. 1662-1671, May 2011

[Ohn2004] **DC voltage sensorless single-phase PFC converter**, Ohnishi T., Hojo M., *IEEE Transactions on Power Electronics*, pp. 404–410, 2004

[Por2007] **Accuracy of hall effect current measurement transducers in Automotive Battery Management Applications using current integration**, R. Portas, L. Colombel, *Automotive Power Electronics*, Sept 2007

[Rot2009] **Current Sensor Fault Detection, Isolation, and Reconfiguration for Doubly Fed Induction Generators**, K. Rothenhagen, F. W. Fuchs, *IEEE Transactions on Industrial Electronics,* vol.56, no.10, pp.4239-4245, Oct 2009

[Wel2004] **Fault tolerant three-phase AC motor drive topologies: a comparison of features, cost and limitations**, B. Welchko, T. Lipo, T. Jahns, S. Schulz, *IEEE Transactions on Power Electronics*, Vol. 19, No. 4, pp: 539-546, July 2004.

[Xin2013] **Fault Diagnosis of DC-Link Capacitors in Three-Phase AC/DC PWM Converters by Online Estimation of Equivalent Series Resistance**, Xing-Si Pu; Thanh Hai Nguyen; Dong-Choon Lee; Kyo-Beum Lee; Jang-Mok Kim, *IEEE Transactions on Industrial Electronics*, vol.60, no.9, pp.4118,4127, Sept. 2013

[Yip2003] **A novel voltage sensorless control technique for a bidirectional AC/DC converter**, Yip S.C., Qiu D.Y., Chung H.S.H., Hui S.Y.R., *IEEE Transactions on Power Electronics*, pp. 1346–1355, 2003

[You2013] **State Observer-Based Sensor Fault Detection and Isolation, and Fault Tolerant Control of a Single-Phase PWM Rectifier for Electric Railway Traction**, A.B. Youssef, S.K. El Khil, I.Slama-Belkhodja, *IEEE Transactions on Power Electronics*, vol.28, no.12, pp.5842,5853, Dec. 2013

Conclusions and Perspectives

The main objective of this thesis focused on the development of a controller tolerant to sensor faults in electrical drives used in the automobile. With growing concern of car manufacturers to increase the reliability, it is necessary to develop real time strategies for fault detection, fault isolation and reconfiguration to ensure a safe continuity of operation.

The cases of the mechanical sensor (for electrical machine rotor position measurement), phase currents and DC bus voltage sensors have been studied and the feasibility of the developed solutions has been evaluated experimentally on a laboratory test bench based on a Permanent Magnet Synchronous Machine (PMSM).

The first chapter has allowed recalling the context of electrical drives in automotive systems.

A state of the art of different diagnostic methods has been presented. The first remark was that the control circuit (control laws and sensors) has the highest failure rate in an energy conversion chain.

In the second chapter, the emphasis was made on the description of the original flexible drive topology designed for the traction and the battery charging. In charging mode, the use of machine windings as inductive filters for the AC / DC converter is one of its features. For the elements of the test bed, a CPU (DS 1006) and a FPGA board (DS 5203) are used for the implementation of the control loops. The general structure of the converter is composed of 3 independent H-bridges.

After the description of the test bed, we've modeled the system for control purposes in traction mode. The implementation of the currents and speed controllers on these devices allowed us to validate the design process based on successive steps of simulation and experimental tests.

Chapter 3 was devoted to the implementation of a position sensor fault tolerant control. First, the different position / speed estimators are studied and their advantages / drawbacks listed. A new estimator based on a differential algebraic approach has been designed and validated experimentally. Then, based on accuracy and implementation criteria, it has been compared to the existing methods. The main advantage of this new estimator is its low computational cost and its good accuracy at low speed, speed range in which traditional methods (Kalman filter

and observer based on EMF) are generally ineffective. Finally, a fault tolerant control with a reconfiguration provided by the algebraic estimator is made and its validity is tested through experimental induced sensor fault. The case of a bias in the measurement and a complete sensor outage are processed. Moreover, the need to use two estimators for the detection and isolation is demonstrated experimentally through a test in adverse operating condition.

In Chapter 4, the phase currents sensors and the DC bus voltage sensor are diagnosed. In this chapter, we've only performed fault detection and isolation. The reconfiguration has not been addressed.

Two methods have been developed for the fault detection and diagnosis of current sensors: an algebraic fault estimator and an analysis of the in the (d,q) reference frame. The isolation step is of great importance because of the use of three phase current sensors.

Thus the two methods are implemented and validated experimentally through fault injections in real time, with an emphasis on the time required for detection. Three fault types are tested: a bias measurement, a gain error and a complete loss of a current sensor. Then, an evaluation on the same operating point has shown that the method based on current waveforms analysis may have a better detection time than the one based on an algebraic approach.

For the DC-link voltage sensor, an observer based on control signals of the inverter and phase currents allowed monitoring the DC voltage.

At the end of this work, several perspectives can be envisaged:

- In Chapter 3, a dead time compensation of the inverter could improve the accuracy of position estimators at low speed. Also, the experimental validation should be extended to the entire torque / speed plane to evaluate the performance of algebraic estimator at very high speed. Reconfiguration possibilities for a fault appearing at high torque in a saturated state are also to be studied.

- In Chapter 4, we should extend the comparison of the developed methods. Indeed, the methods should be tested and compared for different current magnitudes. Fault reconfiguration for the current sensors should also be performed. Although the post-fault reconfiguration solution for a loss of a phase current sensor is trivial when using three sensors, the implementation can be subject to some constraints related to the switching

strategies. Furthermore, it would be interesting to investigate the case where only two sensors are available, that is to say to control the electric drive with only one sensor after a fault.

- Finally, inverter's faults (open & short circuit) could be investigated for a more complete FTC of the electrical drive. From the control point of view, a good starting point would be to use the similarity between an open circuit and current sensor fault with a null gain.

The case of incipient faults should also be addressed with a judicious combination of model-based and data-driven based formulations. It will enhance the detection capability and open the way to prognosis.

Annex 1

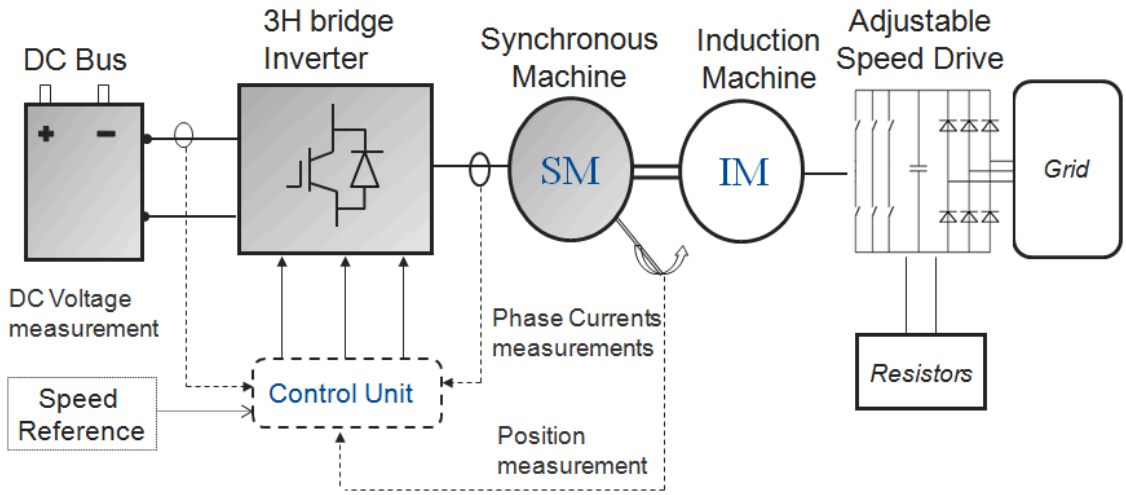

Experimental Test Bench

Asynchronous machine: 5KW, 230/400V, 17 A,

Synchronous machine:

Series Coupling

- Output peak power of 15kW between 3000 and 12000 rpm
- Permanent output power of 10kW between 3000 and 12000 rpm
- Output torque of 29 N.m between 0 and 3300 rpm
- Forced air cooling, ambient temperature inferior to 55° C
- An efficiency superior to 92% over a wide torque/speed range
- DC Link Voltage: 900V ± 20V
- Neutral AC Voltage per phase: 560 V
- AC Current, RMS Value: 15A
- Maximal neutral AC Voltage (at 12720 rpm) : 1850 V

Annex 2

$$\begin{bmatrix} v_a \\ v_b \\ v_c \end{bmatrix} = R_s \begin{bmatrix} i_a \\ i_b \\ i_c \end{bmatrix} + [L_{ss}(\theta)] \frac{d}{dt} \begin{bmatrix} i_a \\ i_b \\ i_c \end{bmatrix} + \omega \frac{d}{d\theta} [L_{ss}(\theta)] \begin{bmatrix} i_a \\ i_b \\ i_c \end{bmatrix} + \begin{bmatrix} e_a(\theta) \\ e_b(\theta) \\ e_c(\theta) \end{bmatrix} \quad (1)$$

Where $[v_a, v_b, v_c]^T$ stands for the stator voltages, $[i_a, i_b, i_c]^T$ the stator phase currents, R_s the stator winding resistance, ϕ_m the flux produced by the magnets and $[L_{ss}(\theta)]$ the stator inductance matrix and is function of the electrical position θ for salient machines. ω is the angular velocity measured in electrical radians per second.

$$L_{ss}(\theta) = \begin{bmatrix} M_{1,1} & M_{1,2} & M_{1,3} \\ M_{2,1} & M_{2,2} & M_{2,3} \\ M_{3,1} & M_{3,2} & M_{3,3} \end{bmatrix}, \quad (2a)$$

$$M_{m,m} = L_{m0} + L_{m2}\cos(2(\theta - (m-1)\frac{2\pi}{3})) + L_{m4}\cos(4(\theta - (m-1)\frac{2\pi}{3}))$$

$$M_{m,n} = L_{mn0} + L_{mn2}\cos(2(\theta - \frac{m+n-2}{2}\frac{2\pi}{3})) + L_{mn4}\cos(4(\theta - \frac{m+n-2}{2}\frac{2\pi}{3}))$$

(2b)

L_{mn0} is the mutual inductance. L_{m2}, L_{m4}, L_{mn2} and L_{mn4} represent the effects of magnetic saliency.

Considering harmonics 1, 3, 5 and 7, the electromagnetic force can be written $\begin{bmatrix} e_a(\theta) \\ e_b(\theta) \\ e_c(\theta) \end{bmatrix}$ as:

$$\begin{aligned} e_a(\theta) &= \omega\phi_m[\sin(\theta) + k_{emf\,3}\sin(3\theta + \phi_{13}) + \\ &\quad k_{emf\,5}\sin(5\theta + \phi_{15}) + k_{emf\,7}\sin(7\theta + \phi_{17})] \\ e_b(\theta) &= \omega\phi_m[\sin(\theta - \frac{2\pi}{3}) + k_{emf\,3}\sin(3(\theta - \frac{2\pi}{3}) + \phi_{13}) + \\ &\quad k_{emf\,5}\sin(5(\theta - \frac{2\pi}{3}) + \phi_{15}) + k_{emf\,7}\sin(7(\theta - \frac{2\pi}{3}) + \phi_{17})] \\ e_c(\theta) &= \omega\phi_m[\sin(\theta + \frac{2\pi}{3}) + k_{emf\,3}\sin(3(\theta + \frac{2\pi}{3}) + \phi_{13}) + \\ &\quad k_{emf\,5}\sin(5(\theta + \frac{2\pi}{3}) + \phi_{15}) + k_{emf\,7}\sin(7(\theta + \frac{2\pi}{3}) + \phi_{17})] \end{aligned} \quad (3)$$

Then, the projection of three phase quantities onto two fixed axes (α,β) is done using Concordia matrix C_{on}:

$$[C_{on}]=\sqrt{\frac{2}{3}}\begin{bmatrix}\frac{1}{\sqrt{2}} & \frac{1}{\sqrt{2}} & \frac{1}{\sqrt{2}}\\ 1 & \cos(\frac{2\pi}{3}) & \cos(\frac{4\pi}{3})\\ 0 & \sin(\frac{2\pi}{3}) & \sin(\frac{4\pi}{3})\end{bmatrix}$$

The rotation matrix $P(\theta)$ needed for the projection in the rotor frame is expressed as follows:

$$[P(\theta)]=\begin{bmatrix}1 & 0 & 0\\ 0 & \cos(\theta) & \sin(\theta)\\ 0 & -\sin(\theta) & \cos(\theta)\end{bmatrix}$$

Applying Concordia transformation and the Rotation to (1) gives:

$$\begin{bmatrix}v_h\\ v_d\\ v_q\end{bmatrix}=R_s\begin{bmatrix}i_h\\ i_d\\ i_q\end{bmatrix}+[L_{ss}(\theta)]_c\frac{d}{dt}\left[[P(\theta)]^T\begin{pmatrix}i_h\\ i_d\\ i_q\end{pmatrix}\right]+\omega[P(\theta)][C_{on}]\frac{d}{d\theta}[L_{ss}(\theta)][C_{on}]^T[P(\theta)]^T\begin{bmatrix}i_h\\ i_d\\ i_q\end{bmatrix}+\begin{bmatrix}e_h(\theta)\\ e_d(\theta)\\ e_q(\theta)\end{bmatrix} \quad (4)$$

Considering that the emf in the three phased frame is given by (3) with $\phi_{13}=\pi,\phi_{15}=\pi,\phi_{17}=0$ being characteristics of SOFRACI topology, the emf in the rotating frame is given by:

$$\begin{aligned}e_h(\theta)&=\omega\phi_m\sqrt{3}k_{emf3}\sin(3\theta)\\ e_d(\theta)&=\omega\phi_m\sqrt{\frac{3}{2}}(k_{emf5}-k_{emf7})\sin(6\theta)\\ e_q(\theta)&=\omega\phi_m\sqrt{\frac{3}{2}}(1+(k_{emf5}+k_{emf7})\cos(6\theta))\end{aligned} \quad (5)$$

Annex 3

Abacus for the response time of $tr_{5\%}.\omega_0$ in function of the damping m

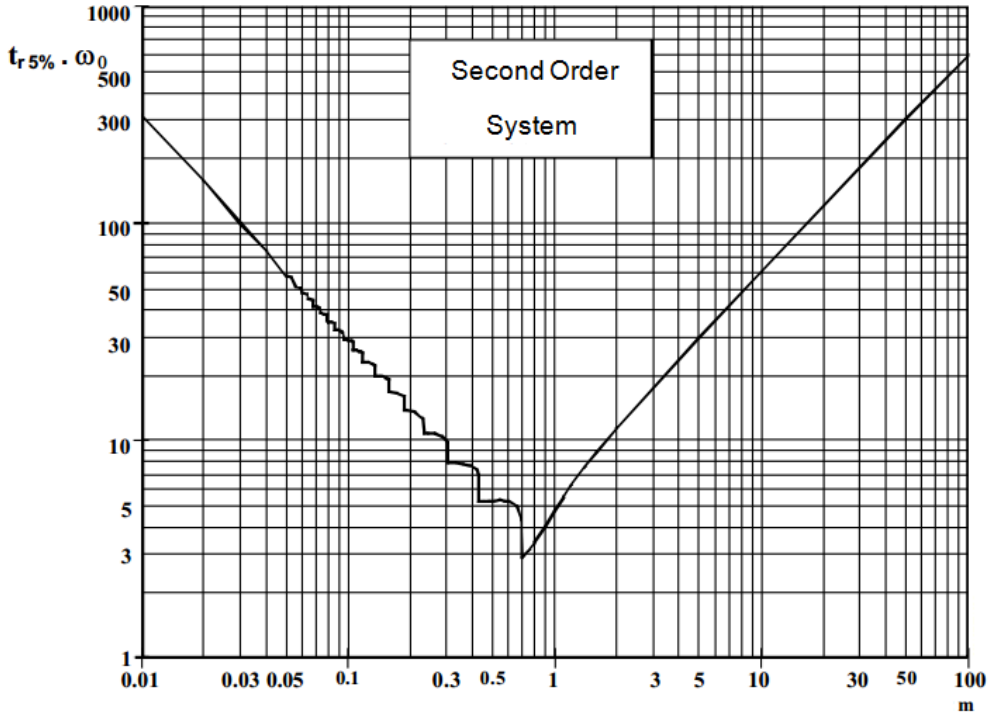

Annex 4

We compare the characteristics of the estimators (EKF and the algebraic estimator) used in sensorless mode. Using the same operating point, we compute theirs speed errors and the associated errors for the *d,q* currents control.

Test with Position Sensor

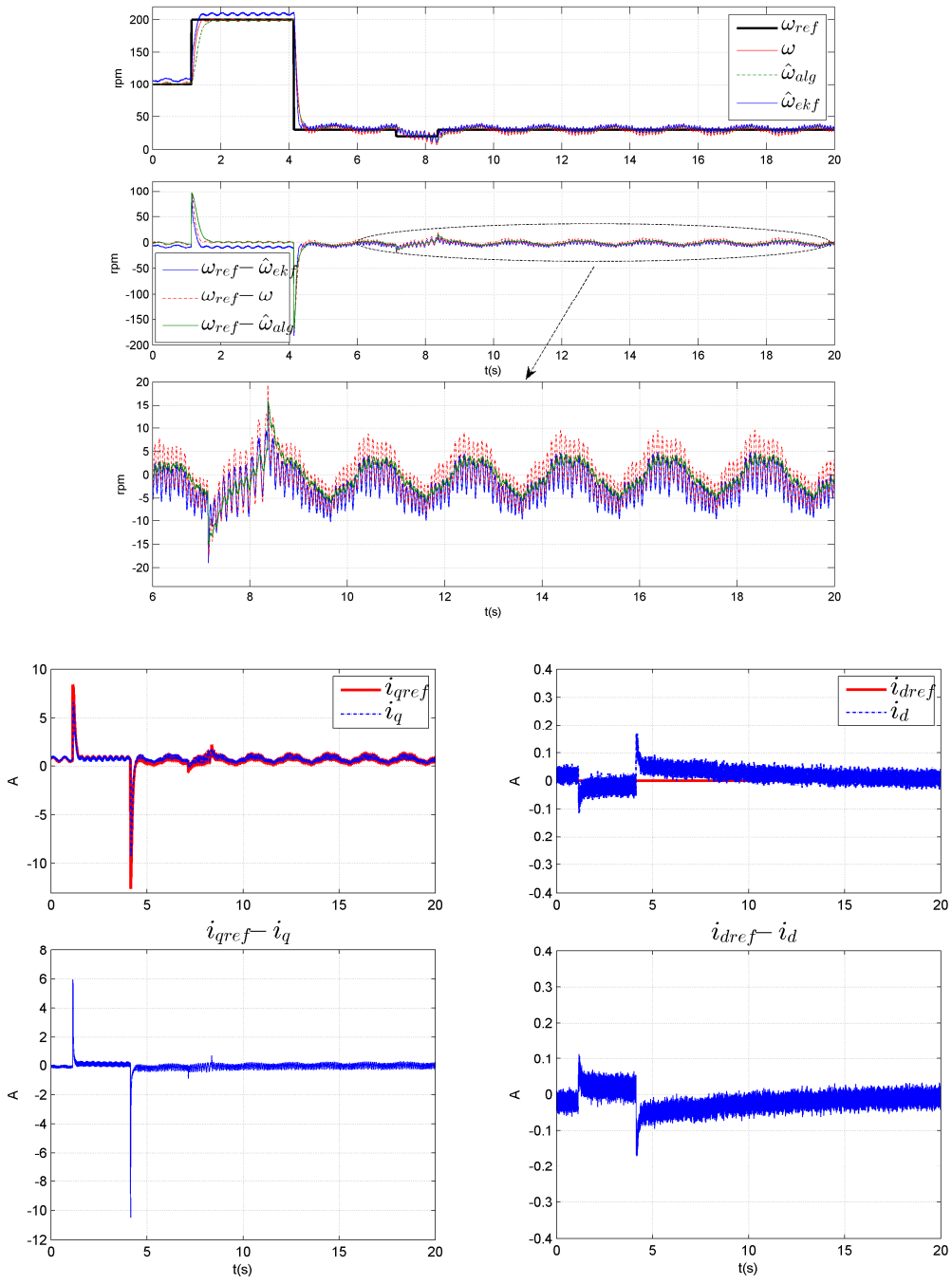

Test in sensorless control with EKF

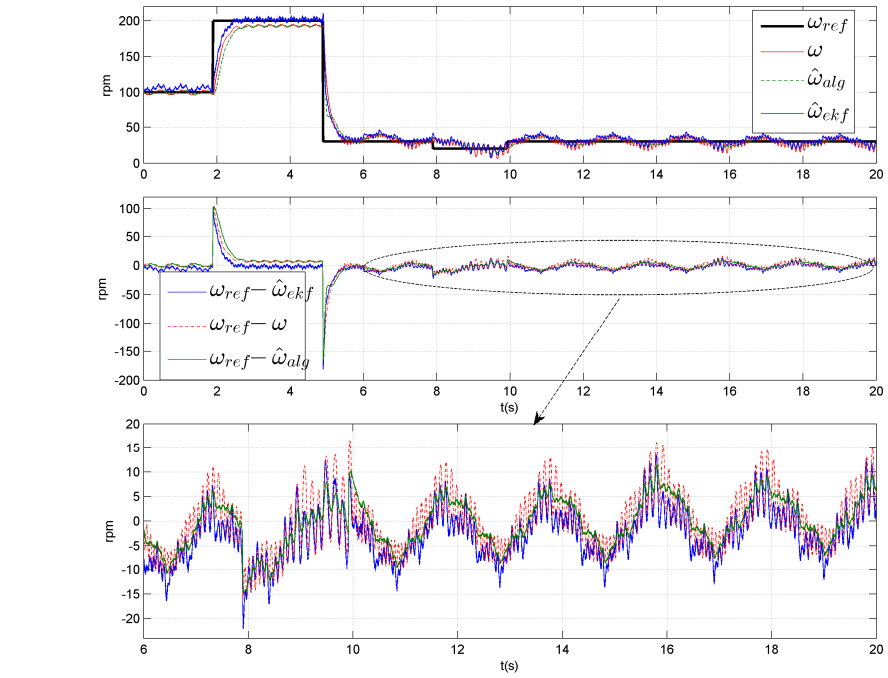

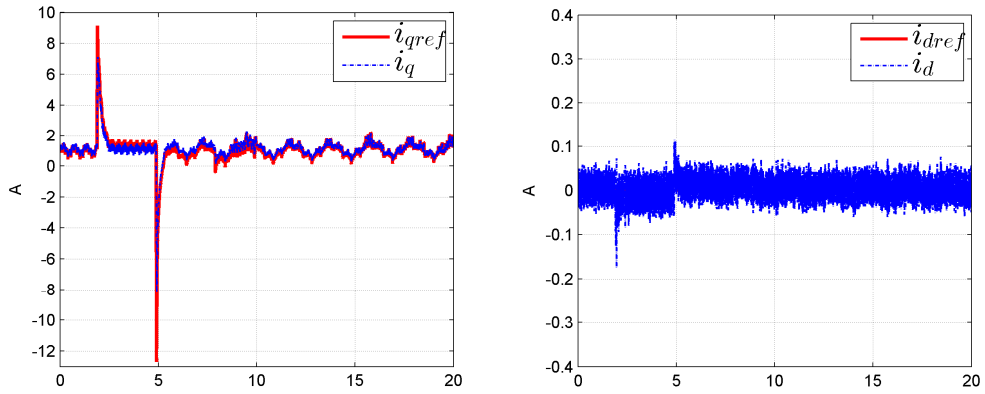

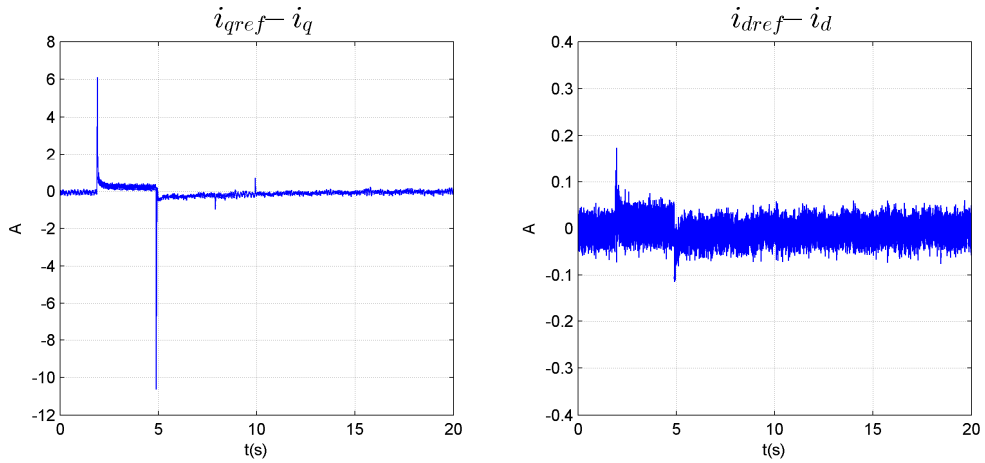

Test in sensorless control with algebraic estimator

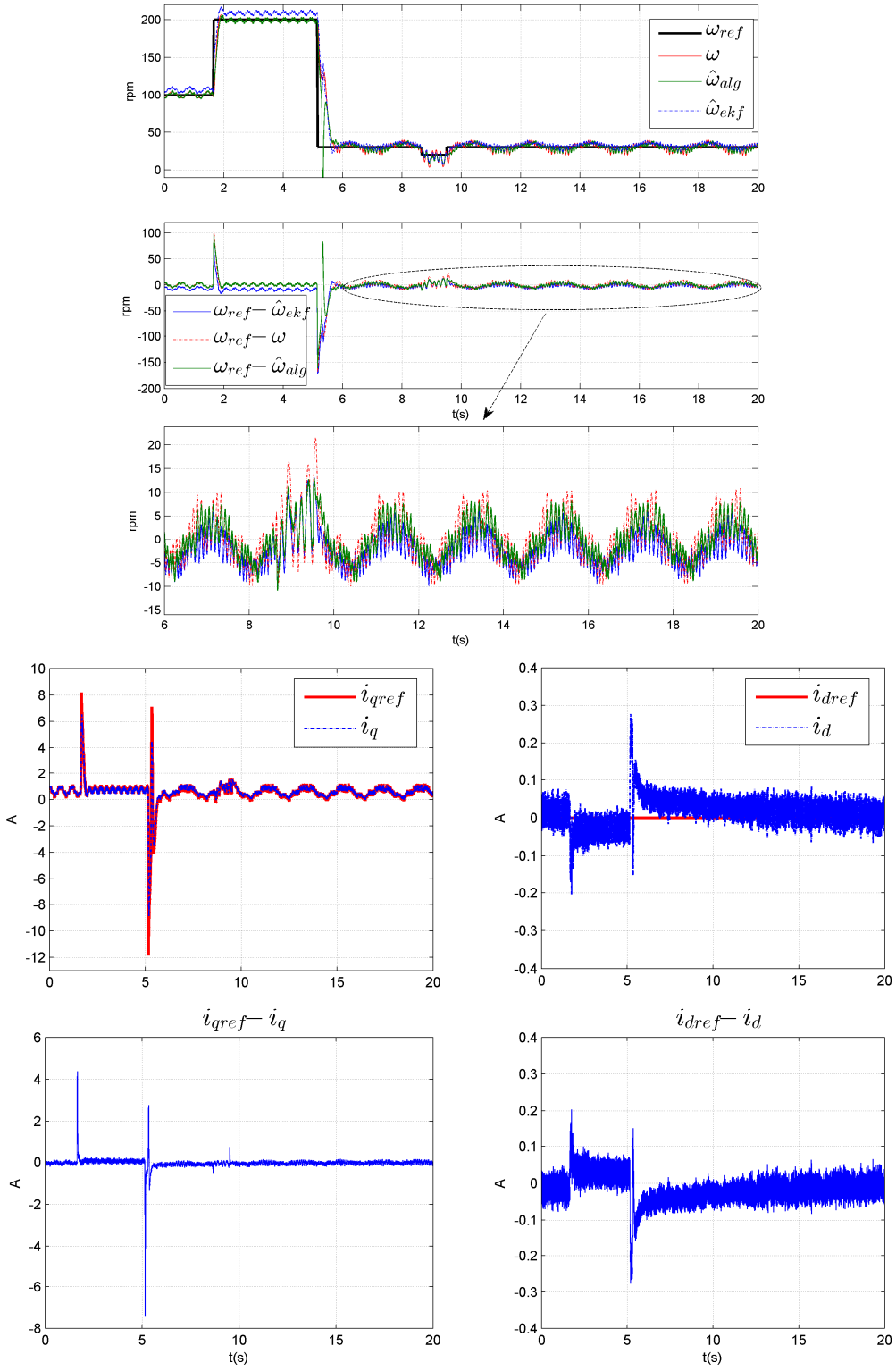

Annex 5

Position Measurement in the Control System

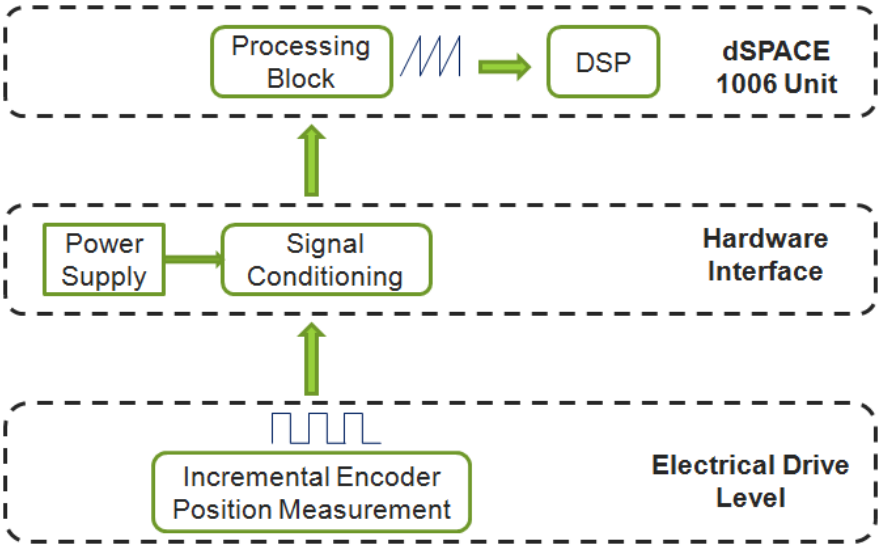

Generally, signals from sensors cannot be directly sent to DSP because the level of voltage output differs with possibilities of input gate of DSP. So a signal conditioning using a hardware interface is necessary to allow a good connection between the sensor and the DSP. Then, a processing block transforms the conditioned rectangular signals in mechanical radians position.

Résumé

La disponibilité de certains capteurs est indispensable pour le contrôle des machines électriques dans une application automobile. Pour pallier une défaillance de ces capteurs, des stratégies sont mises en place pour assurer une continuité de fonctionnement ou un arrêt sûr. Dans le cas de la machine synchrone, les capteurs les plus critiques sont: le capteur de position/vitesse, les capteurs de courant et le capteur de bus de tension continue. C'est dans ce contexte que l'on a développé des algorithmes de commande tolérante aux défauts qui se subdivise en trois parties : détection, isolation et reconfiguration. Ensuite, la validation expérimentale a eu lieu sur un banc composé d'une machine synchrone et d'un onduleur conçus pour la propulsion d'un véhicule électrique. Cette thèse est ainsi organisée en 4 chapitres.

Dans le **premier chapitre**, les défis liés à l'utilisation des entraînements électriques dans l'automobile ainsi que les principes de commande tolérante aux défauts sont rappelés. Les conséquences majeures de certains défauts et les solutions actuelles proposées pour annihiler leur impact sont revisitées.

Le **chapitre 2** décrit le banc de test avec l'application visée. Le système est une architecture novatrice réalisant les fonctions de traction, de régénération et de charge pour un véhicule électrique. Après la modélisation et la simulation de la machine synchrone et son onduleur associé, la commande de l'entraînement électrique est implémentée en temps réel à l'aide de Matlab/dSPACE. Des tests expérimentaux sur le contrôle du couple sont effectués pour illustrer la loi de commande.

Le **chapitre 3** traite de la commande tolérante à un défaut du capteur mécanique de position. Les différents estimateurs de position/vitesse sont étudiés et leurs avantages/inconvénients listés. Ensuite, un nouvel estimateur basé sur une approche d'algèbre différentiel a été conçu et validé expérimentalement. Ensuite, sur des critères de précision et de facilité d'implémentation, il est comparé aux méthodes existantes. Le principal avantage de ce nouvel estimateur est son faible coût algorithmique et sa bonne précision en basse vitesse, plage de vitesse dans laquelle les méthodes traditionnelles (Filtre de Kalman et Observateur basé sur la FEM) sont généralement peu efficaces. Finalement, une commande tolérante aux défauts avec une reconfiguration assurée par l'estimateur algébrique est effectuée et sa validité est testée avec des défauts provoqués expérimentalement.

Le **chapitre 4** est dédié au diagnostic des capteurs de courants de phase et du bus de tension continu. Dans ce chapitre, nous n'effectuons que la détection des défauts et leur isolation, les problématiques de reconfiguration n'étant pas étudiées. Deux méthodes ont été développées pour les capteurs de courant : une approche basée sur du traitement de signal et une approche algébrique de diagnostic. L'étape d'isolation revêt une grande importance du fait de l'utilisation de 3 capteurs pour les courants.

Ainsi les deux méthodes sont implémentées et comparées expérimentalement à travers des injections de défauts en temps réel, avec un accent mis sur le temps nécessaire à la détection. Pour le capteur de bus de tension continue, un observateur construit à partir des signaux de commande de l'onduleur et des courants de phase a permis la surveillance de la mesure de tension continue.

Mots clés : Commande sans capteur, Diagnostic, Observateurs, Capteurs, Machine synchrone